UNIVERZITET U NOVOM SADU
PRIRODNO-MATEMATIČKI FAKULTET
DEPARTMAN ZA FIZIKU

UNIVERZITET U GENTU
PRIRODNO-MATEMATIČKI FAKULTET
DEPARTMAN ZA FIZIKU I ASTRONOMIJU

Mina Petrić

Modeliranje uticaja meteoroloških uslova na dinamiku populacije komarca vektora (Diptera: Culicidae)

-doktorska disertacija-

Novi Sad, 2020.

Modelling the influence of meteorological conditions on mosquito vector population dynamics (Diptera, Culicidae)

May 19, 2020

Thesis committee:

Promotors:
Prof. Dr. Branislava Lalić
University of Novi Sad

Prof. Dr. Piet Termonia
Ghent University

Prof. Dr. Milica Pavkov Hrvojević
University of Novi Sad

Dr. Bert Van Schaeybroeck
Royal Meteorological Institute of Belgium

Industrial promotors:
Dr. Els Ducheyne
Avia-GIS NV

Cedric Marsboom
Avia-GIS NV

Committee members:
Dr. Guy Hendrickx, Avia-GIS NV
Prof. Dr. Vladimir Djurdjević, University of Belgrade
Prof. Dr. Rafiq Hamdi, Ghent University
Prof. Dr. Igor Balaž, University of Novi Sad
Prof. Dr. Herwig Dejonghe, Ghent University

Mina Petrić
Modelling the influence of meteorological conditions on mosquito vector population dynamics (Diptera, Culicidae)

Dissertation presented in partial fulfilment of the requirements for the double degree of Doctor of Science: Physics by UGent and UNS. Academic year 2019–2020

Acknowledgements

I would like to thank my supervisors, Piet, Bert, Branislava, Milica, Cedric and Els for all their support, for everything I have learned from them along the way and for offering me the opportunity to do research on this interesting topic, where physics and mosquitoes communicate.

Bert, thank you for always insisting on the principle of minimum entropy production. A lot of energy went into the construction of this thesis, and the tendencies were not always linear. I very much appreciate the direction and motivation I received from Piet at every progress meeting; thank you for opening new doors of thought and exciting avenues for future research. Branislava and Els, thank you for believing in me. You were the ones who reminded me to pause, and take a breath, and always helped me see the broader picture - bringing to mind the universal postulate of all galactic travellers: DON'T PANIC (and always carry a towel with you). Thank you, Cedric, for creating time when there was none. We all know that time manipulation spells are reserved for 7^{th} level wizards (i.e. high-level engineers). This thesis would not be possible without your support.

Moreover, I would like to personally thank the following people, who assisted with their advice, discussions and guidance: Prof. Dr. Rafiq Hamdi, Prof. Dr. Abdellah Touhafi, Ayman Mohamed, Dr. Daan Degrauwe, Ward Bryssinckx, Dr. Veerle Versteirt, Wesley Tak, Iva Gagović, Vanja Kovač, Tatjana Ostojin and Ana Svetličić.

Thank you, Danilo, for being a worthy adversary. To my family, thank you for your unconditional love and support. Gustav, thank you for being there during the hardest times. I would also like to thank Dr. Guy Hendrickx and Avia-GIS for allowing me to continue pursuing valuable and useful knowledge. Lastly, I would like to thank all the people who are fighting to make knowledge and educational content open and freely available to everyone.

I dedicate this thesis to Tara, the light of my life.

Mina Petrić

Antwerp, February 2020

Abstract

Meteorological conditions have a significant influence on the time of occurrence, abundance and activity of the mosquito vector. In the current context of climate change, it is of great importance to assess the impact of shifts in climatic conditions on the suitability for the establishment and annual activity of the vector species. Moreover, changes in the variability of meteorological elements and their extremes can generate unexpected changes in the mosquito vector population which in turn have an important effect on human health. One of the ways to put these causes and effects into perspective is to simulate the activity of the vector within a process-based framework which allows for the analysis of the contribution of individual factors on the different life stages of the vector. Such analysis is presented by the use of sophisticated dynamical models simulating the characteristics of the biological population, forced by observed meteorological data, capturing the local micro-environment of the vector habitat, and validated by the observed entomology.

Numerical models are being developed to model vector population dynamics and the expected circulation of the virus within a closed system. Two modelling approaches are standardly applied to modelling vector population dynamics: Mechanistic and Stochastic. The advantage of mechanistic over statistical models is that they can provide a deterministic framework allowing for the isolated evaluation of each input parameter and their effect on the modelled system. Mechanistic dynamical models are used to describe the biophysical processes or part of the process as a response to changes in the meteorological conditions.

The work carried out in this thesis can be summarized as follows: (i) Analysis of the association between the most important abiotic drivers influencing the population dynamics, annual activity and time of occurrence of *Culex pipiens* and *Aedes aegypti*; (ii) Identifying the most important climatic factors and model settings as a function of climatic characteristics of the study region; (iii) Modelling the vector population dynamics and stability analysis of the dynamical system (iv) Analysis of different verification techniques and implications in terms of model application; (v) Feasibility analysis of improving the model with a Land-Surface Parameterization scheme and short-range forecasting of pest population dynamics.

Sažetak

Meteorološki uslovi bitno utiču na vreme pojave, brojnost vektora i njihovu aktivnost. U uslovima evidentnih promene klime, od ogromne je važnosti sagledati uticaj očekivanih promena klime na pogodnost uslova na pojavu izabranih vektora. Takodje, značajne promene kolebanja meteoroloških elemenata u odnosu na višegodišnji prosek i sve češće pojave nepovoljnih vremenskih prilika dovode do neočekivanog ponašanja populacije komarca što značajno utiče na kvalitet života i zdravlje ljudi. Jedini način da se sagledaju uzroci i posledice navedenih pojava zasniva se na simulaciji aktivnosti i brojnosti vektora uz mogućnost testiranja uticaja svakog pojedinačnog faktora. Ovu mogućnost pružaju samo visoko sofistikovani dinamički modeli koju su prošli proces kalibracije i validacije zasnovan na izmerenim vrednostima meteoroloških elemenata i karakteristika biološke populacije.

Sofistikovani modeli za simulaciju dinamike populacije vektora i očekivane cirkulacije vektorskih transmisivnih bolesti se koriste sa ciljem modeliranja potencijalnog rizika od zaraze i epidemije. Modeli za simulaciju dinamike vektora mogu da se podele na dve glavne grupe: Mehanističke i Statističke. Prednost mehanističkih modela nad statističkim je što mogu da se koriste za evaluaciju uticaja izolovanog faktora na dinamički sistem i odgovarajuće promene brojnosti unutar svake faze u razvoju vektora. Mehanistički dinamički sistemi se koriste kako bi se opisao mehanizam biofizičkog procesa ili dela procesa u zavisnosti od forsirajuće veličine.

Predmet istraživanja u ovom radu jeste identifikovanje najznačajnijih bioloških i fizičkih procesa kao i odgovarajućih faktora koji utiču na brojnost i aktivnost vektora roda *Aedes* i *Culex*. Ciljevi istraživanja mogu da se sumiraju na sledeći način: (i) analiza najznačajnijih meteoroloških parametara koji utiču na vreme pojave, brojnost i aktivnost vektora *Aedes* i *Culex* roda; (ii) definisanje najznačajnijih klimatskih faktora i stepena osetljivosti procesa na njih; (iii) modeliranje dinamike populacije vektora i analiza stabilnosti dinamičkog sistema; (iv) verifikacija i analiza metoda verifikacije i validacije dinamičkog modela; (v) kratkoročna prognoza dinamike populacije komarca i formulacija hidrološkog modula upotrebom SURFEX površinske šeme sa ECOCLIMAP fiziogeografskim podacima.

Samenvatting

Meteorologische omstandigheden hebben een significante invloed op het tijdstip van voorkomen, het aantal en de activiteit van de muskiet vector. In de huidige context van klimaatverandering is het van groot belang om de verwachte impact van verschuivingen in klimatologische omstandigheden in te schatten op de geschiktheid voor de vestiging en de jaarlijkse activiteit van de vectorsoort. Bovendien kunnen veranderingen in de variabiliteit van meteorologische elementen en hun extremen, onverwachte veranderingen in de populatie van muggenvectoren veroorzaken die op hun beurt een belangrijk effect hebben op de menselijke gezondheid. Eén van de manieren om deze oorzaken en gevolgen in perspectief te plaatsen, is door de activiteit van de vector te simuleren binnen een procesgebaseerd kader dat de bijdragen van individuele factoren op de verschillende levensfasen van de vector analyseert. Een dergelijke analyse wordt uitgevoerd door gebruik te maken van geavanceerde dynamische modellen voor het simuleren van de eigenschappen van de biologische populatie, gedreven door waargenomen meteorologische gegevens, het incorporeren van de lokale micro-omgeving van de vectorhabitat en gevalideerd door de waargenomen entomologie.

Numerische modellen worden ontwikkeld om vectorpopulatiedynamica en de verwachte circulatie van het virus binnen een gesloten systeem te modelleren. Twee modelleringsbenaderingen worden standaard toegepast op dynamische vectorpopulatie modellen: mechanistisch en stochastisch. Het voordeel van mechanistisch ten opzichte van statistische modellen is dat ze een deterministisch raamwerk kunnen bieden voor de geïsoleerde evaluatie van elke invoerparameter en hun effect op het gemodelleerde systeem. Mechanistische dynamische modellen worden gebruikt om de biofysische processen of een deel van het proces te beschrijven als een reactie op een verandering in een meteorologische toestand.

Het werk in dit proefschrift kan als volgt worden samengevat: (i) De analyse van het verband tussen de belangrijkste abiotische factoren die de populatiedynamiek, de jaarlijkse activiteit en het tijdstip van aanwezigheid van *Culex pipiens* en *Aedes aegypti* beïnvloeden; (ii) De identificatie van de belangrijkste klimatologische factoren en modelinstellingen als functie van de klimatologische kenmerken van de onderzoeksregio; (iii) De dynamische modellering van de vectorpopulatie en stabiliteitsanalyse van het dynamische systeem. (iv) De analyse van verschillende verificatietechnieken en de implicaties voor de toepassing van het model; (v) De haalbaarheidsanalyse van het verbeteren van het model met een parametrisatie voor het landgebruik en voorspelling op korte afstand van de dynamiek van de plaagpopulatie.

Contents

List of Figures

List of Tables

List of Abbreviations

ABOS	All But One At a Time
ACF	Autocorrelation Function
ADF	Augmented Dickey Fuller
ASMR-E	Advanced Microwave Scanning Radiometer for EOS
AUC	Area Under the ROC curve
BS	Brier Score
CCF	Cross Correlation Function
CCM	Cross Correlation Maps
CEM	Climate Envelope Model
CLC	Calculus of Looping Sequence
CLC	Corine Land Cover
COI	Cone of Influence
CVM	Contingency Verification Measures
DCW	Digital Chart of the World
DMPS-OLS	Defense Meteorological Satellite Program Operational Linescan System
DRHR	Diurnal Relative Humidity Range
DTR	Diurnal Temperature Range
EAO	East Atlantic Oscillation
EAWR	East-Antarctic West Russia
EBF	Evergreen Broadleaf Forest
EM	Exploratory Methods
ENSO	El Niño–Southern Oscillation
EO	Earth Observation
EOS	NASA Earth Observing System
FB	Frequency Bias
FPR	False Positive Rate
GAM	Generalized Additive Model
GIS	Geographic Information System
GLM	Generalized Linear Model
HSI	Habitat Suitability Index
IFS	Integrated Forecast System
ITCZ	Intertropical Convergence Zone
JJA	June July August
KPSS	Kwiatkowski-Phillips-Schmidt-Shin
LAI	Leaf Area Index
LCCS	Land Cover Classification System
LHS	Latin Hypercube Sampling
MCDA	Multi Criteria Decision Analysis
MJO	Madden-Julian Oscillation
MLP	Multi-Layer Perception

NAO	North Atlantic Oscillation
NIR	No Information Rate
NN	Neural Network
NRT	Near Real Time
NTL	Night Time Light
NWP	Numerical Weather Prediction
ODE	Ordinary Differential Equation
OFAT	One Factor At a Time
OR	Odds Ratio
ORSS	Odds Ratio Skill Score
PACF	Partial Autocorrelation Function
PC	Percentage Correct
PDL	Polynomial Distributed Lag
RF	Random Forest
RMSE	Root Mean Square Error
ROC	Receiver Operating Characteristic
SDM	Species Distribution Model
SST	Sea Surface Temperature
TPR	True Positive Rate
VBD	Vector Borne Disease
WFD	Windowed Fourier Decomposition
WG	Wooded Grassland
WNV	West Nile Virus

Chapter 1

Introduction and research objectives

1.1 Motivation and research rationale

Vector borne disease (VBD) are diseases whose pathogen is transmitted by arthropods which can carry the disease between infected and susceptible humans.

Over 500 million people are infected by Vector Borne Disease (VBD) every year. WHO estimates that, annually, over 3 billion people are at risk of contracting a VBD, of which a large proportion is diseases transmitted by mosquito vectors. More than 2.5 billion people are at risk of contracting Dengue alone, and Malaria causes 600,000 deaths every year globally. The transmission rate during an epidemic is proportional to the population density of the disease vector.

The importance of modelling the population dynamics of the mosquito vector is largely connected to the wide number of VBDs that mosquitoes can transmit. Mosquitoes belonging to the *Aedes* and *Culex* genera are vectors for West Nile virus, Saint Louis encephalitis, Japanese encephalitis, Zika, Dengue and Chikungunya. Proper surveillance and subsequent modelling of the impact that pests and disease have on human health is a pressing issue in numerous segments.

The research topic of this thesis is the identification of the abiotic drivers influencing the time of occurrence, population dynamics and annual activity of two important vectors species in the *Aedes* and *Culex* genera for study locations in (i) Guadeloupe, (ii) Egypt and (iii) Serbia.

1.2 Main objectives

The main research objectives can be summarized as follows: (i) Analysis of the association between the most important abiotic drivers influencing the population dynamics, annual activity and time of occurrence of *Culex pipiens* and *Aedes aegypti*; (ii) Identifying the most important climatic factors and model sensitivity depending on the climatic characteristics of the study region; (iii) Modelling the vector population dynamics and stability analysis of the dynamical system (iv) Analysis of different verification techniques and implications in terms of model application; (v) Feasibility analysis of improving the model with a Land Surface Parameterization scheme and short-range forecasting of pest population dynamics.

1.3 Working structure and thesis roadmap

This thesis consists of five main parts. Following a theoretical introduction in Chapter 2 and overview of methods in Chapter 3, the first part (Chapter 4) deals with time-series analysis in which the main meteorological drivers and their association with the observed entomological series are analysed. The second part (Chapter 5) is an assessment study of the broader climatic suitability for the *Culex* and *Aedes* vectors. The third part (Chapter 6) is the simulation of daily dynamics of the vector population and numerical considerations and stability analysis of the ODE dynamical system.

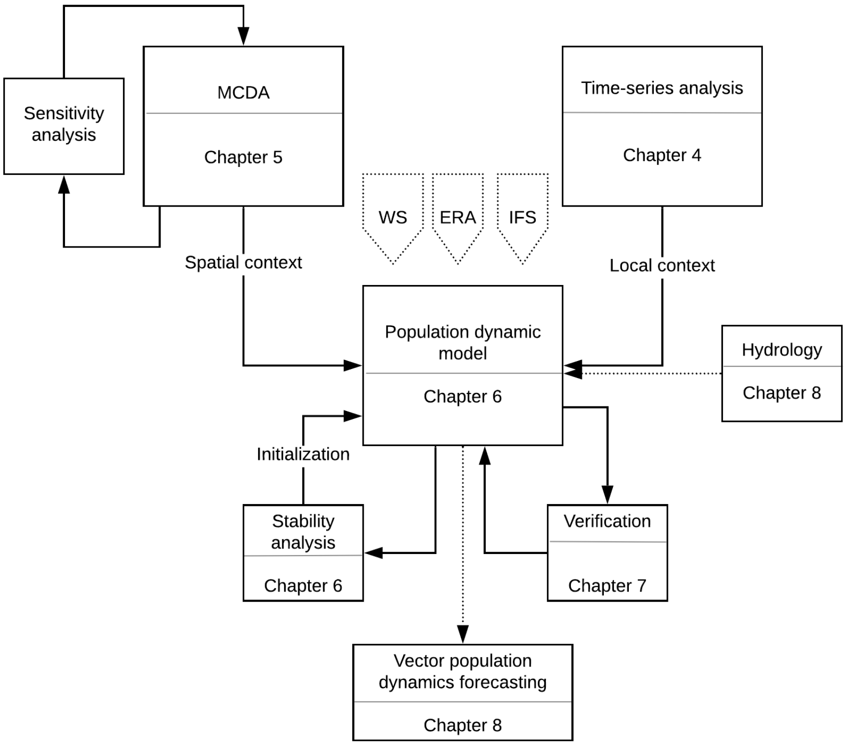

Figure 1.1: Schematic overview of the thesis structure.

The fourth part (Chapter 7) deals with the analysis of different verification methods applied to the validation of the dynamical model. The fifth part (Chapter 8) consists of two use-case scenarios in which the feasibility of improving the model with a hydrology scheme and a possible framework for forecasting the pest population dynamics are explored. Finally, an outline of additional work carried out for (i) the impact of climate change on the suitability for the establishment of an invasive vector species in Serbia and Montenegro; (ii) The feasibility of integrating an environmental Wireless Sensor Network system together with EO and GNSS to force the population dynamics model in near-real time; (iii) Gap-filling of hourly air temperature data with debiased ERA5; (iv) WNV ciruclation and the expected impact of climate change on the malaria vector in Serbia; is given in the Appendix.

Chapter 2

Theoretical introduction

2.1 The influence of abiotic environmental factors on the different life stages of the mosquito vector

Mosquitoes remain one of the most dangerous pest groups because of the many diseases they can transmit. They are poikilothermic arthropods with over 35000 species, order Diptera, family Culicidae. Because of their inability to control their body temperature they are tightly linked to their surrounding environment and maintain a similar or slightly higher temperature than that of the local environmental. Mosquitoes from the *Culex* and *Aedes* genus are differently adapted to the abiotic constrains of their surroundings and thus exhibit different global distributions.

Aedes aegypti originated in Africa and was subsequently transported to America during the period of transatlantic slave trade in the 16^{th} century [6]. To date, it spread globally inhabiting most tropical and sub-tropical regions. Unlike *Ae. albopictus* it did not develop a diapause mechanism and is not suited to overwinter in the colder regions of the higher latitudes.

Mosquitoes of the *Culex pipiens* complex are one of the most common and widespread mosquitoes. Adults from the population diapause during winter, finding shelter in areas that can remain relatively warm during the colder months such as basements and sheds, and start a new generation in spring, typically when outdoor temperatures reach 10 °C, and have several generations per year [7,8].

The global distribution map for *Ae. aegypti* and *Cx. pipiens* is shown in Figure 2.1 indicating the current distribution of both species. Due to its ecology, *Ae. aegypti* is mostly confined to the tropical and subtropical belt [9]. On the other hand, species from the *Cx. pipiens* complex (*Cx. pipiens*, *Cx. quinquefasciatus*) have a worldwide distribution and have justly, due to their eurytopic nature, earned the name northern and southern “house mosquito”, respectively. The vector has been recorded everywhere except the Arctic circle.

The key climatic variables that have been linked to the ability of the mosquito vector to survive and be active in a certain area are rainfall and temperature [10–19]. Regarding the climatic suitability of *Aedes* mosquitoes most ex-

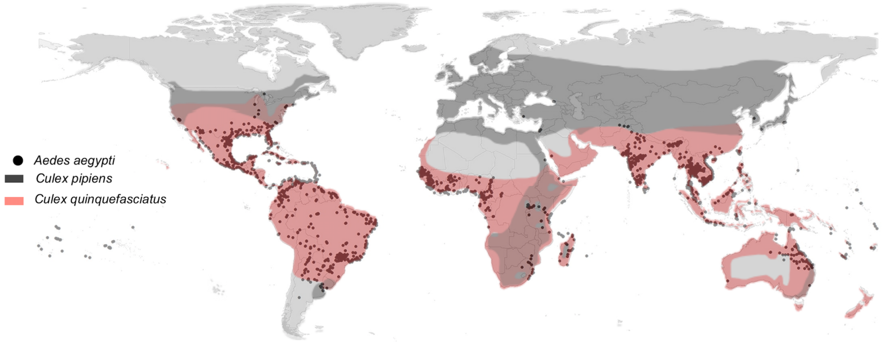

Figure 2.1: Geographic distribution of *Aedes aegypti* (black points) and *Culex. pipiens* (gray) and *Culex quinquefasciatus* (red), adapted from surveys conducted in 2018 for *Ae. egypti* [1] and 2019 for *Cx. pipiens* [2–4].

isting literature was carried out for *Aedes albopictus* [20]. The major difference between these two species is that *Ae. albopictus* has developed an overwintering mechanism which allows him to survive in colder latitudes. Moreover, *Ae. albopictus* has been found to be more tolerant to colder temperatures in general [21]. The most significant parameters linked with vector suitability are the annual and seasonal average temperatures, mean monthly temperature of the coldest month, annual precipitation and frequency of rainy days [10,17–19]. The annual start of activity has been linked to spring temperatures; however, the overall annual activity is mostly linked to the June-July-August (T_{jja}) air temperature and annual precipitation [17]. The northern range of both the *Ae. aegypti* and *Ae.albopictus* vectors is limited by winter temperatures and annual precipitation [10]. *Aedes albopictus* has been found to overwinter in areas with the mean January temperature (T_{jan}) as low as -4 °C [22], while *Ae. aegypti* cannot survive winters bellow T_{jan} = 10 °C [23–26]. In a recent study by Ducheyne et al. [27], data from the *Ae. aegypti* and *Ae. albopictus* compendia by Kramer et al. [28] was used in a Random Forest (RF) modelling framework with a set of 25 variables to build a distribution model for this region and compare the relative importance of the predictors using the Gini impurity criterion. The result indicted that the most important variable for *Ae. aegypti* for the East Mediterranean region was precipitation, while the most important variables for *Ae. albopictus* was night-time light and human population density [27].

Mosquito populations are influenced by weather on different scales: (i) Climatic suitability outlines the niche in which the vector can survive and the expected annual window of activity; (ii) Daily and weekly weather drives the inter-annual population dynamics and has an effect on the development and mortality rates of the different stages in the mosquito life-cycle.

The vector transitions through four main stages during development: (i) Egg, (ii) Larva, (iii) Pupa and (iv) Adult (Figure 2.2). Eggs are deposited on the surface of the water one at a time (*Aedes*) or tied together in raft-like formations (*Culex*). *Aedes* species mostly breed in artificial containers in urban areas, especially *Ae. aegypti* which is extremely anthropophilic. On the other hand, *Culex pipiens* can breed in urban as well as rural areas in a wide range of natural and artificial sites [7, 8]. *Aedes* eggs have anti-desiccation mechanism in place and can start the development process only when they come in contact with water, *Culex* eggs do not have this property and need to be deposited directly on water surface. After the eggs come into contact with water the development into larvae usually happens within 48 hours depending on the species and the temperature. The larva is the most active aquatic stage and the only stage that can navigate the water freely and feed. The larva feeds on the microorganisms and other organic matter in the water and has a specific siphon tube apparatus for breathing oxygen and hanging from the surface. The larva goes through four instar transformations, becoming bigger each time, before it transforms into a pupa. The larval development can be up to eight times longer than the egg development and three to four times longer than the pupa development. The pupa is an immobile resting phase, where the organism has accumulated enough food and is preparing for the final transformation into an adult. The emerging adult rests for a short while allowing for its wings to dry and body to adjust to its new surroundings. Within the adult phase the female mosquito goes through several cycles of mating, searching for blood, gestating and depositing the eggs, so the development of the next generation can commence. The adult female can survive up to 5 months or longer; however, due to high adult mortality, the average female life span is about 6 weeks, with males living only around a week on average [29].

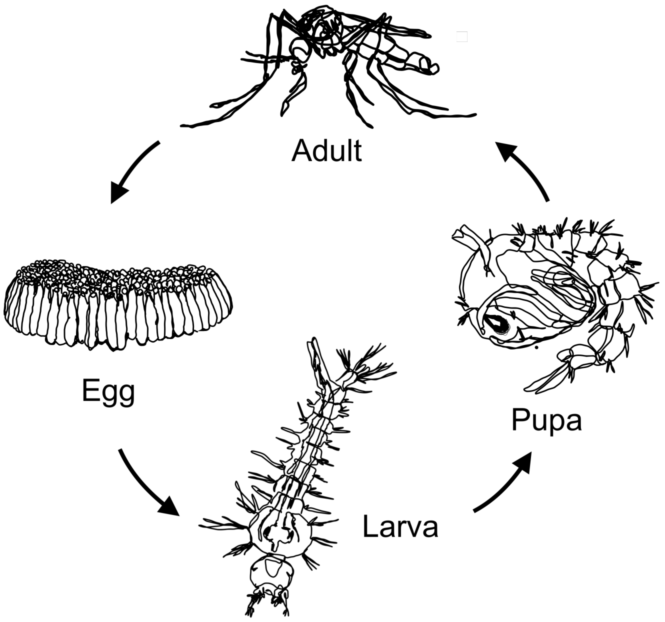

Figure 2.2: Schematic description of the mosquito life cycle.

The lower temperature limit for *Ae. aegypti*, below which movement ceases and mosquitoes enter a torpid state, was determined to be 10 °C [30–33]. The temperature range suitable for activity is 16 °C – 32 °C, with 21 °C being the optimal recorded temperature, in terms of flight duration and average-distance-flown for adults [30, 34]. Interestingly, the maximum flight speed was observed at 32 °C and 50% relative humidity (34 m/min, [30]). The frequency of wing beats increases with temperature, with 365 beats per second observed at 18 °C and 427 beats per second at 25 °C [30]. The mosquito is no longer capable of taking a blood meal at temperatures above 36 °C [33], while temperatures above 40 °C are lethal [30, 33]. Similar temperature ranges are observed for the immature larval stages of *Ae. aegypti* with the upper lethal bound observed at 34 °C and most larvae becoming motionless and dying within a couple of days at temperature below 16 °C, with more rapid mortality occurring at temperatures below 14 °C or above 38 °C [30, 33, 35]. Ranges of the daily diurnal curve above 20 °C were observed to have a negative effect on adult survival [30].

Both adults and immatures of *Cx. pipiens* are more adapted to colder temperatures than *Aedes* species. The lowest temperature under which adult activity stops was reported to be 9.8 °C for females and 8.4 °C for males [36–39]. Complete mortality for adults was observed at 35 °C [37]. Results indicated that longevity was already significantly reduced at temperatures above 27.5 °C [37], no eggs were laid at 32.5 °C and only 20% survival was observed at 30 °C.

The upper limit for the development of immature stages is drastically reduced already at 32.5 °C and completely ceases at 35 °C [36, 37], while the lower limit was found between 11.09 –12.47 °C. The most comfortable range for *Cx. pipiens* development was determined at 15 - 32.5 °C [37]. Ciota et al. [5] examined the effect of a range of temperatures, between 16–32 °C on the life history characteristics of *Culex* vectors. The survival of the immature stages was highest at 16 °C [5].

2.2 Time series analysis

The major aims in current ecological research are directed towards defining the nature of order in biological systems, the separation of endogenous and exogenous interactions and their impact on population growth [40, 41]. Since a precise parameterization of these interactions is very difficult, empirical derived relationships are often used, as well as retrospective time-series analysis, that strongly depend on the quality and frequency of the collected data [42]. Time-series analysis can identify changes in variance of the observed system, as well as emerging periods, which can later be compared with the simulated dynamics. Cazelles et al. [43] point out that transient dynamics appears to be the rule rather than the exception in biological systems, either because of a strong response of the poikilothermic population to changes in the forcing environment, or because of complex endogenous dynamics. The extent of this influence will be different depending on the study location. In temperate, mid-latitude zones only a small percent of the vector population goes through overwintering, effectively reducing the population to zero, while the seasonal peaks is usually achieved in the warmest month. However, even in tropics where the seasonal character of the driving meteorology is less pronounced, and the mosquito is active throughout the year, smaller variations in temperature still influence the mortality and development rates on smaller scales. Because of the cumulative effect of annual, seasonal, and generational variations in the time-series, they are most often non-stationary and traditional time-series analysis methods such as the Fourier and harmonic decomposition cannot be applied directly. Several methods can be utilised to study non-stationary time-series. For example, the Wavelet approach allows us to observe changes in the principal periods and variance as a function of time and does not adhere to the restriction of stationarity. Moreover, in order to find global covariates between the environmental and ecological time-series, the cross-correlation function applied to the lagged values of the more stationary anomaly field of the time series can be explored. Finally, analysing the time interval lagged correlation provides a natural way to model cumulative changes in the forcing by abiotic variables such as precipitation. Several studies used time-series analysis applied to forecasting the dynamics of vector populations [42, 44] and dynamics of VBD virus incidences [42, 45, 46]. The aim in this thesis is mostly exploratory, to show the same species can have a different empirical response to the forcing meteorology at two different locations. This type of analysis can then be used to guide the parameterization of the endogenous and exogenous processes in vector populations [41, 42, 44].

2.3 Modelling the climatic suitability

A climatic assessment study of the suitability of the long-term averaged meteorological characteristics of a particular area for the establishment and annual activity of a vector species is an important consideration for the assessment of potential risk and identification of possible hotspots for vector development and subsequently disease circulation. Particularly, this type of analysis can contribute to the vulnerability assessment of a particular region to the introduction of a new invasive vector species. Two types of models can be distinguished within this topic of research: (i) correlative species distribution models (SDMs); (ii) process-based climatic suitability models. Correlative SDM models employ a top-down stochastic approach based on vector presence/absence data and their association to various abiotic drivers [19, 47–51]. The drivers are usually bioclimatic long-term averages derived from temperature and rainfall climate normals [52]. Process-based models, on the other hand, employ a bottom- up approach, do not require presence/absence vector data and are based on empirical knowledge regarding the known vector ecology [17–19].

Vector SDMs are usually constructed using the following statistical modelling infrastructure: (i) Generalized linear models (GLMs) [50, 53–55]; (ii) Generalized additive models (GAMs) [55, 56]; (iii) Climate envelope techniques (CEMs) [57]; (iv) Random Forest (RF) [27, 50, 54]; (v) Neural networks (NNs) [55].

Jeschke and Strayer [57] considered different studies comparing the performance of different SDM models and found that newer techniques such as model-averaging RF and the Bayesian Weight of Evidence model performed better than older, more widely used methods [58–60]. However, they also stress that the modelling approach needs to be tailored to the application and species.

Process-based models rely on vector physiological thresholds to build the suitability algorithm based on extending research governing the climatic and environmental factors affecting vector populations. These thresholds are usually measured in laboratory conditions and climate chambers and then translated to field populations. Severally widely used modelling techniques in this subcategory are: (1) Mechanistic GIS-based models [10] (2) Multi Criteria Decision

Analysis (MCDA) [16, 18, 22, 61] ; (3) Seasonal activity cut-off models [17].

Because they are process-driven and deterministic, unlike statistical models, they allow for an explicit and direct analysis of the mechanism driving a simulated increase or decrease of vector suitability and generate a broader forum for shared understanding and discussion.

2.4 Vector population dynamics models

A population is defined as "a group of individuals of the same species that occupy a particular area" [62, 63] and population dynamics as the aspect of population ecology dealing with forces that affect changes in population densities or affecting the form of population growth [64].

The change in population density for the mosquito vector occurs as a result of a complex set of interactions between the individuals of the same species, interaction between individuals of different species, interaction with the environment, breeding site availability, food supply etc. [62]. There are different modelling techniques that can be used to simulate this type of population dynamics.

Similar to climatic models, two modelling approaches that are standardly applied to modelling vector population dynamics are: Mechanistic (deterministic models) [65–74] and stochastic models [75–85] . Mechanistic and stochastic models serve different purposes. Stochastic models are good for identifying patterns and making short term predictions, while mechanistic models aim at explaining patterns and incorporate a mathematical representation of underlying physical processes. Stochastic models can have several advantages over mechanistic models: They are considerably less numerically demanding than dynamical mechanistic models [65, 67] and have the additional advantage that stochastic processes are described in stochastic terms without resorting to additional parameterization when the relationship is not clear. The main issue with stochastic models is their dependence on the amount, quality and relevance of the data used. They rely on presence/absence data to train and calibrate the model. On the other hand, mechanistic models have no constricting input requirements regarding the observed distribution and densities.

2.4.1 Stochastic models

In the work by Eastwood et al. [81] a zero-inflated generalized linear model (GLM) with negative binomial error structure to model the spatio-temporal abundance of *Aedes taeniorhynchus* in Galapagos was developed. Theey employed time-lagged variables based on the generational development time for aquatic stages of 7 − 14 days. The inter-annual temperature variations and large scale oscillations such as ENSO were taken into account [81]. A Vuong test, using Kullback-Liebler criterion, was utilised to compare the model performance against standard negative binomial regression. A one-at-a-time backward deletion process, was then applied to determine the factors with the highest association to vector abundance. In the paper by Chuang et al. [84] Cross Correlation Maps (CCM) were used to analyse which meteorological parameters influenced mosquito abundance patters. They used daily temperature and relative humidity with weekly mosquito data for the period 1989 − 2005, for 22 trap sites. It is suggested that the relationships identified by CCM should be taken into consideration together with the selected window of analysis and serial correlation between the lags.

Otero et al. [86] developed a population dynamics models for *Aedes aegypti* using a state dependent Markov chain approach that takes into account the entire life cycle of the mosquito. The transition parameters are modelled as stochastic events with constraints derived from the available empirical data for *Aedes aegypti* as well as the dependence of vector biology on the time variable weather parameters. This model provides an alternative approach for incorporating a stage-structured concept with empirical transition rates for *Aedes aegypti* into as stochastic modelling framework.

A GIS spatial linear regression model was developed by Clackner et al. [79] to estimate the habitat suitability index (HSI) as a indicator of mosquito suitability and expected seasonal abundance related to environmental predictors. Derived habitat descriptors were used to investigate the spatial variation in the entomological data.

In the study by Chuang et al. [80] a polynomial distributed lag (PDL) model with the meteorological data as the independent variables was applied. They compared models incorporating data from the NASA Advanced Microwave Scanning Radiometer on EOS (AMSR-E) and local weather station data to predict vector abundance at different lags. They found that the spatial model supplementing with EO data performed better than the model which used only data from the national meteorological stations.

Oluwagbemi et al. [82] developed a stochastic, spatially explicit model for vector metapopulation dynamics. In the model by Basuki et al. [78] the population dynamics as well as interaction between individuals is modelled by using stochastic Calculus of Looping Sequence (CLC) model. Temperature was highlighted as the most significant driving variable.

Finally, an interesting and novel technique for pest population dynamics modelling is presented in the paper by Patil et al. [83] where a standard feed forward Multi-layer perception (MLP) neural network model with a back-propagation training algorithm was employed in the proposed stochastic system for predicting pest population dynamics for the thrips pest in cotton crop. This model was trained on pest data spanning five year and 247 records and its performance is highly data dependent. The authors present a methodology for pre-processing and cleaning of field surveillance so that it can be useful for machine learning applications.

2.4.2 Mechanistic models

In most mechanistic models, authors use the Egg-Larva-Pupa-Adult transition model to simulate the life cycle of the mosquito. A stage-structured model was developed by Erickson et al. [68] in which each life-stage is modelled with an ordinary differential equation (ODE) and species-specific temperature dependent mortality and development rates. They highlight the importance of forcing the model with variable temperature data.

Existing models of mosquito population dynamics are usually tailored to a specific mosquito species. However, Cailly et al. [69] developed a generic, mechanistic, weather driven model of mosquito population dynamics that can be applied to different vector genera. A generic framework could be useful for comparing the population dynamics of different species at the same location. Aquatic and adult stages are incorporated in a stage-structured framework [69].This model could have important implications for the development of population dynamics models in general and should be considered. A recent study by [73] adapted and tested the model by Cailly et al. [69] for different mosquito species in the south of France.

Another widely used mechanistic model is the CIMSiM model developed by Focks et al. [65] in 1993 that is still applied today. The container-inhabiting mosquito simulation model (CIMSiM) is a dynamic life-table simulation model of *Aedes aegypti*. The framework incorporates a module that account for the presence of artificial and natural vector breeding sites. Even though CIMSiM has demonstrated skill in predicting field mosquito population dynamics, the CIMSiM models are site specific and require local surveys and and ground truthing to parameterize them.

Also interesting is the study by Ahumada et al. [66] in which the authors developed a discrete-time population model which incorporates the effects of temperature and precipitation calibrated for an elevation profile in Hawaii. They used a transition matrix with dynamic parameters to incorporate the effects of the driving meteorology.

The study by Lunde et al. [71] describes a biophysical model to predict species distribution and seasonal variations. Unlike stochastic models, which need presence/absence data, this type of modelling framework can be run with no information with respect to observed filed distribution and densities, thus allowing for the investigation of the isolated effect of temperature and relative humidity on the different aspects of the mosquito life cycle.

In the study by Lana et al. [85] they examine four dynamic models with temperature and population density dependant transition rates. The model incorporating a thermodynamic function for the transition rates, calibrated for *Aedes aegypti* and density dependent larval development rates performed the best, while the model with a temperature dependent step function, which defines the development rates in terms of cut-off temperature categories, and density dependent oviposition rates performed the poorest.

2.4.2.1 Temporally forced models

Temporally forced models are essential for a more realistic description of the patterns occurring in population dynamics. They provide a natural progression from simple models to more complex and realistic ones. Changes in development rates is increasingly recognised as an important dynamic variation in population dynamics. Furthermore, seasonality plays a particular role in vector and VBD dynamics. This time dependency is brought on by temperature variation which affects the adult population but also by breeding site conditions related to the development of aquatic stages that vary throughout a year. For example, during the rainy season in the tropics, mosquito numbers are significantly increased. Even modest fluctuations in the transition rates can result into large changes in the observed population. The seasonality in the model is introduced via the addition of environmental time series of data. Specifically, temperature, precipitation and relative humidity.

In his 1976 paper [87], Box wrote “All models are wrong, but some are useful”. Ordinary Differential Equation (ODE) models help quantify the interaction and mechanisms of different processes that are observed in the vector life-cycle. Process parameterization is in most cases based on empirical results from laboratory studies. These results can be evaluated by comparing the simulated population dynamics to reality. The framework of the ODE stage-structured model described in this study reflects the stages of the mosquito life-cycle (Egg - Larva - Pupa - Adult). It uses temperature dependent functions for the mortality and development rates, which allows for a biologically realistic representation of the transitions between the different stages. Density dependent regulation is incorporated in the modelling of the carrying capacity, which simulates regulation in case of overpopulation in the immature stages (Egg, Larva and Puppa), while adult mortality is temperature and age-dependent, separating the nulliparous from the parous females.

The modelled population is considered to be a closed system, meaning that immigration, emigration and interaction with other species is not modelled, and the population is confined to the study region.

The endogenic population growth/decline in mechanistic models is expressed in terms of birth and mortality rates as well as the development rates of each stage in the development cycle.

2.5 Numerical integration and stability

These types of population models almost always contain non-linear terms and need to be solved numerically, introducing a global and local error which is governed by the accuracy of the numerical integration scheme. Moreover, the initial value problem introduces the issue of initialization which is not straight forward. It is impossible to measure the actual size of the population of the mosquito and an error is already introduced when setting the initial field. Moreover, the simulated transient dynamics and spin-up time, the time it takes for the model to reach a state that is not dependent on the initial conditions, will vary based on initial conditions.

In atmospheric dynamics, typical time scales tied to particular wave motions of the system linearised around the barotropic equilibrium exist. On the other hand, for the dynamics of mosquito populations, considering mosquitoes as agents governed by endogenic and exogenic processes, and biological populations in general, the stable state is not well-defined by research and mainly consists of empirical parameterization of significant sub-processes. The level of complexity and emerging chaotic behaviour of these systems makes it very hard to formulate universal dependencies. Nonetheless, it is a step towards improved model realism if we can see that the characteristic periods that are present in the dynamical system relate to the ones observed in vector populations.

In Chapter 6 we will consider a numerical model for the population dynamics of the mosquito vectors *Ae. aegypti* and *Cx. pipiens*, and examine the behaviour of the simulated dynamical system. We will look at the stability analysis of equilibrium points of the vector population dynamics model and examine the fast and slow modes in the coupled non-linear systems with different amplitudes and time-scales of evolution. In the second part of the chapter, we examine the oscillatory modes present in our system and their corresponding characteristic frequencies and periods. The feasibility of normal mode initialization as a method for removing the high-frequency oscillations in the system is considered. The normal mode identification of a coupled, nonlinear system can be performed by examining the oscillatory solutions of the system linearised around a specific point [88].

From a practical point of view, analysing the stability and eigen-properties of a population dynamics model is extremely important for multiple reasons. First, it is meaningful to look at the way the dynamical system behaves near equilibrium points as a function of different temperatures and how it reacts to perturbations around those states. Secondly, they can help us evaluate the realism of the model, i.e. to see whether the eigen-frequencies correspond to observed biological frequencies, i.e. the truth. Finally, this type of analysis can support model initialization and help in reducing the spin-up time due to short-lived transient behaviour.

2.6 Model verification

In his paper from 1966 Levins [89] defines three main properties of biological population models as: (1) Realism, (2) Precision and (3) Generality and states that each practical model is a trade-off between these three attributes. For example, VBD models wishing to inform public action in case of outbreak require reality and precision in their models. The common practice nowadays is sacrificing generality and realism for precision which means tailoring the model to a specific species for which it can precisely simulate the observed population in terms of quantifiable verification metrics (precision) without simulating the mechanism and processes that corresponds to the known reality of this species (realistic) [62,90,91]. On the other hand, Levins [89] states a preference for the type of model which values realism and generality above precision to the inherent uncertainties and heterogeneities present in the observed populations which might mislead and misinform models driven by precision. This type of model is also known as a conceptual model and can be used for a general understanding of biological principles.

Stage-structure ODE (Ordinary Differential Equation) vector population models fall into the category of realistic and precise while, on the other hand, they attempt to salvage the idea of generality in terms of the modelling framework. Even though the development parameters are different for example for the *Aedes* and *Culex* species examined, the framework and structure stay the same. This type of model can be directly extended to other vector genera. This of-course needs to be supported by basic research to calculate the development and mortality parameters as well as field surveillance and monitoring for validation; and both are extensive and extremely time-consuming activities. Expanding on Levins theorem, Weiss [62] adds that the realism of a model needs to be considered together with the computational time and the numerical exhaustiveness of the runs. A model that is too complex, even though biologically accurate, has no practical use [62].

There is not much literature on the quantitative verification of vector population models since long term and consistent time-series of observed data are rare. The time and cost of the trapping efforts are usually the main limiting factors. Most available data-sets tend to be irregularly spaced and demonstrate large variations over different regions and sampling periods.

Methods of validation are different for different models, with the main question for a predictive model being whether it is acceptable for a certain application such as: (i) predicting the population peaks, (ii) predicting the overall population dynamics throughout the season, (iii) simulating the seasonal or subseasonal trends or (iv) analysis of the day-to-day variability to see whether the sensitivity with respect to temperature change is realistic. In contrast, the main question for a conceptual or theoretical model is finding the true dynamics of a specific population and defining the underlying processes. In this way predictive models are verified against an independent set of observed data and the verification is concerned with how well the model reproduces the data. However, for theoretical models the concern is twofold: (i) how well the model reproduces the observed data and (ii) whether the simulated system truly operates in a realistic way. Even though the first approach is way more common in scientific publications, sometimes very little can be learned from this type of validation [62, 92, 93].

So, the analysis of ODE vector population dynamical models can be considered in many ways depending on what needs to be predicted or discovered, with each method carrying a different type of information. Hence, in this thesis we will investigate several methods for the verification of the ODE stage-structure model described in Chapter 7 for three locations: Bahariya, Petrovaradin and Guadeloupe; forced with two meter air temperature. The trap data represents an subset of the actual population which is lured to the trap by attractants. This type of observed abundance is compared to the aggregated bloodseeking class in the ODE model i.e. the total number of nulliparous and parous bloodseeking females. The analysis was performed according to the following steps: (i) Firstly, a time-series analysis of the observations utilizing the Wavelet transform was performed and compared to the characteristic eigen-periods in the dynamical system. This feeds into the second type of verification described above, realism, since we want to see whether the periods that emerge in our dynamical system exist in real mosquito populations; (ii) Secondly, we consider the standard verification methods for real continuous scalar quantities such as BIAS and RMSE to examine how well the output replicates the observed data; (iii) Thirdly, we examine the extremes and inflection points to test whether the dynamics is correctly represented; (iv) And finally, we introduce thresholds in the data and evaluate the scores for dichotomous simulations to examine the simulation of specific vector population densities which can subsequently have an effect on disease transmission.

Chapter 3

Material and methods

3.1 Datasets

3.1.1 Description of study locations

The meteorological and entomological data were collected in three different technico-environmental settings: (i) Guadeloupe (Lesser Antilles), (ii) Bahariya (Egypt) and (iii) Petrovaradin (Serbia) (Figure 3.1).

Figure 3.1: Study locations: G - Guadeloupe (Egypt); B - Bahariya; P - Petrovaradin (Serbia).

This data was used to analyse the association between the main meteorological drivers and the mosquito population and in a later step to verify the outputs of the ODE population dynamics model. *Aedes aegypti* data was collected in Guadeloupe, and *Culex pipiens* data in Serbia and Egypt.

3.1.1.1 Guadeloupe

Guadeloupe ($\approx$ 1436 km2) is characterized by a tropical climate under the influence of the prevailing trade winds and their maritime surroundings. It forms an archipelago of 12 islands, as well as many uninhabited islands and outcroppings formed as part of the volcanic arc on the outer edge of the Caribbean plate. It is part of the Leeward islands in the Caribbean island group, which are the outermost Caribbean islands situated in the area where the Caribbean Sea boarders the Atlantic Ocean. It belongs to the French overseas department. The largest city and only commercial airport is Pointe-à-Pitre, located just east of the central arc between the west and the east wing.

The west wing of the island is mountainous (La Grande Soufrière; 1467 m) while the east wing is almost completely flat; the west to east elevation profile is shown in Figure 3.2c.

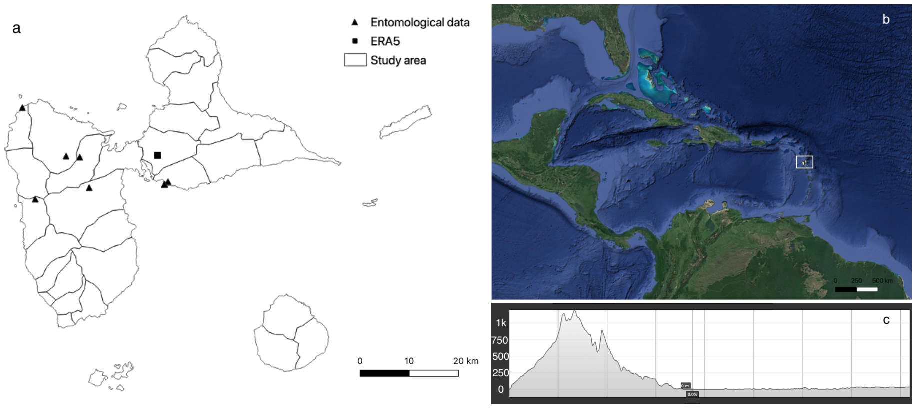

Figure 3.2: Location of the study area, Guadeloupe (Lesser Antilles). (a) Country-level administrative units with Entomological and Meteorological study locations indicated; (b) Region; (c) Elevation profile of a West to East intersection of the island in [m]. A detailed overview of the study sites is given in Appendix A.3.

The corresponding Köppen climate classification subtype is "Af", the tropical rainforest climate. The Antilles together with Central America deviate from the traditional tropical pattern due to their specific position [94]. Cold air is transported from North America with the Appalachian Mountains on the east and the Rocky Mountains on the west forming a funnel directly to the south; on the other hand periodic disturbances known as tropical waves, issued from the African continent, influence the island from the east [95]. The air mass circulation in the Antilles is mostly influenced by the North Atlantic Anticyclone. There are two distinct climatic periods characterized by a seasonal pattern corresponding to the passing of the Intertropical Convergence Zone (ITCZ), while the annual range of temperature and direct radiation are small.

The distribution of precipitation is highly heterogeneous due to the extreme orography of the islands, the Hadley cell circulation, variation in Sea

Surface Temperature (SST) induced by direct solar radiation heating, evaporation and upwelling, as well as the proximity to the subtropical ridge of high pressure [96–98]. The highest peak of Guadeloupe is located on Basse-Terre, while Grande-Terre is mostly flat and allows the easterly winds to cross the island without attenuation. The wind from the north-east pushes the warm moist air along the high orographic gradient. The air is lifted and adiabatically cooled; creating excess precipitation on the windward side of the mountain. These areas experience the highest amount of total precipitation year-round; up to 9000 mm on the windward side of Grande Soufriere in Guadeloupe. A shift in precipitation often occurs with the gradual increase in Pacific SST and ENSO driven westerly winds are observed across the tropical North Atlantic belt [99, 100]. Inter-annual variability was found to be related to Madden-Julian oscillation, which occur with the frequency of $30 - 90$ days [101].

The study area in the Lesser Antilles covers the central island of Guadeloupe, with the sampling sites for *Ae. egypti* located in the coastal areas on the center arc and in the mountainous region on Basse-Terre (Figure 3.2).

The main breeding sites of *Aedes aegypti* across the island are artificial containers that fill up during precipitation events. On the other hand, intense precipitation can cause flushing, which destroys the deposited eggs.

The vegetation is extremely lush due to the fertile volcanic soil and abundant rainfall, with most of the forest areas concentrated on the west wing of the island (Basse-Terre), while the east wing (Grand-Terre) was mostly cleared to make way for agricultural land, chiefly for the traditional sugar cane crop.

3.1.1.2 Egypt

The study area in Egypt is located in the Bahariya or El-Wahat el-Bahariya oasis (≈ 2000 km^2), around 370 km south-east of Cairo in the Western Desert (Figure 3.3). It is characterized by the "BWh", hot dessert climate, Köppen climate type, while the coastline experiences the "BSh", hot steppes climate type, commonly described as arid and semi-arid, characterized by hot, dry summers, moderate winters and erratic rainfall.

Most of the region around Bahariya in Egypt is directly influenced by the Hadley cell and having the trade winds meeting the north-west winds from the Mediterranean and the aperiodic dry Khamsin wind (March - May) shaping the significant dune formations in the Sahara and forming the Sand Sea in the west. The seasonal character of the climate, especially the winter temperature and coastal precipitation variance is influenced by the circulation indices of North-Atlantic Oscillation index (NAO), Mediterranean Oscillation index (MOI) and East Atlantic - West Russian index (EAWR). The northeast trade winds are dominant in the period from October to May which sustains the significant aridity of most of the basin [102, 103]. The proximity to the sea coupled with the prevailing wind direction causes the moderate temperature of the coast belt. Alexandria and Rafah, in the north-east, receive the highest amount of precipitation during the year.

The MOI index has a positive correlation with monthly temperature in Egypt while NAO is found to have a negative influence [104,105]. A significant negative relationship was observed especially for winter, December-January-February (DJF) temperature and NAO [104,105]. NAO was found to have a significantly

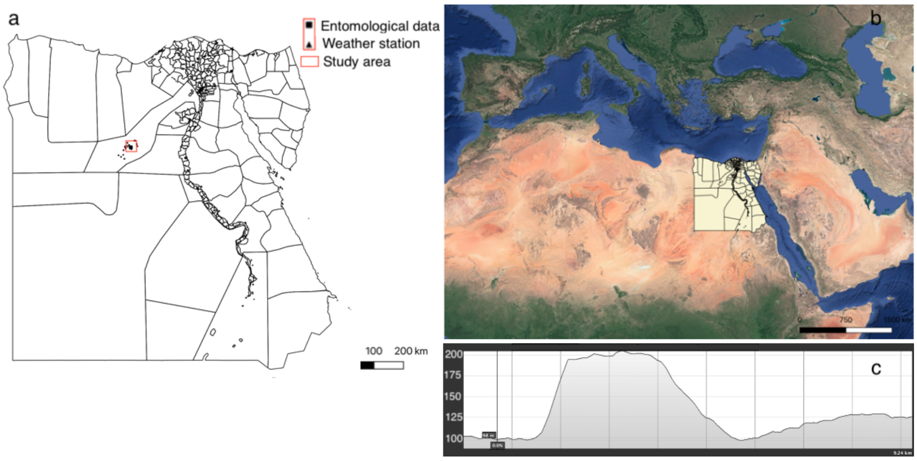

Figure 3.3: Location of the study area, Bahariya (Egypt). (a) Country-level administrative units with Entomological and Meteorological study locations indicated; (b) Region; (c) Elevation profile [m] of a North to South intersection of the Oasis (the study location is indicated with the vertical line). A detailed overview of the study site is given in Appendix A.3.

stronger influence on Egyptian temperature than ENSO circulation [104, 105]. EARW also has a strong influence on DJF temperature.

The study site is located in the northern part of the oasis in a semi rural area. The *Culex pipiens* vector breeding sites are present in the oasis in the form of: (i) Irrigation ditches and canals; (ii) Accumulated well water; (iii) Brackish lakes; (iv) Sewage canals and cesspits. The town of Bawiti is located in the south of the oasis and represents the largest urban area; the rest of the oasis is scattered residential and agricultural tissue, consisting mostly of date orchards.

3.1.1.3 Serbia

The study site in Serbia is located in the city of Petrovaradin, in the southern part of the Vojvodina province, on the banks of the Danube (Figure 3.4). The Vojvodina Province is positioned in the northern part of Serbia and the southern part of the Pannonian lowland (18°51’–21°33’E, 44°37’–46°11’N and 75–641 m.a.s.l. The Fruska Gora border Vojvodina on the south. This region is an essential agricultural area in Serbia with a total surface area of 21,500 km^2. This region is characterised by a continental climate, with elements of a sub-humid and warm climate, it fall under the ”Cfxwbx” Köppen climate type.

The NAO and East Atlantic Oscillation (EAO) both have an influence on extreme temperature variability in Serbia during the winter and summer months [106–109]. Another dominant atmospheric influence for this area of the Pannonian plane is the EAWR (East-Antarctic West Russia). The NAO is the dominant mode of Atmospheric behaviour in the northern part of the Atlantic, EAO is structurally similar with a south-westerly displacement in regards to the NAO nodal lines [107]. The positive NAO phase leads to above-average temperatures and drier conditions over the Mediterranean basin and the southern parts of Europe, while the positive EAO phase is associated with higher tem-

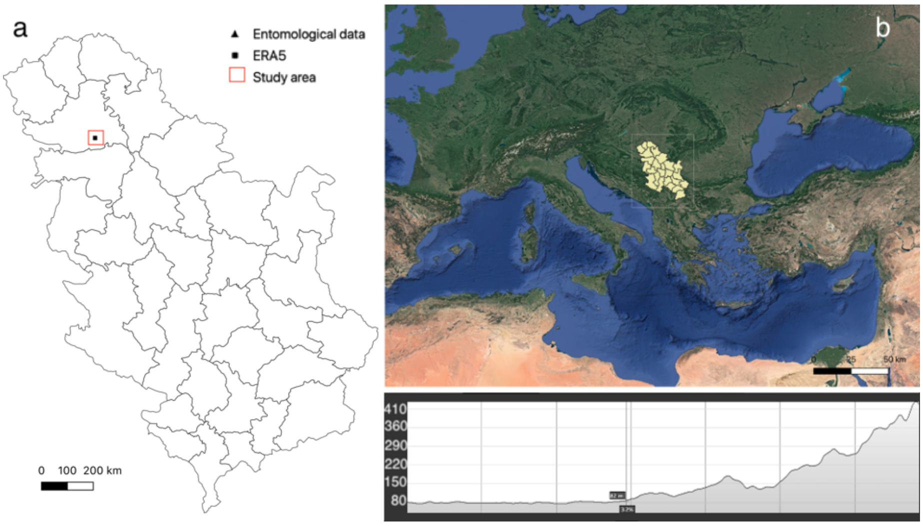

Figure 3.4: Location of the study area, Petrovaradin (Serbia). (a) Country-level administrative units with Entomological and Meteorological study locations indicated; (b) Region; (c) Elevation profile [m] of a North to South intersection passing through Petrovaradin (the study location is indicated with the vertical line). A detailed overview of the study site is given in Appendix A.3.

peratures throughout the year, for the entire continent [109–111]. The EAWR oscillation shifts between different positions associated with different seasons. The positive phase is associated with cold airflow from the north and northwest across the Baltic sea and the Russian plain, white the negative phase is linked with a south and south-easterly flow [107, 109].

The entomological and meteorological data are collected from a garden in the suburban residential area of Petrovaradin. The *Cx. pipiens* breeding sites are mainly natural flood-areas around the Danube, as well as temporary rainwater puddles. In the semi urban area the identified breed sites are often also artificial water containers.

The main characteristics of each study location are presented in Table A.1 and Table A.2. A detailed description of each study site and collected data is given in Appendix A (Meteorological data) and Appendix B (Entomological data) of Chapter 4.

3.1.2 Meteorological data

An overview of the meteorological datasets is given in Table 5. The field data for the Bahariya Oasis (Egypt) was collected within the MosqDyn project for the period 2017–2018. The data was recorded at 15-minute intervals with the Davis Vantage Pro weather station.

The field data for Petrovaradin was collected within the VECTORNET project for the period 2016–2017. The data was recorded at 5-minute intervals with the EasyWeather weather station.

Guadeloupe did not have an in-situ weather station deployed for the duration of the project. Thus, ERA5 reanalysis was used instead to obtain hourly

Table 3.1: Overview of observed meteorological data. The measured variables are: (i) Temperature [°C], (ii) Relative humidity [%], (iv) Precipitation [mm], (v) Wind speed [m/s], (vi) Wind direction; FF - Frequency used for forcing the model.

Locations	Time series	Lat [°]	Lon [°]	Altitude [m]	Time Series type	Frequency	Type	FF
Bahariya	01/04/2017 31/12/2018	28.41	28.93	98	Regular	15 min	Observations	Daily
Guadeloupe	2015–2018	16.26	-61.52	23	Regular	1 hour	ERA5 analysis	Daily
Petrovaradin	2016–2017	45.25	19.87	82	Regular	5 min	Observations	Daily

time-series of wind, precipitation, temperature and relative humidity data. Data obtained from the synoptic weather station close to Pointe-à-Pitre was cleaned and used to check the correlation with the ERA5 time-series for a period from 2015-01-05 to 2017-02-24 ($r = 0.76$, $p < .0001$) . Data from the in-situ station itself was not used for the whole period because of a large amount of missing values and erroneous recordings of minimum and maximum temperature observed for several instances in 2015–2018.

3.1.3 Entomological data

The field data for the Bahariya oasis (Egypt) was collected within the MosqDyn project for the period 2017–2018 (daily). Samples were collected on a daily basis by standardised protocols using the BG Sentinel 2 mosquito trap with the BG lure attractant (Lactic acid, Ammonium hydrogen carbonate, Hexanoic acid). The trap was operating without a light source; light aided traps proved not to have a significant attracting/repelling influence on *Culex* mosquitoes [112].

Table 3.2: Overview of observed entomological data.

Locations		Time series	Lat [°]	Lon [°]	Altitude [m]	Time Series type	Frequency	Species of interest
Bahariya		01/04/2017 31/12/2018	28.41	28.93	97	Regular	Daily	*Cx. pipiens*
Guadeloupe	CRB	11/2015–10/2018	16.207	-61.507	4	Regular	Week-Month	*Ae. aegypti*
	HFR	11/2015–10/2017	16.347	-61.776	6	Irregular	Week-Month	*Ae. aegypti*
	HMC	11/2015–05/2019	16.212	-61.500	5	Irregular	Week-Month	*Ae. aegypti*
	HCB (CAB)	11/2015–10/2018	16.207	-61.507	10	Irregular	Week-Month	*Ae. aegypti*
	Zoo	11/2017-04/2019	16.180	-61.752	164	Irregular	Week-Month	*Ae. aegypti*
	Aporier	11/2017-02/2019	16.259	-61.693	62	Irregular	Week-Month	*Ae. aegypti*
	RV1	11/2017-04/2019	16.201	-61.649	91	Irregular	Week-Month	*Ae. aegypti*
	RV2		16.257	-61.668	41	Irregular	Week-Month	*Ae. aegypti*
	Gosier	11/2017-04/2019	16.212	-61.500	5	Irregular	Week-Month	*Ae. aegypti*
Petrovaradin		2016–2017	45.25	19.87	82	Regular	Daily	*Cx. pipiens*

The field data for Gudeloupe was collected across 8 location within the MosqDyn and SmartSenZ projects for the period 2015–2018. The sampling frequency was weekly to monthly depending on the site. A longitudinal study with daily sampling was conducted for a period of March – May 2017.

The field data for Petrovaradin was collected within the VECTORNET project. Daily collections were carried out for a stationary site in 2016–2017 for 670 trap nights with dry ice-baited traps. The study was carried out in a semi-urban zone with lots of greenery, side drainage channels and many containers suitable for breeding *Culex pipiens*. The locations for the surveillance activities were identified based on the availability of 8 years weekly sampling data for *Cx. pipiens* as an important vector species in Europe (WNV).

3.2 Time series analysis

Time-series analysis is commonly used to identify the scales of the pattern in population fluctuation [41, 42]. The classical Fourier decomposition cannot be applied due to the high non-stationarity of the entomological time-series. Thus, the partitioning of the variance of the time-series and construction of the power spectrum is performed by wavelet analysis.

Moreover, time series analysis based on lagged cross correlation was used to examine the empirical covariates [40, 42, 113] between the entomological and ecological time-series. This is done by examining the cross-correlation function for daily averages of temperature, relative humidity and wind-speed and the interval lagged cross-correlation for precipitation. Accumulated precipitation is expected to increase the total available surface of breeding sites for the mosquito vector and directly impact the specific carrying capacity for the study site. Thus, accumulated precipitation over a certain period might be a more relevant driver of vector populations, rather than a daily precipitation series.

The difference in methods for precipitation is due to the fact that the underlying mechanism in which precipitation has an influence on breeding site dynamics is significantly different.

3.2.1 Stationarity

A time-series is considered stationary if its joint probability distribution does not change with time. For this to be achieved the series has to satisfy the following conditions: (i) a constant mean value over time, i.e. no trend; (ii) constant variance over time; (iv) no seasonal components. In other words, the statistical properties of the time-series stay more or less constant in time.

It is important to consider the stationarity because many methods in time-series analysis rely on it. For example, in spectral analysis, the fourier decomposition performed to examine the frequencies present in the signal assumes that the signal can be expressed by a family of perpetual sine waves with fixed frequency for the whole duration of the series (i.e. for all sampling intervals); this is satisfied in principal for a stationary time-series; however can give erroneous values for a non-stationary one.

Stationarity can be inferred visually by examining the plots of the autocorrelation (ACF) and partial autocorrelation (PCF) function of the series, a time-series with high serial correlation is not stationary. Moreover, several statistical test have been developed to analyse the degree of stationarity. The Ljung-Box test examines the ACF between successive lags under the null hypothesis of independence. Other often used statistics are the Kwiatkowski-Phillips-Schmidt-Shin (KPSS) and the Augmented Dickey-Fuller (ADF) t-statistic test that look for the unit root of a series indicating trend.

3.2.2 Wavelet analysis

Wavelet analysis is a powerful method for analysing the spectral characteristics of non-stationary time series, which is a property most biological time series share [40, 43, 114]. The time scale localisation, makes the Wavelet approach especially attractive for the analysis of non-stationary VBD and other non-stationary systems [114, 115]. Since methods such as the simple Fourier transform, due to the assumption and requirement of stationary, are largely unsuitable for these types of applications [41]; i.e. it provides frequency resolution with no temporal resolution. The continuous Wavelet analysis was developed in the 1980s [116] following the invention of the Windowed Fourier Decomposition (WFD), which replaces the Fourier transform's sinusoidal wave by the product of a sinusoid and a window which is localized in time, [117, 118]. The WFD is not as efficient as the Wavelet transform due to the utilization of constant frequency-scale resolution across the entire signal which results in poor time resolution for certain parts of the interval [119]. This can cause the high frequency transients, present in non-linear systems, to be poorly represented in the power spectrum.

Wavelet analysis performs a decomposition of the original time series into smaller intervals which can be considered as localized in time and space and thus allows the analysis of the evolution of the local variation of power in the entire signal [119–121]. It is constructed in a way that maximizes time and frequency resolution in the transform [119, 122].

Wavelet analysis has had a wide range of applications across many disciplines including ENSO analysis [40, 119, 123–125], the analysis of atmospheric cold fronts and tropical convection [126,127], wave dispersion [120,128] and coherent structures in turbulent flows [129]. In entomological studies it was applied in the analysis of significant periods and coherency in VBD models [40, 41].

Moreover Torrance et al. [119], indicate that the following factors should be considered when choosing the mother function: (i) Orthogonality; (ii) Width; (iii) Whether the function is complex or real; (iv) Shape. Common nonorthogonal wavelet function are Morlet, Paul and DOG (als knows as the "Mexican hat wavelet" for m =2) and on the other side the orthogonal wavelets are for example the Haar and Daubechies wavelet.

The Morlet wavelet function has the shape of a standard plane wave modulated by a Gaussian [116, 130].

$$\Psi(t) = \pi^{-\frac{1}{4}} \cdot e^{i\omega t} e^{-\frac{t^2}{2}} \tag{3.1}$$

Where ω is the angular frequency $[\frac{rad}{s}]$. This is also known as the "mother" wavelet. Since mother has to be localized in time and space with a vanishing mean [119, 129], the corresponding wavelet transform for a time series x_n (for $n = 0 \ldots N-1$) with a constant time step Δt is defined as a convolution of the series of "wavelet daughters". Convolution is a mathematical technique common to Digital Signal Processing in which a series of signals are combined into a group response.

$$\Psi_t(n, s) = \sum_{n'=0}^{N-1} x_n \cdot \Psi_m^* \cdot \left[\frac{(n - n') \cdot \Delta t}{s} \right] \tag{3.2}$$

Where Ψ_m^* is the complex conjugate of the mother wavelet and s is the wavelet scale. In order to make the wavelets directly comparable Ψ_m has to be normalized.

The wavelet power spectrum is defined as the square of the modulus of the transform (Ψ_t) [119,120,131].

$$P(n, s) = \frac{1}{s} \cdot |\Psi_t(n, s)|^2 \tag{3.3}$$

Phase shift and structural breaks in the signal can be examined by analysing the phase of the Wavelet transform which is given by the following equation [130]:

$$\psi(n,s) = arctan\left(\frac{Im(\Psi_t(n,s))}{Re(\Psi_t(n,s))}\right) \tag{3.4}$$

Since the Fourier transform used within Morlet assumes that the data is periodic, and on the other hand the observed time-series is finite, errors will exist at the tails of the wavelet periodogram [116, 119, 120]. The data is often padded with zeros to decrease the edge effect; however, this also has an influence on the amplitude near the padding since zero values are added to the daughter wavelet. This depends on the chosen scale and is expressed in the metric known as e-folding time. This value describes the time needed for the wavelet power at the edge to drop by a e^{-2} [119]. The region defined by this metric is called the Cone of Influence (COI), and simply indicates that in the region outside the COI the edge effects can be disregarded as having no influence on the wavelet power.

The significance levels for the wavelet power spectrum (null hypothesis of "no periodicity") are calculated against a reference/background spectrum. The common practice is to use either a red or white noise Fourier or the standard Gaussian white noise spectrum [119] and the significant areas are calculated at the 10% level [130].

Two time series covering the same period can be compared using the cross-wavelet spectrum. The cross-wavelet transform of x_n^1 and x_n^2 decomposes the Fourier co-spectra and quadrature-spectra in the time-frequency domain [130]:

$$\Psi_t^{x1,x2}(n,s) = \frac{1}{s} \cdot \Psi_t^{x1}(n,s) \cdot \Psi_t^{x2*}(n,s) \tag{3.5}$$

The cross-wavelet power is defined as:

$$P^{x1,x2}(n,s) = \left|\Psi_t^{x^1,x^2}(n,s)\right| \tag{3.6}$$

3.2.3 Lagged cross correlation

The Cross-correlation function was used to identify lagged correlation between the meteorological and entomological time-series. Since the CCF function assumes stationarity the data first need to be transformed. The common methods for balancing an unstationary time series are: (i) first order differencing for linear trend; (ii) log transformation for non-linear trend; (iii) log or seasonal differencing for seasonality; (iv) lastly, a comprehensive method that is often employed in meteorology, calculating the anomaly field.

The first order differenced time-series is a new series with N-1 (where N is the total number of values in the original series) values defined as:

$$x'_t = x_t - x_{t-1} \tag{3.7}$$

In some cases, to obtain stationarity, the order of differencing needs to be increased. Moreover, if the series has a strong seasonal component, seasonal differencing should be applied which is defined as $x_t^{'} = x_t - x_{t,s}$ (s is the number of seasons) [132]. For instance, the elements of the second order differenced time series with seasonal differencing would be calculated as:

$$x_t^{''} = x_t^{'} - x_{t-1}^{'} = x_t - x_{t-1} - x_{t,s} + x_{t,s-1} \tag{3.8}$$

Potential statistical tests to determine the order of differencing needed for stationarity include the unit root tests such as the Phillips-Prons test, the Kwiatkowski-Phillips-Schimdt-Shin (KPSS) test, the ADF-GLS test or the Zivot-Andrews test [132].

For the CCF and Cross Correlation Maps (CCM) analysis it is important that the differenced time series is still interpretable in the context of the original series, and thus higher-order differencing is discouraged [132].

The anomaly field is calculated by subtracting the mean value over a time interval from the data [133]. In our analysis we subtract the monthly climatology from the daily time-series which effectively removes the annual cycle and produces a stationary series.

In the second step the lagged CCF function is calculated for the stationary time-series. The lagged autocovariance function of a series $\{X_t\}$ for lag Δt is defined as:

$$\gamma_X(\Delta t) = Cov(X_{t+\Delta t}, X_t) = E[(X_{t+\Delta t} - \mu_{t+\Delta t})(X_t - \mu_t)] \tag{3.9}$$

Where μ_t is the mean. And then the lagged autocorrelation function (ACF) is defined as:

$$\rho_X(\Delta t) = \frac{\gamma_X(\Delta t)}{\sqrt{\gamma_X(0)^2}} = Corr(X_{t+\Delta t}, X_t) \tag{3.10}$$

Analogously, the lagged cross variance between series $\{X_t, Y_t\}$ with means $\mu_X(t)$ and $\mu_Y(t)$ is defined as:

$$\gamma_{X,Y}(t+\Delta t) = E[(Y_{t+\Delta t} - \mu_{t+\Delta t}^y)(X_t - \mu_t^x)] \tag{3.11}$$

And finally, the lagged cross correlation function (CCF) is:

$$\rho_{X,Y}(\Delta t) = \frac{\gamma_{XY}(\Delta t)}{\sqrt{\gamma_Y(0)\gamma_X(0)}} = Corr(Y_{t+\Delta t}, X_t) \tag{3.12}$$

3.2.4 Interval-lagged cross correlation

Interval lagged cross correlation maps (CCM) are used to identify the effect of meteorological variables accumulated or averaged over a time interval on the daily abundance of the vector. They are defined by the following function [113]:

$$c_{j,k} = Corr(A_i, \sum X_{i-j,i-k}) \tag{3.13}$$

A_i is the vector abundance at day i, and the second term represent the accumulated value of the meteorological variable (in our case precipitation, similarly temperature would be averaged and not summed over the interval) for the time interval starting at i-j and ending at i-k, where k is greater or equal to j. The diagonal displays correlation coefficients corresponding to the CCF.

3.3 Climatic suitability assessment study

A Multi-Critera Decision Analysis model (MCDA) was developed for the analysis of the climatic suitability for the establishment and annual activity of *Ae. aegypti* (Guadeloupe) and *Cx. pipiens* (in Serbia and Egypt) employing sigma fuzzy membership functions. The membership function is defined as a sigma function that governs the mapping of each value of the environmental variable to a membership value corresponding to a specific suitability value. It is a continuous, smooth function defined over the interval delineated by empirically determined minimum and maximum threshold values (T_c, S_c).

The model combines this set of sigma function with standard climate normals for the derived climatic parameters for temperature and precipitation. The membership functions were constructed based on empirical criteria and expert advice for the selected climatological variables: (i) mean annual temperature (T_a); (ii) total annual precipitation (H_a); (iii) mean January temperature (T_{jan}); (iv) mean June-July-August (JJA) temperature (T_{jja}); and (v) annual precipitation frequency (H_ν) i.e. the total number of days with precipitation > 1 mm. The normals were computed as for the 1981—2010 reference climatology.

This process-based mechanistic approach was analogous to that followed by ECDC [19] and explored in [16, 18, 22]. The climate normals listed in Table 3.3 are used as input for the process-based MCDA model. T_c and S_c in Table 3.3 are the critical threshold and saturation values which define the shape of the sigma function. The corresponding sigma functions are shown in Figure 3.5.

Table 3.3: MCDA saturation and threshold values for the climatic parameters: Ta (mean annual temperature), Ha (total annual precipitation), Tjan (Mean January temperature), Tjja (Mean summer temperature), Hv (Frequency of rainy days); AeA - *Ae. aegypti*, CxP - *Culex pipiens*.

Parameter	Ta		Ha		Tjan		Tjja		Hv		NTL	
Species	*AeAi*	*CxP*	*AeA*	*CxP*	*AeA*	*CxP*	*AeA*	*CxP*	*AeA*	*CxP*	*AeA*	*CxP*
T_c	14	11	200	0	10	-	16,40	11,35	60	36	20	10
S_c	21	14	800	600	16	-	19,33	16,27	120	96	40	30

The sigma functions have the following general form:

$$\sigma_s = \frac{a_1}{1 + exp\left(a_2 \cdot (x - a_3)\right)} + a_4 \tag{3.14}$$

where:

$$a_2 = 4/(T_c - S_c) \tag{3.15}$$

and

$$a_3 = (T_c + S_c)/2 \tag{3.16}$$

x is the value of the climatic variable from Table 3.3 with the corresponding T_c and S_c. The final suitability was calculated as

$$\sigma = \left(\prod_{s=1}^{n} \sigma_s^{\omega_s}\right)^{1/\sum\limits_{s=1}^{n} \omega_s}$$

This value is standardized to a 0–100 scale ($a_1 = 100, a_4 = 0$). The final MCDA index is interpreted through the following categories: (i) Not suitable (0.0 – 0.25); (ii) Low suitability (0.25 –0.5); (iii) Medium suitability (0.5 – 0.75); (iv) High suitability (0.75 –1.0).

The situation for *Cx. pipiens* and breeding site availability is complicated and quite different between Egypt and Serbia (governed by the H_a and H_ν parameters in Table 3.3). Based on the local characteristics of the study area, we selected two additional values to represent different mechanisms that can have an influence on the density of available vector breeding sites: night-time light (NTL) and the distance to nearest water bodies. In Egypt, in the oases where the total annual precipitation is often 0 the mosquitoes still have quite enough breeding sites generated by the water pumps, wells and irrigation canals. Hence, the geometric mean was corrected for the cases where H_a is close to zero but Night-Time-Light (NTL) > 10. The H_a sigma is omitted from the geometric mean and we consider that there is enough water to sustain the mosquito population. For Serbia, there is always enough precipitation (in terms of frequency and quantity), however the bigger source of breeding sites are the flood areas around the bigger rivers (Danube, Drina and Morava) and temporary water bodies generated by precipitation and flood events.

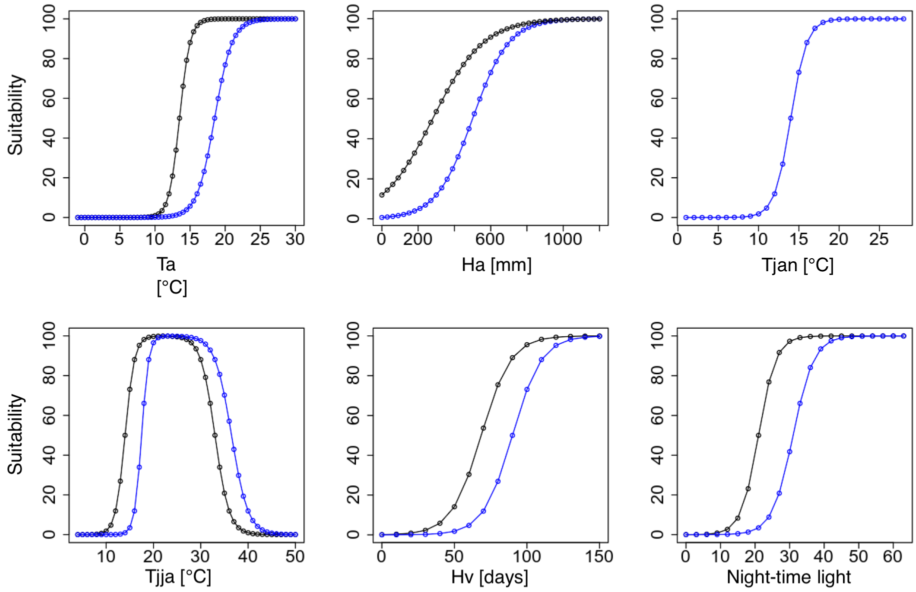

Figure 3.5: Suitability functions following Table 3.3 for *Ae. aegypti* (black) and *Cx. pipiens* (blue).

For calculating the proximity to inland water for Serbia, in a first step the country-level vector data from DCW [134] was rasterized. In second step a proximity algorithm was employed to create a 30 arc second proximity map based on the pixel-to-pixel distance to the nearest inland water cell.

The NTL data are cloud-free composites from the NASA's Earth Observing System (EOS) satellites [135] with 30 arc second resolution, spanning the globe from -65 ° to 75 ° latitudes and longitudes from -180 ° to 180 °. The data is created using all currently available archived DMPS-OLS smooth resolution night-time lights time series. A country mask was applied to determine the country-level rasters.

For the creation of a gridded dataset for all input climatological parameters the data from the native grid was interpolated using a Co-Kriging spatial interpolation algorithm with the SRTM30 digital elevation raster with 30 arc second resolution as the corollary variable.

A sensitivity analysis is conducted to examine the dependence of the MCDA model output on the input climatic parameters. The techniques focus on parameter space exploration following the methodology proposed by [136]. In a first step the input climatic parameter and their probability density functions are specified. In a second step the Latin Hypercube Sampling algorithm [136, 137] is used to create a hypercube of MCDA outputs defined for the specified parameter space. The hypercube size is estimated using the Symmetric Blest Measure of Agreement (SMBA) [136, 138] which takes the values from -1 to 1, indicating total disagreement between runs and total complete agreement between the runs. The sample size is chosen so that the LHS outputs retain strong agreement (>0.7) between runs forced with a lower or higher sample size to the chosen one [136]. In a final step the empirical cumulative distribution function (ECDF), and partial rank correlation coefficient (PRCC) are examined. The ECDF describes the distribution of the MCDA outputs and can highlight areas of high and low probability for the given parameter space. The PRCC illustrates the one factor at a time correlation between each input parameter on the MCDA output, sampled from the defined parameter space, with the linear effect of other parameters removed.

3.4 Modelling the population dynamics

A predictive model of vector population dynamics for *Cx. pipiens* and *Ae. aegypti* was developed following the framework proposed by [68, 69, 139].

The model is a system of 10 coupled, nonlinear, ordinary differential equations (ODE) with each dependent variable representing a stage in the mosquito life cycle: Egg (E), Larva (L), Pupa (P), Emerging Adults (A_{em}), Nulliparous Bloodseeking Adults (A_{b1}), Nulliparous Gestating Adults (A_{g1}), Nulliparous Ovipositing Adults (A_{o1}), Parous Bloodseeking Adults (A_{b2}), Parous Gestating Adults (A_{g2})and Parous Ovipositing Adults(A_{o2}). The prognostic variables represent population densities for each stage.

$$\frac{dE}{dt} = \gamma_{Ao}(\beta_1 A_{o1} + \beta_2 A_{o2}) - (\mu_E + f_E)E \tag{3.17a}$$

$$\frac{dL}{dt} = f_E E - (m_L(1 + \frac{L}{\kappa_L}) + f_L)L \tag{3.17b}$$

$$\frac{dP}{dt} = f_L L - (m_P + f_P)P \tag{3.17c}$$

$$\frac{dA_{em}}{dt} = f_P P \sigma e^{-\mu_{em}(1+\frac{P}{\kappa_P})} - (m_A + \gamma_{Aem})A_{em} \tag{3.17d}$$

$$\frac{dA_{b1}}{dt} = \gamma_{em}A_{em} - (m_A + \mu_r + \gamma_{Ab})A_{b1} \tag{3.17e}$$

$$\frac{dA_{g1}}{dt} = \gamma_{A_b}A_{b1} - (m_A + f_{Ag})A_{g1} \tag{3.17f}$$

$$\frac{dA_{o1}}{dt} = f_{Ag}A_{g1} - (m_A + \mu_r + \gamma_{Ao})A_{o1} \tag{3.17g}$$

$$\frac{dA_{b2}}{dt} = \gamma_{Ao}(A_{o1} + A_{o2}) - (m_A + \mu_r + \gamma_{Ab})A_{b2} \tag{3.17h}$$

$$\frac{dA_{g2}}{dt} = \gamma_{Ab}A_{b2} - (m_A + f_{Ag})A_{g2} \tag{3.17i}$$

$$\frac{dA_{o2}}{dt} = f_{Ag}A_{g2} - (m_A + \mu_r + \gamma_{Ao})A_{o2} \tag{3.17j}$$

The model tracks the number of individuals in each class. Initially the compartments are populated with an initial number of individuals in each stage. The transition between stages, as well as survival and mortality rate are forced by the environmental temperature and depend on the total simulated density of individuals in the respective stage. Following standard notation γ is the development rate and μ is the mortality rate. The parameter functions for *Culex. pipiens* and *Aedes aegypti* are given in Table 3.4.

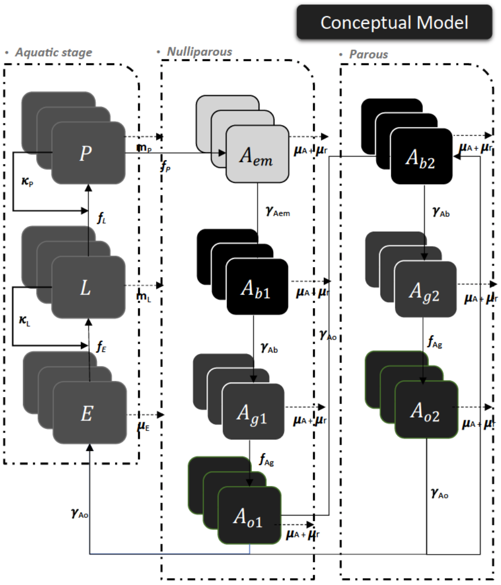

Figure 3.6: Model scheme

All stages are non-negative. Equation (3.17b) and Equation (3.17d) contain nonlinear terms. The parameters are provided in the table below [65, 86, 140–

150]. The information for *Ae. aegypti* was collected by a systematic literature review focused on peer-reviewed research and review papers describing dynamic mathematical models for *Ae. aegypti* and *Ae. albopictus* dynamics [24].

Table 3.4: Overview of model parameters.

Parameter	Description	*Aedes*	*Culex*	Unit
γ_{Aem}	Development rate of emerging adults	0.4	1.143	$days^{-1}$
γ_{Ab}	Development rate of bloodseeking adults	0.222	0.885	$days^{-1}$
γ_{Ao}	Ovipositing adult development rate	0.222	2	$days^{-1}$
$f_E(>0)$	Egg development rate f(T)	1	$0.16 \cdot (e^{0.105\cdot(T-10)} - e^{0.105\cdot(\alpha-10)-\frac{\alpha-T}{5.007}})$ ⋆	$days^{-1}$
f_P	Pupa development rate f(T)	$0.14 \cdot (e^{0.162(T-10)} - e^{0.162(35-10)-\frac{35-T}{5.007}})$	$0.021 \cdot (e^{0.162(T-10)} - e^{0.162\cdot(\alpha-10)-\frac{\alpha-T}{5.007}})$ ⋆	$days^{-1}$
f_L	Larva development rate f(T)	$\frac{f_P}{1.65}$	$\frac{fp}{4}$	$days^{-1}$
$f_{Ag}(>0)$	Development rate of gestating adults f(T)	$f_{Ag} = \frac{T-T_{Ag}}{TDD_{Ag}} = \frac{T-10}{78}$	$f_{Ag} = \frac{T-T_{Ag}}{TDD_{Ag}} = \frac{T-9.8}{64.4}$	$days^{-1}$
m_E	Egg mortality rate f(T)	$m_E = \mu_E$	$m_E = \mu_E$	$days^{-1}$
m_L	Larval mortality rate f(T)	$e^{-T/2} + \mu_L$	$e^{-T/2} + \mu_L$	$days^{-1}$
m_P	Pupa mortality rate f(T)	$e^{-T/2} + \mu_P$	$e^{-T/2} + \mu_P$	$days^{-1}$
$m_A(>\mu_A)$	Mortality rate of A_bf(T)	0.135‡	$-0.005941 + 0.002965 \cdot T$	$days^{-1}$
μ_E	Minimum egg mortality rate	0	0.0262	$days^{-1}$
μ_L	Minimum larval mortality rate	0.0367	0.0304	$days^{-1}$
μ_P	Minimum pupa mortality rate	0.12	0.0146	$days^{-1}$
μ_{em}	Mortality rate during emergence	0.1	0.1	$days^{-1}$
μ_r	Mortality rate during bloodseeking	0.08	0.08	$days^{-1}$
μ_A	Minimum adult mortality rate	0.07	$\frac{1}{43}$	$days^{-1}$
κ_L	Carrying capacity for larvae	$8 \cdot 10^{10}$	$8 \cdot 10^{8}$	nominal
κ_P	Carrying capacity for pupae	10^{8}	10^{7}	nominal
σ	Sex ratio at emergence	0.5	0.5	-
β	Number of eggs per A_o	$\beta_1 = 160(np)\beta_2 = 80(p)$ *	$\beta_1 = 141(np)\beta_2 = 80(p)$ *	-

⋆ $\alpha = 35$°C (Petrovaradin), $\alpha = 38$°C (Bahariya)

‡ Unpublished [24]

* np = nulliparous, p = parous

3.4.1 Stability analysis

In a first step, we will look if the system possesses an equilibrium state $\boldsymbol{X}_{eq} = (E^*, L^*, P^*, A^*_{em}, A^*_{b1}, A^*_{g1}, A^*_{o1}, A^*_{b2}, A^*_{g2}, A^*_{o2})$ for which $F_i(\boldsymbol{X}_{eq}) = 0$. Next, it is important to determine whether this solution is stable or unstable. Conceptually this means looking at the way the system reacts to small perturbation around the equilibrium state. If slight changes in the system state decays back to the equilibrium, the system is stable. On the other hand, if small perturbations grow with time the system is unstable.

The perturbation vector can be defined as $\boldsymbol{X'} = \boldsymbol{X}(t) - \boldsymbol{X}_{eq}(t)$, and $\partial \boldsymbol{X}'/\partial t = \boldsymbol{F}(\boldsymbol{X}_{eq}) + F(\boldsymbol{X} + \boldsymbol{X'})$. Expanding $\boldsymbol{F}(\boldsymbol{X} + \boldsymbol{X'})$ around X_{eq} and eliminating the small perturbation terms we get the general equation for the linearisation of a system of differential equations around an equilibrium point:

$$\frac{d\boldsymbol{X}}{dt} = \hat{J}\boldsymbol{X} \tag{3.18}$$

where J is the Jacobian matrix evaluated at the equilibrium point, with elements

$$\hat{J}_{i,j} = \frac{\partial f_i}{\partial x_j} \qquad i, j = 1, 2, ...10 \tag{3.19}$$

The eigenvalues of the characteristic equation $det\left[\hat{J} - \lambda\hat{I}\right]$ describe the nature of stability of the equilibrium point.

Several classes of stability can be distinguished. In the case when all eigenvalues have negative real parts, the solution decays exponentially and the state is considered to be asymptotically stable. If at least one eigenvalue has a positive real part, the solution is unstable. In case one or more eigenvalues have a vanishing real part, the stability is undetermined.

3.4.2 Transient and modal analysis

There are two methods that are commonly used for analysing the behaviour of dynamical systems: : (i) Transient dynamics analysis; and (ii) Modal analysis. The transient dynamics method looks at the initial behaviour of the system under specific time-dependent constrains for different stability regimes. Modal analysis on the other hand involves determining the inherent modal parameters of the dynamical system such as the characteristic period/frequency, damping coefficient and associated oscillatory modes. The latter is employed here by examining the eigenvectors and eigenvalues for the system for a specific forcing temperature (i.e. constant parameters).

3.4.3 Model Verification

3.4.3.1 Standard first and second-order moment verification

We have used the standard first-order moment verification metrics such as bias and mean absolute error and the second order moment verification of root mean square error to evaluate the continuous model error. The bias or mean systematic error is calculated as follows [151]:

$$B = \frac{1}{N}\sum_{i=1}^{N}(p_i - o_i) \tag{3.20}$$

Where p_i is the model prediction and o_i is the observed value at time i. The Mean Absolute error (MAE) also known as the mean systematic error is given by the following equation [151]:

$$MAE = \frac{1}{N}\sum_{i=1}^{N}|p_i - o_i| \tag{3.21}$$

And finally the root mean square error (RMSE) is defined as follows:

$$RMSE = \sqrt{\frac{1}{N}\sum_{i=1}^{N}(p_i - o_i)^2} \tag{3.22}$$

The uncertainty analysis of the systematic error (B) was performed following the GUM standard [152]. The combined standard uncertainty $u_c(B)$ is obtained from the first-order uncertainty propagation equation:

$$\begin{aligned} u_c^2(ax \pm by) &= a^2u^2(x) + b^2u^2(y) \pm 2ab \cdot u(x,y) \\ &= a^2u^2(x) + b^2u^2(y) \pm 2ab \cdot r(x,y) \cdot u(x) \cdot u(y) \end{aligned} \tag{3.23}$$

with the sensitivity coefficients, $a = b = 1$.

$$u_c^2(B) = u^2(s) + u^2(o) + 2 \cdot u(s) \cdot u(o) \cdot r(s,o) \tag{3.24}$$

where $u(s,o) = r(s,o) \cdot u(s) \cdot u(o)$ is the covariances for all s-o pairs; $u(s)$ and $u(o)$ are the standard simulated and observed uncertainties, which is usually calculated as the standard deviation of the observed and simulated series; $r(s,o)$ is the Pearson correlation coefficient.

The expanded uncertainty, which delineates the uncertainty interval for the systematic error, is defined as $U(B) = k \cdot u_c(B)$, where k is the coverage factor.

Initially, D'Agostino and Pearson's statistical normality tests [153, 154] is used to evaluate if the error distribution satisfies the conditions for a normal distribution. The convergence factor (95% CI) for a normal distribution has the value $k = 1.96$. If the error distribution is not normal, the convergence factor can be estimated from the Chebyshev inequality [155]. According to the inequality at least $1 - 1/k^2$ of the data falls within $k\sigma$ of the mean ($k > 1$), following $P(|X - \mu| \geq k\sigma \leq 1/k^2$. For the 95% CI, $1 - 1/k^2 = 0.95$, and k=4.472.

3.4.3.2 Contingency performance measures

In this section, we examined the verification measures based on the contingency table and the related performance measures for dichotomous variables. A verification measure is defined as a function of the simulation, the observations, or their association but does not quantify the similarity or difference between these two values such as the joint and marginal probabilities [151,156]. On the other hand, performance measures examine the correspondence between the simulated values and observation and include verification measures such as the conditional probabilities, accuracy, frequency bias and others which will be discussed later in this chapter [151,156].

To move from continuous scalar such as vector population to a binary variable we can introduced cut-off thresholds to the observed data. This is useful for assessing if significant peaks in the population are forecasted correctly. The thresholds are employed to construct a contingency table of observed and simulated presence/absence events and generate a set of verification metrics. The Receiver Operating Characteristic (ROC) function can be used to reverse-estimate the cut-off threshold for a dataset by looking at the threshold for which the best trade-off between sensitivity and specificity is achieved.

Table 3.5: Schematic representation of the contingency table, number of observations in each category (a, b, c, d) and corresponding joint and marginal probabilities p - simulated, o - observed.

		Observed		
		Yes	No	Total
Predicted	Yes	a	b	$a + b$
		$p(p = 1, o = 1)$	$p(p = 1, o = 0)$	$p(p = 1)$
	No	c	d	$c + d$
		$p(p = 0, o = 1)$	$p(p = 0, o = 0)$	$p(p = 0)$
	Total	$a + c$	$bc + d$	$a + b + c + d = n$
		$p(o = 1)$	$p(o = 0)$	1.0

The area under the Receiver Operating Characteristic curve (AUC) is used as another way of analysing the accuracy of the forecast system and is presented in Table 1. AUC is a measure of how well a parameter can distinguish between two different event outcomes. A perfect system would have AUC=1 and a no-skill system would have AUC=0.5. The ROC plots the Hit Rate or Sensitivity

Table 3.6: Overview of performance measures.

Verification metrics	Definition	Range
Accuracy (PC)	$\frac{a+d}{n}$	$[0, 1]$
Odds Ratio (OR)	$\frac{a \cdot d}{c \cdot b}$	$[0, \infty]$
OR Skill Score (ORSS)	$\frac{a \cdot d - c \cdot b}{a \cdot d + c \cdot b}$	$[-1, 1]$
Frequency Bias (FB)	$\frac{a+b}{a+c}$	$[0, \infty]$

($\frac{a}{a+c}$) against the False Alarm Rate or 1-Specificity ($\frac{b}{b+d}$) for an ensemble of threshold values [1-0].

And finally, we look at the decomposition of the Brier score and the reliability diagram which plots the observed frequency against a range of prediction probabilities (K) [156]:

$$BS = REL - RES + UNC \tag{3.25}$$

The ROC is conditioned on the variance of the observations, so this can be misleading when dealing with mosquito trap data which has very high variance. Field sampling uncertainties can be high, and site heterogeneity presents a significant factor in measurement uncertainty. It is very difficult to correctly estimate the size of uncertainty that is a result of field sampling of this type.

Chapter 4

Analysis of observed time-series

4.1 Time series analysis

The observations of the vector population for each location are shown in Figure 4.1. The Petrovaradin series consists of 700 data points collected in 2016–2017. The time-series has a pronounced seasonality with the annual population maximum for 2016 and 2017 occurring in July (Figure 4.1 a). The Bahariya series consists of 640 data points for 2017–2018 and does not have such a pronounced seasonal character. The period maximum is achieved in July for 2017 and February for 2018. The summary statistics of the observed catches and site-specific considerations of each time series are discussed in detail in Appendix A.3.

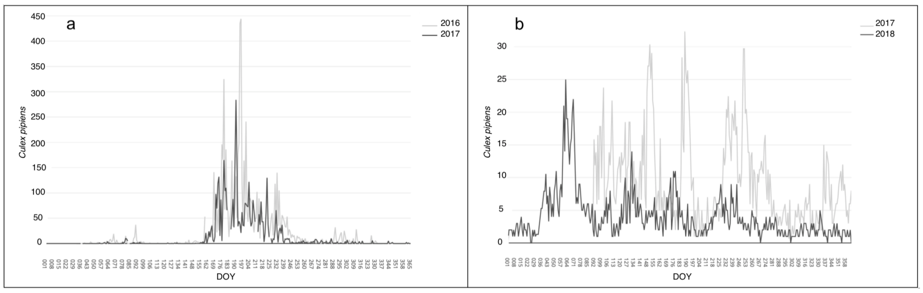

Figure 4.1: Raw time-series for *Culex pipiens* [count] for (a) Petrovaradin 2016 & 2017; and (b) Bahariya for 2017 & 2018.

Due to the irregularity of the time series and difference in frequency and trapping effort for each site, the Guadeloupe longitudinal data were insufficient for a comprehensive time-series analysis and are not included in this chapter, but are subsequently used for model validation. Unlike the daily time-series for Bahariya and Petrovaradin, the Guadeloupe data was collected across multiple locations with monthly and weekly frequencies (detailed in Appendix A.3).

4.1.1 Stationarity

The temporal autocorrelation and partial autocorrelation plots for the Petrovaradin and Bahariya series are shown in Figure 4.2. The seasonality of the Petrovaradin time-series rules out stationarity and this is also reflected in the Autocorrelation Function (ACF, Figure 4.2a,d), with higher correlation coefficients which do not diminish quickly and exhibit serial correlation. For comparison, the ACF function for Gaussian noise (N(0,1), for 600 point) is shown in Figure 4.3. For a stochastic stationary series the ACF drops rapidly after the first lag and the correlation randomly alternates between positive and negative values with no seasonal pattern.

For Bahariya, apart from the change in the mean-level of vector count from 2017 to 2018 (Figure 4.1), the non-stationarity is not so apparent. Cyclical peaks are observed in the series; however, in biological time-series these peaks can be caused not only by the generational cycles but by the carrying capacity of the total available breeding sites and inter-species competition which result in aperiodic peaks. The Ljung-Box statistic was calculated to confirm nonstationarity: $X^2 = 463.53$, $p < .0001$ for Bahariya; and $X^2 = 369.09$, $p < .0001$ for Petrovaradin.

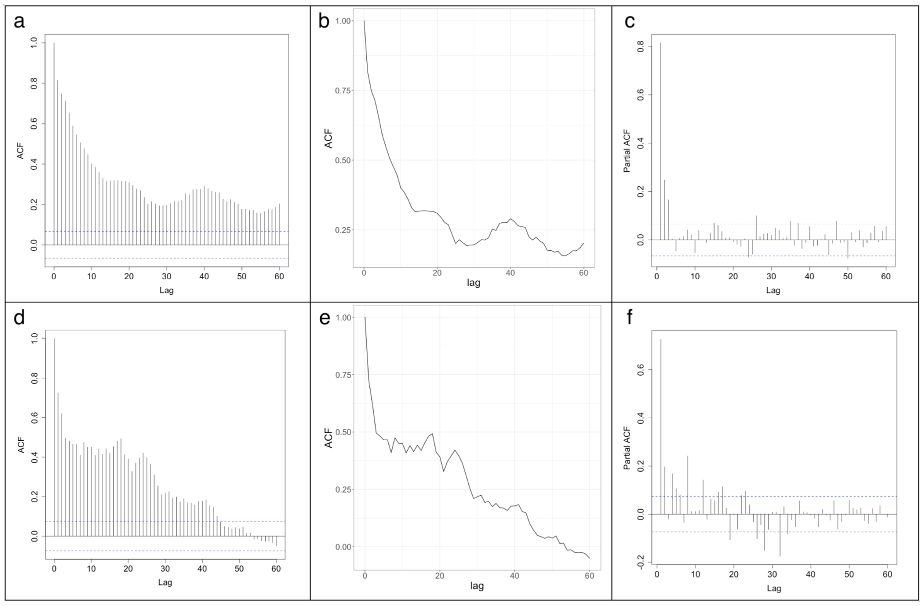

Figure 4.2: Autocorrelation function (ACF) and Partial ACF (PACF) of original abundance data for the first 60 lags [days] for Bahariya (top) and Petrovaradin (bottom).

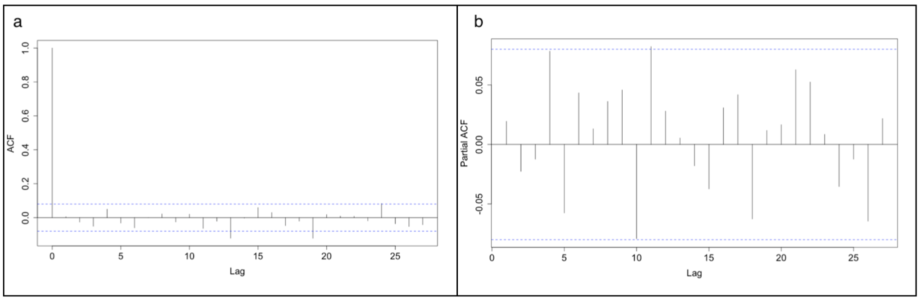

Figure 4.3: Typical autocorrelation function (a); and partial autocorrelation function (b) for white noise.

4.1.2 Wavelet analysis

Both entomological series display periods of transient periodicity as shown on the wavelet power spectrum in Figure 4.4. The time-frequency discrepancy, i.e. the variance of the dominant frequencies with regards to the sampling period (x-axis), is more pronounced for Petrovaradin, reflecting the expected seasonality.

For Bahariya, a higher number of periodic components appears in 2017 than 2018 (Figure 4.4b, e). The lack of significant regions with high power for the second half of 2018 point to a more stochastic distribution of the observed vector population and a lack of periodicity in the series.

The annual periodic component is present for both locations. However, while for Petrovaradin it is also the dominant period, for Bahariya the dominant peak features at higher frequencies.

The periods with the highest power during the summer months in Petrovaradin are the 10, 23, 187 and 314-day periods; and the 187 and 314-day periods corresponding to the autumn end-of-activity for the vector.

For Bahariya, there is no obvious seasonal pattern; however, the most significant periods identified for the: (i) High-temperature summer regime; (ii) The end of summer period with milder temperatures, (iii) And the low-temperature regime corresponding to the coldest winter months are respectively: (i) 20, 28, 45, 85-day period; (ii) 69 and 90-day period and (iii) the 314 period.

The global significance of the wavelet power-spectrum is examined through the average wavelet spectrum (Figure 4.4c,f). This would be identical to the Fourier spectrum periodogram of the non-stationary series, which would ignore the time evolution shown with the wavelet power spectrum. The average spectrum shows significant power at 3, 1–20, 42, 87, 147 and 337 days for Bahariya; and 2, 8, 13 and 20, 119, 181 and 337 days for Petrovaradin.

This analysis shows that the dominant frequencies change with the time-evolution of the system for both locations. In Chapter 7 these periods are used to validate the ODE population dynamics model by comparing the characteristic periods of the observed time series and simulated time series at different points within the observational interval.

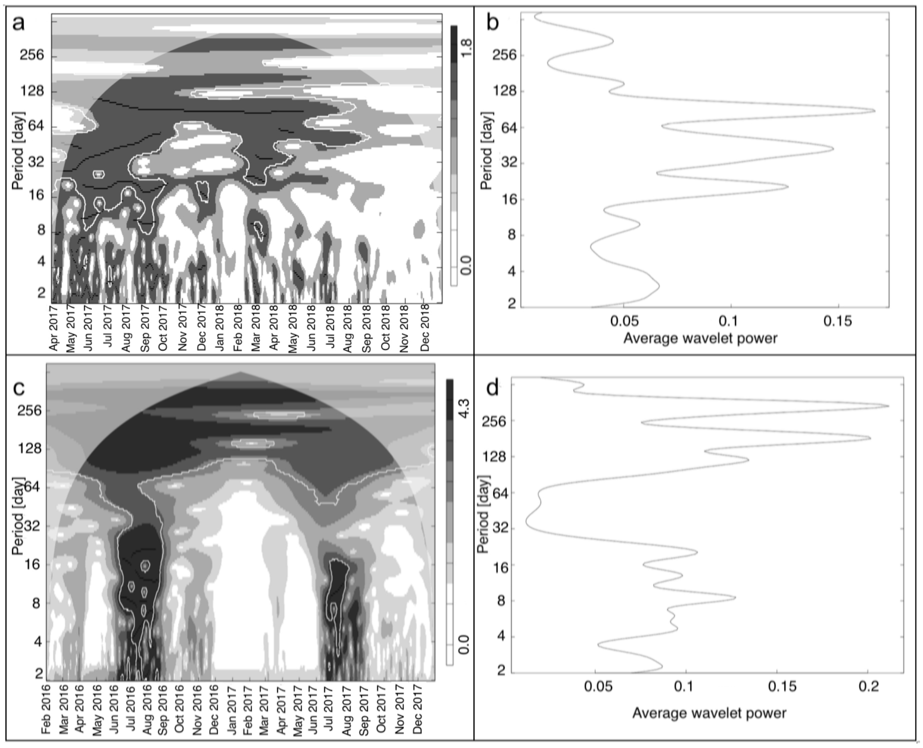

Figure 4.4: Wavelet power spectra (a ,c); and Average wavelet spectra (b,d) for Guadeloupe (top, 2017-2018) and Petrovaradin (bottom, 2016–2017); The colors scale indicates the power of the wavelet power spectrum from white (low power) to dark grey (high power), the shaded area indicates the cone of influence that surround the central region which is not influenced by the edge effect, the white line outlines areas with significant periodicity.

4.1.3 Cross correlation

In this chapter the correlation, lagged cross-correlation and lagged interval cross-correlation between the meteorological and entomological time-series is examined. When looking at the simple correlation for non-lagged data it is important to take into consideration that the association between the meteorology and entomology for parameters measured within the same day, apart from the population density, also reflects the localised activity of the vector for that day; i.e. the probability that the vector would search for a meal under these meteorological conditions and the trapping probability. This is most obvious for the wind speed parameter; since increased wind speed would prevent the mosquito from entering the trap and would hinder mosquito flight and activity. Thus, depending on the strength of the immediate effect of the underlying mechanism, the correlation analysis can reflect abundance as well as mosquito activity for the given day and environmental conditions; the results should be interpreted with this in mind.

The Pearson correlation coefficient (r) is a measure of the linear relationship between two variables. Linear as well as non-linear monotonous associations can, on the other hand, be analysed with the Spearman rank correlation (ρ). The Pearson coefficient $r = 1$ represent the perfect linear agreement, while the Spearman coefficient $\rho = 1$ represent the perfect monotonous agreement between the variables (linear and nonlinear). The rank coefficient is less sensitive to outliers. The time-series were made stationary by removing the nonrandom, seasonal and trend, components.

The Spearman correlation was higher for almost all examined combinations indicating that the association between the meteorological and entomological series is predominantly non-linear.

The highest association was observed for the correlation between minimum daily temperature for Petrovaradin ($\rho = 0.63, p < 2.2e - 16$) and for mean wind speed ($\rho = -0.36, p = 1.2e - 10$)) for Bahariya. On the other hand, the correlation with wind speed is very weak for Petrovaradin ($\rho < 0.20$).

In Tables 4.1 and 4.2 we see that RH has a very weak ($\rho \ \wedge \ r \leq 0.2$) association with the observed population in both Petrovaradin and Bahariya. Temperature is positively correlated with a weak correlation for Bahariya (0.20 $< \rho \leq 0.40$); and a moderate and strong ($0.40 < \rho \ \wedge \ r \leq .80$) correlation for Petrovaradin.

It is interesting to observe that, for Bahariya, the vector series has a negative correlation ($\rho = -0.26$, p = 3.3e-06) with the diurnal range for temperature, while there is almost no association observed for Petrovaradin ($\rho = 0.11, p = 0.04$)).

Table 4.1: Correlation between entomological and meteorological time series for Petrovaradin.

Variable	Description	Pearson	Spearman
T_m	Mean temperature	r = 0.46 (p < 2.2e-16)	ρ = 0.61 (p < 2.2e-16)
T_{min}	Minimum temperature	r = 0.47 (p < 2.2e-16)	ρ = 0.63 (p < 2.2e-16)
T_{max}	Maximum temperature	r = 0.44 (p < 2.2e-16)	ρ = 0.56 (p<2.2e-16)
RH_m	Mean relative humidity	r = -0.10 (p = 0.06)	ρ = -0.12 (p = 0.02)
RH_{min}	Minimum relative humidity	r = -0.12 (p = 0.02)	ρ = -0.13 (p = 0.02)
RH_{max}	Maximum relative humidity	r = -0.11 (p = 0.04)	ρ = -0.16 (p=2.76e-03)
V_m	Mean wind speed	r = 0.06 (p = 0.26)	ρ = 0.09 (p = 0.1)
$\Delta_{di}T$	Diurnal temperature range	r = 0.02 (p = 0.71)	ρ = 0.11 (p = 0.04)
$\Delta_{di}RH$	Diurnal relative humidity range	r = 0.07 (p = 0.19)	ρ = 0.10 (p = 0.06)

Moreover, to examine the response to high-temperatures we looked at the correlation between total hours above 35 °C and the vector population. Temperatures ≥ 35 °C are reported unstable for the survival of the vector. However, a positive correlation is observed for Bahariya ($\rho = 0.24$, p = 4.84e-04).

The effect of meteorology on vector abundance is rarely instantaneous and the correlation should be considered with the appropriate lags. To account for this CCF and CCM applied to time interval lagged data are analysed.

The cross correlation of the observed meteorological and entomological time-series is examined below. The x-axis shows the lag in number of days and the significance level (CI 99%) is depicted by the blue dotted line.

Only the positive lags, i.e. the correlation of lagged meteorology on vector abundance, were considered. Negative correlations would represent the hypothetical influence of lagged mosquito data on the meteorology which is understandably not realistic.

Table 4.2: Correlation between entomological and meteorological time series for Bahariya.

Variable	Description	Pearson	Spearman
T_m	Mean temperature	r = 0.19 (p = 6.76e-04)	ρ = 0.22 (p = 8.30e-05)
T_{min}	Minimum temperature	r = 0.20 (p = 3.47 E-04)	ρ = 0.24 (p = 1.76e-05)
T_{max}	Maximum temperature	r = 0.16 (p = 4.21e-03)	ρ = 0.21 (p = 1.72e-04)
RH_m	Mean relative humidity	r = 0.10 (p = 0.07)	ρ = 0.11 (p = 0.05)
RH_{min}	Minimum relative humidity	r = -0.02 (p = 0.15)	ρ = 0.09 (p = 0.11)
RH_{max}	Maximum relative humidity	r = -0.05 (p = 0.37)	ρ = 0.07 (p = 0.21)
V_m	Mean wind speed	r = - 0.28 (p = 5.47e-07)	ρ = -0.36 (p = 1.19e-10)
$\Delta_{di}T$	Diurnal temperature range	r = -0.19 (p = 7.66e-4)	ρ = -0.26 (p = 3.30e-06)
$\Delta_{di}RH$	Diurnal relative humidity range	r = -0.13 (p = 0.02)	ρ = -0.15 (p = 7.30e-03)

4.1.3.1 Bahariya

The CCF graphs for Bahariya are shown in Figure 4.5, with the lag expressed in days. The 0-day lagged mean and maximum temperature were positively associated with vector abundance. However the 8, 9 and 10-day lagged average and maximum daily temperature were negatively correlated with the daily abundance of *Cx. pipiens*, with the maximum occurring for the 9-day lag (Tavg: ρ = -0.21, p = 1.72e-4; Tmax: ρ = -0.29 p = 2.13e-07). Apart from the 0-day lag, the minimum daily temperature was not significantly correlated with the vector abundance. None of the relative humidity parameters had a significant association with vector abundance ($p > 0.10$).

The wind is negatively correlated with abundance, with the highest association observed for the 0-day lag (ρ = -0.36, p = 1.19e-10).

Furthermore, the relationship with the observed diurnal range for temperature and relative humidity was examined. We see that diurnal range for both variables for Bahariya has a predominantly negative correlation with the vector abundance, with the highest correlation seen for the 0-day lagged value for temperature (ρ = -0.26, p = 3.3e-05) and the 0-day lag for relative humidity (ρ = -0.15, p = 7.3e-03).

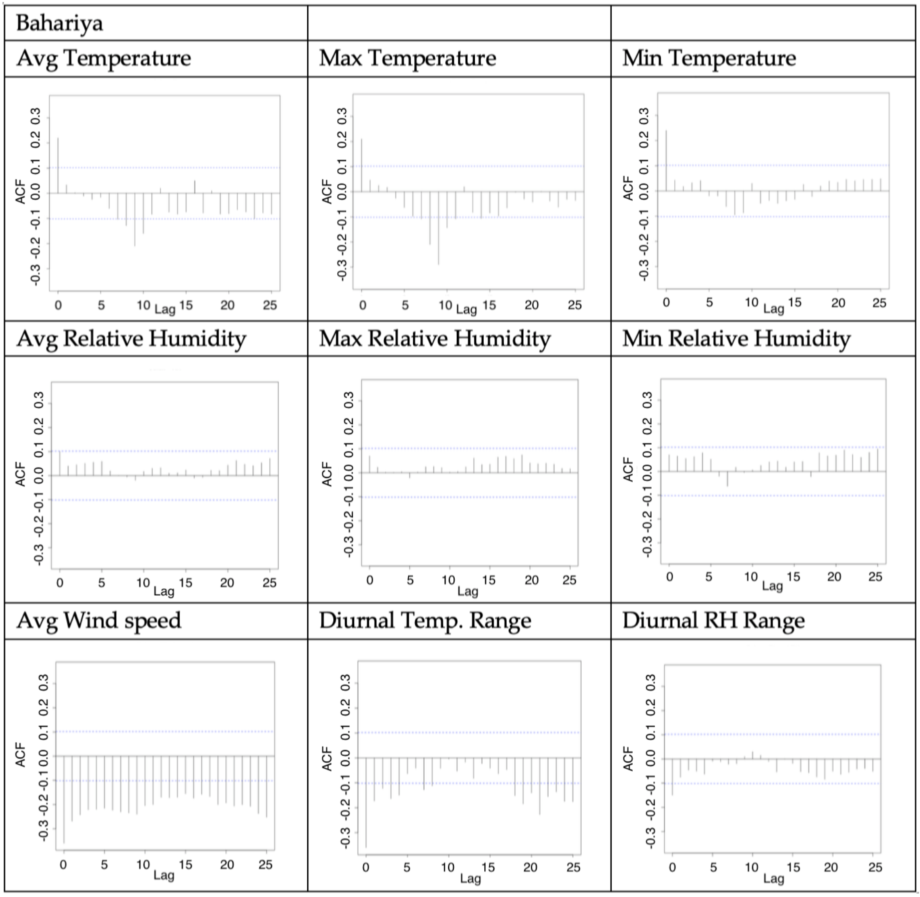

Figure 4.5: CCF plots for the first 25 lags [days] for Bahariya

4.1.3.2 Petrovaradin

For Petrovaradin the association with temperature is predominantly positive with the highest correlation observed for the 0-day lags and the 6–8 lagged values (Tavg: $\rho = 0.20$, p = 1.8e-03; Tmax: $\rho = 0.25$, p = 3.27e-06; Tmin: $\rho = 0.18$, p = 7.73e-04) and 13–15-day lags (Tavg: $\rho = 0.22$, p = 3.86e-05; Tmax: $\rho = 0.24$, p =6.26e-06; Tmin: $\rho = 0.13$, p = 0.01) . The minimum temperature had the highest association for the 0-day lag, however the correlation with average and maximum temperature was stronger for the longer lags.

Relative humidity had a weak negative correlation at the 0-day, but was not significantly correlated with vector abundance at higher lags. The correlation with the avg. daily wind speed was very weak and appeared to be randomly distributed amongst positive and negative correlations ($p > 0.06$).

We see that the cross-correlation function corresponding to the temperature and relative humidity diurnal range has a completely different structure from the Bahariya CCFs. There is a weak positive correlation for the 0-day lag, but apart from that there is no significant correlation with vector abundance ($p > 0.19$).

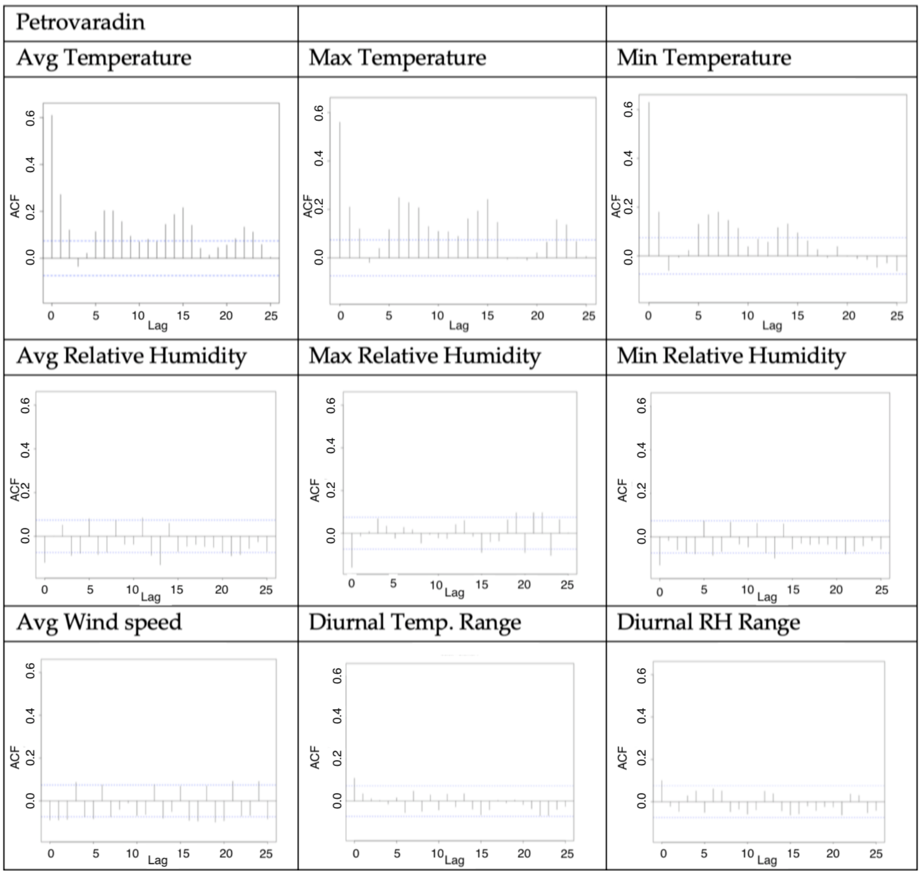

Figure 4.6: CCF plots for the first 25 lags [days] for Petrovaradin

4.1.4 Interval lagged cross correlation

Cross-correlation with precipitation was only examined for the Petrovaradin site, since there was no observed precipitation for Bahariya (single observed event, < 1 mm).

The effect of precipitation, more so than the other variables, is cumulative in nature. This is because it leads to a gradual increase in the total available surface of vector breeding sites, with excess precipitation causing flushing. For this purpose, we examine both the lagged and interval lagged correlation with vector abundance. The interval lagged correlation examines the association of total precipitation from between two dates, defined by lag1 and lag2 below, with the vector abundance.

The CCF function shown in Figure 4.7a shows that there is a positive association with vector abundance for lags over 13 days; the 0-day lagged precipitation has a very weak negative correlation. The CCM shown in Figure 4.7 b, c, indicates the interval lagged correlations. The highest correlation is achieved with the accumulated precipitation between day 26 and 14 prior to the trapping event. The correlation drops for the short-term lags bellow 10 days, as well as for long-term lags corresponding to different-length accumulated periods ending

40 days prior to capture.

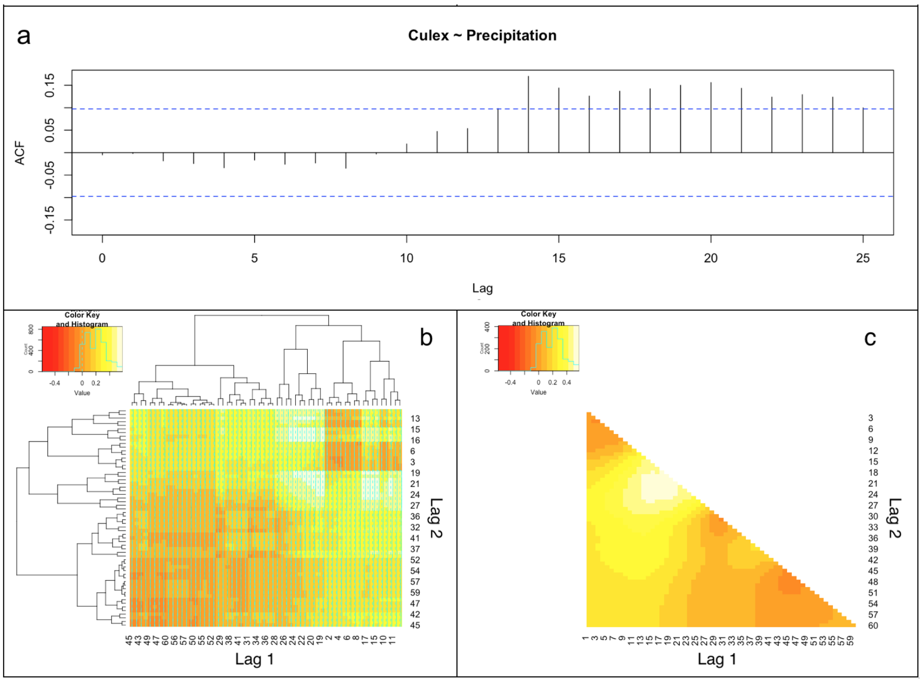

Figure 4.7: (a) CCF for precipitation and *Culex pipiens* abundance for 2016–2017 for lags 0–25 days; (b) dendrogram and (c) ordered CCM for Petrovaradin for time interval lagged precipitation and *Culex pipiens* abundance for 2016–2017, lags from 0–60 days shown in descending order on y-axis and ascending order on x-axis.

4.2 Discussion

The identified lags need to be critically assessed and discussed in terms of a possible biological process, because not all statistically significant lags are representative of the underlying reality. Here it is important to consider the development times for the aquatic stages (egg, larva and pupa). The effect of environmental conditions on these stages would reflect in the change in the adult population (the capture) after their development into adults.

The *Cx. pipiens* development period at 16 °C, 20 °C, 24 ° C, 28 °C and 32 °C are reported by Ciota et al. [5] and shown in Figure 4.8. In another study by Kiarie-Makara et al. [157] the respective lengths of the egg (d_E), larva (d_L) and pupa (d_P) development for *Cx. pipiens* is investigated. The longest development time was reported for d_L, which was consistently three to four times longer than the d_P and eight times longer than the egg development d_E across a temperature range from 20—28 °C [157].

The 8–10 day lagged average temperature is negatively correlated with the *Cx. pipiens* abundance in Bahariya. Very high temperatures can cause thermal wounding of the immature stages, increased senescence and death. The

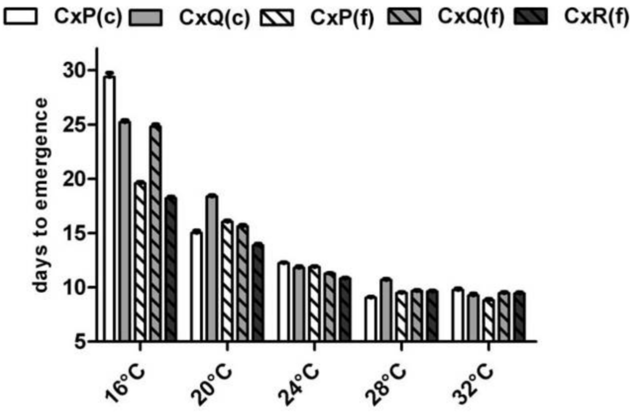

Figure 4.8: Development time in mean days to emergence ± SEM of field (f) and colony (c) *Cx. pipiens* (CxP), *Cx. quinquefasciatus* (CxQ), and *Cx. restuans* (CxR) at various temperatures (adopted from [5]).

increased mortality of the aquatic stages would have a lagged effect in the new generation of emerging adults, in turn this would be reflected on the captured sub-population. The average daily temperature for Bahariya is above 20 °C through almost the whole year and above 25 °C for the summer months (detailed in Figure A.7 in Appendix A.2). Thus, the 10-day lag can be linked to the effect of increased mortality of the aquatic stages due to an increase in temperature. There is a second mechanism that could also be at play here: namely, an increase in temperature leads to higher evaporation rates which are further increased by higher wind-speeds which could lead to the drying out of temporary stagnant water bodies, a reduction in total available breeding sites and a diminished adult population pending development.

For Petrovaradin, on the other hand, this type of generational effect was not identified for the average daily temperature. Since this is a mid-latitude location characterised with more moderate daily temperatures we do not expect to see increased mortality as a result of high temperatures, but we can assume lower adult activity as well as longer development periods for the immature stages as a result of lower temperatures. The 0-day lagged average temperature has a positive effect on abundance, which can be tied to an expected increase of activity of adults with higher temperatures (the optimal air temperature for *Cx. pipiens*, expressed in terms of flight speed, flight distance and oviposition rate is 25 °C). The positive association with the one and two-week lagged temperature suggests a generational character; however, there is no obvious interpretation of this mechanism.

We see that relative humidity is not significantly correlated with the vector abundance in Bahariya. We would expect a positive correlation for the 0-day lagged minimum relative humidity since the observed minimum values for relative humidity are below the values suitable for sustained normal activity for *Cx. pipiens*. But this is not observed, and can indicate that the mosquito can find suitable shelter to survive the low humidity stress. The mosquito would normally seek shelter in areas with shade and vegetation or inside buildings. The distribution of observed relative humidity for Bahariya is right skewed with the median at 45% RH, on the other hand for Petrovaradin the distribution of relative humidity is left skewed with the median at 73.27% (detailed in Appendix A.2). According to literature, *Cx. pipiens* humidity affects the survival of the vector in the following range: a stress curve from 28 to 58% [158], above which the activity is not affected by relative humidity, and below which dessication would occur. We see that in Bahariya even though the mosquito is often exposed to the stressor range of RH it still does not appear to be negatively affected and can successfully shelter. In Petrovaradin, on the other hand we observed a weak negative correlation for the 0-day lag of relative humidity. This might indicate that high relative humidity would impede adult blood-seeking activity and reduce the capture, however this is not supported by literature.

The negative correlation for the 0-lag wind speed for Bahariya is identified.

Wind-speed has a direct impact on mosquito activity and blood-seeking. If the wind speed exceeds the maximum flight speed of the vector the mosquito can no longer navigate and land in order to take blood or direct its movements towards the trap and might seek shelter. In this way wind has a direct influence on trapping-probability and reduces the number of observed mosquitoes, while the total population does not suffer.

For Petrovaradin, the recorded wind speed was relatively low for the trap location (detailed in Appendix A.2) and no correlation with abundance was observed, meaning that the mosquito could navigate the constant flux layer freely to his dorsal vessels content.

Finally, we see that the big diurnal range characteristic for the desert has a negative influence on the observed abundance. This is probably due to the direct stress experienced by the significant environmental change on the poikilotherm body in a short time interval; but, also the fact that a bigger diurnal range invariantly exposes the mosquito to unfavourable temperature and relative humidity states plays a role here. The diurnal range for Petrovaradin was, on the other hand, not correlated with abundance.

Chapter 5

Assessment of climatic suitability

5.1 Assessment study - Guadeloupe

5.1.1 Overview of mean monthly values for two stability regimes

In Appendix A.2, an overview of the mean monthly properties at 0600 and 1500 AST, representing the diurnal temperature minimum and maximum respectively. The analysis is conducted for the 2015–2018 span for which the entomological observations were carried out. Air temperature, relative humidity and the U and V components at 10 m wind speed are shown. The 2 m wind speed was calculated from the 10 m reanalysis using the Monin Obukhov similarity theory (detailed in Appendix A.2). At 0600 hours February is the coldest month (23.82 °C) and September the warmest (26.17 °C). The relative humidity has a maximum in October and a second maximum in May. A prevailing easterly wind component for all months is observed, with a peak in June and July.

Table 5.1: Annual regime of mean properties at 0600 and 1500 AST for Guadeloupe, Pointe-à-Pitre (2015–2018).

	Jan	Feb	Mar	Apr	May	Jun	July	Aug	Sep	Oct	Nov	Dec
0600 AST												
Air temperature 2 m [C]	23.82	23.40	23.71	24.23	24.58	25.54	25.73	25.89	26.17	25.73	25.23	24.31
Relative humidity [%]	84.68	84.93	83.74	85.88	87.52	86.20	87.06	87.76	87.30	88.16	86.48	86.11
U wind speed 10 m [m/s]	-4.10	-4.31	-4.34	-4.02	-4.45	-4.76	-4.73	-4.07	-3.40	-3.22	-3.61	-4.63
V wind speed 10 m [m/s]	-0.65	-0.65	-0.66	0.09	0.10	-0.02	-0.42	-0.32	0.15	0.52	0.08	-0.82
Wind speed 2 m [m/s]	0.70	0.75	0.75	0.67	0.73	0.78	0.78	0.69	0.64	0.56	0.63	0.77
1500 AST												
Air temperature 2 m [C]	25.27	24.85	25.27	25.76	26.19	26.91	27.25	27.48	27.74	27.29	26.69	25.76
Relative humidity [%]	76.36	76.28	74.60	76.98	77.52	76.03	77.27	78.63	78.62	81.23	80.00	78.35
U wind speed 10 m [m/s]	-4.44	-4.59	-4.68	-4.24	-4.95	-5.33	-5.19	-4.33	-3.43	-3.31	-3.76	-4.92
V wind speed 10 m [m/s]	-0.22	-0.15	-0.26	0.80	0.63	0.41	-0.07	0.11	0.64	1.08	0.65	-0.44
Wind speed 2 m [m/s]	0.77	0.81	0.82	0.74	0.83	0.88	0.86	0.74	0.66	0.62	0.68	0.82

For the afternoon 1500 regime we see that temperature and relative humidity follow a similar pattern with the maximum occurring in May being less pronounced. Similarly, the wind speed is characterised with a much stronger U component with an easterly direction.

When comparing the two regimes, it can be observed that there is hardly any yearly cycle in the temperature. The biggest difference within the daily curve is observed in May ($\Delta T = 1.6°\text{C}$). The biggest difference in relative humidity ($\Delta RH = 10.17\%$) and the U wind component ($\Delta U_{10} = 0.56\text{m/s}$) is observed in June, and the biggest difference between the mean morning and mid-day values for the V component ($\Delta V_{10} = 0.7$ m/s) is observed in April.

5.1.2 Annual precipitation regime

The precipitation in Guadeloupe can vary substantially depending on the area, but there are two distinct seasons: (i) the relatively dry season from December to April/May and the (ii) rainy season from June to November. Rain events usually occur in the form of showers or short-lived thunderstorms. Moreover, from Table 5.2 we see that the highest number of high-intensity events occurred in September and November. The threshold for these high intensity events was determined as one standard deviation above the mean value of the observed daily precipitation rate for 2015–2018. Intense precipitation can cause the flushing of vector breeding sites.

Table 5.2: Annual precipitation regime at 0600 and 1500 AST for Guadeloupe, Pointe-à-Pitre (2015–2018).

	Jan	Feb	Mar	Apr	May	Jun	July	Sep	Oct	Nov	Dec
Total precipitation [mm]	59.02	65.32	76.29	84.78	68.32	94.19	132.09	165.95	122.69	147.35	72.20
Total days with precipitation rate above 8.89 mm/day	0	1	4	4	3	4	9	16	8	21	3

5.1.3 Current climate 1981–2010

The climate normals for the 1981–2010 period are shown in the figure below: Annual temperature (Ta); Mean January temperature (Tjan); Mean June-July-August (JJA) temperature (Tjja); Total annual precipitation (Ha).

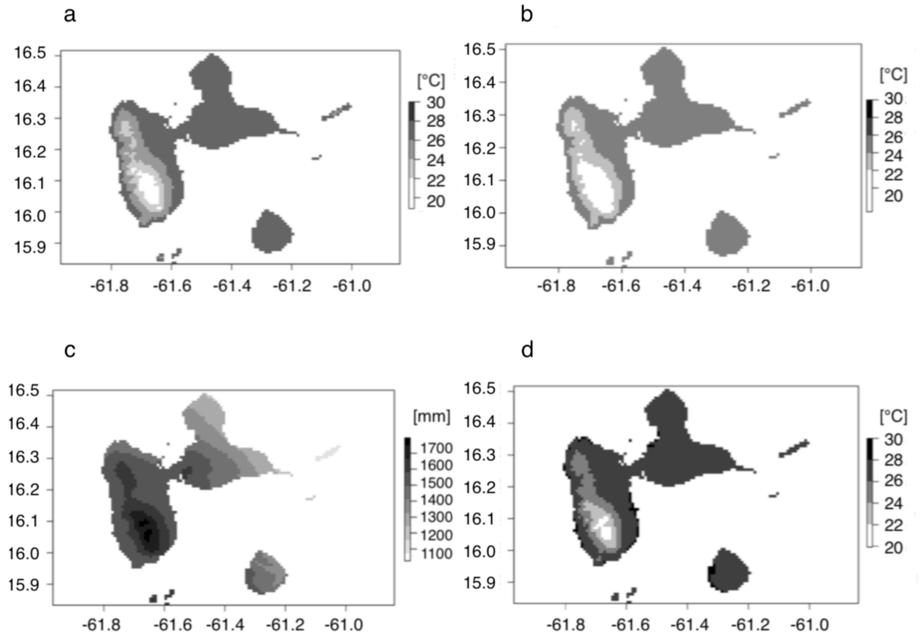

Figure 5.1: Overview of the most significant climate normals (1981-2010) potentially affecting *Ae. aegypti* vector establishment in Guadeloupe: (a) Annual temperature (Ta); (b) Mean January temperature (Tjan); (c) Total annual precipitation (Ha); (d) Mean June-July-August (JJA) temperature (Tjja).

5.1.4 MCDA assessment study Guadeloupe

The suitability for the establishment and overwintering of *Ae. aegypti* is shown in Figure 5.2. The suitability is expressed through the MCDA suitability index on a percent scale from 0 to 100. Areas under 50% are considered unfavourable for the establishment of the vector, and would lead to a significantly reduced population with areas below 25% considered completely unsuitable for vector activity and establishment. The climatic conditions in the lesser Antilles and the greater Caribbean are very suitable for the *Ae. aegypti* mosquito with the temperature keeping above 16 °C (the lower threshold for larval development) across the whole year. A slightly lower suitability is observed for the high-elevation areas in northern Colombia: Pico Cristobal Colon (5km a.s.l) and the La Guajira municipality, on the border with Venezuela, which is characterised by a sparsely populated desert landscape. Similarly, we see a lower suitability for the high-elevation/low-population Pico Duarte and Pico de la Bandera in the Dominican Republic.

The MCDA suitability index for Guadeloupe is shown in Figure 5.3. We see an asymmetric distribution characterising different suitability states for the east and west wing of the island. A decrease in suitability is observed for the high-altitude area of the national park which can be attributed to the decrease in human population density within the park, unlike the coast where the suitability matches the suitability of the west wing.

Figure 5.2: MCDA suitability for *Ae. aegypti* in the Caribbean region for the 1981–2010 climatology.

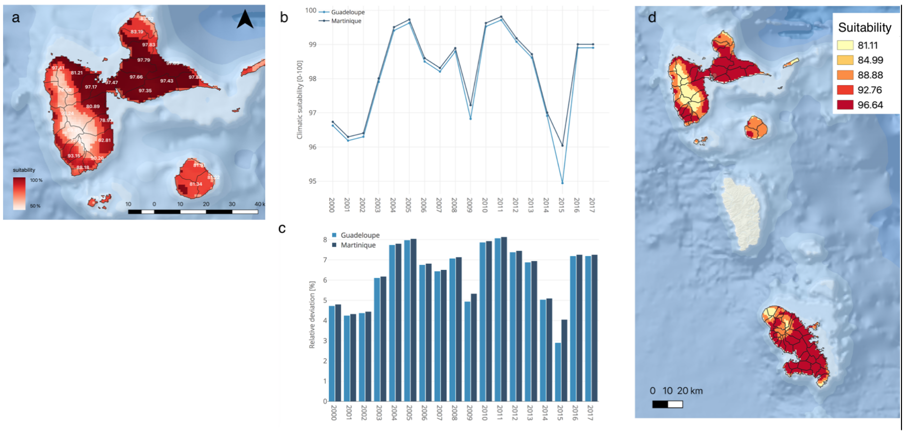

Figure 5.3: (a) MCDA suitability for *Ae. aegypti* based on the 1981–2010 climatology (b) MCDA suitability for individual years for Guadeloupe (Pointe-à-Pitre); (c) Relative deviation from the reference climatology; (d) MCDA for the year 2000 for Guadeloupe and Martinique.

The result implies that the establishment of the mosquito is not limited by the climatic conditions; however, slight oscillations in the suitability index could indicate higher activity and greater population abundance of the vector during the year which has an influence on disease transmission rates.

In Figure 5.3 we see the MCDA index calculated for individual years for the period 2000–2017; and the relative deviation (MCDAi - MCDAc)/(MCDAc) *100) of annual values from the long-term averages. Even though the deviations are of order of 4–10% a slight increase in suitability can be expected to reflect on the total abundance and number of generations even though it does not affect the overall spatial distribution pattern.

5.1.5 Sensitivity analysis

In this chapter we examine the effects of each input parameter on the final MCDA suitability index. The parameters were sampled from a normal distribution around the 1981–2010 spatial mean of the country-level raster and observed standard deviation (Table 5.3).

Table 5.3: Parameter distribution for the sensitivity analysis sampling (Hv – frequency of precipitation expressed as number of days within a year with rain > 1 mm; Ta – mean annual temperature [°C], Tjan – mean January temperature [°C]; Ha – total annual precipitation [mm]; Tjja – mean JJA temperature [°C]; NTL – Night time light).

Parameter	Distribution	Mean	SD
Hv	N(μ,σ)	$\mu = 175$	$\sigma = 12.4$
Ta	N(μ,σ)	$\mu = 24.066$	$\sigma = 1.1$
Tjan	N(μ,σ)	$\mu = 21.095$	$\sigma = 0.6$
Ha	N(μ,σ)	$\mu = 1660$	$\sigma = 60.1$
Tjja	N(μ,σ)	$\mu = 27.2$	$\sigma = 0.73$
NTL	U(a,b)	a = 0	b = 63

Firstly, the parameters were sampled with the Latin Hypercube Sampling (LHS) statistical method for creating a random sample of output values from the multidimensional distribution corresponding to the defined parameter space. Secondly, the partial rank correlation coefficients for each parameter were generated by bootstrapping the LHS values. The correlation coefficients were used to examine the linear relationship between the input parameter and output MCDA value after the linear effects of the other input variables are discounted. The adequate sample size was inferred by comparing several runs with different sample sizes using the Symmetric Blest Measure of Agreement.

The empirical cumulative distribution function of the model results applied to the LHS sample is shown in Figure 5.4. We see that the high probability outputs are within the high suitability MCDA values of 98-99.

The scatterplots shown in Figure 5.5 show the correlation of the output as a function of each input parameter. The strongest relationship is observed with the annual temperature. The ranges for the mean January temperature, total annual precipitation and population density do not have a significant influence on the change of the MCDA output for the Antilles, which corresponds to the small variations observed in the MCDA map in the previous section.

The partial rank correlation coefficients (Figure 5.6) represent a statistical measure of the above-plotted correlation. Annual temperature and frequency of rainy days have the strongest linear association with the MCDA suitability.

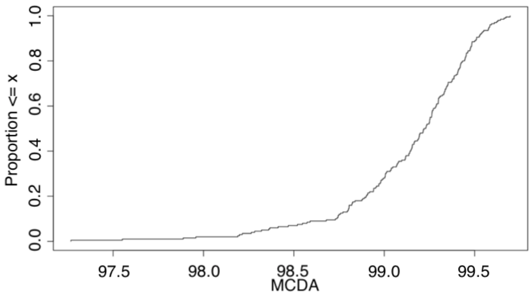

Figure 5.4: ECDF Guadeloupe

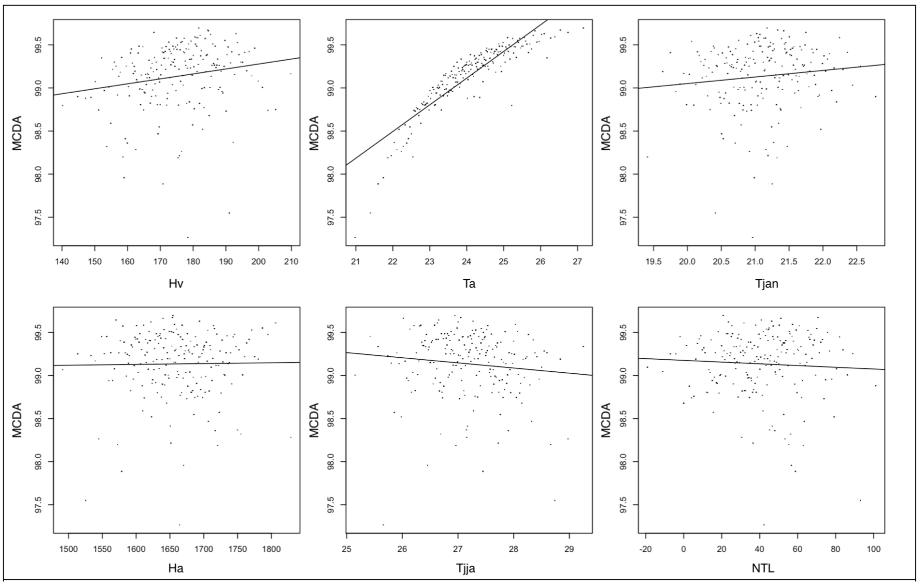

Figure 5.5: The scatterplots of the MCDA output as a function of each input parameter.

The JJA temperature has a negative linear correlation with MCDA suitability, suggesting that high summer temperatures could limit the activity of the vector.

The sensitivity expressed in the terms of partial inclination coefficients, which represent the relationship between the respective parameters and the exploratory variable in a multiple regression model controlling for the remaining explanatory variables, are shown in Table 5.4.

Table 5.4: Partial inclination coefficients

	Hv	Ta	Tjan	Ha	Tjja	NTL
PIC	0.0576	0.30966	0.07627	0.00009	-0.05953	0.000

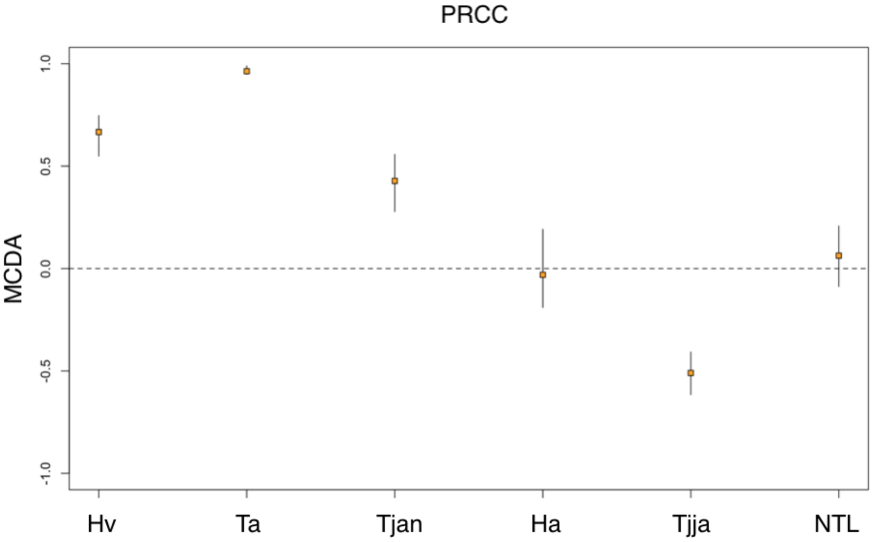

Figure 5.6: Partial rank correlation coefficients for Guadeloupe.

5.2 Assessment study - Bahariya (Egypt)

5.2.1 Overview of mean monthly values for two stability regimes

An overview of the mean monthly properties at 0600 and 1500 EET are presented in the Table below. The analysis is conducted for the 2017–2018 interval for which the entomological observations were carried out (Chapter 3). We see that Bahariya has a very pronounced diurnal temperature cycle with the biggest difference occurring in March (ΔT =17.83 °C). The highest morning temperatures are observed in August (23.74 °C); and in July for the 1500 regime (38.35 °C). Similarly, relative humidity has a pronounced daily cycle with the maximum occurring in December ($\Delta RH = 39.06\%$).

Table 5.5: Annual regime of mean properties at 0600 and 1500 EET for Bahariya (2017–2018).

	Jan	Feb	Mar	Apr	May	Jun	July	Aug	Sep	Oct	Nov	Dec
0600 AST												
Air temperature 2 m [C]	6.67	9.93	11.89	14.69	19.61	21.98	23.18	23.74	21.25	17.31	11.23	9.32
Relative humidity [%]	80.87	75.04	64.03	64.92	61.36	62.70	67.50	70.36	77.00	74.52	80.79	80.43
Wind speed 2 m [m/s]	0.54	0.35	0.54	0.34	0.51	0.31	0.35	0.23	0.25	0.44	0.33	0.42
1500 AST												
Air temperature 2 m [C]	19.87	24.24	29.72	31.25	35.18	37.36	38.35	37.28	34.83	30.69	25.63	21.34
Relative humidity [%]	38.81	31.40	18.51	18.76	18.60	19.35	20.71	25.98	27.52	30.66	34.26	41.37
Wind speed 2 m [m/s]	2.10	1.25	2.82	1.80	2.14	1.81	2.25	2.18	1.70	2.54	1.67	1.81

5.2.2 Current climate 1981–2010

The climate normals for the 1981–2010 period are shown in Figure 5.7: Annual temperature (Ta); Mean January temperature (Tjan); Mean JJA temperature

(Tjja); Total annual precipitation (Ha).

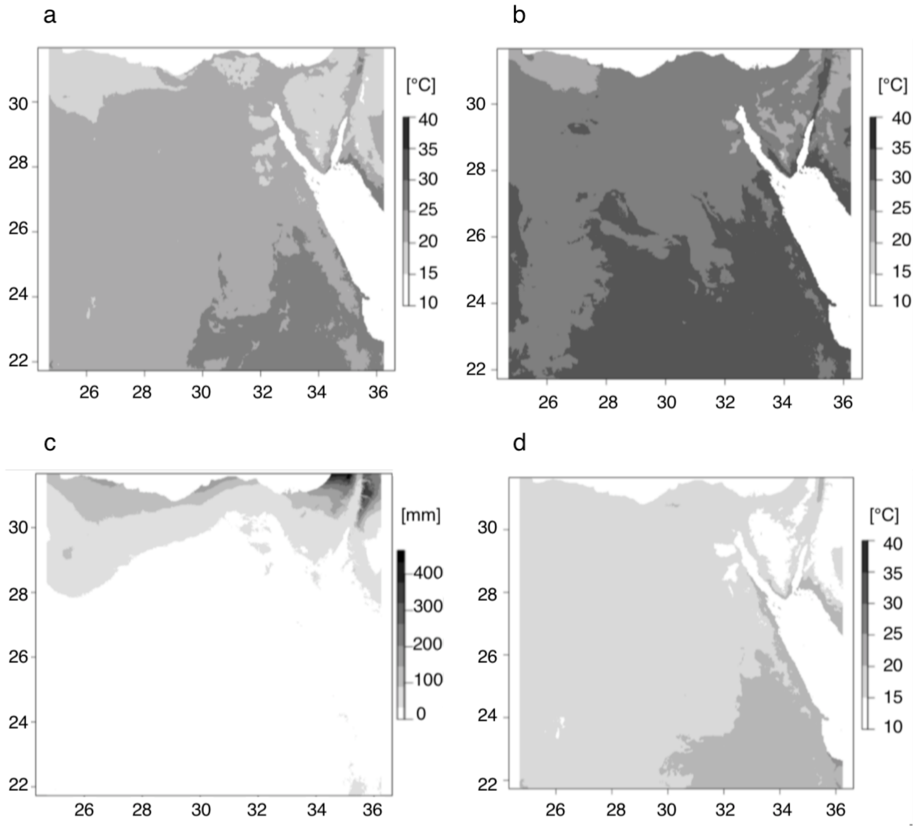

Figure 5.7: Overview of the most significant climate normals (1981-2010) potentially affecting *Cx. pipiens* vector establishment in Egypt: (a) Annual temperature (Ta); (b) Mean January temperature (Tjan); (c) Total annual precipitation (Ha); (d) Mean June-July-August (JJA) temperature (Tjja).

5.2.3 MCDA assessment study Egypt

The suitability for the establishment and activity of *Cx. pipiens* is shown in Figure 5.8. Suitable areas are largely located around the Nile delta and in the irrigated areas along the bank, further inland.

Other areas of suitability correspond to the populated areas on the Mediterranean and Red Sea coast. Finally, high suitability is observed in the locations corresponding to the desert Oasis towns, most notably Karga, Siwa and Bahariya.

Figure 5.9 represents the MCDA index calculated for individual years for the period 2000-2017; and the relative deviation (MCDAi - MCDAc)/(MCDAc) * 100) of annual values from the long-term averages (Figure 5.9). A decrease in suitability can be observed for 2016–2018. This is due an increase in observed summer JJA temperatures which resulted in a lower value for the sigma membership function corresponding to this climatic parameter.

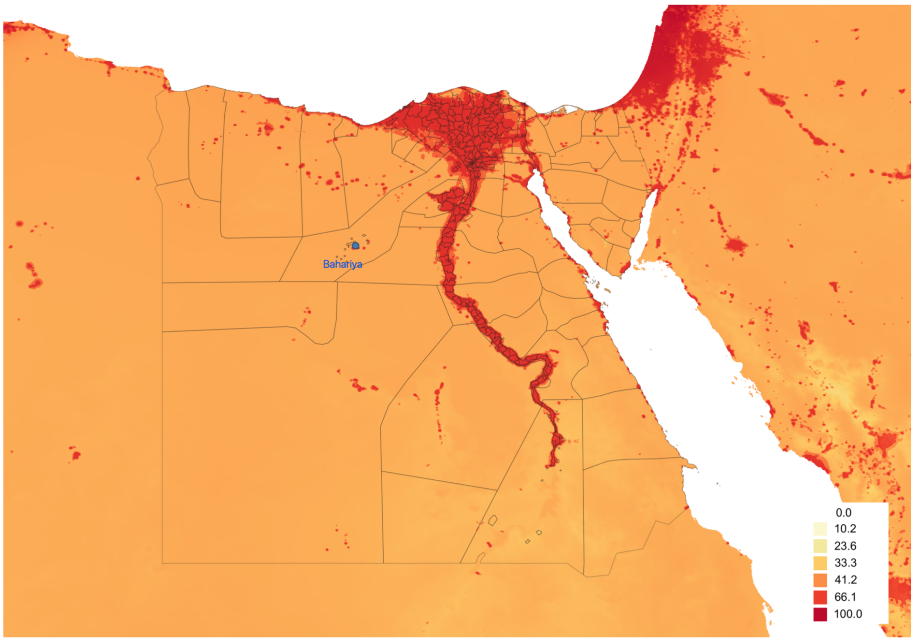

Figure 5.8: MCDA suitability for *Cx. pipiens* based on the 1981–2010 climatology

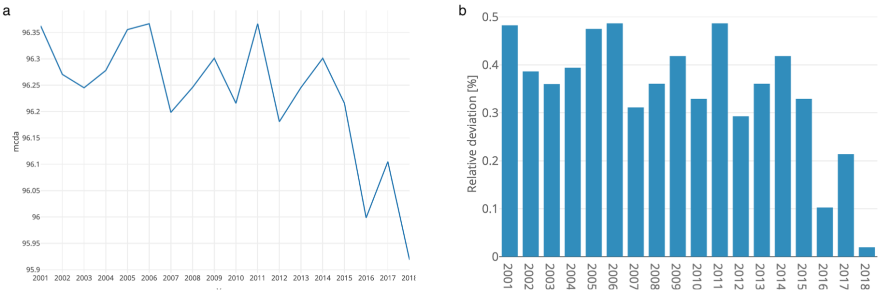

Figure 5.9: (a) MCDA suitability for individual years for Bahariya (DFC); (b) Relative deviation from the reference climatology.

5.2.4 Sensitivity analysis

The parameters were sampled from a normal distribution around the 1981–2010 mean and observed standard deviation (Table 5.6).

The empirical cumulative distribution function (ECDF) of the model results applied to the LHS sample is shown in Figure 5.10. We see that the high probability outputs are between 40-99, with the full range of the MCDA index (0-100) covered. This can be contrasted with the Guadeloupe ECDF where only the 95-100 range is covered, and the high probability outputs are within the 98-99 values.

The scatterplots shown in Figure 5.11 show the correlation of the output as

Table 5.6: Parameter distribution for the sensitivity analysis sampling (Hv – frequency of precipitation expressed as number of days within a year with rain> 1 mm; Ta – mean annual temperature [°C], Tjan – mean January temperature [°C]; Ha – total annual precipitation [mm]; Tjja – mean JJA temperature [°C]; NTL – Night time light).

Parameter	Distribution	Mean	SD
Hv	U(a,b)	a = 0	b = 52
Ta	N(μ,σ)	μ = 22.23	σ = 2.24
Ha	U(a,b)	a = 0	b = 210
Tjja	N(μ,σ)	μ = 29.34	σ = 2.37
NTL	U(a,b)	a = 0	b = 63

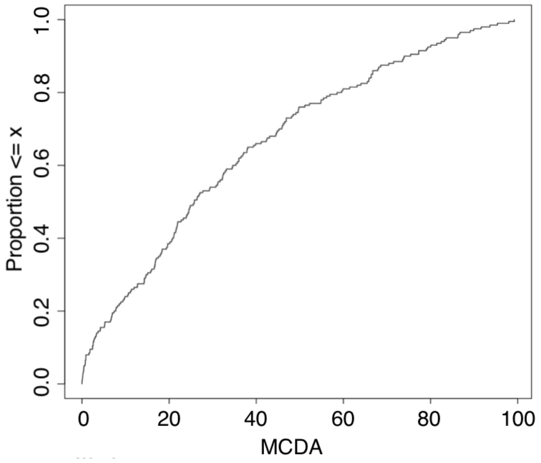

Figure 5.10: ECDF Egypt

a function of each input parameter. The strongest relationship is observed with annual precipitation and NTL. There is almost no correlation with the annual temperature, and there is a weak negative correlation with the JJA temperature. The frequency of precipitation has a moderate positive correlation.

The partial rank correlation coefficients (PRCC Figure 5.12) represent a statistical measure of the above-plotted correlation. Total annual precipitation and NTL have the strongest linear association with the MCDA suitability. The JJA temperature has a negative linear correlation with MCDA suitability, suggesting that high summer temperatures are limiting the activity of the vector.

The sensitivity expressed with the partial inclination coefficient is shown in Table 5.7.

Table 5.7: Partial inclination coefficient

	Hv	Ta	Ha	Tjja	NTL
PIC	0.23756	-0.05218	0.32491	-0.156882	0.84588

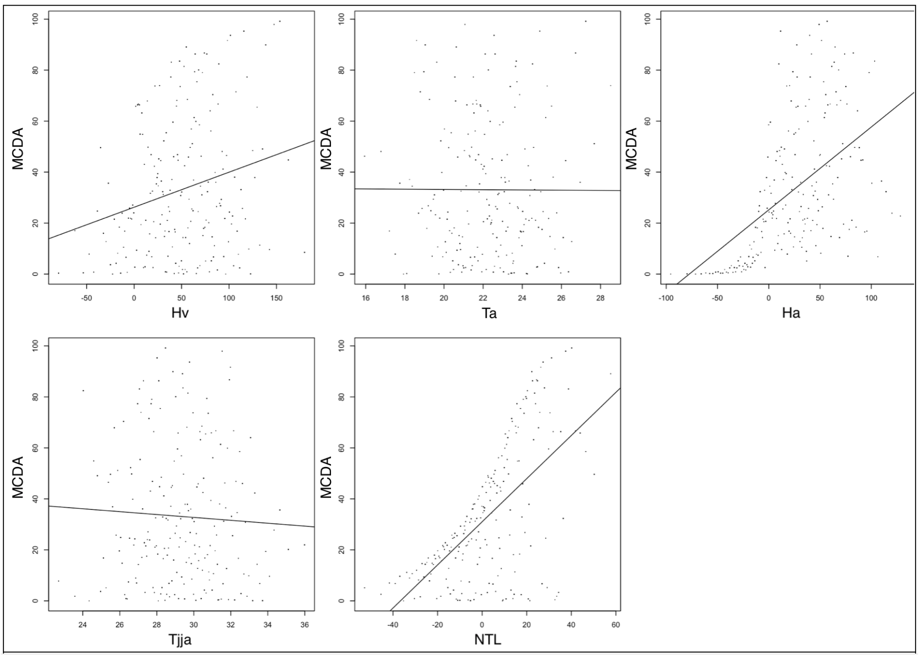

Figure 5.11: The scatterplots of the MCDA output as a function of each input parameter.

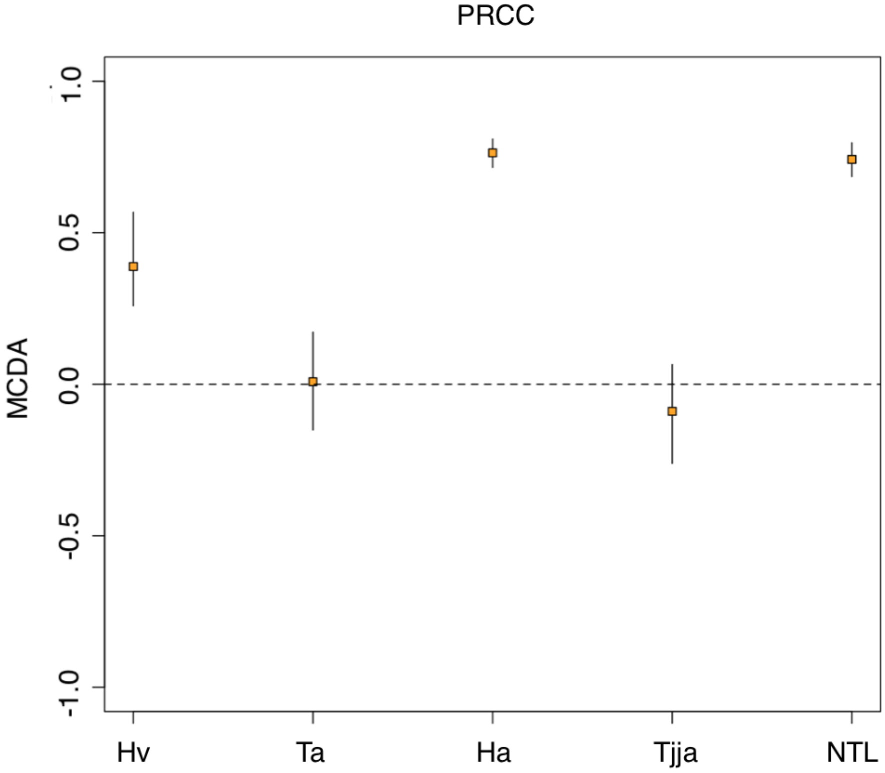

Figure 5.12: Partial rank correlation coefficients for Egypt.

5.3 Assessment study - Petrovaradin (Serbia)

5.3.1 Overview of mean monthly values for two stability regimes

In the tables presented below, an overview of the mean monthly properties at 0600 and 1500 CET is shown. The analysis is conducted for the 2016–2017 span for which the entomological observations were carried out.

Table 5.8: Annual regime of mean properties at 0600 and 1500 CET for Petrovaradin (2016–2017)

	Jan	Feb	Mar	Apr	May	Jun	July	Aug	Sep	Oct	Nov	Dec
0600 AST												
Air temperature 2 m [C]	-3.34	4.15	6.30	8.92	13.62	18.54	19.16	17.87	13.79	8.71	5.76	0.92
Relative humidity [%]	86.35	78.40	81.34	78.05	84.48	81.93	79.51	82.72	87.21	88.14	84.62	81.23
Wind speed 2 m [m/s]	0.42	0.50	0.41	0.45	0.41	0.34	0.35	0.42	0.38	0.46	0.48	0.44
1500 AST												
Air temperature 2 m [C]	1.34	9.89	13.80	18.56	22.37	27.50	29.03	28.91	23.16	16.32	10.31	4.67
Relative humidity [%]	74.05	62.46	53.11	45.95	49.38	48.89	44.07	43.89	51.48	60.26	68.64	70.83
Wind speed 2 m [m/s]	0.47	0.54	0.47	0.57	0.49	0.49	0.48	0.47	0.49	0.57	0.51	0.49

5.3.2 Annual precipitation regime

Table 5.9: Annual regime of mean properties at 0600 and 1500 CET for Petrovaradin (2016–2017).

	Jan	Feb	Mar	Apr	May	Jun	July	Sep	Oct	Nov	Dec
Total precipitation [mm]	40.5	40.4	50.86	64.64	69.65	113	40.2	42.4	66.21	49.6	25.91
Total days with precipitation rate over 7 mm/day	3	3	5	6	8	8	3	5	7	4	7

5.3.3 Current climate 1981–2010

The climate normals for the 1981-2010 period are shown in the figure below: Annual temperature (Ta); Mean January temperature (Tjan); Mean JJA temperature (Tjja); Total annual precipitation (Ha).

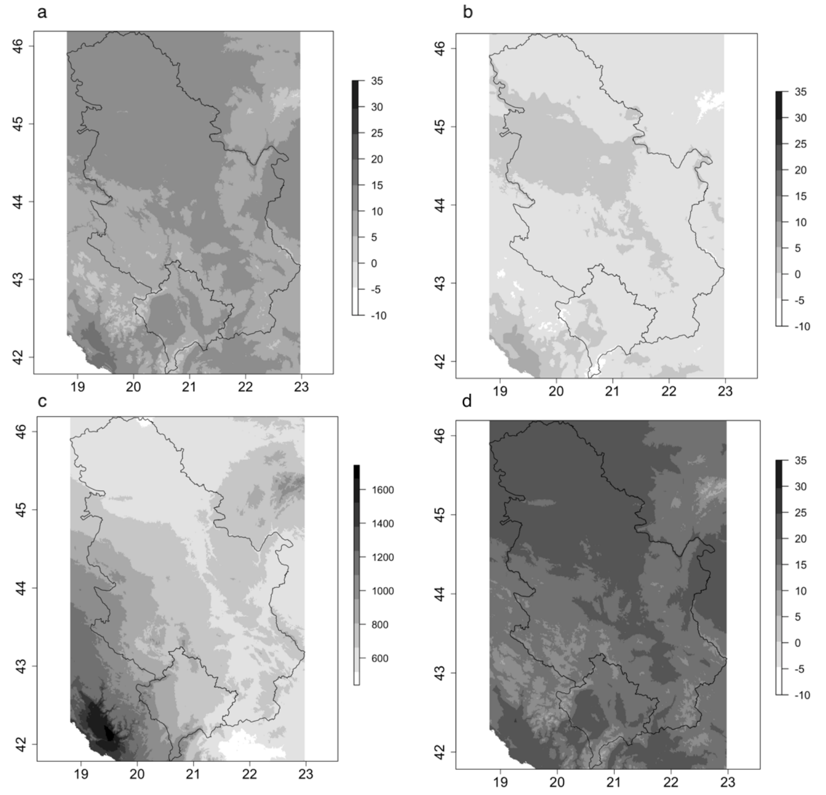

Figure 5.13: Overview of the most significant climate normals (1981-2010) potentially affecting *Cx. pipiens* vector establishment in Serbia: (a) Annual temperature (Ta) [°C]; (b) Mean January temperature (Tjan) [°C]; (c) Total annual precipitation (Ha) [mm]; (d) Mean June-July-August (JJA) temperature (Tjja) [°C].

5.3.4 MCDA assessment study Petrovaradin

The suitability for the overall annual activity of *Cx. pipiens* is shown on Figure 5.14. Here the MCDA is constructed for annual activity rather than establishment and overwinter because (i) *Culex* usually overwinter in basements or other indoor spaces and (ii) is already established in the whole study area. The climatic conditions in Serbia and other mid-latitude areas, especially around larger rivers with flooding areas are very favourable for the *Cx. pipiens*.

We see that the suitability is slightly lower for the high-elevation areas corresponding to: Kopaonik in the South (2.017 m.a.s.l), the highland are on the border with Montenegro, the Carpatian mountains in the north-east, on the border with Romania; and Stara Planina in the south-east which is part of the Balkan mountain range stretching through Bulgaria and Serbia.

The highest suitability stretches along the river basins of the Danube, Drina and Morava rivers. The climatic suitability is high for the whole northern region of the Vojvodina province. In Figure 5.14 we see the MCDA index calculated for

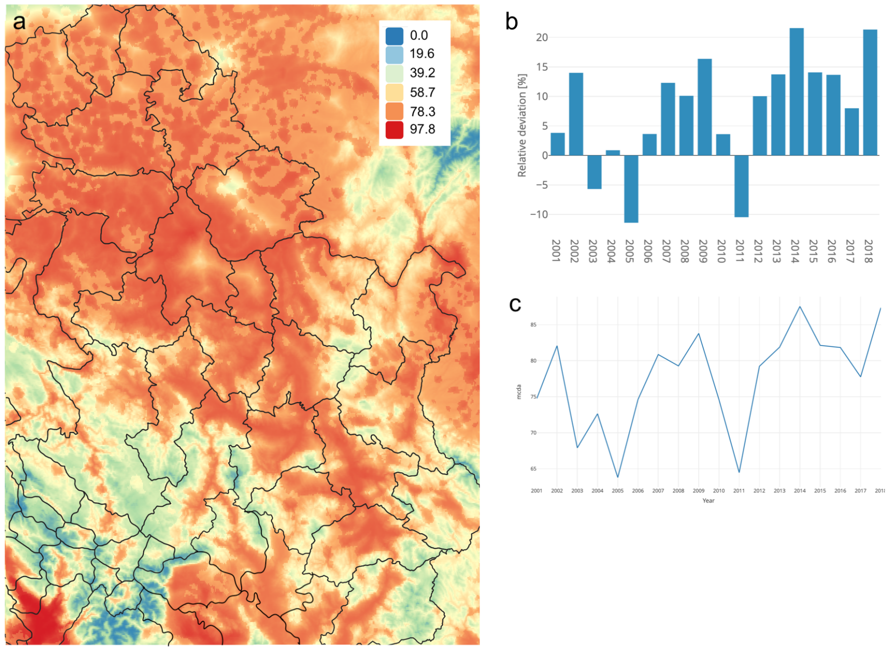

Figure 5.14: (a) MCDA suitability for *Cx. pipiens* based on the 1981-2010 climatology for Serbia; (b) MCDA suitability for individual years; (c) Relative deviation from the reference climatology.

individual years for the period 2000–2017; and the relative deviation of annual values from the long-term averages (Figure 5.14). The decreased suitability for 2005 is a result of lower annual temperature compared to the rest of the period (2001-2018); the second minimum in 2011 occurs as a result of a moderate decrease in mean annual temperature and a decrease in total annual precipitation and number of rainy days (precipitation frequency).

5.3.5 Sensitivity analysis

The parameter distribution for Periovarian is shown in Table 5.10. The parameters were sampled from a normal distribution around the spatial mean and observed standard deviation of the 1981–2010 climate normals.

The empirical cumulative distribution function of the model results applied to the LHS sample is shown on the figure below. We see that the high probability outputs are within the high suitability MCDA values of 60–80, but ranges from 20–90 are also represented.

The scatterplots shown in Figure 5.16 show the correlation of the output as a function of each input parameter. The strongest relationship is observed with the annual temperature and distance to water. NTL has a moderate correlation with MCDA. And we can see that the ranges for the mean JJA temperature, total annual precipitation and precipitation frequency do not have a significant influence on the change of the MCDA output for Petrovaradin.

The partial rank correlation coefficients (Figure 5.17) represent a statistical measure of the above-plotted correlation. Mean annual temperature and

Table 5.10: Parameter distribution for the sensitivity analysis sampling (Hv – frequency of precipitation expressed as number of days within a year with rain> 1 mm; Ta – mean annual temperature [°C], Tjan – mean January temperature [°C]; Ha – total annual precipitation [mm]; Tjja – mean JJA temperature [°C]; NTL – Night time light).

Parameter	Distribution	Mean	SD
Hv	N(μ,σ)	$\mu = 107$	$\sigma = 16.4$
Ta	N(μ,σ)	$\mu = 12.64$	$\sigma = 1.96$
Ha	N(μ,σ)	$\mu = 744.68$	$\sigma = 180.124$
Tjja	N(μ,σ)	$\mu = 18.79$	$\sigma = 2.43$
NTL	U(a,b)	a = 0	b = 63
DistW	U(a,b)	a = 0	b = 37000

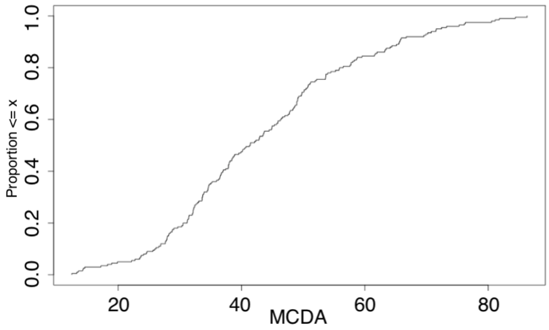

Figure 5.15: ECDF Serbia

Distance from water have the strongest linear association with the MCDA suitability.

The sensitivity expressed with the partial inclination coefficient is shown in Table 5.11.

Table 5.11: Partial inclination coefficient

	Hv	Ta	Ha	Tjja	NTL	WatD
PIC	0.14064	6.01441	0.20975	0.36629	0.31484	-1.93605

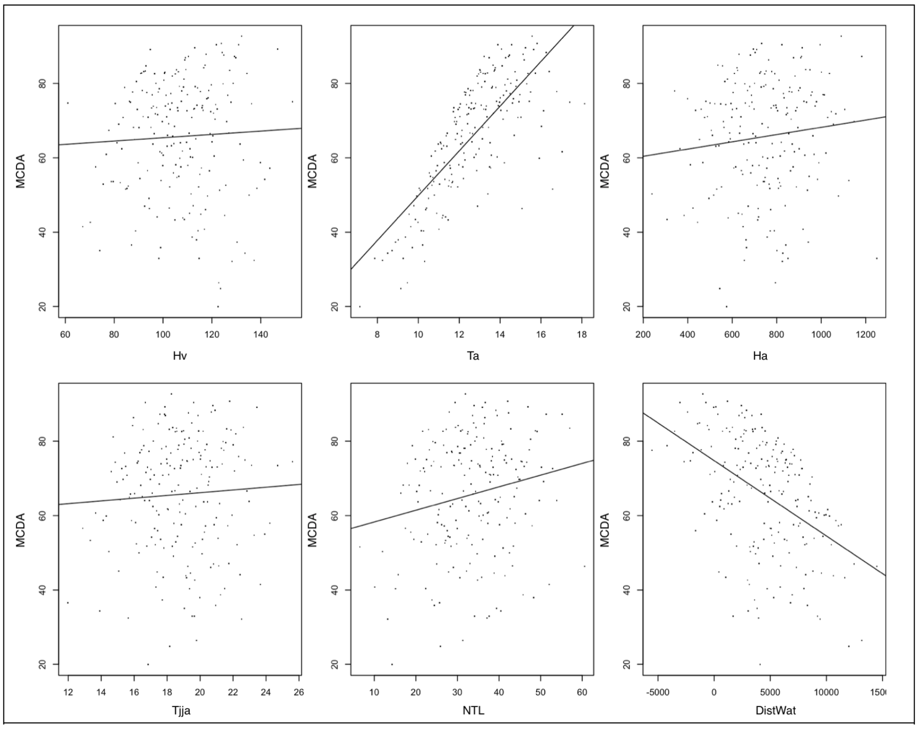

Figure 5.16: The scatterplots of the output as a function of each input parameter

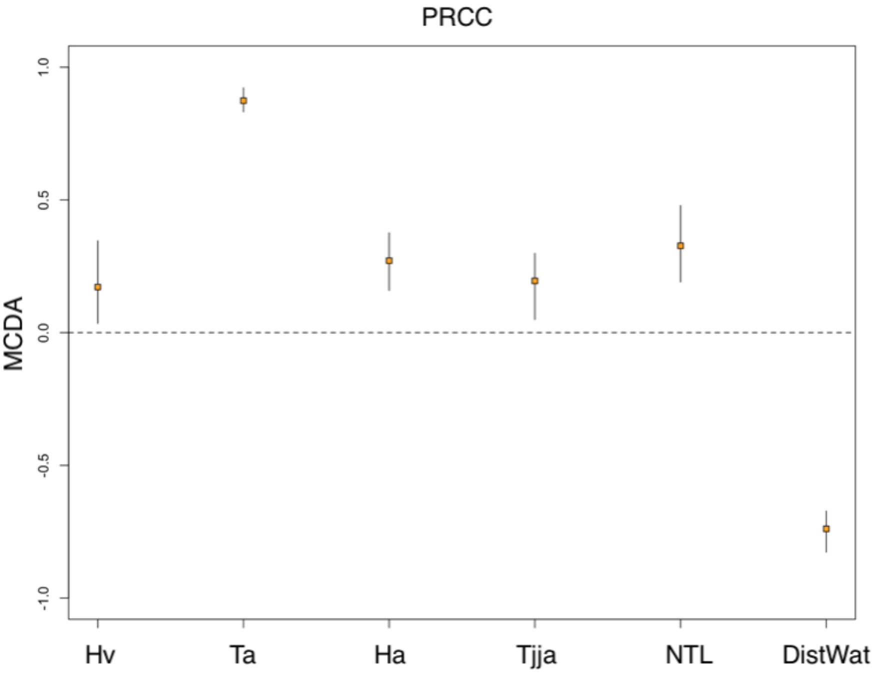

Figure 5.17: Partial rank correlation coefficients for Serbia.

5.4 Discussion

There have been many recent studies focusing on the climatic suitability of *Ae. aegypti* due to the emerging threat of the Zika virus and the annual increase in Dengue cases. According to the World Health Organisation, Dengue fever is the most hazardous VBD in the world, and also the most rapidly spreading. A thirtyfold increase in global incidence over the past five decades has been reported [159]. However, most of the studies were conducted on a global or continental scale [16, 18, 19, 28, 160], this is the first study to consider the suitability on the country level for Guadeloupe. Moreover, we believe this is the first study to analyse the climatic suitability for the establishment and annual activity of *Cx. pipiens* in Serbia as well as Egypt. *Cx. pipiens* is becoming increasingly important with a sharp rise in the number of WNV cases compared to the last decade. The most affected countries in Europe, listed by number of cases are: (1) Serbia; (2) Italy and (3) Greece [161, 162].

The MCDA model is useful in the analysis of emerging hot spots or high-risk areas for vector activity influenced by the local climate. Moreover, looking at annual departures in suitability from the long-term averages can indicate a more or less favourable year for the inter-annual activity of the vector. Even slight changes in the suitability index could indicate higher activity and greater population abundance of the vector during the year; which has an influence on disease transmission rates.

The overall suitability for Guadeloupe was very high for the entire region, the highest sensitivity between the MCDA output and the input climatic variables was identified for annual temperature (Ta). Peaks in the suitability were identified for 2005, 2010-2011 and 2016-2017. This coincides with the reported Dengue outbreaks in Guadelouope and Martinique: 2005 (July, DENV4), 2010 (May, DENV1) [163] with the highest number of cases observed in 2010; the final peak can be associated with the Zika outbreak in 2016 [164].

The suitability for Egypt was confined to the populated areas along the coast and the Nile delta as well as the desert oases. The simulated suitability pattern matches the reported cases for *Cx. pipiens* in Egypt [165]. The highest sensitivity was observed with NTL. For Serbia, the highest suitability stretches along the river basins of the Danube, Drina and Morava rivers. The climatic suitability is high for the whole northern region of the Vojvodina province. The highest sensitivity was observed with mean annual temperature (Ta).

The relationship with NTL has different implications for the three study sites: (i) Availability of breeding sites; (ii) Blood meal availability, (iii) Availability of overwintering sites. The assumption is that with an increase in population, the number of artificial containers that can serve as vector breeding sites increases, this is of course dependent on many socio-economic factor such as poverty, water-use habits and irrigation practices, the analysis of which could be important but is beyond the scope of this thesis. The availability of breeding sites linked to population is especially important for Egypt, where there is practically no precipitation during the year, and the vector completely relies on human generated water (in the desert) and Nile flooding (along the delta).

Blood meal availability linked to the human population density is most relevant for Guadeloupe, because *Ae. aegypti* is highly anthropophilic with a high preference for urban environments [166–168].On the other hand, *Cx. pipiens* is known to feed on other endothermic vertebrates consulting the class Mammalla and Aves. The increased suitability due to the availability of overwintering sites is relevant only for the Serbia study locations, since *Ae. aegypti* does not have an overwintering mechanism. Due to the warm dessert climate the *Cx. pipiens* species in Egypt do not seek shelter during winter.

Chapter 6

Population dynamics model

6.1 Dynamical models and stability

The mathematical infrastructure of the theory of stability was first developed by the Russian physicist and mathematician Aleksandr Mikhailovich Lyapunov in his thesis in 1884 [169]. The later development of the qualitative theory of stability of dynamical systems is attributed to Aleksandr Aleksandrovich Andronov, Vladimir Igorevich Arnold and their students [170–175]. Since then it has been applied to study dynamics of biological dynamical systems. From a practical point of view, analysing the stability and eigen-properties of a population dynamics model is important for multiple reasons. It is meaningful to look at the way our dynamical system behaves near equilibrium points as a function of different temperatures and how it reacts to perturbations around those states. The characteristic frequencies can help us evaluate the realism of the model, i.e. to see whether the eigen-frequencies correspond to observed biological frequencies (the ground truth). The frequencies are calculated in this chapter and the internal verification is carried out in Chapter 7. This type of analysis can support model initialization and help in reducing the spin-up time due to short-lived transient behaviour.

6.2 Stability analysis

In this chapter the 10-stage ODE population dynamics model outlined in Chapter 3 is examined in terms of numerical integration, stability and initial dynamics. To assess the stability properties, first the equilibrium states of the dynamical system are determined. In a second step, the stability of each state and the manner in which a trajectory in phase space would eventually approach the equilibrium (if stable) or diverge from it (if unstable) is examined.

The dynamical system can be written as $\frac{dX_i}{dt} = F_i\left(X_1, X_2, ..., X_n, \lambda\right) (i = 1 : 10)$ with λ signifying the control parameters governing stage-specific development and mortality rates, and X_i represents the different stages in the mosquito development cycle. The potential equilibrium points can be determined by solving the equation $\frac{dX_i}{dt} = 0$. In phase space $F_i(X_{eq}, \lambda)$ is a stationary state, i.e. the system does not change over time.

6.2.1 System Jacobian

The Jacobian of the system is given as $\hat{J}_{i,j} = \frac{\partial f_i}{\partial x_j}$ and is presented in the matrix below:

$$\hat{J} = \begin{pmatrix} -(f_E+\mu_E) & 0 & 0 & 0 & 0 & 0 & \beta_1\gamma_{Ao} & 0 & 0 & \beta_2\gamma Ao \\ f_E & -(f_L+m_L+2\frac{m_L}{K_L}L) & 0 & 0 & 0 & 0 & 0 & 0 & 0 & 0 \\ 0 & f_L & -(f_P+m_P) & 0 & 0 & 0 & 0 & 0 & 0 & 0 \\ 0 & 0 & e^{-(1+\frac{P}{kP})\mu_{em}} f_P\sigma - \frac{e^{-(1+\frac{P}{k_P}} f_P P\mu_e m\sigma}{k_P} & -(m_A+\gamma_{Aem}) & 0 & 0 & 0 & 0 & 0 & 0 \\ 0 & 0 & 0 & \gamma_{Aem} & -(m_A+\gamma_{Ab}+\mu_r) & 0 & 0 & 0 & 0 & 0 \\ 0 & 0 & 0 & 0 & \gamma_{Ab} & -(f_{Ag}+m_A) & 0 & 0 & 0 & 0 \\ 0 & 0 & 0 & 0 & 0 & f_{Ag} & -(m_A+\gamma_{Ao}+\mu_r) & 0 & 0 & 0 \\ 0 & 0 & 0 & 0 & 0 & 0 & \gamma_{Ao} & -(m_A+\gamma_{Ab}+\mu_r) & 0 & \gamma_{Ao} \\ 0 & 0 & 0 & 0 & 0 & 0 & 0 & \gamma_{Ab} & -(f_{Ag}+m_A) & 0 \\ 0 & 0 & 0 & 0 & 0 & 0 & 0 & 0 & f_{Ag} & -(m_A+\gamma_{Ao}+\mu_r) \end{pmatrix}$$

The divergence of the flow is $\nabla \cdot \boldsymbol{F} = \sum_{i=1}^{i=10} \frac{\partial F_i}{\partial X_i}$ which is the trace of the Jacobian and is equal to the scalar:

$$\begin{aligned} \nabla \cdot \boldsymbol{F} = -((f_E + \mu_E) + (m_P + f_P) + (m_A + \gamma_{Aem}) + 2 \cdot (m_A + \mu_r + \gamma_{Ao}) + \\ +2 \cdot (m_A + \mu_r + \gamma_{Ab}) + 2 \cdot (m_A + f_{Ag}) + (m_L + 2\frac{m_L}{\kappa_L} + f_L)) \end{aligned} \tag{6.1}$$

which is always negative for the temperature interval [−60°C, 80°C]. Since $\nabla \cdot \boldsymbol{F} < 0$ for $t > t_0$ it shows that the system is dissipative. A volume $\Delta\Gamma$ in phase space Γ (which is the 10 dimensional space of model states $\boldsymbol{X}$) will for $t \to \infty$ tend to a subset of Γ whose dimension is strictly less than 10.

6.2.2 Determining the equilibrium points

Solving for $\frac{dX_i}{dt} = 0$ we determined two equilibrium states: $\boldsymbol{X}_{eq}^1 = (0, 0, 0, 0, 0, 0, 0, 0, 0, 0)$ and $\boldsymbol{X}_{eq}^2 = (E^*, L^*, P^*, A_{em}^*, A_{b1}^*, A_{g1}^*, A_{o1}^*, A_{b2}^*, A_{g2}^*, A_{o2}^*)$. The trivial solution $\mathbf{X}_{eq}^1 = 0$ is the obvious equilibrium solution corresponding to no-population. The non-trivial equilibrium is shown in Figure 6.1c and corresponds to the following solution: $L = -\frac{W_n\left(-\frac{c \cdot exp(-ac/b)}{b}\right)}{c} - \frac{a}{b}$; with the other variables expressed through L (detailed in Appendix A.7). The parameters a, b, c are different functions of the development and mortality rates.

The results show that the system operates in two stability regimes. The system is stable for the 1^{st} equilibrium and unstable for the 2^{nd} equilibrium for all runs below a characteristic temperature ($T_{th} = 9.8$°C); and alternately, stable for the 2^{nd} and unstable for the 1^{st} equilibrium for all values above this threshold. Qualitatively, we can see that for the first regime (Figure 6.1a) all solutions quickly converge to the zero equilibrium while for the second regime the null solution is unstable and all solutions diverge (Figure 6.1b). The same behaviour is observed for different initial conditions (indicated by dashed lines in Figure 6.1).

If the system for the second regime is allowed to run for a larger number of iterations than in Figure 6.1b we see that the solutions converge on a second stable cycle (fig. 6.1c). The 2nd equilibrium point is stable for all examined temperatures in the 10°C−40°C range i.e. has negative real parts of all eigenvalues of the Jacobian evaluated at constant temperature.

The phase portraits for Larva-Pupa (LP) stages for the study locations in Pointe-à-Pitre (Guadeloupe), Bahariya (Egypt) and Petrovaradin (Serbia) are

Table 6.1: Summary of the stability of fixed points with assortment (detailed in Appendix A.7)

Independent Equilibrium Points	Nature of equilibrium points	
	Case I ($T < 9.8°$C)	Case II ($T \geq 9.8°$C)
$\boldsymbol{X}_{eq}^{1} = (0,0,0,0,0,0,0,0,0,0)$	Stable node	Unstable node
$\boldsymbol{X}_{eq}^{2} = (E^{*}, L^{*}, P^{*}, A_{em}^{*}, A_{b1}^{*}, A_{g1}^{*}, A_{o1}^{*}, A_{b2}^{*}, A_{g2}^{*}, A_{o2}^{*})$	Unstable node	Stable node

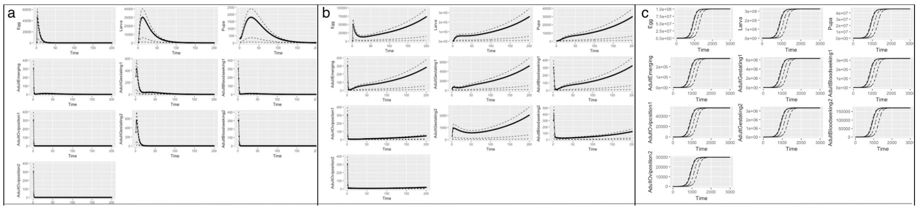

Figure 6.1: Numerical solution for (a) $T = 9°$ C for 200 iterations (x-axis), (b) $T = 11°$C for 200 iterations, (c) $T = 11°$C and 3000 iterations and initial conditions X = (300, 300, 300, 300, 300, 300, 300, 300, 300, 300); the y-axis represents the number of vectors in each stage.

shown in Figure 6.2. We see that for Guadeloupe (Figure 6.2c) the system is always in the II regime. This is a result of the high temperatures characteristic of this location with very low annual variation, which in turn produces relatively small osculations around the second equilibrium (L^{*}, P^{*}). Bahariya (Figure 6.2b) has a similar temperature profile however with a broader annual range, creating larger oscillations around the second equilibrium. On the other hand, for the system in Petrovaradin (Figure 6.2a) we can clearly see the two annual cycles and a return to regime I (stable, null equilibrium).

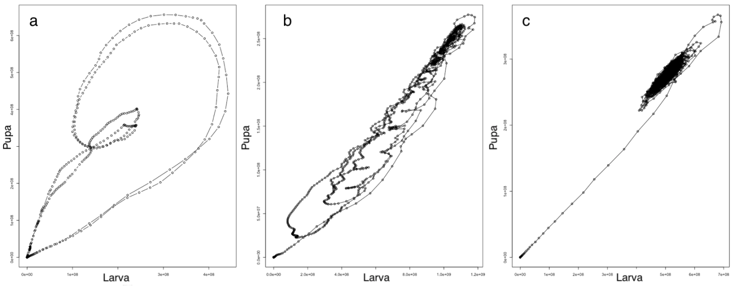

Figure 6.2: Larva-Pupa (LP) phase portrait for (a) Petrovaradin (*Cx. pipiens*), (b) Bahariya (*Cx. pipiens*), and (c) Guadeloupe (*Ae. aegyti*) initialized with X = (300, 300, 300, 300, 300, 300, 300, 300, 300, 300).

To further illustrate this point, we can observe (Figure 6.3) the difference between the LP phase portraits for Bahariya for a system forced with: (a) Constant temperature ($T = 20^{circ}C$, regime II); (b) A sine wave that switches between regime I and regime II $\phi = Asin(2\pi\nu t) + D$ (A = 10, $\nu = 1/365, D =$ 10); (c) The observed temperature for Bahariya (detailed in Appendix A.2)

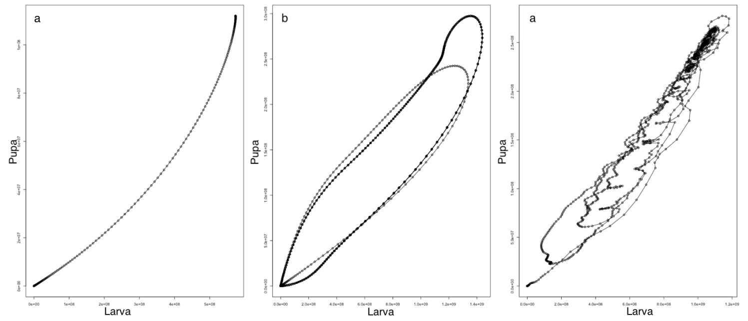

Figure 6.3: LP phase portrait for *Cx. pipiens* (Bahariya), forced with: (a) Constant temperature ($T = 20^{circ} C$, regime II); (b) A sine wave that switches between regime I and regime II $\phi = Asin(2\pi\nu t) + D$ (A = 10, $\nu = 1/365, D = 10$); (c) The observed temperature for Bahariya (detailed Chapter 4) initialized with X = (300, 300, 300, 300, 300, 300, 300, 300, 300, 300).

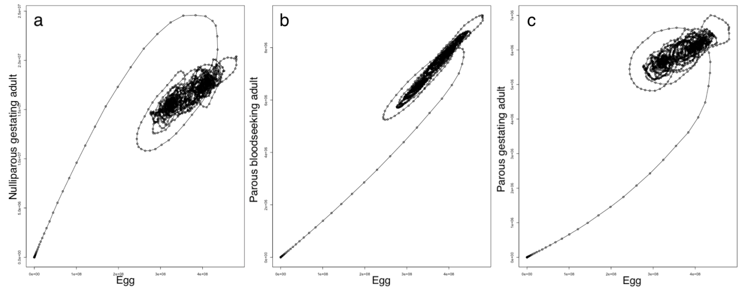

Figure 6.4: Phase portraits for the: (a) E-A_{g1}, (b) E-A_{b2}, (c) E-A_{g2} *Ae. aegypti* model (Guadeloupe) initialized with X = (300, 300, 300, 300, 300, 300, 300, 300, 300, 300).

6.2.3 Initial dynamics – Transient analysis and initialization

To examine the transient response of the model to initialisation, the short term model behaviour following initialization is analysed. In Figure 6.5 we see that, for a model forced with constant temperature (T = 20 °C) all stages reach the equilibrium at around 200 days after initialization. This characteristic length scale decreases with an increase in temperature (Figure 6.6). Magnitudes of the different stages differ significantly with the largest values corresponding to the aquatic stages: larva, egg and pupa, respectively. The equilibrium for the adult stages was the highest for the parous gestating adults (A_{g2}).

When the stage is initialized with a value greater than the steady state for that temperature, damped oscillation around the equilibrium point is observed.

The short-term dynamics will depend on the initial condition. Since the runs require 200 days (> 6 months) at T = 20° C, spin-up time is an important consideration for simulating short-term, near-real time dynamics of the vector. The above analysis is performed for the model with constant temperatures. If temperature changes, the equilibrium point will change and the system will try

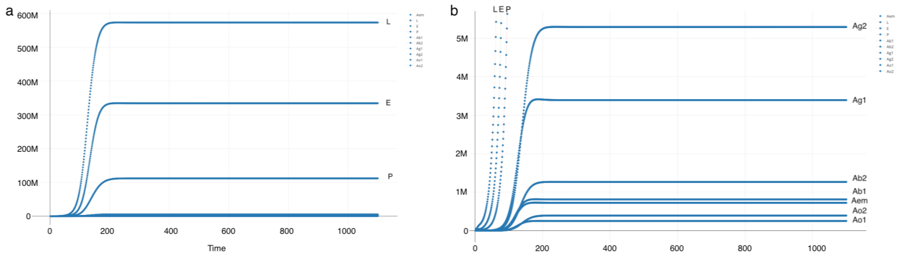

Figure 6.5: Output for model forced with constant temperature:(a) aquatic stages and (b) adult stages.

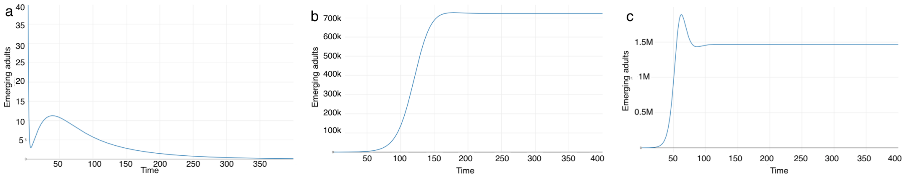

Figure 6.6: Output of model (emerging adults) forced with different constant temperatures: (a) 10 °C, (b) 20 °C, (c) 30 °C.

to converge to that point. However, the convergence rate will be in competition with the characteristic time of changing temperature .

To reduce this spin up time the model can be initialized from the non-trivial equilibrium evaluated corresponding to the initial temperature ($T(t = 0)$). This is shown in Figure 6.7.

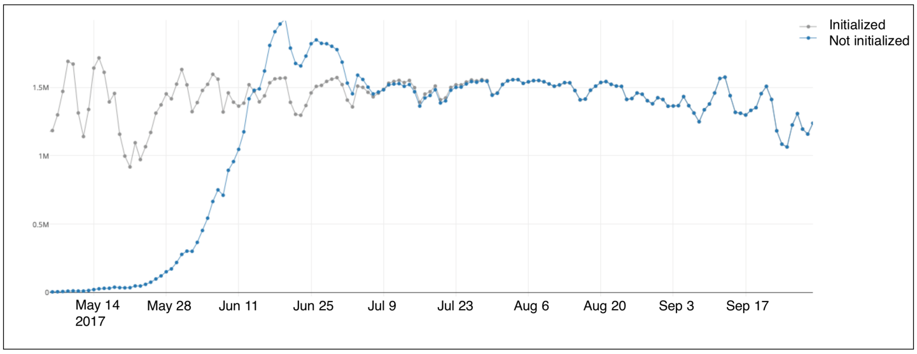

Figure 6.7: Comparison of non-initialized model (*blue*) to model initialized with the non-trivial equilibrium (*gray*).

6.3 Analysis of the eigenproperties of the ODE vector population dynamics model

In this section we examine the properties of the system around the unstable null equilibrium and explain the basic ideas and methods for conducting the stability analysis. An important consideration for any equilibrium is the manner in which a small perturbation would approach or escape the equilibrium state. The null equilibrium, specifically, has two biological interpretations corresponding to two identified stability regimes. (i) In a spring, start-of-season, scenario the biological population of the *Cx. pipiens* vector goes from a winter minimum (close to zero) to the first spring peak. In the model this change is characterized by the transition of X^1_{eq} from stable -> unstable. (ii) The autumn, end-of-season, scenario in which the population drops to zero and the model X^1_{eq} shifts from unstable -> stable. Analysing the oscillatory dynamics as well as the decay and growth terms of the normal modes describe the speed and manner in which this transitions occur in the model.

In a first step we perform a linearisation of the system around the equilibrium point. Second, we investigate the system linearised around several characteristic points during the model run to investigate the emerging doubling in the oscillatory modes and a shift to higher frequencies with an increase in temperature. A linearised system is always a local approximation about the operating point: as the operating point changes, the linearised model changes, for the same non-linear system. Linearisation can be used to give important information about how the system behaves in the neighbourhood of relevant points where we want to use a linear system to approximate the behaviour of the non-linear system.

6.3.1 Linearisation

The values of the independent variable close to the equilibrium point can be expressed as $x = x^* + x'$. Differentiation for x' the expression becomes $dx'/dt = dx/dt - dx^*/dt$. Since the time-derivative evaluated at the equilibrium is zero it can be evaluated as $dx'/dt = dx/dt$. The system can then be written as:

$$\frac{dE'}{dt} = \gamma_{Ao}(\beta_1 A_{o1} + \beta_2 A_{o2}) - (\mu_E + f_E)E \tag{6.2}$$

$$\frac{dL'}{dt} = f_E E - (m_L(1 + \frac{L}{\kappa_L}) + f_L)L \tag{6.3}$$

$$\frac{dP'}{dt} = f_L L - (m_P + f_P)P \tag{6.4}$$

$$\frac{dA'_{em}}{dt} = f_P P \sigma e^{-\mu_{em}(1+\frac{P}{\kappa_P})} - (m_A + \gamma_{Aem})A_{em} \tag{6.5}$$

$$\frac{dA'_{b1}}{dt} = \gamma_{em} A_{em} - (m_A + \mu_r + \gamma_{Ab})A_{b1} \tag{6.6}$$

$$\frac{dA'_{g1}}{dt} = \gamma_{Ab} A_{b1} - (m_A + f_{Ag})A_{g1} \tag{6.7}$$

$$\frac{dA'_{o1}}{dt} = f_{Ag}A_{g1} - (m_A + \mu_r + \gamma_{Ao})A_{o1} \tag{6.8}$$

$$\frac{dA'_{b2}}{dt} = \gamma_{Ao}(A_{o1} + A_{o2}) - (m_A + \mu_r + \gamma_{Ab})A_{b2} \tag{6.9}$$

$$\frac{dA'_{g2}}{dt} = \gamma_{Ab}A_{b2} - (m_A + f_{Ag})A_{g2} \tag{6.10}$$

$$\frac{dA'_{o2}}{dt} = f_{Ag}A_{g2} - (m_A + \mu_r + \gamma_{Ao})A_{o2} \tag{6.11}$$

Due to the existence of non-linear terms the variables can be written in terms of deviations as $x = x^* + x'$:

$$\frac{dE'}{dt} = \gamma_{Ao}(\beta_1(A^*_{o1} + A^{'}_{o1}) + \beta_2(A^*_{o2} + A^{'}_{o2})) - (\mu_E + f_E)(E^* + E^{'}) \tag{6.12}$$

$$\frac{dL'}{dt} = f_E(E^* + E^{'}) - \left((m_L + f_L)(L^* + L^{'}) + 2\frac{m_L}{k_L}L^*L^{'} + \frac{m_L}{k_L}L^{*2} + \frac{m_L}{k_L}L^{'2}\right) \tag{6.13}$$

$$\frac{dP'}{dt} = f_L(L^* + L^{'}) - (m_P + f_P)(P^* + P^{'}) \tag{6.14}$$

$$\frac{dA'_{em}}{dt} = f_P(P^* + P^{'})\sigma e^{-\mu_{em}} e^{-\mu_{em}\frac{P^*}{\kappa_P}} e^{-\mu_{em}\frac{P^{'}}{\kappa_P}} - (m_A + \gamma_{Aem})(A^*_{em} + A^{'}_{em}) \tag{6.15}$$

$$\frac{dA'_{b1}}{dt} = \gamma_{em}(A^*_{em} + A^{'}_{em}) - (m_A + \mu_r + \gamma_{Ab})(A^*_{b1} + A^{'}_{b1}) \tag{6.16}$$

$$\frac{dA'_{g1}}{dt} = \gamma_{A_b}(A^*_{b1} + A^{'}_{b1}) - (m_A + f_{Ag})(A^*_{g1} + A^{'}_{g1}) \tag{6.17}$$

$$\frac{dA'_{o1}}{dt} = f_{Ag}(A^*_{g1} + A^{'}_{g1}) - (m_A + \mu_r + \gamma_{Ao})(A^*_{o1} + A^{'}_{o1}) \tag{6.18}$$

$$\frac{dA'_{b2}}{dt} = \gamma_{Ao}((A^*_{o1} + A^{'}_{o1}) + (A^*_{o2} + A^{'}_{o2})) - (m_A + \mu_r + \gamma_{Ab})(A^*_{b2} + A^{'}_{b2}) \tag{6.19}$$

$$\frac{dA'_{g2}}{dt} = \gamma_{Ab}(A^*_{b2} + A^{'}_{b2}) - (m_A + f_{Ag})(A^*_{g2} + A^{'}_{g2}) \tag{6.20}$$

$$\frac{dA'_{o2}}{dt} = f_{Ag}(A^*_{g2} + A^{'}_{g2}) - (m_A + \mu_r + \gamma_{Ao})(A^*_{o2} + A^{'}_{o2}) \tag{6.21}$$

The product of $x_i^{'}x_j^{'}$ is small compared to the other terms and can be ignored. This leaves only the exponential term in equation (6.15). Since $-\mu_{em}\frac{P^{'}}{k_P}$ is a very small number, we can substitute the linear approximation for $e^x \approx 1 + x$ so that (6.15) becomes:

$$\begin{aligned}\frac{dA'_{em}}{dt} &= f_P(P^* + P^{'})\sigma e^{-\mu_{em}} e^{-\mu_{em}\frac{P^*}{\kappa_P}} e^{-\mu_{em}\frac{P^{'}}{\kappa_P}} - (m_A + \gamma_{Aem})(A^*_{em} + A^{'}_{em}) \\ &= f_P(P^* + P^{'})\sigma e^{-\mu_{em}(1+\frac{P^*}{\kappa_P})}(1 - \mu_{em}\frac{P^{'}}{\kappa_P}) - (m_A + \gamma_{Aem})(A^*_{em} + A^{'}_{em}) \\ &= f_P\sigma e^{-\mu_{em}(1+\frac{P^*}{\kappa_P})}(P^* + P^{'} - \frac{\mu_{em}}{k_P}P^*P^{'} - \frac{\mu_{em}}{k_P}P^{'2}) - (m_A + \gamma_{Aem})(A^*_{em} + A^{'}_{em})\end{aligned} \tag{6.22}$$

The first exponential term is a constant because the state values at equilibrium are constants. When we subtitute the values at the trivial equilibrium $(E^* = 0, L^* = 0, P^* = 0, A^*_{em} = 0, A^*_{b1} = 0, A^*_{g1} = 0, A^*_{o1} = 0, A^*_{b2} = 0, A^*_{g2} = 0, A^*_{o2} = 0)$ we get the final set of equations for the linearised system:

$$\frac{dE'}{dt} = \gamma_{Ao}(\beta_1 A^{'}_{o1} + \beta_2 A^{'}_{o2}) - (\mu_E + f_E)E^{'} \tag{6.23}$$

$$\frac{dL'}{dt} = f_E E^{'} - (m_L + f_L)L^{'} \tag{6.24}$$

$$\frac{dP'}{dt} = f_L L^{'} - (m_P + f_P)P^{'} \tag{6.25}$$

$$\frac{dA'_{em}}{dt} = f_P\sigma e^{-\mu_{em}}P^{'} - (m_A + \gamma_{Aem})A^{'}_{em} \tag{6.26}$$

$$\frac{dA'_{b1}}{dt} = \gamma_{em}A^{'}_{em} - (m_A + \mu_r + \gamma_{Ab})A^{'}_{b1} \tag{6.27}$$

$$\frac{dA'_{g1}}{dt} = \gamma_{A_b}A^{'}_{b1} - (m_A + f_{Ag})A^{'}_{g1} \tag{6.28}$$

$$\frac{dA'_{o1}}{dt} = f_{Ag}A^{'}_{g1} - (m_A + \mu_r + \gamma_{Ao})A^{'}_{o1} \tag{6.29}$$

$$\frac{dA'_{b2}}{dt} = \gamma_{Ao}(A^{'}_{o1} + A^{'}_{o2}) - (m_A + \mu_r + \gamma_{Ab})A^{'}_{b2} \tag{6.30}$$

$$\frac{dA'_{g2}}{dt} = \gamma_{Ab}A^{'}_{b2} - (m_A + f_{Ag})A^{'}_{g2} \tag{6.31}$$

$$\frac{dA'_{o2}}{dt} = f_{Ag}A^{'}_{g2} - (m_A + \mu_r + \gamma_{Ao})A^{'}_{o2} \tag{6.32}$$

6.3.2 Defining the eigensystem

The steps for obtaining the normal modes of the dynamical system can be outlined as follows [88]: (i) Linearise the system around the state corresponding to a specific temperature; (ii) Express the dependent variables as $y = y \cdot e^{i\omega t}$; (iii) Formulate the eigenvalue problem $[M - \lambda I]\,\Psi = 0$, where $\lambda = -i\omega$; solve $detM = 0$ for ω; (iv) Diagonalize the matrix as $GDG^T = M$. Where G is a matrix of eigenvectors; (v) Transform to eigenspace; (vi) Formulate the normal mode system of equations; (vii) Solve for E and P, keeping the adult stages and the aquatic larva stage constrained (X_s); (viii) Transform back to real space.

First we re-write the linear system of equations setting: $X' = \hat{X} \cdot e^{i\omega t}$. For bookkeeping purposes it is convenient to write these solutions in vector form:

$$\begin{pmatrix} E(t) \\ L(t) \\ P(t) \\ A_{em}(t) \\ A_{b1}(t) \\ A_{g1}(t) \\ A_{o1}(t) \\ A_{b2}(t) \\ A_{g2}(t) \\ A_{o2}(t) \end{pmatrix} = \begin{pmatrix} \hat{E} \\ \hat{L} \\ \hat{P} \\ \hat{A}_{em} \\ \hat{A}_{b1} \\ \hat{A}_{g1} \\ \hat{A}_{o1} \\ \hat{A}_{b2} \\ \hat{A}_{g2} \\ \hat{A}_{o2} \end{pmatrix} \cdot e^{i\omega t}$$

Plugging these estimates into the linearised system (Equations (6.23) to (6.32)) we get:

$$i\omega\hat{E}e^{i\omega t} = \gamma_{A_o}(\beta_1\hat{A}_{o1} + \beta_2\hat{A}_{o2})e^{i\omega t} - (\mu_E + f_E)\hat{E}e^{i\omega t} \tag{6.33}$$

$$i\omega\hat{L}e^{i\omega t} = f_E\hat{E}e^{i\omega t} - (m_L + f_L)\hat{L}e^{i\omega t} \tag{6.34}$$

$$i\omega\hat{P}e^{i\omega t} = f_L\hat{L}e^{i\omega t} - (m_P + f_P)\hat{P}e^{i\omega t} \tag{6.35}$$

$$i\omega\hat{A}_{em}e^{i\omega t} = f_P\hat{P}\sigma e^{i\omega t}e^{-\mu_{em}} - (m_A + \gamma_{Aem})\hat{A}_{em}e^{i\omega t} \tag{6.36}$$

$$i\omega\hat{A}_{b1}e^{i\omega t} = \gamma_{A_{em}}\hat{A}_{em}e^{i\omega t} - (m_A + \mu_r + \gamma_{Ab})\hat{A}_{b1}e^{i\omega t} \tag{6.37}$$

$$i\omega\hat{A}_{g1}e^{i\omega t} = \gamma_{Ab}\hat{A}_{b1}e^{i\omega t} - (m_A + f_{Ag})\hat{A}_{g1}e^{i\omega t} \tag{6.38}$$

$$i\omega\hat{A}_{o1} = f_{Ag}\hat{A}_{g1}e^{i\omega t} - (m_A + \mu_r + \gamma_{Ao})\hat{A}_{b1}e^{i\omega t} \tag{6.39}$$

$$i\omega\hat{A}_{b2}e^{i\omega t} = \gamma_{Ao}(\hat{A}_{o1} + \hat{A}_{o2})e^{i\omega t} - (m_A + \mu_r + \gamma_{Ao})\hat{A}_{b2}e^{i\omega t} \tag{6.40}$$

$$i\omega\hat{A}_{g2}e^{i\omega t} = \gamma_{Ab}\hat{A}_{b2}e^{i\omega t} - (m_A + f_{Ag})\hat{A}_{g2}e^{i\omega t} \tag{6.41}$$

$$i\omega \hat{A_{o2}} e^{i\omega t} = f_{Ag} \hat{A_{g2}} e^{i\omega t} - (m_A + \mu_r + \gamma_{Ao}) \hat{A_{o2}} e^{i\omega t} \tag{6.42}$$

Sorting and dividing both sides with $e^{i\omega t}$ we obtain:

$$\begin{pmatrix} a_{1,1} & 0 & 0 & 0 & 0 & 0 & a_{17} & 0 & 0 & a_{1,10} \\ a_{2,1} & a_{2,2} & 0 & 0 & 0 & 0 & 0 & 0 & 0 & 0 \\ 0 & a_{3,2} & a_{3,3} & 0 & 0 & 0 & 0 & 0 & 0 & 0 \\ 0 & 0 & a_{4,3} & a_{4,4} & 0 & 0 & 0 & 0 & 0 & 0 \\ 0 & 0 & 0 & a_{5,4} & a_{5,5} & 0 & 0 & 0 & 0 & 0 \\ 0 & 0 & 0 & 0 & a_{6,5} & a_{6,6} & 0 & 0 & 0 & 0 \\ 0 & 0 & 0 & 0 & 0 & a_{7,6} & a_{7,7} & 0 & 0 & 0 \\ 0 & 0 & 0 & 0 & 0 & 0 & a_{8,7} & a_{8,8} & 0 & a_{810} \\ 0 & 0 & 0 & 0 & 0 & 0 & 0 & a_{9,8} & a_{9,9} & 0 \\ 0 & 0 & 0 & 0 & 0 & 0 & 0 & 0 & a_{10,9} & a_{10,10} \end{pmatrix} \begin{pmatrix} \hat{E} \\ \hat{L} \\ \hat{P} \\ \hat{A_{em}} \\ \hat{A_{b1}} \\ \hat{A_{g1}} \\ \hat{A_{o1}} \\ \hat{A_{b2}} \\ \hat{A_{g2}} \\ \hat{A_{o2}} \end{pmatrix} = \begin{pmatrix} 0 \\ 0 \\ 0 \\ 0 \\ 0 \\ 0 \\ 0 \\ 0 \\ 0 \\ 0 \end{pmatrix} \tag{6.43}$$

With the parameters $a_{ij} (i = 1, ..., 10, j = 1, ..., 10)$ listed below. The only way to escape the trivial solution is if the inverse of the matrix does not exist and this is achieved if the determinant of the matrix is equal to zero. Another constraint for the system is that the perturbations must lead to positive densities in order to be realistic.

$$\begin{aligned}
a_{1,1} &= i\omega + \mu_E + f_E \\
a_{1,7} &= -\gamma_{Ao} \cdot \beta_1 \\
a_{1,10} &= -\gamma_{Ao} \cdot \beta_2 \\
a_{2,1} &= -f_E \\
a_{2,2} &= i\omega + m_L + f_L \\
a_{3,2} &= -f_L \\
a_{3,3} &= i\omega + m_P + f_P \\
a_{4,3} &= -f_P \sigma e^{-\mu_{em}} \\
a_{4,4} &= i\omega + m_A + \gamma_{Aem} \\
a_{5,4} &= -\gamma_{Aem} \\
a_{5,5} &= i\omega + m_A + \mu_r + \gamma_{Ab} \\
a_{6,5} &= -\gamma_{Ab} \\
a_{6,6} &= i\omega + m_A + f_{Ag} \\
a_{7,6} &= -f_{Ag} \\
a_{7,7} &= i\omega + m_A + \mu_r + \gamma_{Ao} \\
a_{8,7} &= -\gamma_{Ao} \\
a_{8,8} &= i\omega + m_A + \mu_r + \gamma_{Ab}
\end{aligned}$$

$$\begin{aligned}
a_{8,10} &= -\gamma_{Ao} \\
a_{9,8} &= -\gamma_{Ab} \\
a_{9,9} &= i\omega + m_A + f_{Ag} \\
a_{10,9} &= -f_{Ag} \\
a_{10,10} &= i\omega + m_A + \mu_r + \gamma_{Ao}
\end{aligned}$$

The parameters functions are listed in Chapter 3, Table 3.4. Solving for a specific temperature we obtain the system frequencies ω_i (i =1, .., 10). Note that Eq. 6.43 can be written in the form:

$$\begin{pmatrix}
a_{1,1}-i\omega & 0 & 0 & 0 & 0 & 0 & a_{17} & 0 & 0 & a_{1,10} \\
a_{2,1} & a_{2,2}-i\omega & 0 & 0 & 0 & 0 & 0 & 0 & 0 & 0 \\
0 & a_{3,2} & a_{3,3}-i\omega & 0 & 0 & 0 & 0 & 0 & 0 & 0 \\
0 & 0 & a_{4,3} & a_{4,4}-i\omega & 0 & 0 & 0 & 0 & 0 & 0 \\
0 & 0 & 0 & a_{5,4} & a_{5,5}-i\omega & 0 & 0 & 0 & 0 & 0 \\
0 & 0 & 0 & 0 & a_{6,5} & a_{6,6}-i\omega & 0 & 0 & 0 & 0 \\
0 & 0 & 0 & 0 & 0 & a_{7,6} & a_{7,7}-i\omega & 0 & 0 & 0 \\
0 & 0 & 0 & 0 & 0 & 0 & a_{8,7} & a_{8,8}-i\omega & 0 & a_{810} \\
0 & 0 & 0 & 0 & 0 & 0 & 0 & a_{9,8} & a_{9,9}-i\omega & 0 \\
0 & 0 & 0 & 0 & 0 & 0 & 0 & 0 & a_{10,9} & a_{10,10}-i\omega
\end{pmatrix}
\begin{pmatrix} \hat{E} \\ \hat{L} \\ \hat{P} \\ \hat{A_{em}} \\ \hat{A_{b1}} \\ \hat{A_{g1}} \\ \hat{A_{o1}} \\ \hat{A_{b2}} \\ \hat{A_{g2}} \\ \hat{A_{o2}} \end{pmatrix}
= -i\omega
\begin{pmatrix} \hat{E} \\ \hat{L} \\ \hat{P} \\ \hat{A_{em}} \\ \hat{A_{b1}} \\ \hat{A_{g1}} \\ \hat{A_{o1}} \\ \hat{A_{b2}} \\ \hat{A_{g2}} \\ \hat{A_{o2}} \end{pmatrix}$$

or

$$(L - \lambda I)\Psi = 0 \tag{6.44}$$

So what we did above was solve for the eigenvectors and eigenvalues of this matrix around the null solution. Each eigenvector is defined up to a multiplicative constant (listed in Appendix A). Expressing the solutions in the terms of the eigenvalue $\lambda = -i\omega$

The solution for a specific temperature gives a set of 10 eigenvalues and corresponding eigenvectors (Detailed in Appendix A.4). Depending on the characteristic temperature the number of oscillatory terms and complex conjugate pairs changes.

6.3.3 Normal modes

So far we have linearised the model around the null solution and determined a set of normal modes which can be evaluated for a specific temperature (detailed in Appendix A.4). Next we will look at eigenvalue decomposition to obtain a set of coupled fast mode and slow mode predictive equations. A matrix is diagonalizable if and only if for each eigenvalue the dimension of the eigenspace is equal to the multiplicity of the eigenvalue. Since our matrix (Eq. 6.43) is neither real nor symmetrical, the obtained eigenvectors do not have to be orthogonal and do not yield an orthonormal. We transform the underlying system of equations into a special set of coordinate axes in which the matrix takes this canonical form by eigenvalue decomposition ($L = EDE^{-1}$ where D is the diagonal matrix of eigenvalues). E is a matrix composed of eigenvectors. Defining $\Omega_i (i = 1, 10)$ as the complex expansion coefficients for the modes we can write:

$$\begin{pmatrix} E(t) \\ L(t) \\ P(t) \\ A_{em}(t) \\ A_{b1}(t) \\ A_{g1}(t) \\ A_{o1}(t) \\ A_{b2}(t) \\ A_{g2}(t) \\ A_{o2}(t) \end{pmatrix} = E \cdot \begin{pmatrix} \Omega_1(t) \\ \Omega_2(t) \\ \Omega_3(t) \\ \Omega_4(t) \\ \Omega_5(t) \\ \Omega_6(t) \\ \Omega_7(t) \\ \Omega_8(t) \\ \Omega_9(t) \\ \Omega_{10}(t) \end{pmatrix} \tag{6.45}$$

Where E is the matrix of eigenvectors of L (Eq. 6.44):

$$E = \begin{pmatrix}
\psi_1^E & \psi_2^E & \psi_3^E & \psi_4^E & \psi_5^E & \psi_6^E & \psi_7^E & \psi_8^E & \psi_9^E & \psi_{10}^E \\
\psi_1^L & \psi_2^L & \psi_3^L & \psi_4^L & \psi_5^L & \psi_6^L & \psi_7^L & \psi_8^L & \psi_9^L & \psi_{10}^L \\
\psi_1^P & \psi_2^P & \psi_3^P & \psi_4^P & \psi_5^P & \psi_6^P & \psi_7^P & \psi_8^P & \psi_9^P & \psi_{10}^P \\
\psi_1^{Aem} & \psi_2^{Aem} & \psi_3^{Aem} & \psi_4^{Aem} & \psi_5^{Aem} & \psi_6^{Aem} & \psi_7^{Aem} & \psi_8^{Aem} & \psi_9^{Aem} & \psi_{10}^{Aem} \\
\psi_1^{Ab1} & \psi_2^{Ab1} & \psi_3^{Ab1} & \psi_4^{Ab1} & \psi_5^{Ab1} & \psi_6^{Ab1} & \psi_7^{Ab1} & \psi_8^{Ab1} & \psi_9^{Ab1} & \psi_{10}^{Ab1} \\
\psi_1^{Ag1} & \psi_2^{Ag1} & \psi_3^{Ag1} & \psi_4^{Ag1} & \psi_5^{Ag1} & \psi_6^{Ag1} & \psi_7^{Ag1} & \psi_8^{Ag1} & \psi_9^{Ag1} & \psi_{10}^{Ag1} \\
\psi_1^{Ao1} & \psi_2^{Ao1} & \psi_3^{Ao1} & \psi_4^{Ao1} & \psi_5^{Ao1} & \psi_6^{Ao1} & \psi_7^{Ao1} & \psi_8^{Ao1} & \psi_9^{Ao1} & \psi_{10}^{Ao1} \\
\psi_1^{Ab2} & \psi_2^{Ab2} & \psi_3^{Ab2} & \psi_4^{Ab2} & \psi_5^{Ab2} & \psi_6^{Ab2} & \psi_7^{Ab2} & \psi_8^{Ab2} & \psi_9^{Ab2} & \psi_{10}^{Ab2} \\
\psi_1^{Ag2} & \psi_2^{Ag2} & \psi_3^{Ag2} & \psi_4^{Ag2} & \psi_5^{Ag2} & \psi_6^{Ag2} & \psi_7^{Ag2} & \psi_8^{Ag2} & \psi_9^{Ag2} & \psi_{10}^{Ag2} \\
\psi_1^{Ao2} & \psi_2^{Ao2} & \psi_3^{Ao2} & \psi_4^{Ao2} & \psi_5^{Ao2} & \psi_6^{Ao2} & \psi_7^{Ao2} & \psi_8^{Ao2} & \psi_9^{Ao2} & \psi_{10}^{Ao2}
\end{pmatrix} \tag{6.46}$$

The linearised system of the model can be written as:

$$\left| \frac{dE}{dt}\ \frac{dL}{dt}\ ...\ \frac{dAo2}{dt} \right|^T = -1 \cdot L \cdot \left| \hat{E}\ \hat{L}\ ...\ \hat{A_{o2}} \right|^T \tag{6.47}$$

The application of 6.45 to 6.47 gives:

$$(\frac{d\Omega_1}{dt} \frac{d\Omega_2}{dt} \frac{d\Omega_3}{dt} \frac{d\Omega_4}{dt} \frac{d\Omega_5}{dt} \frac{d\Omega_6}{dt} \frac{d\Omega_7}{dt} \frac{d\Omega_8}{dt} \frac{d\Omega_9}{dt} \frac{d\Omega_{10}}{dt})^T = -E^{-1}LE \cdot \begin{pmatrix} \Omega_1 \\ \Omega_2 \\ \Omega_3 \\ \Omega_4 \\ \Omega_5 \\ \Omega_6 \\ \Omega_7 \\ \Omega_8 \\ \Omega_9 \\ \Omega_{10} \end{pmatrix} \tag{6.48}$$

The columns of E are eigenvectors of L, yielding $\Lambda = E^{-1}LE$. Finally we can solve the system, obtaining the normal modes:

$$\Omega_i(t) = \Omega_i(0) \cdot e^{-\lambda_i t}\ (i = 1, .., 10) \tag{6.49}$$

Relating to the eigenvalues the nodes form corresponding complex conjugate pairs. The modes with amplitude set to 1 are visualized in Appendix A.4.

If we plug the above system of equations for the normal modes back into 6.45, expressing $\Omega_i(0)$ in terms of (E(0), ..., Ao2(0)) we can obtain a decoupled representation of the original system. This type of model can be used to directly filter out undesirable modes present in the dynamical system by solving for $\Omega_i(0) = 0$. The higher frequencies generated by the ODE system do not necessarily need to have a biological counterpart and can be the result of the equations and numerical integration. Moreover, fast modes tend to generate spurious, and noisy dynamics which could be considered undesirable. This method is knows as normal model initialization and is investigated in Appendix A.5.

6.3.4 Temperature and normal mode bifurcation

The decay and oscillatory terms of the normal modes were evaluated at different temperatures and are presented in Figure 6.8. We have observed a doubling in the number of oscillatory modes and a decrease in the characteristic period with an increase in temperature. For the system linearised around the trivial equilibrium we have one oscillatory pair (two modes) at temperatures below 16.5 °C, two pairs (four modes) below 25°C and three pairs (six modes) for T>25 °C. The frequency and decays rates of all oscillatory modes emerging at a specific temperature for a system linearised around a point in the model integration are shown in Figure 6.8.

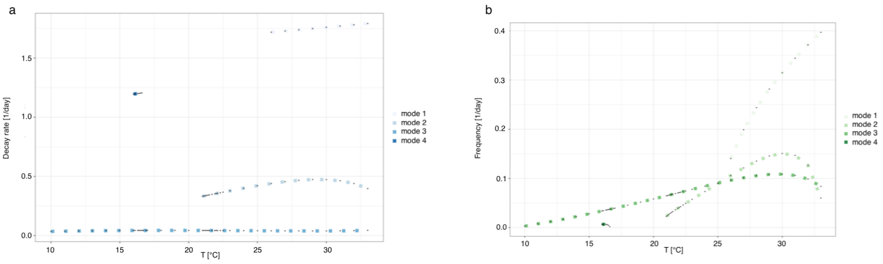

Figure 6.8: Decay rates [$1/day$] (a) and frequencies [$1/day$] (b) for all oscillatory modes emerging at a specific temperature for the linearised system.

This is further investigated in the next chapter and used to conduct an internal validation of the ODE model, i.e. to assess weather the characteristic frequencies identified at a certain temperature for the simulated are replicated for the frequencies obtained by the wavelet decomposition of the observed time series. We see that, depending on the temperature, the frequency of the modes can assume a wide range of values. The high-frequency modes generate noisy oscillations in the output that might not correspond to reality and could be considered undesirable. The normal mode initialization technique provides a way of eliminating the unwanted harmonics, by transforming the original set of equations into a system that allows initialization which controls the amplitudes of the modes in such a way that the high-frequency modes are not excited.

In Appendix A.5 the feasibility of applying normal modes initialization for a specific run of the ODE *Culex pipiens* model was investigated. With the main aim of producing a more balanced integration which would result in a smoother and less noisy curve.

Chapter 7

Model Verification

Below we discuss the output and verification of the ODE vector population dynamics model for the three ecosystems in Egypt (*Cx. pipiens*), Serbia (*Cx. pipiens*) and Guadeloupe (*Ae. aegypti*). The model is described in detail in the previous chapter (Chapter 6).

There is not much literature on the quantitative verification of vector population models since long term and consistent time-series of observed data are extremely rare. The time and cost of the trapping efforts are usually the main limiting factors. Most available data-sets tend to be irregularly spaced and demonstrate large variations over different regions and sampling periods.

Methods of validation are different for different models, with the main question for a predictive model being whether it is acceptable for a certain application such as: (i) predicting the population peaks, (ii) predicting the overall population dynamics throughout the season, (iii) simulating the seasonal or subseasonal trends or (iv) analysis of the day-to-day variability to see whether the sensitivity with respect to temperature change is realistic. The main question for a conceptual or theoretical model in contrast is finding the true dynamics of a specific population and defining the underlying processes. In this way predictive models are verified against an independent set of observed data and the verification is concerned with how well the model reproduces the data. While for theoretical models the concern is twofold: (i) How well the model reproduces the observed data and (ii) Whether the simulated system truly operates in a realistic way. Even though the first approach is way more common in scientific publications, sometimes very little can be learned from this type of validation [62, 92, 93].

So, as we see, the analysis of ODE vector population dynamics models can be considered in many ways depending on what we want to predict or discover, with each method carrying a different type of information. Hence, we investigate several methods for the verification of the ODE stage-structure model described in Chapter 6 for three locations: Bahariya, Petrovaradin and Guadeloupe; forced with 2 m air temperature. The analysis was performed according to the following steps: Firstly, a time-series analysis of the observations utilizing the Wavelet transform was performed and compared to the characteristic eigen-periods in the dynamical system. This feeds into the second type of verification described above, realism, we want to see whether the periods that emerge in our dynamical system exist in real mosquito populations. Secondly, we consider the standard verification methods for real continuous scalar quantities such as BIAS and RMSE to examine how well the output replicates the observed data. Thirdly, we examine the extremes and inflection points to test whether the dynamics is correctly represented. And finally, we introduce thresholds in the data and evaluate the scores for dichotomous simulations to examine the simulation of specific vector population densities which can subsequently have an effect on disease transmission.

7.1 Internal Validation

In Chapter 4 we applied the wavelet decomposition analysis to the observed univariate time-series in Petrovaradin and Bahariya using the Morlet wavelet. First, we tested the stationarity of the time series and examined the ACF and PACF functions to prove nonstationarity. The wavelet power-spectrum was analysed to identify the significant periods in the non-stationary time-series (Figure 7.2).

In Chapter 6 the characteristic periods of the simulated system were identified for a range of temperatures. A sample of the results is shown in Figure 7.1. Each point represent a specific frequency of the dynamical system linearised around a state corresponding to the x-axis temperature. Each oscillatory mode that was calculated in Chapter 6 has the following form $\Omega(t) = \Omega(0) \cdot e^{(\lambda_1 + i\lambda_2)t}$ where λ_1 (Real) specifies the decay or growth rate and λ_2 the frequency of the oscillations, $\{\lambda_1, \lambda_2\} \in \mathbb{R}$. Both were examined for a range of temperatures. A shift to higher frequencies with the increase in temperature and the emergence of a higher number of characteristic oscillatory pairs in the system was observed.

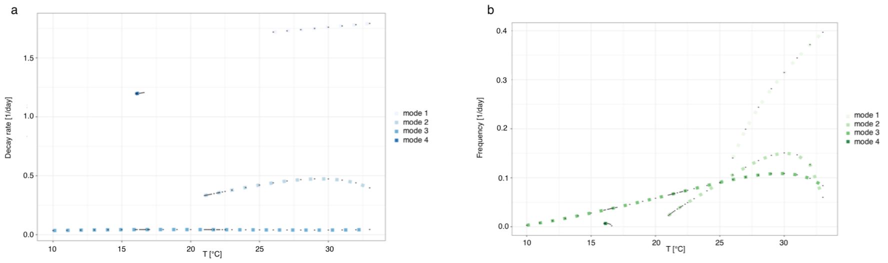

Figure 7.1: Decay rates [1/*day*] (a) and frequency [1/*day*] (b) of all oscillatory modes identified for the dynamic system linearised around the state corresponding to the temperature indicated on the x-axis (*Cx. pipiens* model).

For the purpose of this comparison we selected three characteristic points (i.e. temperature-date combinations) for Bahariya (Table 1) and Petrovaradin (Table 3). For Bahariya the first point corresponds to the high-temperature summer regime with four oscillatory modes, the second is a point with milder temperature corresponding to the end of the summer period in Egypt and the third is characteristic of a low-temperature regime during the coldest winter month. Similarly, for Petrovaradin, we have one point representative of the high-temperature mid-latitude summer regime and one point in autumn which can be linked to the annual end-of-activity for the *Culex* vector.

The observed frequencies are shown in Table 7.3 for Bahariya and Table 7.4 for Petrovaradin. The values of the identified model frequencies for the temperature points for which we carry out the verification are shown in Table 7.1 for the *Cx. pipiens* model run for Bahariya, and Table 7.2 for *Cx. pipiens* model run for Petrovaradin.

This type of internal validation can show whether the fundamental periods in the observed time-series are reproduced within the dynamical ODE system. In a further step, we examined the wavelet coherency between the simulated population and the observed count.

Table 7.1: Eigenperiods for the *Cx. pipiens* model for Bahariya linearised around the state evaluated at: S1 - 30.14 °C; S2 - 23.35 °C; and S3 - 11.24 °C.

Scenario index	T [°C]	ω [rad/day]	No of nodes	Period [days]	Date	DOY
S1	30.14	0.318565	4	19.72340	30/07/2017	211
		0.221092		28.41887		
		0.139444		45.05884		
		0.0739336		84.98417		
S2	23.35	0.0905338	2	69.40154	19/10/2017	292
		0.069465		90.45109		
S3	11.24	0.0200057	1	314.0698	25/01/2018	25 (390)

Table 7.2: Eigenperiods for the *Cx. pipiens* model for Petrovaradin linearised around the state evaluated at: S1 - 30.77 °C; and S2 - 11.80 °C.

Scenario index	T [°C]	ω [rad/day]	No of nodes	Period [days]	Date	DOY
S1	30.77	0.33763	4	18.6	10/08/2017	222 (588)
		0.24049		26.113		
		0.13338		47.0822		
		0.03343		187.831		
S2	11.80	0.03394	1	185.032	22/10/2017	295 (661)

The wavelet periodograms of the observed *Cx. pipiens* time series for Petrovaradin and Bahariya are shown in Figure 7.2. The values for the verification dates-temperature points and extracted the dominant periods are shown in Tables 7.3 and 7.4. Many methods exist which can be employed to define the size of occurring peaks in the data: from the trivial "drop" method which is essentially an qualitative assessment of where the peak starts and where it ends, to tangent skimming, and peak deconvolution. In our analysis we used a linear cut-off for the base of each peak and extracted the period value on both sides of the peak (max − base)/2. This gives us the full width at half maximum (FWHM), and consequently HWHM (FWHM / 2).

Looking at the identified frequencies for the model run for Bahariya shown in Table 7.1 and Table 7.3, we see that, similar to the simulation, the number of significant periods is higher for the scenarios corresponding to the higher-temperatures, as well as a shift to higher frequencies (lower periods). This can be observed for both years although they are not completely symmetrical and higher frequencies appear more significant in 2017 than 2018.

For Scenario 3, the periods match fairly well with the annual period of

Table 7.3: Wavelet periods identified for the observed *Cx. pipiens* time series for Bahariya corresponding to the air temperature: S1 - 30.14 °C; S2 - 23.35 °C; and S3 - 11.24 °C.

Scenario index	T [°C]	No of sig periods	Period ± HWHM [days]	Magnitude	DOY
S1	30.14	4	23.3751 (±2)	278.2712	211
			46.7508 (±7.5)	**1041.929**	
			93.5004 (±10)	678.7976	
			314.497 (±65)	843.9883	
S2	23.35	3	**93.5004 (±18)**	**1126.61**	292
			157 (±15)	407.6774	
			314.497 (±60)	792.6944	
S3	11.24	2	**93.5004 (±19)**	**965.6138**	390
			314.497(±55.5)	698.1827	

Table 7.4: Wavelet periods identified for the observed *Cx. pipiens* time series for Petrovaradin corresponding to the air temperature: S1 - 30.77 °C; and S2 - 11.80 °C.

Scenario index	T [°C]	No of sig periods	Period ± HWHM [days]	Magnitude	DOY
S1	30.77	4	9.828 (±1.75)	3535.4360	222 (588)
			23.375 (±8.0)	7237.9760	
			187.001 (±15.5)	56989.9061	
			314.497 (±55.5)	111235.6630	
S2	11.80	2	187.001 (±17.5)	45976.5725	295 (661)
			314.497 (±55.25)	93951.7787	

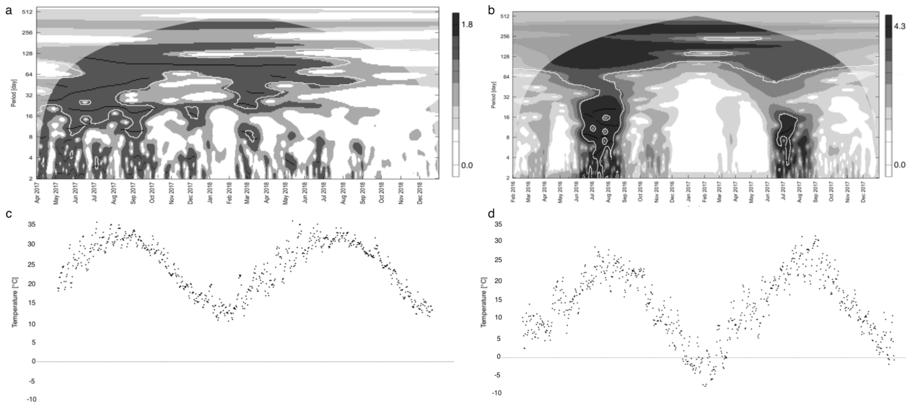

Figure 7.2: Wavelet periodogram (*top*) and temperature time-series (*bottom*) for (a, c) Bahariya and (b, d) Petrovaradin.

314 recognized exactly. For Scenario 2, the identified eigen-period of 90.45 days directly matches the observed period of 93.5 days. The second frequency corresponding to 69.4 days is present in the periodogram but is not significant. Finally, the most significant period for Scenario 1 (46.38 days) is matched by the 45.06 eigen-period, the longest period is not observed in the model for the high-temperature regime. The 84.98 day eigen-period can be linked to the 93.5

peak since the HWHM is 10 days, making the 84.98 period still significant. And lastly, the 19.72 day eigen-period falls to the tails of the first significant peak in the periodogram (23.375 days).

For Petrovaradin (Tables 7.2 and 7.4), we also see a doubling of the number of significant periods with temperature and a shift to higher frequencies for the higher-temperature regimes. The annual component does not emerge in the model however the 187 day period is mirrored in the 185.032 eigen-period. Similarly, to the low-temperature scenario the 187.001 day period is exactly represented in the dynamical model and the 18.6 and 26.113 day eigen-periods fall within the 23.375 peak. The 47.082 day eigen-period is present in the wavelet periodogram however not significant and reversely, the 9.828 day peak is not observed in the model.

7.1.0.0.1 Cross-wavelet analysis:

Finally, we look at the cross-wavelet power spectrum for the observed and simulated time series (Figure 7.3). Arrows in the positive direction of the x axis indicate that the compared time-series are in phase for that specific period with vanishing phase differences. Arrows directed in the negative direction of the x axis indicate anti-phase, the orientations in-between represent a smaller phase shift. Only the areas for which a significant correlation was identified show the phase, indicated by the white contour lines in Figure 7.3. The underlying colors indicate the cross-wavelet power.

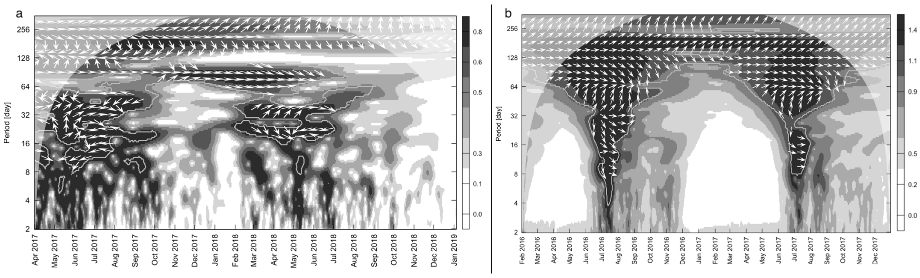

Figure 7.3: Cross-wavelet periodogram for the observed time-series of *Cx. pipiens* for (a) Baharya and (b) Petrovaradin.

For Bahariya we see an asymmetric pattern for the 152 day period in which the series are in phase for 2018 but not for 2017. This is depicted in Figure 7.4

Moreover, we can see a significant correlation in-phase for the 80 day period; a significant correlation and anti-phase for the 50 day period while the highest wavelet power and in-phase correlation is observed for the 32 day period. The highest wavelet power for the high-frequency periods is observed for DOY 150 (2017) and DOY 132 for 2018.

For Petrovaradin, we see a strong agreement in phase across all significant days and periods. There is a strong correlation across the whole interval for the 181 day. The highest cross-wavelet power is observed for DOY 130 for (2016) with a peak at the 8 day period (Figure 7.5), and DOY 131 for 2017 (with a peak at the 11 day period, Figure 7.5) where we see high power across almost all periods. Figure 7.5 shows the cross-wavelet spectrum power as a function of the period in days, for a specific day of the year. Moreover, in

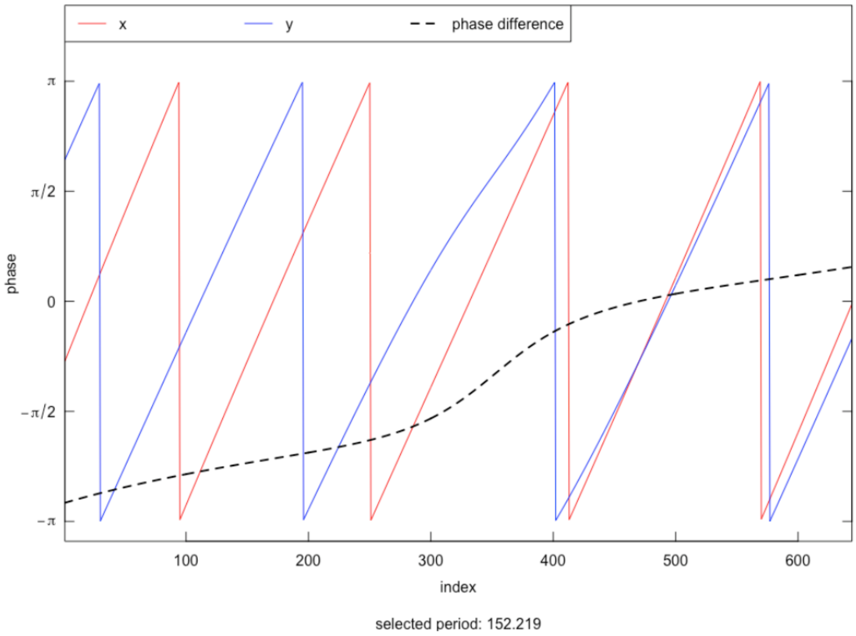

Figure 7.4: Phase and phase difference (dashed line) evaluated at the 152 period where the red line corresponds to the observed and the blue line to the simulated time-series.

Figure 7.3 we see that the high-frequency matching for 2018 for Petrovaradin is less significant than for 2017. The most obvious differences in the cross-wavelet matching between the observations and the model for the two locations appears as a results of a more pronounced annual cycle for Petrovaradin with a clearly defined seasonal dynamics that matches the annual temperature cycle (which is reflected in the model). For Bahariya, the annual temperature cycle does not induce population die-off during the winter months (the average monthly temperature of the coldest month stays above 10 °C); the seasonal relationship to temperature is less obvious and the simulated dynamics has a less pronounced seasonal character.

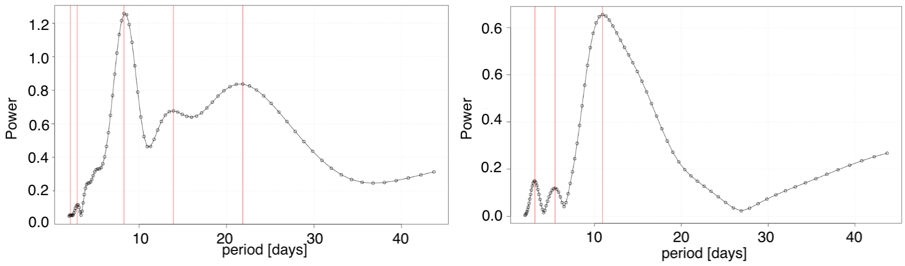

Figure 7.5: Cross-wavelet power as a function of period for (a) DOY 130 2016 and (b) DOY 131 for 2017.

The global significance is examined through the average wavelet spectrum (Figure 7.6). The *Cx. pipiens* series shows significant power at 3, 1-20, 42, 87, 147 and 337 days for Bahariya, and 2, 8, 13 and 20, 119, 181 and 337 days for Petrovaradin.

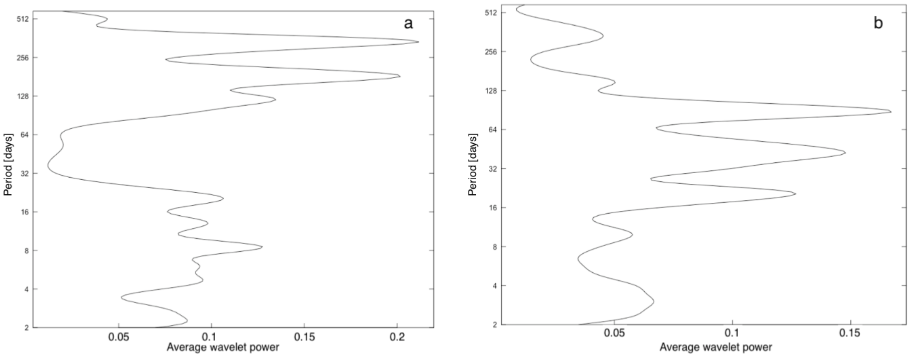

Figure 7.6: The (2016-2017) Average cross-wavelet power spectrum for (a) Petrovaradin and (b) Bahariya.

7.2 Standard first and second-order moment verification

In this chapter we will examine the Root Mean Square Error and Bias for the simulated population dynamics. The observations and model output were rescaled to [0,1]. For Guadeloupe, the model output was aggregated to monthly values to match the trapping frequency for *Ae. aegypti* (detailed in Appendix A.3). The observed data is compared with the aggregated blood-seeking adults ($A_b = A_{b1} + A_{b2}$, Cf. model description in Chapter 6).

7.2.1 Overview of simulated dynamics

The aggregated monthly simulated abundance for the three locations are shown in Figures 7.7 and 7.8. The following measures of central tendency and variability are indicated in the box plot for each month: Range, interquartile range (IQR), mean and median values.

The model runs were performed for the period 2015–2018 for Guadeloupe, 2017–2018 for Bahariya and 2016–2017 for Petrovaradin; with a 6 month spin-up time for each location. The model is forced with observed 2 m temperature for Petrovaradin and Bahariya. For Guadeloupe, the model is forced with ERA5 2 m temperature.

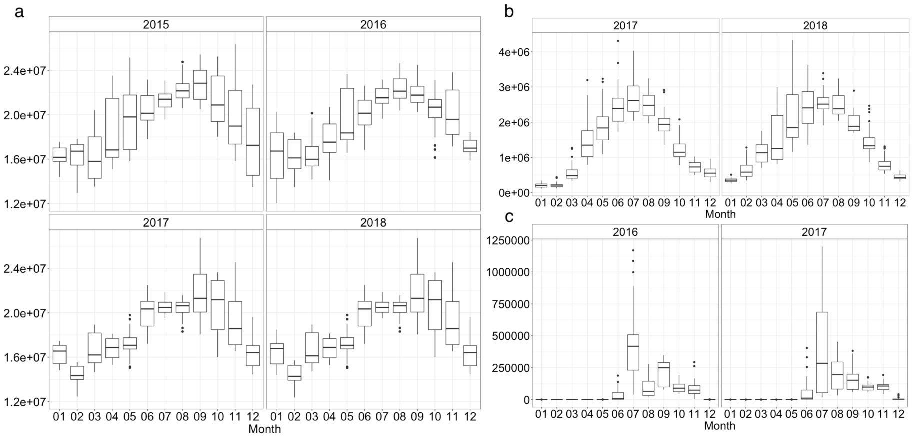

Figure 7.7: Overview of aggregated monthly values for the simulated abundance of (a) *Aedes*, Guadeloupe, (b) *Culex*, Bahariya, and (c) *Culex*, Petrovaradin.

Table 7.5: Summary statistics of the daily simulated time series for Guadeloupe (*Ae. aegypti*); Bahariya (*Cx. pipiens*) and Petrovaradin (*Cx. pipiens*).

	Max	Mean	Median	Relative Dispersion	Range
Guadeloupe (2015 - 2018)	4340319	18837013	18558583	0.1529487	14704744
Bahariya (2017 - 2018)	4340319	1454285	1328346	0.6450054	4227108
Petrovaradin (2016 - 2017)	1198892	84024.4	2950	1.983748	1198892

We see that the simulated annual maximum and cumulative peak for Guadeloupe for all years occurs in September (Figure 7.7). The maximum population

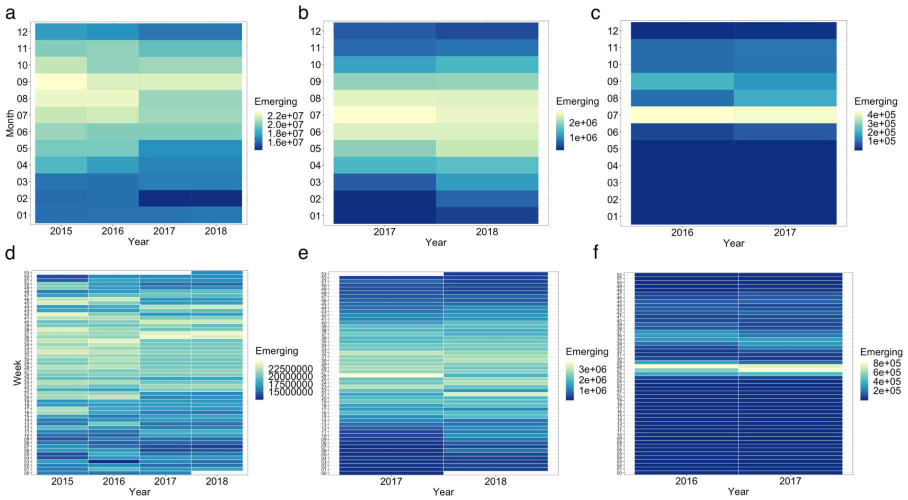

Figure 7.8: Overview of mean monthly (a, b, c) and weekly (d, e, f) values for the simulated abundance of (a, d) *Aedes aegypti*, Guadeloupe, (b, e) *Culex pipiens*, Bahariya, and (c, f) *Culex* Petrovaradin. The y-axis indicates the total simulated abundance of bloodseeking adults.

value for 2015–2018 is simulated in 2017. In Bahariya the aggregated monthly peak is simulated in July however the population maximum occurs in June for 2017 (4.31e6) and in May for 2018 (4.34e6). The minimum is simulated in January (1.13e5 in 2017; and 2.73e5 in 2018) for both years. Lastly, for Petrovaradin the cumulative peak as well as the population maximum is simulated for July (1.17e6 in 2016; and 1.2e6 i 2017) and overwintering minimum for the period from December to April (2 – 50 adults).

When comparing the monthly values the seasonality in Petrovaradin is clearly reflected in the observed spread (relative dispersion, sd/mean = 1.984). The seasonal character for Bahariya, with relative dispersion = 0.645, is not so pronounced as Petrovaradin, but more pronounced than Guadeloupe (relative dispersion = 0.153).

The simulated range of the population (max - min) is 14.7e6, 1.2e6 and 4.2e6 for Guadeloupe, Petrovaradin and Bahariya, respectively. For Guadeloupe, the months with the largest range are November (2015), January (2016), September (2017) and September (2018). For Bahariya, the largest range is in June (2017) and May (2018). For Petrovaradin the largest monthly range of simulated values is in July for both years (2016 and 2017). These simulation periods were chosen to match the observed vector data (detailed in Appendix A.3).

7.2.2 Verification

In the following chapters the RMSE verification of the model output with observed data is presented, scaled to [0,1]. For Guadeloupe, we evaluate the same model run (forced with ERA5 2 m temperature) against observations from eight different locations across the island. This choice is argued in Appendix A.8.

7.2.2.0.1 Guadeloupe:

As we have seen in Figure 7.7, the highest abundance is simulated for September; however, the simulated peak spans June, July and August. The comparison of the simulated and observed relative abundance is shown in Figures 7.9 and 7.10. We see that this maximum as well as the December-May minimum is replicated for the 1st observational site. For the other three observational sites, we see a similar pattern for the lent minimum; however, the summer maximum is skewed towards June and July and a secondary peak occurs towards the end of the year. This can be linked to the month that experiences the highest amount of precipitation (detailed. Chapter 4).

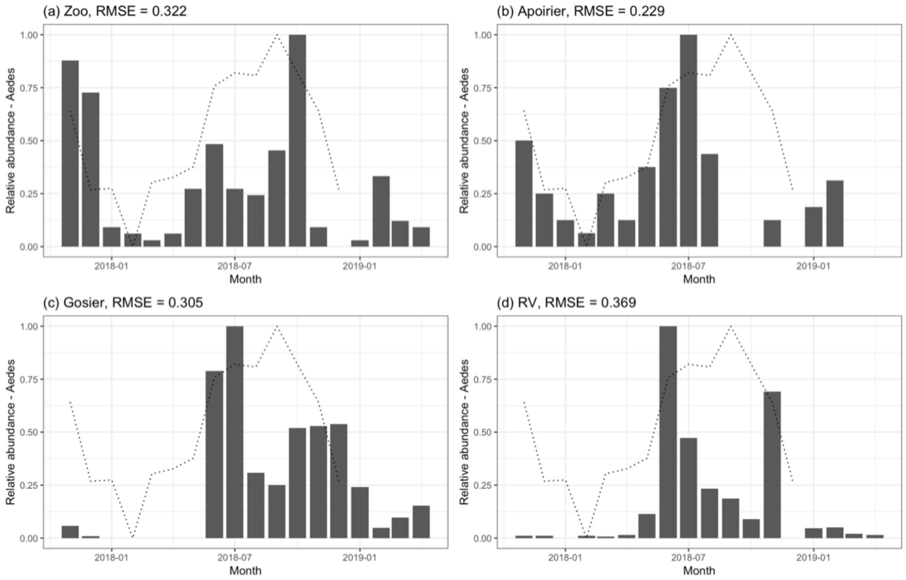

Figure 7.9: Relative monthly abundance of *Aedes* mosquitoes of A_b model output (line) vs observed catches (grey bars) for the four locations: (a) Zoo, (b) Apoirier, (c) Gosier, (d) Rv.

7.2.2.0.2 Bahariya:

The correspondence of the observed and simulated relative abundance of *Cx. pipiens* for Bahariya is shown in Figures 7.11 and 7.12. We see a fairly good agreement for both years with the simulated dynamics matching the observed for most periods except in the summer months where it is overestimating the abundance for both years.

7.2.2.0.3 Petrovaradin:

The comparison of the observed and simulated *Cx. pipiens* time series for Petrovaradin is shown in Figures 7.13 and 7.14

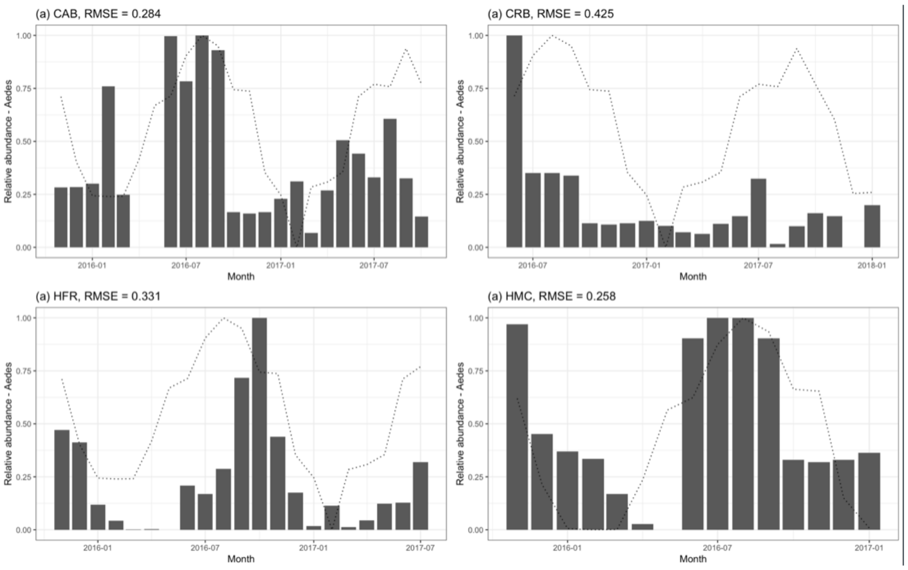

Figure 7.10: Relative monthly abundance of *Aedes* mosquitoes of A_b model output (line) vs average observed catches (grey bars) for the four locations: (a) CAB, (b) CRB, (c) HFR, (d) HMC.

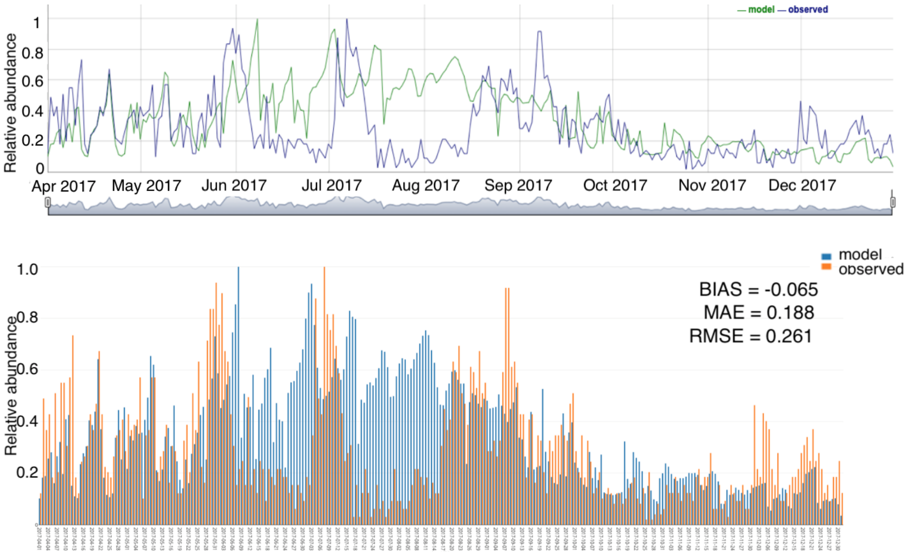

Figure 7.11: Relative simulated daily abundance of *Culex pipiens* (A_b) versus the observed catches for Apr 2017 – Dec 2017 (x-axis) for Bahariya.

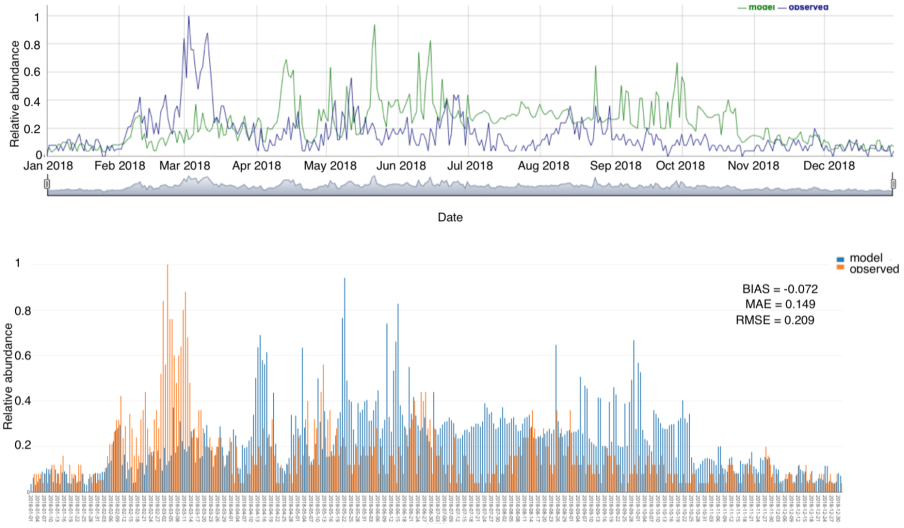

Figure 7.12: Relative simulated daily abundance of *Culex pipiens* (A_b) versus the observed catches for Jan 2018 – Dec 2018 (x-axis) for Bahariya.

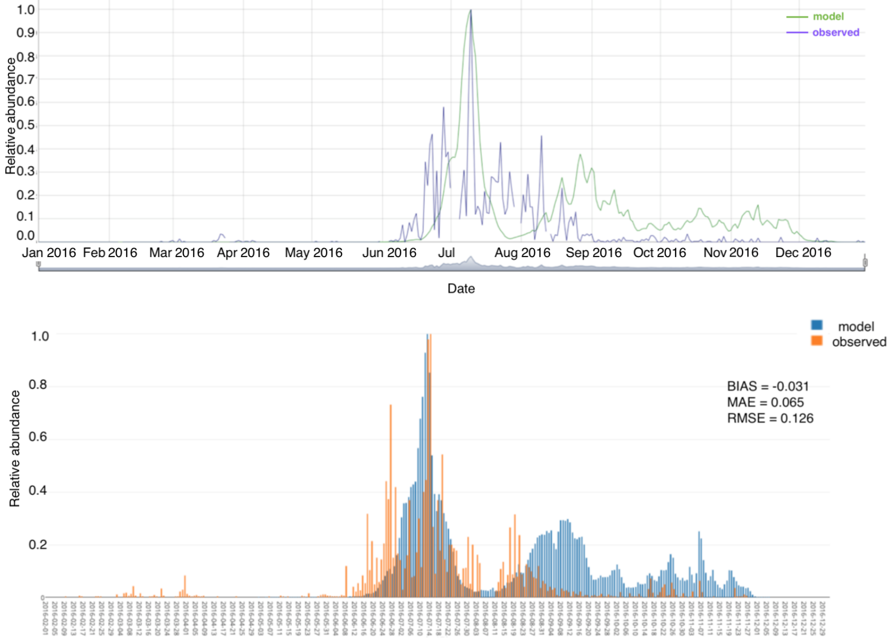

Figure 7.13: Relative simulated daily abundance of *Culex pipiens* (A_b) versus the observed catches for Jan 2016 – Dec 2016 (x-axis) for Petrovaradin.

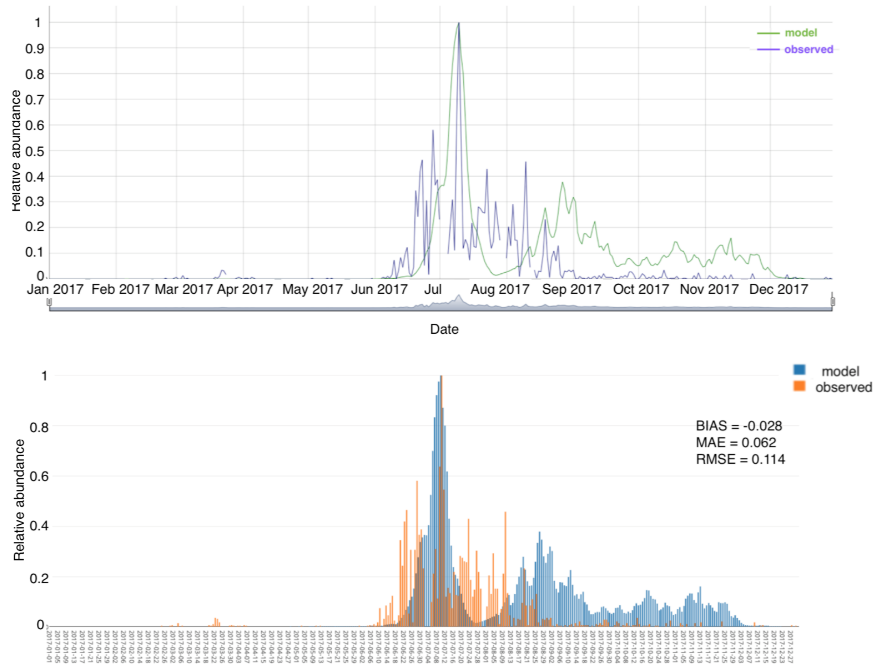

Figure 7.14: Relative simulated daily abundance of *Culex pipiens* (A_b) versus the observed catches for Jan 2017 – Dec 2017 (x-axis) for Petrovaradin.

7.2.3 Error profile and uncertainty

The daily bias profiles are shown in Figures 7.15 and 7.16. We see that they both follow a similar profile with maximum error occurring for the summer period JJA.

The combined standard uncertainty of the systematic bias shown in Table 7.6 is calculated by the difference uncertainty propagation formula (GUM) [152] and covariance between the observed and simulated estimates is presented in the form of the estimated Pearson correlation coefficient $r(s, o)$.

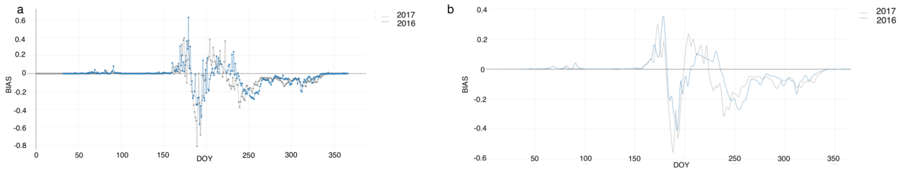

Figure 7.15: Daily error $(o_i - p_i)$ time-series for Petrovaradin, with DOY indicated on x-axis.

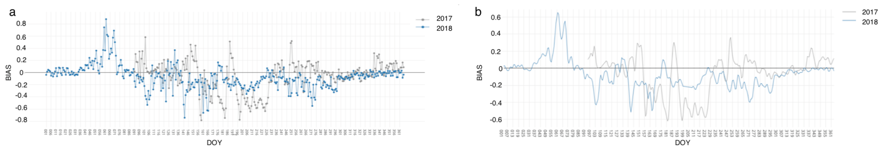

Figure 7.16: Daily error $(o_i - p_i)$ time-series for Bahariya, with DOY indicated on x-axis.

where B is the systematic bias, p is predicted population, o is the observed population and r is the Pearson correlation coefficient for the simulated and observed series.

Table 7.6: Bias uncertainty

Year	u(p)	u(o)	r	u_c(B)	U(B)	Shapiro-Wilk test (p-value)
Bahariya						
2017	0.2104353	0.2061357	0.2584243	0.3304465	1.47757	0.9517 (p <.0001)
2018	0.1460298	0.1455461	0.09189397	0.2154405	0.963449	0.93355 (p <.0001)
Petrovaradin						
2016	0.1397918	0.1186238	0.649	0.2348607	1.050297	0.81239 (p <.0001)
2017	0.145865	0.1092358	0.571	0.2267493	1.014023	0.76425 (p <.0001)

Table 7.7: Correlation overview

	Year	Pearson	Spearman	Kendall
Petrovaradin	2016	r = 0.649 (p <.001)	$\rho = 0.624(p < .0001)$	$\tau = 0.460(p < .0001)$
	2017	r = 0.571 (p <.001)	$\rho = 0.601(p < .0001)$	$\tau = 0.457(p < .0001)$
	Both years	r = 0.56 (p <.0001)	$\rho = 0.604(p < .0001)$	$\tau = 0.452(p < .0001)$
Bahariya	2017	r = 0.232 (p <.0001)	$\rho = 0.21(p < .0001)$	$\tau = 0.150(p < .0001)$
	2018	r = 0.092 (p<.0001)	$\rho = 0.281(p < .0001)$	$\tau = 0.195(p < .0001)$
	Both years	r = 0.191(<.0001)	$\rho = 0.245(p < .0001)$	$\tau = 0.168(p < .0001)$

The same measurement uncertainty $u(O)$ appears in the Brier Uncertainty component. As a measure of variance in the observation it can be interpreted as the difficulty of the forecast situation. The good correlation for Petrovaradin is most probably due to the yearly cycle. An anomaly correlation could be a better metric for locations with a pronounced seasonality.

7.3 Analysis of inflection points

7.3.1 Extrema

Below we looked at the most significant peaks (highest observed population) for Bahariya, Petrovaradin and Guadeloupe and compared them to the corresponding simulated peaks. The results are given in Table 7.8 and Table 7.9. The date of the peak is given as DOY for Bahariya and Petrovaradin; and MOY for Guadeloupe. The peak data is reported together with HWHM as a measure of the span and size of the peak.

Table 7.8: Date of occurrence (DOY ± HWHM [days]) of three highest peaks (peak 1 > peak2 > peak3) in the observed population and the corresponding simulated peak for Bahariya (2017–2018) and Petrovaradin (2016–2017).

		Bahariya 2017	Bahariya 2018	Petrovaradin 2016	Petrovaradin 2017
		DOY ± HWHM	DOY ± HWHM	DOY ± HWHM	DOY ± HWHM
Peak 1	Observed	188 ± 4.5	62 ± 3	196 ± 1	191 ± 1
	Model	184 ± 2	65 ± 4	195 ± 3	191 ± 3
Peak 2	Observed	251 ± 3	132 ± 1.5	179 ± 1	179 ± 3
	Model	255 ±2	130 ± 1	179 ± 0.5	-
Peak 3	Observed	151 ± 4.1	176 ± 1	232 ± 1	222 ±1
	Model	151 ± 1	173 ± 1	234 ± .5	224 ± .5

Table 7.9: Date of occurrence (MOY ± HWHM [months]) of the highest peak in the observed population and the corresponding simulated peak for 8 loctions across Guadeloupe (CAB, HMC, Gosier, CRB, RV, HFR, Apoirier and Zoo; detailed in Appendix A.3).

		Guadeloupe 2016	Guadeloupe 2017	Guadeloupe 2018
		MOY ± HWHM	MOY ± HWHM	MOY ± HWHM
CAB	Observed	8 ± 2.5	8 ± 1.33	
	Model	8 ± 3.75	9 ± 2.66	
HMC	Observed	8 ± 3		
	Model	8 ± 3.75		
Gosier	Observed			7 ± 1.66
	Model			9 ± 2.93
CRB	Observed		7 ± 0.66	
	Model		9 ± 2.66	
RV	Observed			6 ± 0.5
	Model			9 ± 2.93
HFR	Observed	10 ± 1		
	Model	8 ± 3.75		
Apoirier	Observed			7 ± 1.25
	Model			9 ± 2.93
Zoo	Observed			10 ± 0.7
	Model			9 ± 2.93

We can see that the simulated dynamics falls within the top half of the observed peak for 4 out of 6 examined peaks for Bahariya and 3 out of 6 for Petrovaradin when considering the daily dynamics. For Guadeloupe the simulated monthly dynamics falls within the top half of the observed annual peak for 4 out of 8 examined locations.

The annual maximum was simulated very successfully for Petrovaradin, and the simulated August peaks for both years miss the observed peak by 2 days.

7.3.2 Inflection points

In a next step we examine the inflection points of the annual and start of season peaks in Petrovaradin (Figures 7.18 and 7.19). First, a Fourier filtering technique is applied to eliminate the smaller-scale derivatives and smooth the observed and simulated data, the result is shown in Figure 7.17, with the model shown in blue and the observed series in black.

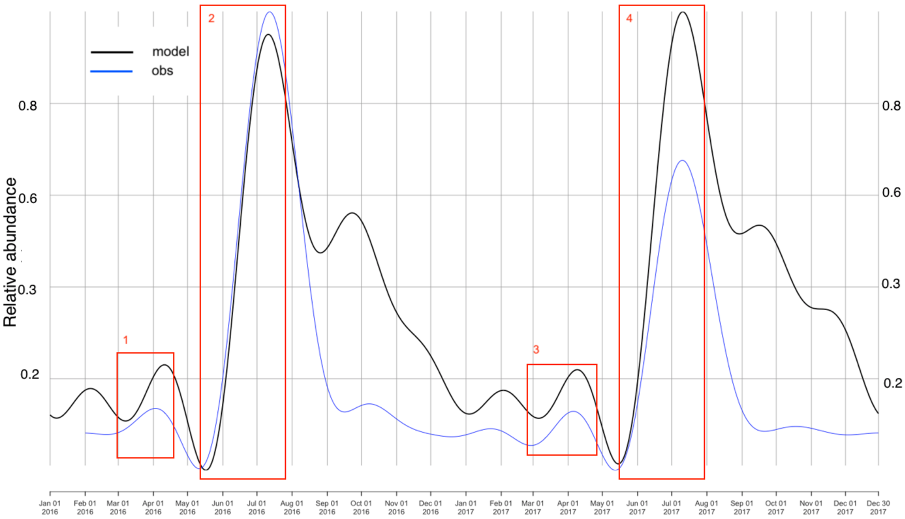

Figure 7.17: FF smooth of observed (blue) and simulated (black) data for 2016 – 2017 for Petrovaradin.

The peaks for which the inflection points will be compared are outlined. The start of season peak is not significant in magnitude and hence was not included in the previous analysis of the extrema, however it is an important feature of the entomological time-series and is observed every year in the mosquito population in Serbia (unpublished DP).

The inflection for the spring maximum is simulated 4 days after the observed inflection for 2016 (Figure 7.18a,c) and 8 days after the observed inflection for 2017 (Figure 7.19a,c). The inflection for the annual maximum is simulated exactly for 2016 (Figure 7.18b,d) and 1 day after the observed inflection for 2017 (Figure 7.19b,d).

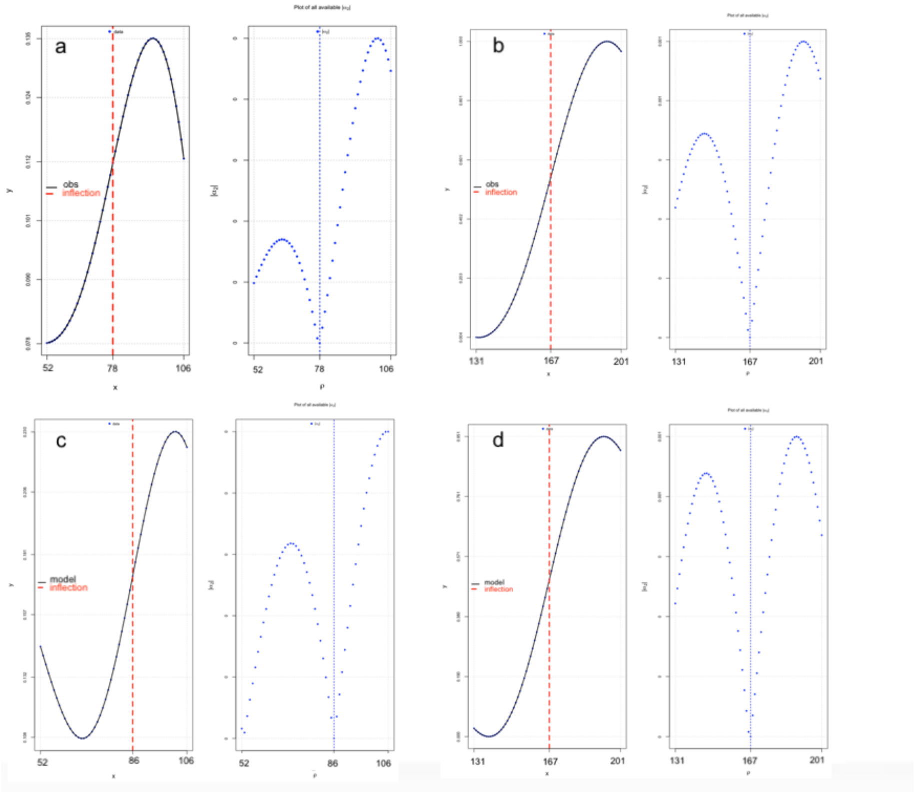

Figure 7.18: Inflection points for the spring (a - obs, c - model) and annual maximum (c - obs, d - model) inflection points for 2016.

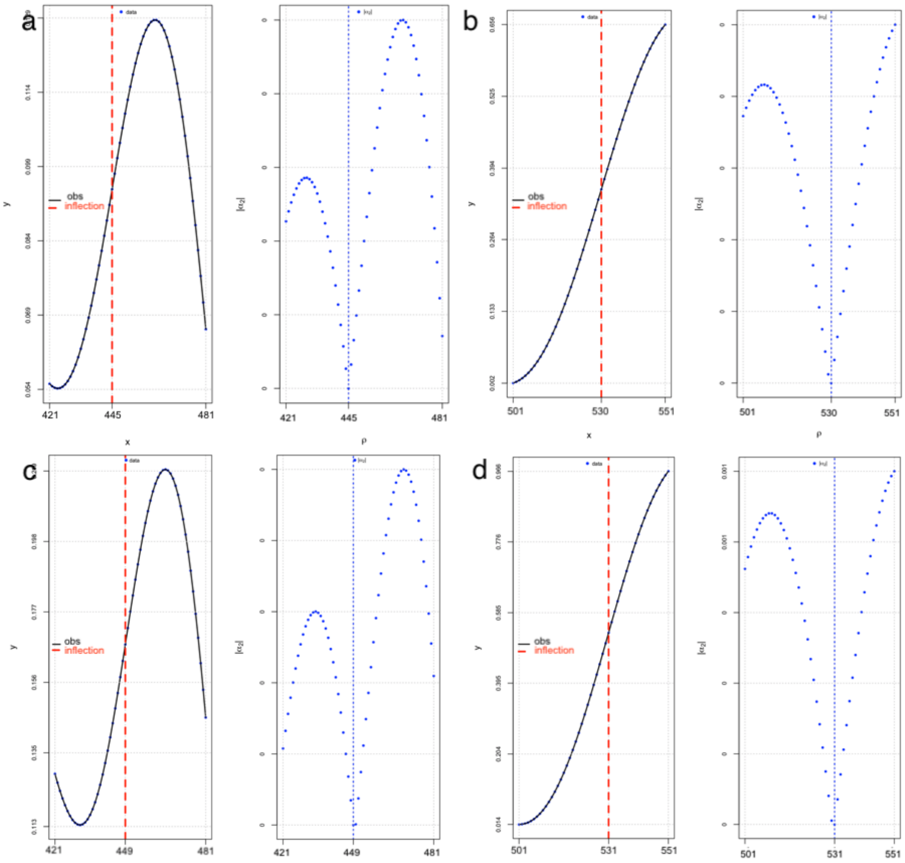

Figure 7.19: Inflection points for the spring (a - obs, c - model) and annual maximum (c - obs, d - model) inflection points for 2017.

7.4 Contingency metrics

We introduced several thresholds to the relative observed count for *Culex pipiens* as well as the relative simulated values to move from continuous count data to a binary variable in order to examine whether the significant peaks in the population are simulated correctly. These thresholds are used to construct a contingency table of observed and simulated presence/absence "events", where only significant abundance is classified as an event, and generate a set of verification metrics.

Care should be taken when selecting an appropriate threshold, and in defining what an "event" constitutes. There is another way of reverse-estimating the best cut-off threshold for a dataset by finding the threshold for which the highest sensitivity (TPR) and specificity (1 -FPR) is achieved. As we will later see, this can be done by plotting the Receiver Operating Characteristic Curve for an ensemble of threshold values applied to the same dataset. This method also needs to be utilized cautiously and is not suitable for all types of analysis, while maximizing these metrics it might suggest a useless threshold. In our analysis, we use the mean value as the cut-off for Bahariya, Petrovaradin and Guadeloupe and calculate the verification metrics for each year separately. Using the mean instead of the median is sensible for this frequency-distribution since we want to focus on the significant peaks occurring in the population and data is right skewed for all location-years (Figure 7.20). This pulls the mean towards the higher values. The median cut-off would in contrast classify a lot of the low-population peaks as "events" which is something we want to avoid.

Table 7.10: Overview of verification scores for Bahariya, Petrovaradin and Guadeloupe.

Performance measure	Bahariya		Petrovaradin		Guadeloupe
	2017	2018	2016	2017	2015-2019
Accuracy (PC)	0.65	0.63	0.79	0.78	0.69
p-value (Acc >NIR)	0.12	0.017	0.00998	0.00994	0.00325
Odds Ratio (OR)	3.92	4.61	6.51	6.28	7.69
OR Skill Score (ORSS)	0.59	0.643	0.73	0.73	0.77
Frequency Bias (FB)	1.35	1.54	1.52	1.66	1.43

The **Accuracy** or Percentage Correct (PC) shows what overall fraction of the forecast was correct [0,1]. This metric can be misleading since it is shaped by the most populated category (in our case absences, small population density). In order to assess the significance of this metric it needs to be considered together with the No Information Rate (NIR). The NIR indicates the relative weight of the largest category and is basically the probability of guessing correct just based on the distribution of the observed classes. For example, we see that the accuracy for Bahariya for 2017 is higher than the accuracy for 2018, but more importantly the Accuracy/NIR ratio is better for 2018 with p-value indicating significance ($p = 0.017488$). The highest Accuracy is observed for Petrovaradin.

The Odds Ratio gives us an estimate of what the ratio of odds of a "yes" simulation being correct to the odds of a "yes" simulation being wrong. In our case the odds of an event that is simulated correctly are roughly 4 times greater than the odds of it being incorrectly simulated for Bahariya, and 6 and

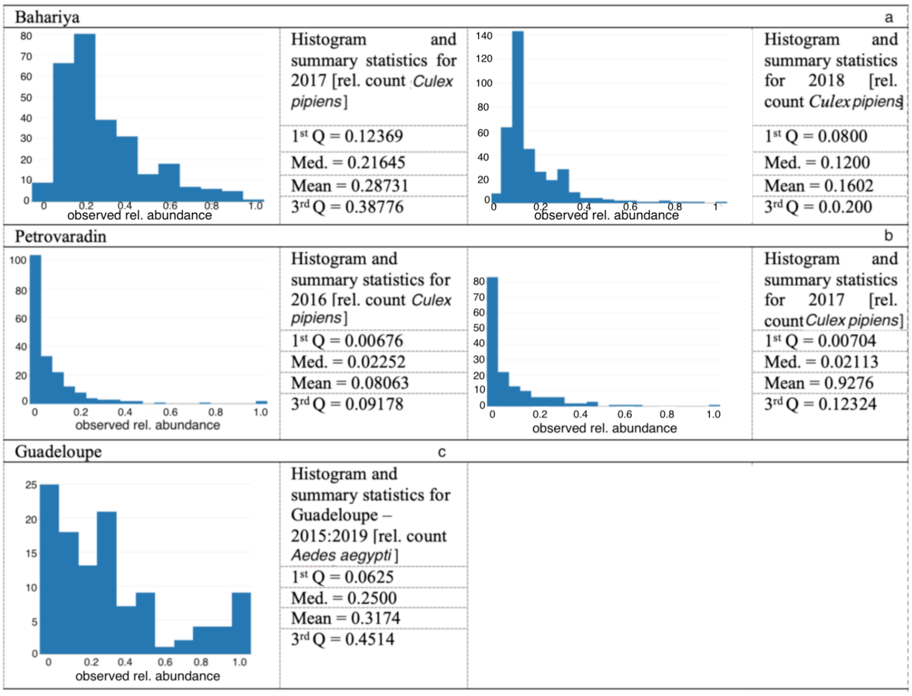
Bahariya a

Histogram and summary statistics for 2017 [rel. count *Culex pipiens*]
1st Q = 0.12369
Med. = 0.21645
Mean = 0.28731
3rd Q = 0.38776

Histogram and summary statistics for 2018 [rel. count *Culex pipiens*]
1st Q = 0.0800
Med. = 0.1200
Mean = 0.1602
3rd Q = 0.0.200

Petrovaradin b

Histogram and summary statistics for 2016 [rel. count *Culex pipiens*]
1st Q = 0.00676
Med. = 0.02252
Mean = 0.08063
3rd Q = 0.09178

Histogram and summary statistics for 2017 [rel. count *Culex pipiens*]
1st Q = 0.00704
Med. = 0.02113
Mean = 0.9276
3rd Q = 0.12324

Guadeloupe c

Histogram and summary statistics for Guadeloupe – 2015:2019 [rel. count *Aedes aegypti*]
1st Q = 0.0625
Med. = 0.2500
Mean = 0.3174
3rd Q = 0.4514

Figure 7.20: Histogram and summary statistics for the observed vector abundance scaled to [0,1] (a) Bahariya, (b) Petrovaradin, (c) Guadeloupe.

7 for Petrovaradin and Guadeloupe respectively. Similarly, the Odds Ratio Skill Score (ORSS) indicates if the model performs better than random chance, 0 indicates no skill and 1 is the perfect score. The ORSS is greater than 0.5 for Bahariya and greater than 0.7 for both Petrovaradin and Guadeloupe.

The Frequency Bias (FB) compares how the total number of simulated events compare to the total number of observed events. The perfect score is 1. The observed frequency bias (> 1) indicates overforecasting of mosquito occurrence for all location-years with a more moderate bias for 2017 for Bahariya. This does not indicate the accuracy of the model, i.e. how the simulation corresponds to the observations, it only assesses the relative frequencies.

7.4.1 ROC

The ROC curves and reliability diagrams for the specific year-locations are shown in Figure 7.22. The Area Under the ROC curve values are show in Table 7.11.

The AUC of defines the probability that a randomly chosen positive example will be ranked higher than a randomly chosen negative example. Scores$>$ 0.5 indicate that our model is performing better than random, relatively poor for Bahariya ($0.6 < AUC < 0.7$) and fairly good ($0.7 < AUC < 0.8$) for Petrovaradin and Guadeloupe. The Brier Score can be decomposed into Reliability, Uncertainty and Resolution Scores (Table 7.12) and the different BS contributions can be represented on the reliability plot diagram.

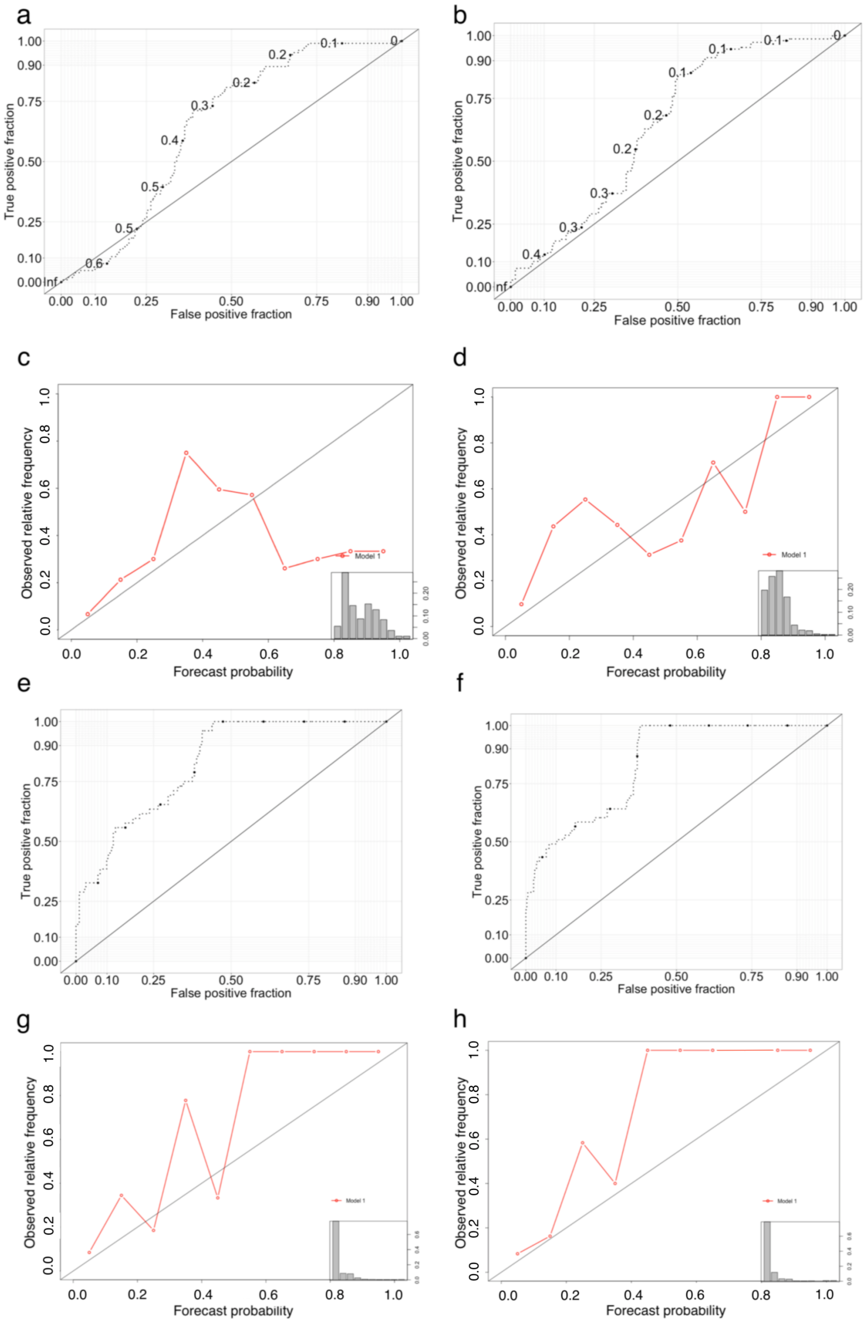

Figure 7.21: ROC and Reliability plot for (a–d) Bahariya, (e–h) Petrovaradin.

The reliability plot diagrams are shown in Figure 7.22, the observed frequency is plotted against forecast probability for all probabilities. Since we are dealing with a finite sample, the reliability curve will always exhibit variations around the diagonal. Deviation from the diagonal points out a significant con-

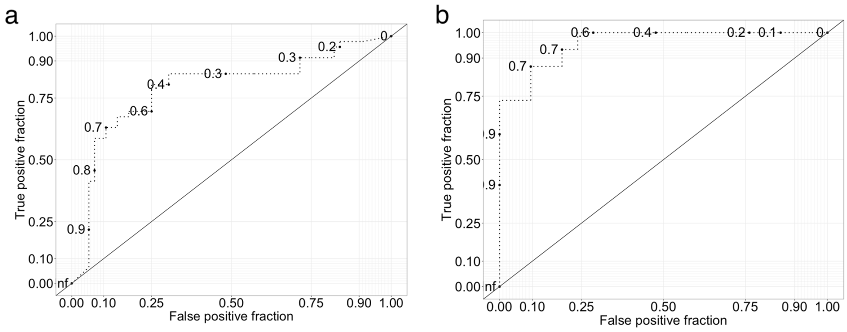

Figure 7.22: ROC plot for Guadeloupe for (a) 2015–2018; (b) 2016.

Table 7.11: Area Under the ROC curve

AUC	Bahariya		Petrovaradin		Guadeloupe
	2017	2018	2016	2017	2015-2019
Value	0.6627868	0.66224	0.7018891	0.700813	0.7363825
p-value	8.62e-08	1.73e-10	1.55e-10	1.46e-10	1.323e-06
Power	0.9968992	0.999778	0.9975426	0.9978564	0.9868904

ditional bias for both runs, indicating that the model is both overforecasting and underforecasting occurrences, as we have seen in the previous chapter. By looking at the ability of the model to forecast extreme probability (0 or 1) we can see that the sharpness is high for threshold 1 for all locations (bin to the left) but low overall.

The positive slope for Bahariya 2018 indicates that as the simulated probability of “yes” events increases so does the actual probability of observing the event in reality. This indicates that the model indeed has some reliability for this location-period. The closer the slope is to the diagonal the higher the overall reliability is.

Table 7.12: Brier decomposition

	Bahariya		Petrovaradin		Guadeloupe
	2017	2018	2016	2017	2015-2019
Brier Score (BS)	0.2414091	0.2623904	0.109903	0.09887363	0.1783824
Reliability	0.04584754	0.05093006	0.01143587	0.00772766	0.03177436
Resolution	0.02960551	0.02960551	0.03266232	0.03325779	0.1009891
Uncertainty	0.2351603	0.2410659	0.1311294	0.1244038	0.2475971

The ROC can also be used to reverse-estimate the “best” cut-off threshold for a dataset by looking at the threshold for which we obtain the highest sensitivity (TPR) and specificity (1 -FPR) pair. However, even though this would produce the best score it does not support the information regarding the significant population peaks that we wanted to convey.

The BS (Table 7.12) tells us what is the size of the probabilistic error. Perfect score is 1. The BSS answers the question of what is the relative skill of the model in terms of simulating whether an event occurred or not. The Brier reliability term is an overall measure of reliability equal to the mean square distance of the curve from the diagonal (Figure 7.22). This term is zero for a perfectly reliable system. The Brier score decomposition is shown in Table 7.12. While reliability is a description of the correspondence between each class of simulation and the according distribution of observations, uncertainty and resolution are independent attributes. Uncertainty is a measure of the observations and indicates the degree to which the observed system of events is predictable, and resolution is similarly independent of reliability and shows how well different forecast classes can differentiate cases with different observed events.

The different Brier scores cannot be directly compared since the uncertainty attribute is a function solely of the observed dataset and greater uncertainty will increase the score. However, we can consider the attributes for each location-year separately. We see that the ratio of reliability to resolution is greater than one for all locations except Petrovaradin. This could be due to the strong seasonality present for this population and may need to be transformed before further analysis.

7.5 Discussion

In this chapter we examined different verification measures for the ODE model vector population model with observations collected for the three study locations in Egypt, Serbia and Guadeloupe.

A verification measure is a function of the simulation, the observations, or their relationship but is not concerned with the correspondence between forecast and observation. On the other hand, performance measures constitute a subset of verification measures that focus on the correspondence between forecasts and observation on an individual or collective basis, for example, conditional probabilities, hit rate and false alarm rate. A specific case of performance measures that is not only a sample statistic but is defined for each individual pair of simulation and observation are quantitative measure of continuous variables such as the RMSE and the BIAS.

The most widely used ROC-based measure of skill is the area under the curve. The ROC is conditioned on the observations (given that a critical number of mosquitoes was observed what was the corresponding simulation), this can be misleading when dealing with mosquito trap data which has very high variance. Field sampling uncertainties can be significant, and site heterogeneity presents a significant factor in measurement uncertainty. It is very difficult to correctly estimate the size of uncertainty that is a result of field sampling of this type.

Verification of the characteristic internal frequencies identified for the observations in Chapter 4 and the model Chapter 6 showed that the model captures the observed frequencies fairly well with a better correspondence in phase for Petrovaradin than Bahariya. The normalized RMSE for Petrovaradin was lower for 2017 (0.11) than for 2016 (0.13). A higher RMSE is observed for Bahariya (0.26 for 2017; 0.21 for 2018). For Guadeloupe, the standard first and second-order moment verification were performed for aggregated monthly values for eight locations across the island (0.23 – 0.42). The population maximum and minimum were replicated correctly by the model; however, a minimum in

September is observed for all capture sites and is not simulated by the model. This could be linked to larval flushing due to extensive precipitation. This claim is further justified by the observed precipitation pattern for Guadeloupe (detailed in Chapter 5 and Appendix A.2) which shows that the annual maximum in precipitation for 2015–2018 is achieved in September and November. The AUC was highest for Guadeloupe (0.73), fairly good for Petrovaradin (0.70) and relatively poor for Bahariya (0.66).

Chapter 8

Improving the model with SURFEX

8.1 Research rationale

In the previous section we showed that the model forced solely by temperature can perform fairly well. The model could be improved by including a precipitation routine; we investigate this here.

In this chapter we will consider two possible ways in which Land Surface Models (LSMs) modelling can be an added value to vector population dynamics models: (1) Improving the hydrology routine; (2) Using LSMs to improve the accuraccy of NWP models which can be used in real-time forecasting of vector population dynamics. Temperature is the most significant driver of population, in case of missing NRT ground data, SURFEX can be used to improve the 2 m accuracy of NWPs.

8.2 Introduction

It is well established that the abiotic factor such as landscape characteristics and meteorological conditions [42, 44, 176, 177] affect the population dynamics of the vector. However, the availability of temporary bodies of water and the total density of breeding sites also has an impact [42, 176].

Temperature and precipitation are the most significant driving variables of mosquito vector population identified in literature [10–19]. Precipitation has a significant effect on vector populations of both *Aedes* and *Culex* species. However, it will affect *Aedes* and *Culex* mosquitoes in different ways due to the difference in the breeding habits of the two genera.

Aedes aegypti and *Aedes albopictus* breed primarily in artificial containers. The main identified breeding sites for *Ae. aegypti* in Guadeloupe were artificial containers, flower pots, used tires, tree hollows, manhole covers and concrete block hollows (detailed in Appendix A.3). Rainfall increases the total surface of available breeding sites, however, it can also have a negative effect due to flushing in cases of extensive precipitation [178, 179].On the other hand, *Culex* can lay his eggs on virtually any stagnant water surface, with the preferred breeding sites being precipitation generated pools and natural areas of standing water, as well as floodwater, depending on the biotype. *Culex pipiens* lays his eggs in rafts of 150–350 eggs. Example breeding sites include ditches, rain barrels, clogged rain gutters, ground pools and puddles with murky water. The standard estimated time from egg to immature stage to adults can take from one to two weeks, depending on environmental conditions.

Some recent work on incorporating a hydrology routine in vector population dynamics modelling already exists for *Anopheles* mosquitoes, which can vector malaria [180–182] . Abiodun et al. [179] modelled the association between temperature, precipitation and the observed abundance of *Anopheles arabiensis* in South Africa. The model incorporates the hydrology routine developed by Tompkins et. al [178]. The dynamics is parameterized as an exchange between the precipitation and evapotranspiration rate. A simpler framework with a similar subroutine for pond dynamics was first proposed by Porphyre et al. [183]. Ahumada et al. [66] developed a model for the population dynamics of *Culex quinquefasciatus* along an elevation gradient in Hawaii, however the model mainly focuses on the effect of draught on the egg desiccation since the local *Cx. quinquefasciatus* unlike *Cx. pipiens* is predominantly a cavity breeder [66, 184, 185].

The models which incorporate puddle dynamics rely on the correct representation of infiltration rate; moreover, parameters such as volumetric water content in the surface layer, surface drainage and runoff can play a significant role in modelling of the dynamics [178].

In meteorology, the exchange between precipitation and evapotranspiration is the main process that drives the interaction between the lower layers of the atmosphere and the ground. The nature of this interaction is explained through the energy and water balance equations [186]. The key forcing is the net incoming radiation at the surface which is the sum of non-reflected solar radiation and the atmospheric long-wave radiation directed towards the surface. The amount of reflected radiation is governed by the albedo of the surface and the long-wave radiation is governed by the temperature of the emitting body, as described by the Stefan–Boltzmann law. This sum is balanced by the partitioning of energy into sensible heat (H), latent heat flux (LE) and the ground heat flux (G) [186]. This ratio is determined by the water balance equation. Rainfall that is intercepted by the canopy further modifies the surface water balance, reducing the amount of precipitation that reaches the soil. The interception rate is a function of the precipitation rate, the leaf area index (LAI), water storage capacity and roughness length of the canopy [186]. The infiltration rate on the other hand, represents the amount of water that enters the soil from the ground surface and is a function of the throughfall rate (sum of canopy drip and precipitation) and the surface runoff.

In the surface modelling platform developed by Météo-France SURFEX [187], runoff and interception are influenced by the aggregated tile physiography as well as volumetric soil water content with the main parameter being the fraction of clay and sand in the soil. SURFEX uses ECOCLIMAP [188] as the physiographic layer that differentiates between different types of land cover, which regulates the surface energy budget and water cycle. In addition to land cover ECOCLIMAP provides albedo and LAI.

In this chapter we first examine whether including a precipitation routine improves the temperature forced model described in Chapter 6 and Chapter 7. Second, we examine the feasibility of improving the precipitation subroutine by using SURFEX. And finally, we examine whether SURFEX can be used to improve the temperature forcing from a NWP model allowing us to run the model in NRT and generate short range predictions.

8.3 Methods

SURFEX is a land surface scheme developed by Météo-France [187, 189]. The scheme uses a tiling approach to compute the relative contribution from lakes, vegetation and urban surface parts. A high-resolution physiographic dataset called ECOCLIMAP [188] is used as input for land cover types. SURFEX consists of several physical models for natural land surfaces, urbanized areas, lakes and oceans. SURFEX can be initialised offline and run independently of the forcing atmospheric model. The natural continental surfaces are modelled with the ISBA land surface scheme (Interaction Soil Biosphere Atmosphere). The Town Energy Balance (TEB) model [189] simulates turbulent fluxes for urban areas.

8.3.1 ISBA prognostic equations and surface fluxes

The ISBA scheme was run with a 3-level soil scheme [187]. ECOCLIMAP physiographic characteristics are used to estimate the surface resistance coefficients. The main prognostic equations in ISBA are:

$$\frac{\partial Ts}{\partial t} = C_T(R_n - H - LE) - \frac{2\pi}{\tau}(T_s - T_2) \tag{8.1}$$

$$\frac{\partial T_2}{\partial t} = \frac{1}{\tau}(T_s - T_2) \tag{8.2}$$

$$\frac{\partial w_g}{\partial t} = \frac{C_1}{\rho_w d_1}(P_g - E_g) - \frac{C_2}{\tau}(w_g - w_{geq}) \tag{8.3}$$

$$\frac{\partial w_2}{\partial t} = \frac{1}{\rho_w d_2}(P_g - E_g - E_{tr}) - \frac{C_3}{d_2 \tau} max[0, (w_2 - w_{fc})] \tag{8.4}$$

$$\frac{\partial W_r}{\partial t} = vegP - (E_v - E_{tr}) - R_r; 0 \leq W_r \leq W_{rmax} \tag{8.5}$$

The five main prognostic variables are: Surface temperature (T_s); Deep soil temperature (T_2); Deep soil water content (w_2); Top soil water content (w_g); Interception water storage (W_r). H and LE are the sensible and latent heat fluxes, R_n is the net solar radiation at the surface, the coefficient C_T is a function of the vegetation-to-soil fraction and the ground, snow and vegetation heat capacities [187]. P_g is the flux of liquid water arriving at the soil surface and E_g is the evaporation at the soil surface, E_{tr} is the transpiration rate, ρ_w the water density and d_1 the arbitrary normalization depth which is set to 1 cm, τ represent the 1 day time-frame used in the Force-Restore method (originally proposed by Blackadar [190] and Bhumralkar [191]). The equilibrium surface volumetric moisture, w_{geq}, C_1 and C_2 are taken from calibration tables constructed for different soil textures and moisture content [187, 192].

Possible soil models in ISBA include: (i) 2-L model corresponding to the system of equations depicted above i.e. T_s and T_2 describing the temperature profile and w_g and w_2 describing the hydrology profile (ii) 3-L parameterization i.e. T_s and T_2 describing the temperature profile and w_g, w_1 (root zone) and w_2 (sub-root zone) describing the hydrology profile (iii) N-L Diffusive model i.e. N possible layers for the temperature and hydrology profile [187,193–196]. Specific options in the soil model are the run-off and sub-grid drainage routine [197].

In case of the 3-L soil model the system of equations is expanded to include a prognostic equation for w_3, and the bulk soil layer (w_2 in the above-defined system of equations) is split into a root zone d_2 and a base-flow layer $d_3 - d_2$.

$$\frac{\partial w_2}{\partial t} = \frac{1}{\rho_w d_2}(P_g - E_g - E_{tr}) - \frac{C_3}{d_2 \tau} max[0, (w_2 - w_{fc})] - \frac{C_4}{\tau}(w_2 - w_3) \quad (8.6)$$

$$\frac{\partial w_3}{\partial t} = \frac{d2}{d3 - d2}\left(\frac{C_3}{d2\tau} max[0, (w_2 - w_{fc})] + \frac{C_4}{\tau}(w_2 - w_3)\right) - \frac{C_3}{(d3 - d2)\tau} max[0, (w_3 - w_{fc})] \quad (8.7)$$

C_4 is the vertical diffusion coefficient defines as $C_4 = C_{4ref} \bar{w_{2,3}}^{C_{4b}}$ where $\bar{w_{2,3}}$ represents the representative interpolated volumetric water content at d2. The C coefficients are defined according to the soil content.

8.3.2 Data

A verification of the surface temperature from SURFEX [187] is performed against MODIS Land Surface Temperature (LST) [198] for the study site in Petrovaradin. The LST data (MOD11) are retrieved at a horizontal resolution of (i) ≈ 30 arc second with the generalized split-window algorithm; (ii) ≈ 3 arc minutes with the day/night algorithm [198]. For Guadeloupe on the other hand, near-surface variables are more important: verification of 2 m temperature is performed against the ERA5 [199] reanalysis for the nearest point in the native ERA5 grid.

8.3.3 SURFEX forcing

For Guadeloupe, SURFEX is forced with the 50 m temperature and wind from the Integrating Forecasting System (IFS) deterministic model [200] to obtain the 2 m temperature. The 50 m forcing was generated from the deterministic 8-km IFS forecast at model level 3 (≈ 50 m). This SURFEX run is verified against ERA5 hourly 2 m temperature for Guadeloupe. For Petrovaradin, SURFEX is forced with 2 m and 10 m ERA5 [199]. This run is verified against MODIS land surface temperature. These verification sets were selected in order to ensure that the forcing and verification series are not the same and escape false accuracy due to this pitfall.

Depending on the application, SURFEX can be forced with: surface variables or forcing at the three lowest atmospheric model levels. The following two scenarios can be distinguished: (1) If we are interested in surface variables, as opposed to near surface variables at 2 m or 10 m; then SURFEX can be forced and is sufficiently reliable with parameters at 2 m (temperature forcing) or at 10 m (wind forcing); (2) In case the near surface variables are important SURFEX must be forced with data at 50 m (3rd model level, IFS).

The variables used to prepare the forcing were: surface solar radiation downwards (J m^{-2}), surface thermal radiation downwards (J m^{-2}), rain rate (kg $m^{-2}s^{-1}$), temperature (K), u and v wind speed (m s^{-1}), specific humidity (kg kg^{-1}). The radiation parameters were transformed to (Wm^{-2}) for the forcing.

8.3.4 Precipitation routine

8.3.4.1 Model 1

In the first study a simple lagged model is considered. The larva and pupa carrying capacities are scaled using the accumulated precipitation between day 26 and day 14 prior to the trapping event (detailed in Chapter 4, shown here in Figure 8.1):

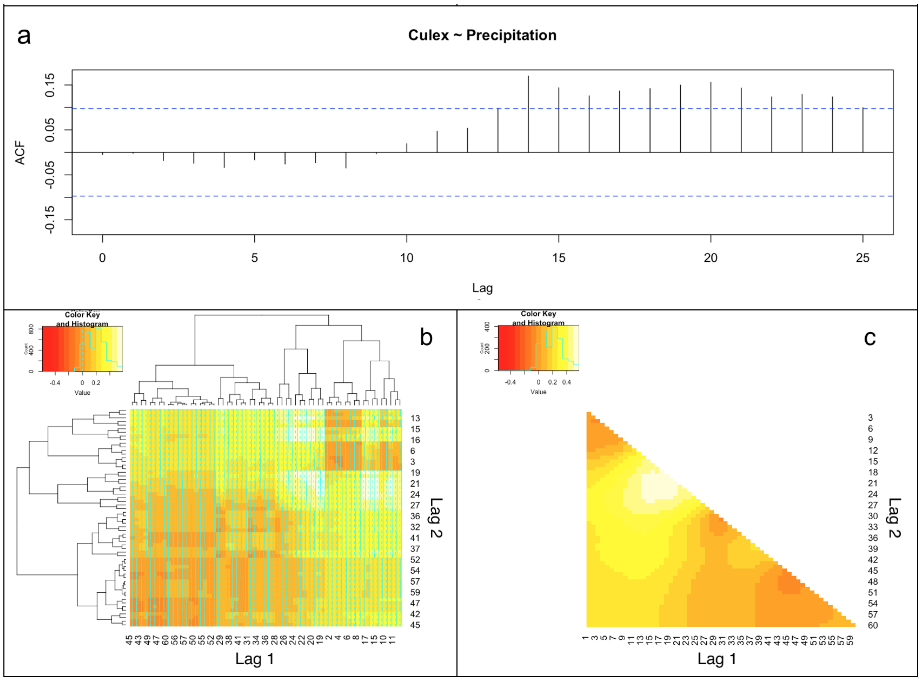

Figure 8.1: (a) CCF for precipitation and *Culex pipiens* abundance for 2016–2017 for lags 0–25 days; (b) dendrogram and (c) ordered CCM for Petrovaradin for time interval lagged precipitation and *Culex pipiens* abundance for 2016–2017, lags from 0–60 days shown in descending order on y-axis and ascending order on x-axis.

$$\kappa^i_{L,P}(H^i_{norm}) = \kappa^i_{L,P} \cdot (1 + H^j_{norm}) \tag{8.8}$$

H_{norm} is the value of the accumulated precipitation for day j normalized between 0 and 1:

$$H^i_{acc} = \sum_{i-k}^{i-j} H_n \tag{8.9}$$

Where i is the trapping day, k = 26 and j = 14.

8.3.4.2 Model 2

In this study, it is assumed in line with [71, 178, 179, 201], that the carrying capacity κ is a function of the total surface of the available breeding sites. This model includes a subroutine for the fraction of the total available breeding sites per unit area as:

$$\frac{\partial w_{pond}}{\partial t} = K_\nu \left(H \cdot (w_{max} - w_{pond}) - w_{pond}(E + I)\right) \tag{8.10}$$

The run-off is scaled by a linear factor $1 - \frac{w_{pond}}{w_{max}}$. Once the pond fraction reaches w_{max}, the contribution from precipitation overflows and is lost [178,179].

The fraction of available breeding sites is mapped to a sigma stress function for the carrying capacity $K = K_{max} \cdot \sigma_{wp}$, where K_{max} is the maximum carrying capacity per surface area.

Infiltration losses are often highly variable and non-linear. In literature, a constant infiltration rate of 5 mm/day is assumed [178, 179]. We investigate whether the precipitation routine is improved by forcing from SURFEX.

The evaporation rate from the puddle is calculated following Hamon's equation:

$$E = 2.1 \cdot h_t^2 \cdot \left(\frac{e_s}{Ta + 273.3}\right) \tag{8.11}$$

Where h_t is the average number of daylight hours per day during the month in which day t falls, e_s is the saturation vapour pressure calculated as:

$$e_s(T_a) = 0.6108 e^{\left(\frac{17.27 T_a}{T_a + 237.3}\right)} \tag{8.12}$$

Infiltration rate $[\frac{mm}{day}]$ is estimated as: $I = min(R_t - Q_r, -F_{max0})$ [187], R_t is the through-fall rate calculated as the sum of canopy drip and precipitation, and F_{max0} is the maximum water flux into the surface soil layer, Q_r is the surface run-off [187].

The SURFEX outputs that are used in the precipitation routine are: (i) The change of water on canopy, i.e. through-fall rate (DWR) (ii) Total run-off for the surfaces present in the tile.

Important parameters for the correct simulation of infiltration and run-off are the clay and sand fractions of the top soil layer and the temperature of the water near the surface. In literature it is assumed that the temperature of small volumes quickly reaches thermodynamic equilibrium with the surrounding air and can be assumed to be the same as air temperature. The clay and sand fractions of the soil were specified according to the physico-chemical characteristics of the soil type for this region of Serbia [202].

8.3.4.3 Numerical weather prediction model

The deterministic 8-km Integrated Forecast System [200] numerical weather prediction (NWP) runs for the first 25 hours, started at 00h and 12h, were used to obtain short-range forecasts for the population dynamics of *Ae. aegypti* population in Guadeloupe.

We first compare the IFS and SURFEX 2 m temperature against ERA for Guadeloupe to see if the accuracy of the forcing temperature is improved by SURFEX. Second we generate the forecast steps in SURFEX and run a short-range forecast scenario for the vector population dynamics (25 hours).

The IFS variables used to force SURFEX were: surface solar radiation downwards (J m^{-2}), surface thermal radiation downwards (J m^{-2}), rain rate (kg $m^{-2}s^{-1}$), temperature (K), u and v wind speed (m s^{-1}), specific humidity (kg kg^{-1}). The radiation parameters were transformed to (Wm^{-2}) for the forcing.

8.4 Results

8.4.1 Verification of ECOCLIMAP

Due to high levels of landscape fragmentation, especially at mid-latitudes [188], we first compare the ECOCLIMAP outputs to CLC and ground-truth information for the study sites.

The bar plot (Figure 8.2) summarizes the fraction of each cover type for the two datasets. The fraction of each cover in the CLC layer is calculated by looking at the ratio of pixels corresponding to certain layers to the total number of pixels in the CLC subset, matching the extent of the SURFEX tile.

Land Cover names can vary depending on the database. Following the paper by Tchueté et al. [203], the corresponding legends from CLC and ECOCLIMAP are reconciled by re-classifying them according to the LCCS (Land Cover Classificaiton System) standard [204]: (i) The “Forest/Mixed Forest” aggregated class containing the central American evergreen broad leaf forest for Guadeloupe, and Broadleaf forest type for Serbia; (ii) The “Cropland” including different agricultural tissue (iii) The “Grassland” aggregated class including central-American and tropical wooded grassland for Guadeloupe; and central Eastern European pastures for Serbia (iv) The “Urban and built-up” aggregated class which includes airports and other low-rise human structures. Other classes that correspond to the LCCS (level 1) standard and are not present in this tile are the woodland/shrubland type, the bare land and the inland water class.

We see that the agreement between the mixed SURFEX tile and the CLC aggregated classes is fairly good for both study location. For Guadeloupe, the observed pixel to total number of pixels ratio in the CLC classes for the single-point-run tile is 48% Urban consisting of discontinuous urban fabric; and 52% Nature consisting of cropland (22%) and broadleaf forests (30%) (Table 8.1, Figure 8.2a). The Forest and Urban tissue is replicated in ECOCLIMAP, however, instead of the crop cover ECOCLIMAP shows wooded grassland. The grassland cover matches the ground-truthing reports from the local team better than crop which is located further to the north of the study location. The specific land cover classes identified in ECOCLIMAP: Central American evergreen broadleaved forest (EBF), and central American tropical wooded grassland (WG) are all confirmed on the island.

The Mixed SURFEX tile for Petrovaradin has a better correspondence to CLC (Figure 8.2b). The observed CLC ratio is 76% Urban consisting of discontinuous urban fabric (47%) and industrial and commercial units (29%); and 24% Nature consisting of broadleaved forest areas (19%) and complex cultivation patterns (5%). All land cover classes identified in ECOCLIMAP (Table 8.2) were compared against ground truth information and city records for this district and are all present except for the complex cultivation which are not commonly found in this suburban region.

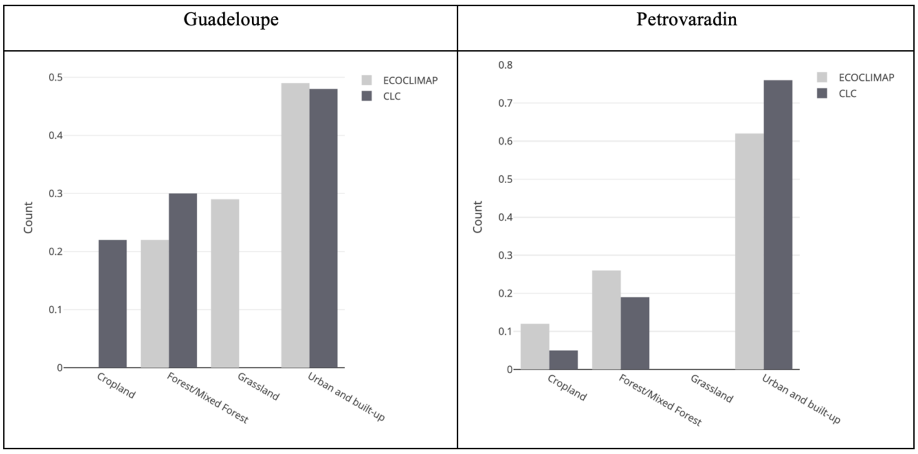

Figure 8.2: Tile fraction comparison

Table 8.1: Nomenclature of the ECOCLIMAP and CLC (control) land cover types being used for the SURFEX tile for Guadeloupe.

	Source	Cover	Fraction [%]	Aggregated classes
SURFEX	ECOCLIMAP	Cent. America Tr. wind EBF	22	Forest/Mixed Forest
		Cent. Amer. Tr. wind & trop. WG	29	Grassland
		Urban and built-up	49	Urban and built-up
CLC	CLC	Discontinuous urban fabric	48	Urban and built-up
		Agricultural tissue	22	Cropland
		Broadleaf forest	30	Forest/Mixed Forest

Table 8.2: Nomenclature of the ECOCLIMAP and CLC (control) land cover types being used for the SURFEX tile for Petrovaradin.

	Source	Cover	Fraction [%]	Aggregated classes
SURFEX	ECOCLIMAP	Urban and built-up	62	Urban and built-up
		Balkanish complex cultivation pat.	12	Cropland
		Agro-forestry areas	26	Forest/Mixed Forest
CLC	CLC	Discontinuous urban fabric	47	Urban and built-up
		Industrial and commercial units	29	Urban and built-up
		Complex cultivation pat.	5	Cropland
		Broadleaf forest	19	Forest/Mixed Forest

8.4.2 Verification of OFFLINE SURFEX

The testing of SURFEX, within the ALADIN and ALARO models, has been performed extensively during the last couple of years [205–207]. The results showed that the runs with SURFEX did not significantly change the output for surface, pressure, precipitation, cloud cover and 10 m wind direction, however, they improved the scores for 2 m humidity and temperature and 10 m wind speed.

In this section a verification of 2 m and surface temperature will be presented for the two use-cases in Bahariya and Petrovaradin.

8.4.2.1 Guadeloupe

We consider three scenarios for Guadeloupe: (i) SURFEX over a 100% Nature tile; (ii) SURFEX over a 100% Urban tile; (iii) and SURFEX over a mixed tile corresponding to the ECOCLIMAP fraction.

Table 8.3 represents the scores obtained for 2 m temperature for the reanalysis point located next to the Pointe-à-Pitre station in a semi-rural area. The accuracy scores of the SURFEX runs for three tiles with different physiographic characteristic and the IFS two-meter temperature are compared. There is an improvement in BIAS and RMSE with SURFEX compared to IFS, with the mixed tile performing the best.

Table 8.3: BIAS (M-O) and RMSE for 2 m air temperature against hourly ERA.

	NAT	URB	MIX	IFS
BIAS	-0.531	1.282	0.375	-1.253
RMSE	1.798	1.596	1.116	1.985
Corr	r = 0.76 (p <2.2E-16)	r = 0.72 (p <2.2E-16)	r = 0.81 (p <2.2E-16)	r = 0.68 (p <2.2E-16)

This is in accordance with the ECOCLIMAP results, since the mixed tile corresponds best to the observed land cover.

8.4.2.2 Petrovaradin

The scores obtained for the comparison of SURFEX surface temperature and MODIS land surface temperature are presented in Table 8.4 and Figure 8.3.

Table 8.4: BIAS (M-O) and RMSE MODIS LST daily.

	NAT	URB	MIX
BIAS	-0.816	0.384	-0.352
RMSE	2.08	1.917	1.904
Correlation	r = 0.8468 (p <2.2E-16)	r = 0.8504 (p <2.2E-16)	r = 0.8986 (p <2.2E-16)

Again we see that the mixed tile performs the best, i.e. has the highest accuracy (RMSE, BIAS) and best association with the remote sensing LST data for Petrovaradin.

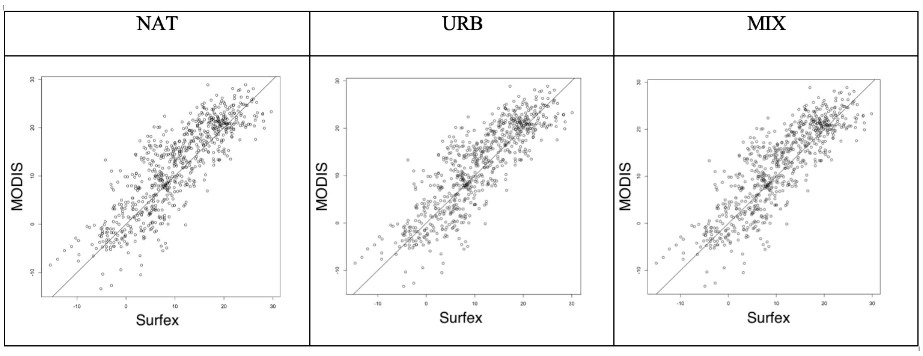

Figure 8.3: Correlation graphs MODIS LST vs SURFEX surface temperature for (a) 2016 and (b) 2017 for Petrovaradin.

8.4.3 Precipitation routine

The two precipitation schemes are compared against the original model. The improvement in the model is depicted in Table 8.5 showing the difference between the verification scores for the baseline and the new model (RMSE(New) – RMSE(Baseline)).

The model output is between 0 and 1, the RMSE and BIAS should be considered accordingly. The dynamic model forced with SURFEX performed the best across all three scores. The dynamics model forced with SURFEX performed better than the dynamic model forced with constant infiltration rate (I = 5 mm/day [178, 179]). The reduction in BIAS (i.e. improvement in accuracy) for the model with constant infiltration was -8·10^{-3}, and the reduction in BIAS for SURFEX forced model was -1.65·10^{-2}.

Table 8.5: Difference in verification score (RMSE(New) – RMSE(Baseline)). Negative value indicates improvement

	Lagged	Dynamic	Dynamic Forced with SURFEX
Δ RMSE	-0.005766	-0.03501049	-0.067446
Δ BIAS	-0.001429	-0.008673	-0.0165111
Δ AIC	-3.2	-4.8	-6.2

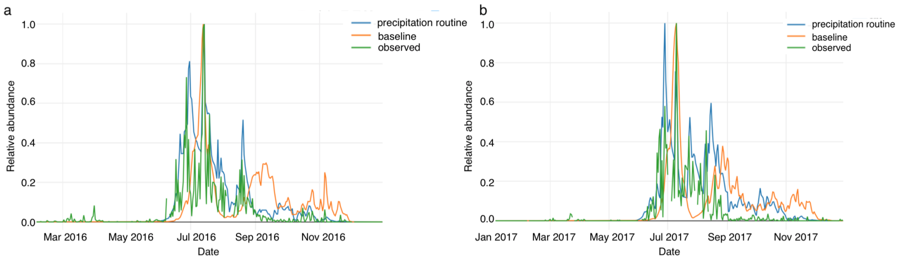

Figure 8.4: Comparison of the baseline temperature-forced model (*orange*) and model including a precipitation routine with SURFEX (*blue*).

The improved cannot be considered to be significant since the verification scores for all three model are lower than the observational uncertainty ($u(o) = 0.12$ and $u(o) = 0.11$ for Petrovaradin for 2016 and 2017, respectively - calculated in Chapter 7). However, the simulated dynamics does appear to better capture the observed dynamics for the peaks following the July maximum (Figure 8.4).

Even though the improvement in accuracy is not significant it does improve the reality of the model and can inform vector treatment that targets the immature stages in the mosquito life cycle. Applying larvicide to the breeding sites for a period in which the total fraction of available breeding sites exceed a safe threshold could reduce the control effort and maximize efficiency. This type of information does not exist in the model forced solely by temperature.

8.4.4 Short range forecast of vector population dynamics

Pest population dynamics are driven by environmental factors at the global and local scale, as well as different temporal frequencies. The forecasting period can be considered at different temporal scales: Short term (few days) which focusses on high-resolution processes; medium range (up to 10 days) synoptic scale; and monthly and seasonal forecasts (linked to global circulation patterns). The 25 hour forecast can give valuable information on the change in trend in the population dynamics. The forecasted values are shown in red in Figure 8.5.

The local change in trend corresponds to the global change in trend. The total deviation from the 0-time step forced SURFEX is 0.009. For a sample period shown in Figure 8.5 we see that the two critical points on the 25th and 26th of March corresponding to the base and peak of the maximum were correctly forecasted.

Figure 8.5: *Ae. aegypti* short-range forecast for (a) the full observational interval (Mar - May 2017) and (b) a 20 day sub-interval (Mar 23 - Apr 12 2017) (observed: *blue*; model: *black*; forecast: *red*).

8.5 Discussion

In this chapter we considered two possible ways in which the SURFEX land-surface platform can be an added value to vector population dynamics models: (1) Improving the hydrology routine; (2) using SURFEX to improve the accuracy of the IFS forcing and generate short-range forecasts for the population dynamics model.

Adding precipitation to the baseline population dynamics model improved the accuracy of the model, however the improved scores are within the observational uncertainty and cannot conclusively be considered significant. The underlying reason could be that the actual observed population does not have such a strong correlation with precipitation and breeding sites are generated through other mechanisms. This is can be linked to the results obtained in the cross-correlation analysis for Petrovaradin in Chapter 4. The correlation showed only a moderate association with precipitation and the observed population density. Meaning that the main mechanism for generating the flood areas suitable for *Cx. pipiens* reproduction around Petrovaradin might not be precipitation but a combination of precipitation and flooding due to the rise in water levels.

The accuracy of the IFS forcing is improved with SURFEX. As far as we know, there are no existing papers which report a model that is used to for forecasting pest population dynamics. This could be an interesting avenue for future research and IPM applications which can support NRT processing of vector population dynamics models.

Chapter 9

General discussion and conclusions

The population dynamics of vector species and the consequential circulation of Vector-Borne Disease (VBD) is simulated by numerical models of different scales and complexity. These models require species-specific parameters forced by meteorology representative of the vector micro-habitat in order to produce useful simulations of population densities for each stage. The main contributions of this thesis are: (i) a methodology for the analysis of the climatic suitability and a dynamic weather-driven simulation of the population dynamics for *Aedes aegypti* and *Culex pipiens* for specific locations in Guadeloupe, Egypt and Serbia; (ii) an improved understanding of the sensitivity of the Multi Criteria Decision Analysis (MCDA) model parameters in different eco-climatic conditions; (iii) a functional understanding of the impact of model stability on initialization and spin-up time; (iv) a practical framework for forecasting pest population dynamics in scenarios where in-situ near-real time data is not available. These main contributions are attained by: (i) systematically investigating the relation between the observed vector population and the meteorological conditions at 3 locations (Chapter 4); (ii) a MCDA suitability assessment at these sites and identification of the most important climatic factors and model settings as a function of climatic characteristics of the study region (Chapter 5); (iii) modelling the vector population dynamics and stability analysis of the dynamical system (Chapter 6); (iv) the analysis of different verification techniques and implications in terms of model application (Chapter 7); and (v) a feasibility analysis of improving the model with the SURFEX Land-Surface Parameterization platform and short-range forecasting of pest population dynamics with IFS data (Chapter 8).

Relation between observed vector population and meteorological conditions: Fluctuations in local environmental conditions not only influence the immediate activity and survival, but also the development and transition rates between the different stages within the life-cycle of the mosquito vector. A qualitative understanding of the local strength and nature of association and time-scales of this interaction can be used as input for vector population dynamics models in order to forecast population spikes through meteorological observations. The association between the observed vector population and the most important meteorological variables driving vector mortality and development was investigated in Chapter 4. This was carried out by means of time-series analysis and lagged cross-correlation of abundance with the following variables temperature, relative humidity, precipitation and wind speed. The association between the meteorological and entomological time series was found to be predominantly non-linear. The results demonstrated a significant correlation between the vector population and daily temperature at both sites. While different studies have identified relative humidity to have a crucial impact on vector dynamics [71,179,208,209], no significant association was found with vector abundance for the study sites in Bahariya and Petrovaradin. Low values of relative humidity have been known to negatively influence the survival rate of adult mosquitoes, however, the population is capable of surviving in a high-stress environments, pertaining to both low relative humidity and high temperature. This can be due to multiple factors such as human influence, and the existence of natural cover or more suitable micro-habitats. The generalizability of the results is limited by the number and specific setting of the study sites. Further investigations, on multiple sites, are needed to examine the sensitivity curve of vector mortality and development rates with respect to the observed relative humidity range in field conditions. Generational coupling with temperature was identified with a negative correlation with air temperature and vector abundance at the 8–10 day lag for Bahariya. For Petrovaradin, a positive correlation with one and two-week lagged air temperature suggests a similar generational character for a mid-latitude location, however additional analysis is needed to identify the interval-lagged nature of this mechanism in the context of variable aquatic development times in semi-controlled conditions. The seasonal character of the vector time-series was less pronounced for Bahariya and the wavelet analysis indicated that the time-series had a more stochastic character for the second half of the period compared to the first. Further work could be carried out to compare the wavelet spectrum of the forcing meteorology with the entomological observation and assess whether this shift is reflected in the meteorological time-series. The results of the time-series analysis confirm existing evidence that the diurnal temperature range (DTR) can negatively affect the development and survival rates of the vector and decrease the population density [30, 210, 211]. DTR as well as the diurnal relative humidity range (DRHR) had a predominantly negative association with the observed catches for Bahariya. This is a desert location in Egypt with extreme variation in the daily temperature cycle often observed. Such harsh conditions could exhibit a direct stress to poikilothermic organisms and invariantly expose the vector to unfavourable temperature and relative humidity conditions that negatively impact survival. The correlation of vector abundance with wind was negative for the 0-day lag and should be considered during surveillance and data processing, i.e. high wind speed could produce lower catches. Further work should be carried out to calibrate this scaling factor. The standard temperature range for the activity of *Cx. pipiens* is 11 °C – 35 °C [7,8], with immobility and death occurring at temperatures above 35 °C. However, we have found that the vector can adapt to the environment and was even observed to have higher activity with the increase of total hours above 35 °C for the study site in Bahariya, Egypt. This suggests that the response of the vector to local environmental conditions can be significantly different between sites. Further research should be done to quantify this link for *Culex pipiens* in the hot arid desert climate (Köppen classification, CWh).

Climatic suitability assessment: A country-level climatic assessment study was carried out for Guadeloupe, Egypt and Serbia to examine the broader suitability for the establishment and inter-annual activity of the vectors (Chapter 5). A mechanistic MCDA model was used to translate the climatic parameters into a measure of suitability for each vector. The MCDA model is useful in the analysis of emerging hot spots or high-risk areas arising from the characteristics of the local climate. An increase in the suitability index could indicate higher activity and greater population abundance of the vector during the year, which has an influence on the disease transmission rate [30, 179, 212]. This is especially important for the species considered in this study since they can vector some of the most hazardous and rapidly spreading diseases in the world; namely Zika, Chikungunya, Dengue (*Ae. aegypti*), St. Louis Encephalitis and WNV (*Cx. pipiens*). The MCDA model had the highest sensitivity to the Ta (annual temperature) climatic parameter in Guadeloupe, for *Ae. aegypti*; the night-time-light parameter in Bahariya, for *Cx. pipiens*; and again the Ta (annual temperature) parameter in Serbia, for *Cx. pipiens.* The association could suggest an expected increase in suitability as a result of climate change for all three locations following any climatic scenario in which an increase in population is assumed and an increase in the mean annual temperature is projected. In an additional study, presented in Appendix A.1, we examined the expected impact of climate change using a multi-model approach for the establishment of the Asian tiger mosquito (*Aedes albopictus*) in Serbia. The results indicate that most of the country will become suitable for this invasive vector by the end of the century. Future work should be carried out to examine the change in suitability in the context of climate change for Egypt and Guadeloupe. The sensitivity analysis carried out in this thesis examined a one-factor-at-a-time (OFAT) sensitivity analysis i.e. an analysis of the MCDA output for each variable in the parameter space while keeping the others constrained. In future research, the all-but-one-at-a-time global sensitivity analysis (ABOS) will be employed to explore the interaction effects of the input parameters.

Dynamical model and stability analysis: A mechanistic, nonlinear ODE vector population dynamics model for *Ae. aegypti* and *Cx. pipiens* was formulated and analyzed in Chapter 6. The model consists of 10 compartments and simulates the entire life-cycle of the mosquito vector. It incorporates age and density dependent processes within the closed system of the simulated population. The development and mortality rates are temperature dependent functions. The model is run with a daily time step. The stability of the dynamical ODE system was examined, and two equilibrium states were identified. The practical implication of determining the stationary states of the dynamical system were demonstrated within the purpose of reducing the model spin-up time and internal model validation. The equilibrium is defined for an autonomous system, i.e. a specific temperature state. When the system is initialized with a value greater than the steady state for the temperature value corresponding to a particular integration step, damped oscillation around the equilibrium point is observed. The exact value for the different stages of the mosquito population cannot be captured by measurements, thus most models integrate from a best-guess initial state based on literature and allow for a longer spin-up time. The spin-up time when initializing from an arbitrary state was estimated to be around 200 days. We demonstrated that the spin up time can be considerably reduced by initializing with the equilibrium state corresponding to the temperature at the t=0 timestep.

Model Verification: In Chapter 7 the verification and validation of the model was performed. There is little literature on the quantitative verification of vector population models since long term and consistent time-series of observed data are rare. The time and cost of the trapping efforts are usually the main limiting factors. Most available data-sets tend to be irregularly spaced and demonstrate high variability over different regions and sampling periods. Moreover, the information and data are often time and resolution specifics to the considered period of observation. Sometimes multi-year data needs to be collected to quantify the seasonal relationship of the vector population and its environment. Thus, collecting field data is a slow and expensive process.

The verification methods for this type of ODE models need to be selected based on their practical application. For meteorological forecasts, the verification metrics can be grouped in three respective groups: scientific, economic and administrative [151]. A similar classification can be applied to vector models. From a scientific point of view the focus is on the improved understanding of the modelled biological system. It can be argued that this is the broadest of the three categories, because it needs the widest range of verification metrics and an underlying explanation of why the model performed well for a certain metric and less well for another, and an analysis of this verification score in terms of the underlying modelling framework. This type of analysis could lead to a better understanding of the biases present in either the observational or modelling procedures and to an improved understanding of the underlying processes. Within this category the methods outlined in Chapter 7 were: (i) internal verification employing Wavelet analysis, which was used to assess whether the frequencies occurring in the observed population are replicated in the model; (ii) exploratory methods (EM) which deal with the graphical comparison of the observed and modelled data as well as the comparison of the basic summary statistics of each set; (iii) RMSE and BIAS verification metrics which can indicate in which interval of the total observational period the accuracy or association of the simulation and observations decreases; (iv) analysis of extrema and inflection points which demonstrate weather the significant peaks and the dynamics leading to a peak is correctly represented by the model; and (v) contingency verification measures (CVM) which indicate whether "higher-abundance" events, defined by a threshold are correctly simulated by the model.

The wavelet analysis showed that the dominant frequencies for both the observed and simulated dynamics change with the time evolution of the system and that the summer period corresponded to a higher number of significant frequencies as well as shift to higher frequencies for both Bahariya and Petrovaradin. The cross-wavelet analysis demonstrated that this was replicated in the simulated system. The model performed fairly well for all locations with the best scores obtained for Petrovaradin, then Guadeloupe and lastly Bahariya.

From an economic point of view the main focus is on the specific role the model is performing within the real-word application and can be expressed in terms of model value. For example, a population dynamics model can be used to inform control measures for a specific location with the aim of reducing the annual cost of spraying and pesticides. The user often needs information regarding a specific threshold in the vector population. For this application the correct simulation of significant peaks and inflection points is most relevant as well as CVM for a threshold determined by the user.

Finally, the administrative point has a focus on improving the overall performance of the model based on a smaller sub-set of verification metrics and is mainly concerned with model accuracy. These types of verification could guide next steps and help make decisions about the future research avenues in a more general manner. However, to be able to utilise this type of reasoning within the field of vector modelling, a consensus needs to be reached on the most representative verification metrics, which is currently not the case. Hopefully this thesis is a step towards understanding the utility and context of different verification scores for evaluation vector population dynamics models and their interpretation.

Hydrology routine and pest population dynamics forecasting: In Chapter 8 two possible ways in which the SURFEX land-surface platform can be an added value to vector population dynamics models was considered: (i) Improving the hydrology routine; (ii) using SURFEX to improve the accuracy of the IFS forcing and generate short-range forecasts for the population dynamics model. Temperature has the most significant effect on the mortality and development rates of the vector population, while precipitation has an impact on the provision and total surface of available breeding sites. We examined a simple, process-based surface hydrology subroutine which provides the fractional water coverage, based on an exchange between precipitation, the canopy fall-through rate and evaporation, for each numerical integration step. This routine covers the effect of precipitation on temporary water bodies that can serve as vector breeding sites; however, it does not include other processes that could influence the availability of breeding sites. Land cover has been found to affect the larval development rate through the effect on water temperature [179, 213]. Other missing parameters that should be considered in future studies are irrigation and flood areas, which can be implemented in SURFEX through the flooding scheme coupled to ISBA. Existing flood areas can confound the traditional relationship between precipitation frequency and the total available surface of breeding sites by being dependent on up-stream meteorological processes such as spring snow-melting, or even during low water-levels and drought periods in which the river bed dries up and stagnant water-pockets develop [178]. Similar time-series analysis techniques as described in Chapter 4 should be utilized to examine the association between these new variables and the observed vector population. Moreover, data regarding the abundance of the aquatic stages could significantly improve the verification efforts for this routine and will be used to calibrate and validate the model in future work.

Finally, a short-range forecast run for the vector population dynamics forced with SURFEX 2 m temperature was examined. These finding could be valuable in an early warning IPM system to indicate the change of trend in the population dynamics and inform timely control. In future, we would like to examine the feasibility of medium and long-range forecasts of vector populations. Here error propagation and uncertainty is an important consideration since the predictability for the forcing meteorology rapidly decreases with the forecast time. Moreover, quantifying the seasonal link between vector populations and global scale patterns such as the North Atlantic Oscillation index, the Madden Julian Oscillation index and the El Niño Southern Oscillation index, and relating them to the local scale could pave the road for seasonal population dynamics forecasting.

Bibliography

[1] M. Kamal, M. A. Kenawy, M. H. Rady, A. S. Khaled, and A. M. Samy, "Mapping the global potential distributions of two arboviral vectors *Aedes aegypti* and *Ae. albopictus* under changing climate," *PloS one*, vol. 13, no. 12, 2018.

[2] M. S. Shocket, A. B. Verwillow, M. G. Numazu, H. Slamani, J. M. Cohen, F. El Moustaid, J. R. Rohr, L. R. Johnson, and E. A. Mordecai, "Transmission of west nile virus and other temperate mosquito-borne viruses occurs at lower environmental temperatures than tropical diseases," *bioRxiv*, p. 597898, 2019.

[3] J. L. Smith and D. M. Fonseca, "Rapid assays for identification of members of the *Culex (Culex) pipiens* complex, their hybrids, and other sibling species (diptera: Culicidae)," *The American journal of tropical medicine and hygiene*, vol. 70, no. 4, pp. 339–345, 2004.

[4] A. Farajollahi, D. M. Fonseca, L. D. Kramer, and A. M. Kilpatrick, ""bird biting" mosquitoes and human disease: a review of the role of *Culex pipiens* complex mosquitoes in epidemiology," *Infection, genetics and evolution*, vol. 11, no. 7, pp. 1577–1585, 2011.

[5] A. T. Ciota, A. C. Matacchiero, A. M. Kilpatrick, and L. D. Kramer, "The effect of temperature on life history traits of *Culex* mosquitoes," *Journal of medical entomology*, vol. 51, no. 1, pp. 55–62, 2014.

[6] J. E. Brown, B. R. Evans, W. Zheng, V. Obas, L. Barrera-Martinez, A. Egizi, H. Zhao, A. Caccone, and J. R. Powell, "Human impacts have shaped historical and recent evolution in *Aedes aegypti*, the dengue and yellow fever mosquito," *Evolution*, vol. 68, no. 2, pp. 514–525, 2014.

[7] A. Werblow, S. Klimpel, S. Bolius, A. W. Dorresteijn, J. Sauer, and C. Melaun, "Population structure and distribution patterns of the sibling mosquito species *Culex pipiens* and *Culex torrentium* (diptera: Culicidae) reveal different evolutionary paths," *PLoS One*, vol. 9, no. 7, p. e102158, 2014.

[8] E. B. Vinogradova, *Culex pipiens pipiens mosquitoes: taxonomy, distribution, ecology, physiology, genetics, applied importance and control.* Pensoft Publishers, 2000, no. 2.

[9] J. Liu-Helmersson, H. Stenlund, A. Wilder-Smith, and J. Rocklöv, "Vectorial capacity of aedes aegypti: effects of temperature and implications for global dengue epidemic potential," *PloS one*, vol. 9, no. 3, 2014.

[10] M. Kobayashi, N. Nihei, and T. Kurihara, "Analysis of northern distribution of *Aedes albopictus* (diptera: Culicidae) in japan by geographical information system," *Journal of Medical Entomology*, vol. 39, no. 1, pp. 4–11, 2002.

[11] O. J. Brady, M. A. Johansson, C. A. Guerra, S. Bhatt, N. Golding, D. M. Pigott, H. Delatte, M. G. Grech, P. T. Leisnham, R. Maciel-de Freitas *et al.*, "Modelling adult *Aedes aegypti* and *Aedes albopictus* survival at different temperatures in laboratory and field settings," *Parasites & vectors*, vol. 6, no. 1, p. 351, 2013.

[12] T. W. Scott, P. H. Amerasinghe, A. C. Morrison, L. H. Lorenz, G. G. Clark, D. Strickman, P. Kittayapong, and J. D. Edman, "Longitudinal studies of *Aedes aegypti* (diptera: Culicidae) in thailand and puerto rico: blood feeding frequency," *Journal of medical entomology*, vol. 37, no. 1, pp. 89–101, 2000.

[13] S. Nawrocki, W. Hawley *et al.*, "Estimation of the northern limits of distribution of *Aedes albopictus* in north america." *Journal of the American Mosquito Control Association*, vol. 3, no. 2, pp. 314–317, 1987.

[14] S. M. Thomas, U. Obermayr, D. Fischer, J. Kreyling, and C. Beierkuhnlein, "Low-temperature threshold for egg survival of a post-diapause and non-diapause european aedine strain, *Aedes albopictus* (diptera: Culicidae)," *Parasites & vectors*, vol. 5, no. 1, p. 100, 2012.

[15] D. Roiz, R. Rosa, D. Arnoldi, and A. Rizzoli, "Effects of temperature and rainfall on the activity and dynamics of host-seeking *Aedes albopictus* females in northern italy," *Vector-Borne and Zoonotic Diseases*, vol. 10, no. 8, pp. 811–816, 2010.

[16] Y. Proestos, G. Christophides, K. Ergüler, M. Tanarhte, J. Waldock, and J. Lelieveld, "Present and future projections of habitat suitability of the asian tiger mosquito, a vector of viral pathogens, from global climate simulation," *Philosophical Transactions of the Royal Society B: Biological Sciences*, vol. 370, no. 1665, p. 20130554, 2015.

[17] J. M. Medlock, D. Avenell, I. Barrass, and S. Leach, "Analysis of the potential for survival and seasonal activity of *Aedes albopictus* (diptera: Culicidae) in the united kingdom," *Journal of Vector Ecology*, vol. 31, no. 2, pp. 292–305, 2006.

[18] C. Caminade, J. M. Medlock, E. Ducheyne, K. M. McIntyre, S. Leach, M. Baylis, and A. P. Morse, "Suitability of european climate for the asian tiger mosquito *Aedes albopictus*: recent trends and future scenarios," *Journal of the Royal Society Interface*, vol. 9, no. 75, pp. 2708–2717, 2012.

[19] ECDC, "Development of *Aedes albopictus* risk maps," European Centre for Disease Prevention and Control, Tech. Rep., 2009.

[20] D. Fischer, S. Thomas, M. Neteler, N. Tjaden, and C. Beierkuhnlein, "Climatic suitability of *Aedes albopictus* in europe referring to climate change projections: comparison of mechanistic and correlative niche modelling approaches," *Eurosurveillance*, vol. 19, no. 6, 2014.

[21] L. Tippelt, D. Werner, and H. Kampen, "Tolerance of three *Aedes albopictus* strains (diptera: Culicidae) from different geographical origins towards winter temperatures under field conditions in northern germany," *PloS one*, vol. 14, no. 7, 2019.

[22] M. Petrić, B. Lalić, E. Ducheyne, V. Djurdjević, and D. Petrić, "Modelling the regional impact of climate change on the suitability of the establishment of the asian tiger mosquito (*Aedes albopictus*) in serbia," *Climatic Change*, vol. 142, no. 3-4, pp. 361–374, 2017.

[23] L. Valdez, G. Sibona, and C. Condat, "Impact of rainfall on *Aedes aegypti* populations," *Ecological modelling*, vol. 385, pp. 96–105, 2018.

[24] C. Marsboom, D. Roiz, J. Charlier, V. De Waele, E. Ducheyne, F. Jourdain, L. Marama, G. Nicolas, I. Reulte, M. Petric, B. Roche, B. Sudre, V. Versteirt, and O. Briet, "A systematic literature review of mathematical models for *Aedes*-borne disease spread and control," 2019, unpublished.

[25] L. Eisen, A. J. Monaghan, S. Lozano-Fuentes, D. F. Steinhoff, M. H. Hayden, and P. E. Bieringer, "The impact of temperature on the bionomics of *Aedes* (stegomyia) *aegypti*, with special reference to the cool geographic range margins," *Journal of medical entomology*, vol. 51, no. 3, pp. 496–516, 2014.

[26] L. Eisen and C. G. Moore, "*Aedes* (stegomyia) *aegypti* in the continental united states: a vector at the cool margin of its geographic range," *Journal of medical entomology*, vol. 50, no. 3, pp. 467–478, 2013.

[27] E. Ducheyne, N. N. T. Minh, N. Haddad, W. Bryssinckx, E. Buliva, F. Simard, M. R. Malik, J. Charlier, V. De Waele, O. Mahmoud *et al.*, "Current and future distribution of *Aedes aegypti* and *Aedes albopictus* (diptera: Culicidae) in who eastern mediterranean region," *International journal of health geographics*, vol. 17, no. 1, p. 4, 2018.

[28] M. U. Kraemer, M. E. Sinka, K. A. Duda, A. Q. Mylne, F. M. Shearer, C. M. Barker, C. G. Moore, R. G. Carvalho, G. E. Coelho, W. Van Bortel *et al.*, "The global distribution of the arbovirus vectors *Aedes aegypti* and *Ae. albopictus*," *elife*, vol. 4, p. e08347, 2015.

[29] VDCI, "Mosquito Biology, Understanding the Life Cycle of the Mosquito," Vector Disease Control INternational, Tech. Rep., 2009.

[30] J. M. Reinhold, C. R. Lazzari, and C. Lahondère, "Effects of the environmental temperature on *Aedes aegypti* and *Aedes albopictus* mosquitoes: a review," *Insects*, vol. 9, no. 4, p. 158, 2018.

[31] M. Otto and R. O. Neumann, “Studien über gelbfieber in brasilien,” *Zeitschrift für Hygiene und Infektionskrankheiten*, vol. 51, no. 1, pp. 357–503, 1905.

[32] D. Lewis, “Observations on *Aedes aegypti*, l.(dipt. culic.) under controlled atmospheric conditions,” *Bulletin of Entomological Research*, vol. 24, no. 3, pp. 363–372, 1933.

[33] S. R. Christophers, *Aedes aegypti: The yellow fever mosquito.* CUP Archive, 1960.

[34] W. A. Rowley and C. L. Graham, “The effect of temperature and relative humidity on the flight performance of female *Aedes aegypti*,” *Journal of Insect Physiology*, vol. 14, no. 9, pp. 1251–1257, 1968.

[35] J. Couret, E. Dotson, and M. Q. Benedict, “Temperature, larval diet, and density effects on development rate and survival of *Aedes aegypti* (diptera: Culicidae),” *PLoS One*, vol. 9, no. 2, p. e87468, 2014.

[36] V. Loetti, N. Schweigmann, and N. Burroni, “Development rates, larval survivorship and wing length of *Culex pipiens* (diptera: Culicidae) at constant temperatures,” *Journal of Natural history*, vol. 45, no. 35-36, pp. 2203–2213, 2011.

[37] C. G. Spanoudis, S. S. Andreadis, N. K. Tsaknis, A. P. Petrou, C. D. Gkeka, and M. Savopoulou-Soultani, “Effect of temperature on biological parameters of the west nile virus vector *Culex pipiens* form ‘molestus’(diptera: Culicidae) in greece: Constant vs fluctuating temperatures,” *Journal of medical entomology*, vol. 56, no. 3, pp. 641–650, 2018.

[38] P. B. Ribeiro, P. R. Costa, A. E. Loeck, É. E. Vianna, and P. Silveira Júnior, “Thermal requeriments of *Culex quinquefasciatus* (diptera, culicidae) in pelotas, rio grande do sul, brazil,” *Iheringia. Série Zoologia*, vol. 94, no. 2, pp. 177–180, 2004.

[39] D. Madder, G. Surgeoner, and B. Helson, “Number of generations, egg production, and developmental time of *Culex pipiens* and *Culex restuans* (diptera: Culicidae) in southern ontario,” *Journal of medical entomology*, vol. 20, no. 3, pp. 275–287, 1983.

[40] B. Cazelles, M. Chavez, A. J. McMichael, and S. Hales, “Nonstationary influence of el nino on the synchronous dengue epidemics in thailand,” *PLOS medicine*, vol. 2, no. 4, p. e106, 2005.

[41] B. Cazelles, M. Chavez, D. Berteaux, F. Ménard, J. O. Vik, S. Jenouvrier, and N. C. Stenseth, “Wavelet analysis of ecological time series,” *Oecologia*, vol. 156, no. 2, pp. 287–304, 2008.

[42] T. A. Groen, G. L’ambert, R. Bellini, A. Chaskopoulou, D. Petric, M. Zgomba, L. Marrama, and D. J. Bicout, “Ecology of west nile virus across four european countries: empirical modelling of the *Culex pipiens* abundance dynamics as a function of weather,” *Parasites & vectors*, vol. 10, no. 1, p. 524, 2017.

[43] B. Cazelles, K. Cazelles, and M. Chavez, “Wavelet analysis in ecology and epidemiology: impact of statistical tests,” *Journal of the Royal Society Interface*, vol. 11, no. 91, p. 20130585, 2014.

[44] Y. Jian, S. Silvestri, J. Brown, R. Hickman, and M. Marani, “The temporal spectrum of adult mosquito population fluctuations: conceptual and modeling implications,” *PloS one*, vol. 9, no. 12, p. e114301, 2014.

[45] D. A. Cummings, R. A. Irizarry, N. E. Huang, T. P. Endy, A. Nisalak, K. Ungchusak, and D. S. Burke, “Travelling waves in the occurrence of dengue haemorrhagic fever in thailand,” *Nature*, vol. 427, no. 6972, p. 344, 2004.

[46] M. A. Johansson, D. A. Cummings, and G. E. Glass, “Multiyear climate variability and dengue—el nino southern oscillation, weather, and dengue incidence in puerto rico, mexico, and thailand: a longitudinal data analysis,” *PLoS medicine*, vol. 6, no. 11, p. e1000168, 2009.

[47] D. Roiz, M. Neteler, C. Castellani, D. Arnoldi, and A. Rizzoli, “Climatic factors driving invasion of the tiger mosquito (*Aedes albopictus*) into new areas of trentino, northern italy,” *PloS one*, vol. 6, no. 4, 2011.

[48] L. K. Koch, S. Cunze, A. Werblow, J. Kochmann, D. D. Dörge, H. Mehlhorn, and S. Klimpel, “Modeling the habitat suitability for the arbovirus vector *Aedes albopictus* (diptera: Culicidae) in germany,” *Parasitology research*, vol. 115, no. 3, pp. 957–964, 2016.

[49] A. Guisan and W. Thuiller, “Predicting species distribution: offering more than simple habitat models,” *Ecology letters*, vol. 8, no. 9, pp. 993–1009, 2005.

[50] D. Cianci, N. Hartemink, and A. Ibáñez-Justicia, “Modelling the potential spatial distribution of mosquito species using three different techniques,” *International journal of health geographics*, vol. 14, no. 1, p. 10, 2015.

[51] D. Fischer, P. Moeller, S. M. Thomas, T. J. Naucke, and C. Beierkuhnlein, “Combining climatic projections and dispersal ability: a method for estimating the responses of sandfly vector species to climate change,” *PLoS neglected tropical diseases*, vol. 5, no. 11, 2011.

[52] J. Ramírez Villegas and A. Bueno Cabrera, “Working with climate data and niche modeling: I. creation of bioclimatic variables,” 2009.

[53] L. Bagny, H. Delatte, N. Elissa, S. Quilici, and D. Fontenille, “*Aedes* (diptera: Culicidae) vectors of arboviruses in mayotte (indian ocean): distribution area and larval habitats,” *Journal of medical entomology*, vol. 46, no. 2, pp. 198–207, 2009.

[54] R. R. Simons, S. Croft, E. Rees, O. Tearne, M. E. Arnold, and N. Johnson, “Using species distribution models to predict potential hot-spots for rift valley fever establishment in the united kingdom,” *PloS one*, vol. 14, no. 12, 2019.

[55] G. Grenouillet, L. Buisson, N. Casajus, and S. Lek, “Ensemble modelling of species distribution: the effects of geographical and environmental ranges,” *Ecography*, vol. 34, no. 1, pp. 9–17, 2011.

[56] M. E. Sinka, N. Golding, N. C. Massey, A. Wiebe, Z. Huang, S. I. Hay, and C. L. Moyes, “Modelling the relative abundance of the primary african vectors of malaria before and after the implementation of indoor, insecticide-based vector control,” *Malaria journal*, vol. 15, no. 1, p. 142, 2016.

[57] J. M. Jeschke and D. L. Strayer, “Usefulness of bioclimatic models for studying climate change and invasive species,” *Annals of the New York Academy of Sciences*, vol. 1134, no. 1, pp. 1–24, 2008.

[58] J. J. Lawler, D. White, R. P. Neilson, and A. R. Blaustein, “Predicting climate-induced range shifts: model differences and model reliability,” *Global Change Biology*, vol. 12, no. 8, pp. 1568–1584, 2006.

[59] O. Broennimann, U. A. Treier, H. Müller-Schärer, W. Thuiller, A. Peterson, and A. Guisan, “Evidence of climatic niche shift during biological invasion,” *Ecology letters*, vol. 10, no. 8, pp. 701–709, 2007.

[60] P. Zeman and G. Lynen, “Evaluation of four modelling techniques to predict the potential distribution of ticks using indigenous cattle infestations as calibration data,” *Experimental & applied acarology*, vol. 39, no. 2, pp. 163–176, 2006.

[61] M. Petrić, B. Lalić, I. Pajović, S. Micev, V. Djurdjević, and D. Petrić, “Expected changes of montenegrin climate, impact on the establishment and spread of the asian tiger mosquito (*Aedes albopictus*), and validation of the model and model-based field sampling,” *Atmosphere*, vol. 9, no. 11, p. 453, 2018.

[62] H. Weiss, *A Mathematical Introduction to Population Dynamics.* IMPA, 2009.

[63] J. V. Wells and M. E. Richmond, “Populations, metapopulations, and species populations: what are they and who should care?” *Wildlife Society Bulletin (1973-2006)*, vol. 23, no. 3, pp. 458–462, 1995.

[64] C. Jawale, “Insect populations and population dynamics,” 2000.

[65] D. A. Focks, D. Haile, E. Daniels, and G. A. Mount, “Dynamic life table model for *Aedes aegypti* (diptera: Culicidae): analysis of the literature and model development,” *Journal of medical entomology*, vol. 30, no. 6, pp. 1003–1017, 1993.

[66] J. A. Ahumada, D. Laoointe, and M. D. Samuel, “Modeling the population dynamics of *Culex quinquefasciatus* (diptera: Culicidae), along an elevational gradient in hawaii,” *Journal of medical entomology*, vol. 41, no. 6, pp. 1157–1170, 2004.

[67] C. R. Williams, P. H. Johnson, S. A. Long, L. P. Rapley, and S. A. Ritchie, “Rapid estimation of *Aedes aegypti* population size using simulation modeling, with a novel approach to calibration and field validation,” *Journal of Medical Entomology*, vol. 45, no. 6, pp. 1173–1179, 2008.

[68] R. A. Erickson, S. M. Presley, L. J. Allen, K. R. Long, and S. B. Cox, "A stage-structured, *Aedes albopictus* population model," *Ecological Modelling*, vol. 221, no. 9, pp. 1273–1282, 2010.

[69] P. Cailly, A. Tran, T. Balenghien, G. L'Ambert, C. Toty, and P. Ezanno, "A climate-driven abundance model to assess mosquito control strategies," *Ecological Modelling*, vol. 221, no. 9, pp. 1273–1282, 2010.

[70] L. M. Beck-Johnson, W. A. Nelson, K. P. Paaijmans, A. F. Read, M. B. Thomas, and O. N. Bjørnstad, "The effect of temperature on *Anopheles* mosquito population dynamics and the potential for malaria transmission," *PLOS one*, vol. 8, no. 11, p. e79276, 2013.

[71] T. M. Lunde, D. Korecha, E. Loha, A. Sorteberg, and B. Lindtjørn, "A dynamic model of some malaria-transmitting anopheline mosquitoes of the afrotropical region. i. model description and sensitivity analysis," *Malaria journal*, vol. 12, no. 1, p. 28, 2013.

[72] A. Tran, G. L'Ambert, G. Lacour, R. Benoît, M. Demarchi, M. Cros, P. Cailly, M. Aubry-Kientz, T. Balenghien, and P. Ezanno, "A rainfall-and temperature-driven abundance model for *Aedes albopictus* populations," *International journal of environmental research and public health*, vol. 10, no. 5, pp. 1698–1719, 2013.

[73] P. Ezanno, M. Aubry-Kientz, S. Arnoux, P. Cailly, G. L'Ambert, C. Toty, T. Balenghien, and A. Tran, "A generic weather-driven model to predict mosquito population dynamics applied to species of *Anopheles, Culex* and *Aedes* genera of southern france," *Preventive veterinary medicine*, vol. 120, no. 1, pp. 39–50, 2015.

[74] G. Guzzetta, F. Montarsi, F. A. Baldacchino, M. Metz, G. Capelli, A. Rizzoli, A. Pugliese, R. Rosa, P. Poletti, and S. Merler, "Potential risk of dengue and chikungunya outbreaks in northern italy based on a population model of *Aedes albopictus* (diptera: Culicidae)," *PLoS neglected tropical diseases*, vol. 10, no. 6, p. e0004762, 2016.

[75] M. Otero, H. G. Solari, and N. Schweigmann, "A stochastic population dynamics model for *Aedes aegypti*: formulation and application to a city with temperate climate," *Bulletin of mathematical biology*, vol. 68, no. 8, pp. 1945–1974, 2006.

[76] A. S. Walsh, G. E. Glass, C. R. Lesser, and F. C. Curriero, "Predicting seasonal abundance of mosquitoes based on off-season meteorological conditions," *Environmental and Ecological Statistics*, vol. 15, no. 3, pp. 279–291, 2008.

[77] N. A. Honório, C. T. Codeço, F. d. C. Alves, M. d. A. Magalhães, and R. Lourenço-de Oliveira, "Temporal distribution of *Aedes aegypti* in different districts of rio de janeiro, brazil, measured by two types of traps," *Journal of medical entomology*, vol. 46, no. 5, pp. 1001–1014, 2009.

[78] T. A. Basuki, A. Cerone, R. Barbuti, A. Maggiolo-Schettini, P. Milazzo, and E. Rossi, "Modelling the dynamics of an *Aedes albopictus* population," *arXiv preprint arXiv:1008.3301*, 2010.

[79] H. L. Cleckner, T. R. Allen, and A. S. Bellows, "Remote sensing and modeling of mosquito abundance and habitats in coastal virginia, usa," *Remote Sensing*, vol. 3, no. 12, pp. 2663–2681, 2011.

[80] T.-W. Chuang, G. M. Henebry, J. S. Kimball, D. L. VanRoekel-Patton, M. B. Hildreth, and M. C. Wimberly, "Satellite microwave remote sensing for environmental modeling of mosquito population dynamics," *Remote sensing of environment*, vol. 125, pp. 147–156, 2012.

[81] G. Eastwood, S. J. Goodman, A. A. Cunningham, and L. D. Kramer, "*Aedes taeniorhynchus* vectorial capacity informs a pre-emptive assessment of west nile virus establishment in galapagos," *Scientific reports*, vol. 3, p. 1519, 2013.

[82] O. O. Oluwagbemi, C. M. Fornadel, E. F. Adebiyi, D. E. Norris, and J. L. Rasgon, "Anospex: a stochastic, spatially explicit model for studying *Anopheles* metapopulation dynamics," *PloS one*, vol. 8, no. 7, p. e68040, 2013.

[83] J. Patil and V. Mytri, "A prediction model for population dynamics of cotton pest (thrips tabaci linde) using multilayer-perceptron neural network," *International Journal of Computer Applications*, vol. 67, no. 4, 2013.

[84] T.-W. Chuang, E. L. Ionides, R. G. Knepper, W. W. Stanuszek, E. D. Walker, and M. L. Wilson, "Cross-correlation map analyses show weather variation influences on mosquito abundance patterns in saginaw county, michigan, 1989–2005," *Journal of medical entomology*, vol. 49, no. 4, pp. 851–858, 2012.

[85] R. M. Lana, T. G. Carneiro, N. A. Honório, and C. T. Codeço, "Seasonal and nonseasonal dynamics of *Aedes aegypti* in rio de janeiro, brazil: Fitting mathematical models to trap data," *Acta tropica*, vol. 129, pp. 25–32, 2014.

[86] M. Otero, H. G. Solari, and N. Schweigmann, "A stochastic population dynamics model for *Aedes aegypti*: formulation and application to a city with temperate climate," *Bulletin of mathematical biology*, vol. 68, no. 8, pp. 1945–1974, 2006.

[87] G. E. Box, "Robustness in the strategy of scientific model building," in *Robustness in statistics.* Elsevier, 1979, pp. 201–236.

[88] R. Daley, *Atmospheric data analysis.* Cambridge university press, 1993, no. 2.

[89] R. Levins, "The strategy of model building in population biology," *American scientist*, vol. 54, no. 4, pp. 421–431, 1966.

[90] R. Roelofs, "Measuring generalization and overfitting in machine learning," Ph.D. dissertation, UC Berkeley, 2019.

[91] S. Wenger and J. Olden, "Assessing transferability of ecological models: an underappreciated aspect of statistical validation, methods ecol. evol., 3, 260–267," 2012.

[92] H. Caswell, “The validation problem, systems analysis and simulation in ecology iv bc patten, 313–325,” 1976.

[93] B. P. Zeigler and T. I. Oren, “Theory of modelling and simulation,” *IEEE Transactions on Systems, Man, and Cybernetics*, vol. 9, no. 1, pp. 69–69, 1979.

[94] R. Stone, “Frolow on synoptic analysis of caribbean weather,” *Bulletin of the American Meteorological Society*, vol. 22, no. 5, pp. 198–200, 1941.

[95] C. A. de Beauville, “Air mass characteristics as related to tropical wave precipitation over lesser antilles archipelago,” *Atmospheric research*, vol. 36, no. 1-2, pp. 157–170, 1995.

[96] I. Gouirand, M. R. Jury, and B. Sing, “An analysis of low-and high-frequency summer climate variability around the caribbean antilles,” *Journal of Climate*, vol. 25, no. 11, pp. 3942–3952, 2012.

[97] M. R. Jury and I. Gouirand, “Decadal climate variability in the eastern caribbean,” *Journal of Geophysical Research: Atmospheres*, vol. 116, no. D21, 2011.

[98] D. W. Gamble and S. Curtis, “Caribbean precipitation: review, model and prospect,” *Progress in Physical Geography*, vol. 32, no. 3, pp. 265–276, 2008.

[99] I. Gouirand, M. R. Jury, and B. Sing, “An analysis of low-and high-frequency summer climate variability around the caribbean antilles,” *Journal of Climate*, vol. 25, no. 11, pp. 3942–3952, 2012.

[100] A. Anthony Chen and M. A. Taylor, “Investigating the link between early season caribbean rainfall and the el niño+ 1 year,” *International Journal of Climatology: A Journal of the Royal Meteorological Society*, vol. 22, no. 1, pp. 87–106, 2002.

[101] E. R. Martin and C. Schumacher, “Modulation of caribbean precipitation by the madden–julian oscillation,” *Journal of Climate*, vol. 24, no. 3, pp. 813–824, 2011.

[102] E. Britannica *et al.*, *Encyclopædia britannica.* Chicago: University of Chicago, 1993.

[103] M. Domroes and A. El-Tantawi, “Recent temporal and spatial temperature changes in egypt,” *International Journal of Climatology: A Journal of the Royal Meteorological Society*, vol. 25, no. 1, pp. 51–63, 2005.

[104] H. Hasanean, “Wintertime surface temperature in egypt in relation to the associated atmospheric circulation,” *International Journal of Climatology: A Journal of the Royal Meteorological Society*, vol. 24, no. 8, pp. 985–999, 2004.

[105] E. Elmallah and S. Elsharkawy, “Influence of circulation indices upon winter temperature variability in egypt,” *Journal of Atmospheric and Solar-Terrestrial Physics*, vol. 73, no. 4, pp. 439–448, 2011.

[106] M. Unkašević and I. Tošić, "Trends in temperature indices over serbia: relationships to large-scale circulation patterns," *International journal of climatology*, vol. 33, no. 15, pp. 3152–3161, 2013.

[107] B. Basarin, T. Lukić, D. Pavić, and R. L. Wilby, "Trends and multi-annual variability of water temperatures in the river danube, serbia," *Hydrological Processes*, vol. 30, no. 18, pp. 3315–3329, 2016.

[108] A. G. Barnston and R. E. Livezey, "Classification, seasonality and persistence of low-frequency atmospheric circulation patterns," *Monthly weather review*, vol. 115, no. 6, pp. 1083–1126, 1987.

[109] M. Ruml, E. Gregorić, M. Vujadinović, S. Radovanović, G. Matović, A. Vuković, V. Počuča, and D. Stojičić, "Observed changes of temperature extremes in serbia over the period 1961- 2010," *Atmospheric Research*, vol. 183, pp. 26–41, 2017.

[110] J. C. Rogers, "Patterns of low-frequency monthly sea level pressure variability (1899–1986) and associated wave cyclone frequencies," *Journal of Climate*, vol. 3, no. 12, pp. 1364–1379, 1990.

[111] J. W. Hurrell, "Decadal trends in the north atlantic oscillation: regional temperatures and precipitation," *Science*, vol. 269, no. 5224, pp. 676–679, 1995.

[112] D. Petrić, "Sezonska i dnevna aktivnost komaraca (diptera, culicidae) u vojvodini," *Disertation. University of Novi Sad, Novi Sad*, 1989.

[113] K. Lebl, K. Brugger, and F. Rubel, "Predicting *Culex pipiens/restuans* population dynamics by interval lagged weather data," *Parasites & vectors*, vol. 6, no. 1, p. 129, 2013.

[114] M. J. Klapwijk, J. A. Walter, A. Hirka, G. Csóka, C. Björkman, and A. M. Liebhold, "Transient synchrony among populations of five foliage-feeding lepidoptera," *Journal of Animal Ecology*, vol. 87, no. 4, pp. 1058–1068, 2018.

[115] Y. Kahramaner, G. Özdemir, I. G. Demiriz, and Z. Aslan, "Implementation of wavelets to detection of fish population," *İstanbul Aydın Üniversitesi Dergisi*, vol. 2, no. 7, pp. 52–65.

[116] J. Morlet, G. Arens, E. Fourgeau, and D. Glard, "Wave propagation and sampling theory—part i: Complex signal and scattering in multilayered media," *Geophysics*, vol. 47, no. 2, pp. 203–221, 1982.

[117] G. Kaiser, "A friendly guide to wavelets, birkhauser, boston," 1994.

[118] D. Gabor, "Theory of communication. part 1: The analysis of information," *Journal of the Institution of Electrical Engineers-Part III: Radio and Communication Engineering*, vol. 93, no. 26, pp. 429–441, 1946.

[119] C. Torrence and G. P. Compo, "A practical guide to wavelet analysis," *Bulletin of the American Meteorological society*, vol. 79, no. 1, pp. 61–78, 1998.

[120] P. C. Liu, “Wavelet spectrum analysis and ocean wind waves,” in *Wavelet Analysis and Its Applications.* Elsevier, 1994, vol. 4, pp. 151–166.

[121] I. Daubechies, “The wavelet transform, time-frequency localization and signal analysis,” *IEEE transactions on information theory*, vol. 36, no. 5, pp. 961–1005, 1990.

[122] K.-M. Lau and H. Weng, “Climate signal detection using wavelet transform: How to make a time series sing,” *Bulletin of the American meteorological society*, vol. 76, no. 12, pp. 2391–2402, 1995.

[123] D. Gu and S. Philander, “Secular changes of annual and interannual variability in the tropics during the past century,” *Journal of Climate*, vol. 8, no. 4, pp. 864–876, 1995.

[124] B. Wang, “Interdecadal changes in el nino onset in the last four decades,” *Journal of Climate*, vol. 8, no. 2, pp. 267–285, 1995.

[125] B. Wang and Y. Wang, “Temporal structure of the southern oscillation as revealed by waveform and wavelet analysis,” *Journal of Climate*, vol. 9, no. 7, pp. 1586–1598, 1996.

[126] N. Gamage and W. Blumen, “Comparative analysis of low-level cold fronts: Wavelet, fourier, and empirical orthogonal function decompositions,” *Monthly weather review*, vol. 121, no. 10, pp. 2867–2878, 1993.

[127] H. Weng and K. Lau, “Wavelets, period doubling, and time–frequency localization with application to organization of convection over the tropical western pacific,” *Journal of the atmospheric sciences*, vol. 51, no. 17, pp. 2523–2541, 1994.

[128] S. D. Meyers, B. G. Kelly, and J. J. O’Brien, “An introduction to wavelet analysis in oceanography and meteorology: With application to the dispersion of yanai waves,” *Monthly weather review*, vol. 121, no. 10, pp. 2858–2866, 1993.

[129] M. Farge, “Wavelet transforms and their applications to turbulence,” *Annual review of fluid mechanics*, vol. 24, no. 1, pp. 395–458, 1992.

[130] A. Roesch and H. Schmidbauer, *WaveletComp: Computational Wavelet Analysis*, 2018, r package version 1.1. [Online]. Available: https://CRAN.R-project.org/package=WaveletComp

[131] R. Carmona, W.-L. Hwang, and B. Torresani, *Practical Time-Frequency Analysis: Gabor and wavelet transforms, with an implementation in S.* Academic Press, 1998, vol. 9.

[132] R. J. Hyndman and G. Athanasopoulos, *Forecasting: principles and practice.* OTexts, 2018.

[133] C. Wang, Z. Song, F. Qiao, and S. Dong, “What signals are removed and retained by using an anomaly field in climatic research?” *International Journal of Oceanography*, vol. 2009, 2010.

[134] D. C. of the World. (2011) Inland water, free country level data. [Online]. Available: http://www.diva-gis.org/Data

[135] NASA. (2013) Version 4 dmsp-ols nighttime lights time series. [Online]. Available: https://ngdc.noaa.gov/eog/dmsp/downloadV4composites.html

[136] A. Chalom, P. I. d. K. de Prado *et al.*, "Parameter space exploration of ecological models," *arXiv preprint arXiv:1210.6278*, 2012.

[137] R. L. Iman, "L atin hypercube sampling," *Wiley StatsRef: Statistics Reference Online*, 2014.

[138] C. Genest and J.-F. Plante, "On blest's measure of rank correlation," *Canadian Journal of Statistics*, vol. 31, no. 1, pp. 35–52, 2003.

[139] C. Christiansen-Jucht, K. Erguler, C. Shek, M.-G. Basanez, and P. Parham, "Modelling *Anopheles gambiae* ss population dynamics with temperature-and age-dependent survival," *International journal of environmental research and public health*, vol. 12, no. 6, pp. 5975–6005, 2015.

[140] D. Focks, D. Haile, E. Daniels, and G. Mount, "Dynamic life table model for *Aedes aegypti* (diptera: Culicidae): simulation results and validation," *Journal of medical entomology*, vol. 30, no. 6, pp. 1018–1028, 1993.

[141] E. B. Vinogradova, "Experimental investigation of the ecological fac- tors causing diapause of the adults of blood-sucking mosquitoes (diptera, culicldae)," *Entomol. Obozr.*, vol. 39, pp. 327–340, 1960.

[142] A. Clements, "The biology of mosquitoes volume 1: Development," *Nutrition and Reproduction*, pp. 231–234, 2000.

[143] N. Becker, D. Petrić, C. Boase, J. Lane, M. Zgomba, C. Dahl, and A. Kaiser, *Mosquitoes and their control.* Springer, 2010, vol. 2.

[144] C. Roumieux, "Modélisation de la dynamique saisonnière des éclosions d'*Aedes* (ochlerotatus) caspius (pallas, 1771)(culicidae) dans un contexte de changement climatique," Ph.D. dissertation, Aix-Marseille, 2012.

[145] H. Padmanabha, D. Durham, F. Correa, M. Diuk-Wasser, and A. Galvani, "The interactive roles of *Aedes aegypti* super-production and human density in dengue transmission," *PLoS neglected tropical diseases*, vol. 6, no. 8, p. e1799, 2012.

[146] M. Otero, N. Schweigmann, and H. G. Solari, "A stochastic spatial dynamical model for *Aedes aegypti*," *Bulletin of mathematical biology*, vol. 70, no. 5, p. 1297, 2008.

[147] T. J. Hladish, C. A. Pearson, D. L. Chao, D. P. Rojas, G. L. Recchia, H. Gómez-Dantés, M. E. Halloran, J. R. Pulliam, and I. M. Longini, "Projected impact of dengue vaccination in yucatán, mexico," *PLoS neglected tropical diseases*, vol. 10, no. 5, p. e0004661, 2016.

[148] H. Salje, J. Lessler, T. P. Endy, F. C. Curriero, R. V. Gibbons, A. Nisalak, S. Nimmannitya, S. Kalayanarooj, R. G. Jarman, S. J. Thomas *et al.*, "Revealing the microscale spatial signature of dengue transmission and immunity in an urban population," *Proceedings of the National Academy of Sciences*, vol. 109, no. 24, pp. 9535–9538, 2012.

[149] K. Richardson, A. A. Hoffmann, P. Johnson, S. Ritchie, and M. R. Kearney, "Thermal sensitivity of *Aedes aegypti* from australia: empirical data and prediction of effects on distribution," *Journal of medical entomology*, vol. 48, no. 4, pp. 914–923, 2011.

[150] K. Magori, M. Legros, M. E. Puente, D. A. Focks, T. W. Scott, A. L. Lloyd, and F. Gould, "Skeeter buster: a stochastic, spatially explicit modeling tool for studying *Aedes aegypti* population replacement and population suppression strategies," *PLoS neglected tropical diseases*, vol. 3, no. 9, p. e508, 2009.

[151] I. T. Jolliffe and D. B. Stephenson, *Forecast verification: a practitioners guide in atmospheric science.* John Wiley & Sons, 2012.

[152] H. Caswell, "Iso 1995 guide to the expression of uncertainty in measurement," 1995.

[153] R. B. D'Agostino, "An omnibus test of normality for moderate and large size samples," *Biometrika*, vol. 58, no. 2, pp. 341–348, 1971.

[154] R. D'Agostino and E. S. Pearson, "Tests for departure from normality. empirical results for the distributions," *Biometrika*, vol. 60, no. 3, pp. 613–622, 1973.

[155] F. Pavlovčič, J. Nastran, and D. Nedeljković, "Determining the 95% confidence interval of arbitrary non-gaussian probability distributions," 2009.

[156] A. H. Murphy, "The value of climatological, categorical and probabilistic forecasts in the cost-loss ratio situation," *Monthly Weather Review*, vol. 105, no. 7, pp. 803–816, 1977.

[157] M. W. Kiarie-Makara, P. M. Ngumbi, and D.-K. Lee, "Effects of temperature on the growth and development of *Culex pipiens* complex mosquitoes (diptera: Culicidae)," *Journal of Pharmacy and Biological Sciences*, vol. 10, pp. 1–10, 2015.

[158] A. N. Clements, *The physiology of mosquitoes: International series of monographs on pure and applied biology: Zoology.* Elsevier, 2013, vol. 17.

[159] W. H. Organisation. (2019) Dengue and severe dengue, key facts. [Online]. Available: https://www.who.int/news-room/fact-sheets/detail/dengue-and-severe-dengue

[160] D. Fischer, S. Thomas, M. Neteler, N. Tjaden, and C. Beierkuhnlein, "Climatic suitability of *Aedes albopictus* in europe referring to climate change projections: comparison of mechanistic and correlative niche modelling approaches," *Eurosurveillance*, 2014.

[161] W. H. Organisation. (2017) West nile virus, key facts. [Online]. Available: https://www.who.int/news-room/fact-sheets/detail/west-nile-virus

[162] E. C. for Disease Prevention and Control. (2018) Epidemiological update: West nile fever in europe - number of infections so far exceeds the total number in the previous five years. [Online]. Available: https://www.ecdc.europa.eu/en/news-events/epidemiological-update-west-nile-fever-europe-number-infections-so-far-exceeds-total

[163] M. L'Azou, A.-F. Taurel, C. Flamand, and P. Quenel, "Recent epidemiological trends of dengue in the french territories of the americas (2000–2012): a systematic literature review," *PLoS neglected tropical diseases*, vol. 8, no. 11, p. e3235, 2014.

[164] P. A. H. Organization, "Zika-epidemiological report, guadeloupe," 2016.

[165] B. J, R. A, G. B, A. G, and H. JP. (2011) Les culicidae d'afrique méditerranéenne, *Culex pipiens.* [Online]. Available: http://bioinfo-web.mpl.ird.fr/identiciels/culmed/html/index.html

[166] A. Ponlawat and L. C. Harrington, "Blood feeding patterns of *Aedes aegypti* and *Aedes albopictus* in thailand," *Journal of medical entomology*, vol. 42, no. 5, pp. 844–849, 2005.

[167] J. B. Zahouli, J. Utzinger, M. A. Adja, P. Müller, D. Malone, Y. Tano, and B. G. Koudou, "Oviposition ecology and species composition of *Aedes* spp. and *Aedes aegypti* dynamics in variously urbanized settings in arbovirus foci in southeastern côte d'ivoire," *Parasites & vectors*, vol. 9, no. 1, p. 523, 2016.

[168] E. J. Kweka, V. Baraka, L. Mathias, B. Mwang'onde, G. Baraka, L. Lyaruu, and A. M. Mahande, "Ecology of *Aedes* mosquitoes, the major vectors of arboviruses in human population," in *Dengue Fever-A resilient threat in the face of innovation.* IntechOpen, 2018.

[169] L. Hatvani, "Aleksandr lyapunov, the man who created the modern theory of stability," *Electronic Journal of Qualitative Theory of Differential Equations*, vol. 2019, no. 26, pp. 1–9, 2019.

[170] V. I. Arnol'd, "Loss of stability of self-oscillations close to resonance and versal deformations of equivariant vector fields," *Functional Analysis and its Applications*, vol. 11, no. 2, pp. 85–92, 1977.

[171] V. Arnold and Y. S. Ilyashenko, "Dynamical systems i, ordinary differential equations," *Encyclopaedia Math. Sci*, vol. 1, 1988.

[172] V. I. Arnold, V. Afrajmovich, Y. S. Il'yashenko, and L. Shil'nikov, *Dynamical systems V: bifurcation theory and catastrophe theory.* Springer Science & Business Media, 2013, vol. 5.

[173] A. A. Andronov, *Qualitative theory of second-order dynamic systems.* Halsted Press, 1973, vol. 22054.

[174] A. A. Andronov, *Theory of bifurcations of dynamic systems on a plane.* Israel Program for Scientific Translations, 1971, vol. 554.

[175] A. A. Andronov, A. A. Vitt, and S. E. Khaikin, *Theory of Oscillators: Adiwes International Series in Physics.* Elsevier, 2013, vol. 4.

[176] R. Rosà, G. Marini, L. Bolzoni, M. Neteler, M. Metz, L. Delucchi, E. A. Chadwick, L. Balbo, A. Mosca, M. Giacobini *et al.*, "Early warning of west nile virus mosquito vector: climate and land use models successfully explain phenology and abundance of *Culex pipiens* mosquitoes in north-western italy," *Parasites & vectors*, vol. 7, no. 1, p. 269, 2014.

[177] M. Carrieri, P. Fariselli, B. Maccagnani, P. Angelini, M. Calzolari, and R. Bellini, "Weather factors influencing the population dynamics of *Culex pipiens* (diptera: Culicidae) in the po plain valley, italy (1997-2011)," *Environmental entomology*, vol. 43, no. 2, pp. 482–490, 2014.

[178] A. M. Tompkins and V. Ermert, "A regional-scale, high resolution dynamical malaria model that accounts for population density, climate and surface hydrology," *Malaria journal*, vol. 12, no. 1, p. 65, 2013.

[179] G. J. Abiodun, R. Maharaj, P. Witbooi, and K. O. Okosun, "Modelling the influence of temperature and rainfall on the population dynamics of *Anopheles arabiensis*," *Malaria journal*, vol. 15, no. 1, p. 364, 2016.

[180] A. Bomblies, J.-B. Duchemin, and E. A. Eltahir, "Hydrology of malaria: Model development and application to a sahelian village," *Water Resources Research*, vol. 44, no. 12, 2008.

[181] J. Shaman, M. Spiegelman, M. Cane, and M. Stieglitz, "A hydrologically driven model of swamp water mosquito population dynamics," *ecological modelling*, vol. 194, no. 4, pp. 395–404, 2006.

[182] N. Endo *et al.*, "Simulation of hydrology and population dynamics of *Anopheles* mosquitoes around the koka reservoir in ethiopia," Ph.D. dissertation, Massachusetts Institute of Technology, 2014.

[183] T. Porphyre, D. Bicout, and P. Sabatier, "Modelling the abundance of mosquito vectors versus flooding dynamics," *Ecological modelling*, vol. 183, no. 2-3, pp. 173–181, 2005.

[184] L. Rueda, K. Patel, R. Axtell, and R. Stinner, "Temperature-dependent development and survival rates of *Culex quinquefasciatus* and *Aedes aegypti* (diptera: Culicidae)," *Journal of medical entomology*, vol. 27, no. 5, pp. 892–898, 1990.

[185] T. Oda, K. Uchida, A. Mori, M. Mine, Y. Eshita, K. Kurokawa, K. Kato, and H. Tahara, "Effects of high temperature on the emergence and survival of adult *Culex pipiens* molestus and *Culex quinquefasciatus* in japan," *Journal of the American Mosquito Control Association-Mosquito News*, vol. 15, no. 2, pp. 153–156, 1999.

[186] J. Noilhan and J.-F. Mahfouf, "The isba land surface parameterisation scheme," *Global and planetary Change*, vol. 13, no. 1-4, pp. 145–159, 1996.

[187] P. Le Moigne, A. Boone, J. Calvet, B. Decharme, S. Faroux, A. Gibelin, C. Lebeaupin, J. Mahfouf, E. Martin, V. Masson *et al.*, “Surfex scientific documentation,” *Note de centre (CNRM/GMME), Météo-France, Toulouse, France*, 2009.

[188] S. Faroux, A. Kaptué Tchuenté, J.-L. Roujean, V. Masson, E. Martin, and P. L. Moigne, “Ecoclimap-ii/europe: A twofold database of ecosystems and surface parameters at 1 km resolution based on satellite information for use in land surface, meteorological and climate models,” *Geoscientific Model Development*, vol. 6, no. 2, pp. 563–582, 2013.

[189] V. Masson, P. Le Moigne, E. Martin, S. Faroux, A. Alias, R. Alkama, S. Belamari, A. Barbu, A. Boone, F. Bouyssel *et al.*, “The surfexv7. 2 land and ocean surface platform for coupled or offline simulation of earth surface variables and fluxes,” 2013.

[190] A. K. Blackadar, “Modelng the nocturnal boundary layer,” in *Preprints, Third Symp. on Atmospheric Turbulence, Diffusion, and Air Quality, Raleigh.* Amer. Meteor. Soc., 1976.

[191] C. M. Bhumralkar, “Numerical experiments on the computation of ground surface temperature in an atmospheric general circulation model,” *Journal of Applied Meteorology*, vol. 14, no. 7, pp. 1246–1258, 1975.

[192] J. Noilhan and S. Planton, “A simple parameterization of land surface processes for meteorological models,” *Monthly weather review*, vol. 117, no. 3, pp. 536–549, 1989.

[193] A. Boone, “Modelisation des processus hydrologiques dans le schema de surface isba: Inclusion d’un reservoir hydrologique, du gel et modelisation de la neige,” *These de doctorat, Université Paul Sabatier (Toulouse III)*, 2000.

[194] A. Boone, V. Masson, T. Meyers, and J. Noilhan, “The influence of the inclusion of soil freezing on simulations by a soil–vegetation–atmosphere transfer scheme,” *Journal of Applied Meteorology*, vol. 39, no. 9, pp. 1544–1569, 2000.

[195] F. Habets, J. Noilhan, C. Golaz, J. Goutorbe, P. Lacarrere, E. Leblois, E. Ledoux, E. Martin, C. Ottlé, and D. Vidal-Madjar, “The isba surface scheme in a macroscale hydrological model applied to the hapex-mobilhy area: Part i: Model and database,” *Journal of Hydrology*, vol. 217, no. 1-2, pp. 75–96, 1999.

[196] F. Habets, J. Noilhan, C. Golaz, J. Goutorbe, P. Lacarrere, E. Leblois, E. Ledoux, E. Martin, C. Ottlé, and D. Vidal-Madjar, “The isba surface scheme in a macroscale hydrological model applied to the hapex-mobilhy area: Part ii: Simulation of streamflows and annual water budget,” *Journal of Hydrology*, vol. 217, no. 1-2, pp. 97–118, 1999.

[197] F. Habets and G.-M. Saulnier, “Subgrid runoff parameterization,” *Physics and Chemistry of the Earth, Part B: Hydrology, Oceans and Atmosphere*, vol. 26, no. 5-6, pp. 455–459, 2001.

[198] L. Busetto and L. Ranghetti, "Modistsp: an r package for preprocessing of modis land products time series," *Computers and Geosciences*, vol. 97, pp. 40–48, 2016. [Online]. Available: https://github.com/ropensci/MODIStsp

[199] H. Hersbach, "The era5 atmospheric reanalysis." in *AGU Fall Meeting Abstracts*, 2016.

[200] P. W. White, *IFS documentation: Part III: Dynamics and numerical procedures (CY21r4).* European Centre for Medium-Range Weather Forecasts, 2000.

[201] J.-M. O. Depinay, C. M. Mbogo, G. Killeen, B. Knols, J. Beier, J. Carlson, J. Dushoff, P. Billingsley, H. Mwambi, J. Githure *et al.*, "A simulation model of african *Anopheles* ecology and population dynamics for the analysis of malaria transmission," *Malaria journal*, vol. 3, no. 1, p. 29, 2004.

[202] M. Jelić, J. Milivojević, S. Trifunović, I. G. Djalović, D. S. Milošev, and S. I. Šeremešić, "Distribution and forms of iron in the vertisols of serbia," *J. Serb. Chem. Soc*, vol. 76, no. 5, pp. 781–794, 2011.

[203] A. T. K. Tchuenté, J.-L. Roujean, and S. M. De Jong, "Comparison and relative quality assessment of the glc2000, globcover, modis and ecoclimap land cover data sets at the african continental scale," *International Journal of Applied Earth Observation and Geoinformation*, vol. 13, no. 2, pp. 207–219, 2011.

[204] A. Di Gregorio, *Land cover classification system: classification concepts and user manual: LCCS.* Food & Agriculture Org., 2005, vol. 2.

[205] A. Delcloo, R. Hamdi, A. Deckmyn, H. De Backer, G. Forêt, P. Termonia, and H. Van Langenhove, "A one year evaluation of the ctm chimere using surfex/teb within the high resolution nwp models alaro and aladin for belgium," in *Air Pollution Modeling and its Application XXIII.* Springer, 2014, pp. 495–498.

[206] R. Hamdi, D. Degrauwe, A. Duerinckx, J. Cedilnik, V. Costa, T. Dalkilic, K. Essaouini, M. Jerczynki, F. Kocaman, L. Kullmann *et al.*, "Evaluating the performance of surfexv5 as a new land surface scheme for the aladincy36 and alaro-0 models," *Geoscientific Model Development*, vol. 7, no. 1, pp. 23–39, 2014.

[207] A. Duerinckx, "The potential of an extended kalman filter for soil analysis in conjunction with a 3d-var system in a limited area nwp model," Ph.D. dissertation, Ghent University, 2015.

[208] T. K. Yamana, "Mechanistic modelling of the links between environment, mosquitoes and malaria transmission in the current and future climates of west africa," Ph.D. dissertation, Massachusetts Institute of Technology, 2015.

[209] T. K. Yamana and E. A. Eltahir, "Incorporating the effects of humidity in a mechanistic model of *Anopheles gambiae* mosquito population dynamics in the sahel region of africa," *Parasites & vectors*, vol. 6, no. 1, p. 235, 2013.

[210] L. B. Carrington, S. N. Seifert, N. H. Willits, L. Lambrechts, and T. W. Scott, "Large diurnal temperature fluctuations negatively influence *Aedes aegypti* (diptera: Culicidae) life-history traits," *Journal of medical entomology*, vol. 50, no. 1, pp. 43–51, 2013.

[211] L. Lambrechts, K. P. Paaijmans, T. Fansiri, L. B. Carrington, L. D. Kramer, M. B. Thomas, and T. W. Scott, "Impact of daily temperature fluctuations on dengue virus transmission by *Aedes aegypti*," *Proceedings of the National Academy of Sciences*, vol. 108, no. 18, pp. 7460–7465, 2011.

[212] W. K. Reisen, "Effect of temperature on *Culex tarsalis* (diptera: Culicidae) from the coachella and san joaquin valleys of california," *Journal of medical entomology*, vol. 32, no. 5, pp. 636–645, 1995.

[213] R. S. Defries, L. Bounoua, and G. J. Collatz, "Human modification of the landscape and surface climate in the next fifty years," *Global Change Biology*, vol. 8, no. 5, pp. 438–458, 2002.

[214] M. Lompar, B. Lalić, L. Dekić, and M. Petrić, "Filling gaps in hourly air temperature data using debiased era5 data," *Atmosphere*, vol. 10, no. 1, p. 13, 2019.

[215] D. Petri, "Seasonal and daily activity of mosquitoes (diptera: Culicidae) in vojvodina," Ph.D. dissertation, 1989.

[216] A. Ponlawat, P. Khongtak, B. Jaichapor, A. Pongsiri, and B. P. Evans, "Field evaluation of two commercial mosquito traps baited with different attractants and colored lights for malaria vector surveillance in thailand," *Parasites & vectors*, vol. 10, no. 1, p. 378, 2017.

Appendix A

Appendices

A.1 APPENDIX A - Additional published work

A.1.1 Wireless Sensor Networks in IPM

Status: Book Chapter, submitted

Petrić M, Marsboom C, Vandendriessche J. Chapter: *Wireless Sensor Network in IPM*, Book: *Social, Legal, and Ethical Implications of IoT, Cloud, and Edge Computing Technologies.* IGI-Global. 2020. Cornetta J. Pennsylvania, USA.

Abstract: Wireless Sensor Network technology is already widely used in a plethora of scientific and commercial applications, and this number will only increase with the expected rise of the IoT market. An emerging field for environmental WSN systems is entomological vector surveillance. Sensor technology can be used to shoulder ecologically friendly practices within the Integrated Pest Management (IPM) approach. Proper surveillance and subsequent modelling of the impact that pest and disease have on human health and crop agriculture is a pressing issue in numerous segments. Over 500 million people are infected by Vector Borne Disease (VBD) every year. WHO estimate that , annually, over 3 billion people are at risk of contracting a VBD, of which a large proportion is diseases transmitted by mosquito vectors. More than 2.5 billion people are at risk of contracting Dengue alone, and Malaria causes 600,000 deaths every year globally.

Numerical models are being developed to generate information regarding the population dynamics of vector species and the expected circulation of Vector Borne Disease (VBD). These models require detailed micrometeorological forcing representative of the vector habitat to generate accurate simulations. IPM translates expert knowledge of pest biology and ecology into a tailored control strategy to reduce local vector populations to the lowest level possible. Earth Observation (EO) data can be coupled to the WSN system and used to compliment the collected sensor data. It can be used to determine micro-climatic zones in a region, by providing additional data which the WSN cannot collect such as information on a regional or continental scale and long-term historic data. Autonomous networks of connected sensors together with EO data can provide near-real time input for numerical models used to forecast pest populations, thus supporting efficient Integrated Pest Management in scenarios where continuous human surveillance is not possible. Lack of field measurements, collected over long periods and at biologically significant spatial granularity, hinders scientific understanding of how small-scale environmental factors drive pest population dynamics. Data offload in remote areas with flexible channels of communication for complex and heterogeneous topographies is an important component in this type of application. WSNs utilized in combination with satellite communication can provide reliable, in-situ, high precision monitoring of high frequency processes.

As a contemporary technology, WSNs integrate the capabilities of sensors, digital network transmission, automation control and information storage and processing. To be of scientific value for IPM, the sensor and network design should be driven by the following requirements: (i) Measurement fidelity; (ii) Sampling frequency; (iii) Accuracy, precision and range; (iv) An energy harvesting solution for autonomous field operations; and (v) Robustness in terms of harsh environmental conditions. Before the sensor output can be incorporated into mathematical models as well as used for comparison with other sources data cleaning and aggregation algorithms have to be developed. Bias and error in sensor measurements should be analysed and a sensor readings adjustment routine applied if necessary. The most important part of quality assurance is critical quality control. Quality control (QC) should be automated and carried out in nearreal time to ensure measurement fidelity and reduce the time needed for problem mitigation. In this chapter we will provide an overview of the scope and best-practice approaches in applying WSN technology to drive IPM models.

A.1.2 Assessment of climate change impact on the malaria vector *Anopheles hyrcanus*, West Nile disease, and incidence of melanoma in the Vojvodina Province (Serbia) using data from a regional climate model

Status: Published.

Mihailović DT, Petrić D, Petrović T, Hrnjaković-Cvjetković I, Djurdjevic V, Nikolić-Djorić E, Arsenić I, Petrić M, Mimić G, Ignjatović-Ćupina A. *Assessment of climate change impact on the malaria vector Anopheles hyrcanus, West Nile disease, and incidence of melanoma in the Vojvodina Province (Serbia) using data from a regional climate model.* PLoS One. 2020 Jan 15;15(1):e0227679.

Abstract: Motivated by the One Health paradigm, we found the expected changes in temperature and UV radiation (UVR) to be a common trigger for enhancing the risk that viruses, vectors, and diseases pose to human and animal health. We compared data from the mosquito field collections and medical studies with regional climate model projections to examine the impact of climate change on the spreading of one malaria vector, the circulation of West Nile virus (WNV), and the incidence of melanoma. We analysed data obtained from ten selected years of standardised mosquito vector sampling with 219 unique location-year combinations, and 10 years of melanoma incidence. Trends in

the observed data were compared to the climatic variables obtained by the coupled regional Eta Belgrade University and Princeton Ocean Model for the period 1961–2015 using the A1B scenario, and the expected changes up to 2030 were presented. Spreading and relative abundance of *Anopheles hyrcanus* was positively correlated with the trend of the mean annual temperature. We anticipated a nearly twofold increase in the number of invaded sites up to 2030. The frequency of WNV detections in *Culex pipiens* was significantly correlated to overwintering temperature averages and seasonal relative humidity at the sampling sites. Regression model projects a twofold increase in the incidence of WNV positive *Cx. pipiens* for a rise of 0.5°C in overwintering TOctober–April temperatures. The projected increase of 56% in the number of days with Tmax $\geq$ C (Hot Days—HD) and UVR doses (up to 1.2%) corresponds to an increasing trend in melanoma incidence. Simulations of the Pannonian countries climate anticipate warmer and drier conditions with possible dominance of temperature and number of HD.

A.1.3 Autonomous Wireless Sensor Networks in an IPM Spatial Decision Support System

Status: Published.

Petrić M, Vandendriessche J, Marsboom C, Matheussen T, Ducheyne E, Touhafi A. *Autonomous wireless sensor networks in an ipm spatial decision support system.* Computers. 2019 Jun;8(2):43.

Abstract: Until recently data acquisition in integrated pest management (IPM) relied on manual collection of both pest and environmental data. Autonomous wireless sensor networks (WSN) are providing a way forward by reducing the need for manual offload and maintenance; however, there is still a significant gap in pest management using WSN with most applications failing to provide a low-cost, autonomous monitoring system that can operate in remote areas. In this study, we investigate the feasibility of implementing a reliable, fully independent, low-power WSN that will provide high-resolution, near-real-time input to a spatial decision support system (SDSS), capturing the small-scale heterogeneity needed for intelligent IPM. The WSN hosts a dual-uplink taking advantage of both satellite and terrestrial communication. A set of tests were conducted to assess metrics such as signal strength, data transmission and bandwidth of the SatCom module as well as mesh configuration, energetic autonomy, point to point communication and data loss of the WSN nodes. Finally, we demonstrate the SDSS output from two vector models forced by WSN data from a field site in Belgium. We believe that this system can be a cost-effective solution for intelligent IPM in remote areas where there is no reliable terrestrial connection.

A.1.4 Expected Changes of Montenegrin Climate, Impact on the Establishment and Spread of the Asian Tiger Mosquito (*Aedes albopictus*), and Validation of the Model and Model-Based Field Sampling

Status: Published.

Petrić M, Lalić B, Pajović I, Micev S, Djurdjević V, Petrić D. E*xpected changes of Montenegrin climate, impact on the establishment and spread of the Asian tiger mosquito (Aedes albopictus), and validation of the model and model-based field sampling.* Atmosphere. 2018 Nov;9(11):453.

Abstract: *Aedes albopictus* has become established in many parts of Europe since its introduction at the end of the 20th century. It can vector a range of arboviruses, of which Chikungunya and Dengue are most significant for Europe. An analysis of the expected climate change and the related shift in Köppen zones for Montenegro and impact on the establishment of *Ae. albopictus* was conducted. Outputs of a mechanistic *Aedes albopictus* model were validated by 2245 presence/absence records collected from 237 different sites between 2001 and 2014. Finally, model-based sampling was designed and performed at 48 sites in 2015, in a previously unexplored northern part of Montenegro, and results were validated. The Eta Belgrade University (EBU)-Princeton Ocean Model (POM) regional climate model was used with the A2 emissions scenario for the 2001–2030 and 2071–2100 integration periods. The results point to a significant increase in suitability for the mosquito and a vertical shift to higher altitudes by the end of the century. The model showed excellent results with the area under the receiver operating characteristic curve (AUC) of 0.94. This study provides a tool for prioritizing surveillance efforts (model-based surveillance), especially when resources are limited. This is the first published analysis of Climate Change that incorporates observations from the national synoptic grid and the subsequent impact on *Ae. albopictus* in Montenegro.

A.1.5 Filling Gaps in Hourly Air Temperature Data Using Debiased ERA5 Data

Status: Published.

Lompar M, Lalić B, Dekić L, Petrić M. *Filling gaps in hourly air temperature data using debiased ERA5 data.* Atmosphere. 2019 Jan;10(1):13.

Abstract: Missing data in hourly and daily temperature data series is a common problem in long-term data series and many observational networks. Agricultural and environmental models and climate-related tools can be used only if weather data series are complete. To support user communities, a technique for gap filling is developed based on the debiasing of ERA5 reanalysis data, the fifth generation of the European Centre for Medium-RangeWeather Forecasts (ECMWF) atmospheric reanalyses of the global climate. The debiasing procedure includes in situ measured temperature. The methodology is tested for different landscapes, latitudes, and altitudes, including tropical and midlatitudes. An evaluation of results in terms of root mean square error (RMSE) obtained using hourly and daily data is provided. The study shows very low average RMSE for all gap lengths ranging from 1.1 C (Montecristo, Italy) to 1.9 C (Gumpenstein, Austria).

A.1.6 Modelling the regional impact of climate change on the suitability of the establishment of the Asian tiger mosquito (*Aedes albopictus*) in Serbia

Status: Published.

Petrić M, Lalić B, Ducheyne E, Djurdjević V, Petrić D. *Modelling the regional impact of climate change on the suitability of the establishment of the Asian tiger mosquito (Aedes albopictus) in Serbia.* Climatic Change. 2017 Jun 1;142(3-4):361-74.

Abstract: The Asian tiger mosquito, *Aedes albopictus*, is one of the world's most dangerous invasive species. It has vector competence for a wide range of arboviruses such as chikungunya, dengue, Zika and Rift Valley fever viruses. The vector originated in Asia but has recently spread to the temperate regions of Europe and North America. Further spread to the north and the east and a shift to higher altitudes could be expected as a result of climate change. This makes modelling the regional climatic suitability for the establishment of *A. albopictus* in naïve regions a pressing issue. The future suitability and subsequent seasonal activity of the vector were investigated using three mechanistic models, with climatic data from the Eta Belgrade University-Princeton Ocean Model regional climate model. The results showed that after a slight decrease in suitability for the first part of the century, most of Serbia would become significantly more suitable for the establishment of *A. albopictus.* This is due to the simulated rise in seasonal and annual temperatures by the end of the twenty-first century. This study allows for the incorporation of regional heterogeneity in vector modelling. The spatial resolution of the maps obtained from a regional analysis is much higher than that acquired by a global model, allowing for detailed risk assessment and planning of surveillance focused on the habitats where the main introduction routes and climatic suitability are coupled. This work should be applied to all countries in the region with the risk of introduction or further spread of *A. albopictus.*

A.1.7 West Nile virus 'circulation' in Vojvodina, Serbia: mosquito, bird, horse and human surveillance

Status: Published.

Petrić D, Petrović T, Cvjetković IH, Zgomba M, Milošević V, Lazić G, Ćupina AI, Lupulović D, Lazić S, Dondur D, Vaselek S. *West Nile virus 'circulation'in Vojvodina, Serbia: Mosquito, bird, horse and human surveillance.*

Molecular and cellular probes. 2017 Feb 1;31:28-36.

Abstract: Efforts to detect West Nile virus (WNV) in the Vojvodina province, northern Serbia, commenced with human and mosquito surveillance in 2005, followed by horse (2009) and wild bird (2012) surveillance. The knowledge obtained regarding WNV circulation, combined with the need for timely detection of virus activity and risk assessment resulted in the implementation of a national surveillance programme integrating mosquito, horse and bird surveillance in 2014. From 2013, the system showed highly satisfactory results in terms of area specificity (the capacity to indicate the spatial distribution of the risk for human cases of West Nile neuroinvasive disease - WNND) and sensitivity to detect virus circulation even at the enzootic level. A small number (n = 50) of *Culex pipiens* (*pipiens* and *molestus* biotypes, and their hybrids) females analysed per trap/night, combined with a high number of specimens in the sample, provided variable results in the early detection capacity at different administrative levels (NUTS2 versus NUTS3). The clustering of infected mosquitoes, horses, birds and human cases of WNND in 2014-2015 was highly significant, following the south-west to north-east direction in Vojvodina (NUTS2 administrative level). Human WNND cases grouped closest with infected mosquitoes in 2014, and with wild birds/mosquitoes in 2015. In 2014, sentinel horses showed better spatial correspondence with human WNND cases than sentinel chickens. Strong correlations were observed between the vector index values and the incidence of human WNND cases recorded at the NUTS2 and NUTS3 levels. From 2010, West Nile virus was detected in mosquitoes sampled at 43 different trap stations across Vojvodina. At 14 stations (32.56%), WNV was detected in two different (consecutive or alternate) years, at 2 stations in 3 different years, and in 1 station during 5 different years. Based on these results, integrated surveillance will be progressively improved to allow evidence-based adoption of preventive public health and mosquito control measures.

A.1.8 Model-based design and analysis of life table experiments for insect vectors

Status: Submitted to bioRxiv.

Erguler K, Demirok MC, Gunay F, Petric M, Kavran M, Dušan P, Alten BS *Model-based design and analysis of life table experiments for insect vectors.* bioRxiv 2020

Life tables can help identify physiological differences in distinct development stages and detect potential vulnerabilities for conservation and control. However, cataloguing mortality, development, and fecundity by following each individual could be challenging in insects due to interweaving generations and development stages. Here, we propose to use age- and stage- structured population dynamics modelling to help derive life table characteristics from the observed dynamics of reared populations. We examine a hypothetical case, a simulated population with known life parameters, and two experimental cases, observations of the population dynamics of the mosquito vector *Culex quinquefasciatus* and *Culex pipiens*, to demonstrate that model-based inference can

correctly identify life parameters from longitudinal observations. The analysis reveals not only the differential physiological behaviour of distinct development stages, but also identifies the degree to which each parameter can be inferred from the data. The methods introduced constitute a model-based approach to identifying life table characteristics from incomplete longitudinal data, and help to improve the design of life table experiments. The approach is readily applicable to the development of climate and environment-driven population dynamics models for important vectors of disease.

A.2 APPENDIX B - Meteorological observations

In this section we will give a detail site-specific description of the collected meteorological and entomological data. In Section 1.A the overview of meteorological observations is given for the three study location (Figure A.1). In Section 1.B the overview of entomological data is given.

Figure A.1: Study locations: G - Guadeloupe (Egypt); B - Bahariya; P - Petrovaradin (Serbia).

An overview of the meteorological datasets is given in Table 5. The field data for the Bahariya Oasis (Egypt) were collected within the MosqDyn project for the period 2017-2018. The data was recorded at 15-minute intervals with the Davis Vantage Pro weather station.

The field data for Petrovaradin was collected within the VECTORNET project for the period 2016–2017. The data was recorded at 5-minute intervals with the EasyWeather weather station.

Guadeloupe did not have an in-situ weather station deployed for the duration of the project. ERA5 reanalysis was used instead to obtain hourly time-series of wind, precipitation, temperature and relative humidity data. Data obtained from the synoptic weather station close to Pointe-à-Pitre was cleaned and used to check the correlation with the ERA5 time-series for a period from 2015-01-05 to 2017-02-24 ($r = 0.76$, $p < .0001$). Data from the in-situ station itself was not used for the whole period because of a large amount of missing values and erroneous recordings of minimum and maximum temperature observed for several instances in 2015–2018.

Table A.1: Overview of observed meteorological data. The measured variables are: (i) Temperature [°C], (ii) Relative humidity [%], (iv) Precipitation [mm], (v) Wind speed [m/s], (vi) Wind direction; FF - Frequency used for forcing the model.

Locations	Time series	Lat [°]	Lon [°]	Altitude [m]	Time Series type	Frequency	Type	FF
Bahariya	01/04/2017 31/12/2018	28.41	28.93	98	Regular	15 min	Observations	Daily
Guadeloupe	2015–2018	16.26	-61.52	23	Regular	1 hour	ERA5 analysis	Daily
Petrovaradin	2016–2017	45.25	19.87	82	Regular	5 min	Observations	Daily

A.2.1 Preprocessing

A.2.1.1 Gap filling

An automated quality control script was developed for checking incoming data for Bahariya and Petrovaradin which consisted of a: (i) plausible value check; (ii) internal consistency check (comparison of dew point temperature, relative Humidity and air temperature); (iii) time step check; (iv) check for rate of change between the steps. Missing data in the time series was eliminated using an algorithm for generating debiased ERA5 data based on the characteristics of the local time series developed by Lompar et al. [214]. The biggest gap occurred for Bahariya from 24/07/2017 to 03/08/2017 due to a power issue causing the loss of the archived data.

A.2.1.2 Wind correction for Guadeloupe

Since ERA5 reanalysis offers wind speed a the 10 m height, the wind speed at the 2 m height was calculating using the Monin Obukvhov similarity theory. This Monin Obukhov equation describes the relationship between the vertical flux of a variable and its vertical gradient. The Monin Obukhov equation is only applicable in the Constant Flux Layer (CFL) which is a layer of the lower atmosphere of a standard height of around 50 m above the earth's surface in which the turbulent displacement stress τ can be considered to be constant. From this invariability of displacement stress with height the following relationship for any displaceable quantity whose distribution is homogeneous in space and stationary in time was derived:

$$\frac{\partial \bar{s}}{\partial z} = \frac{s_*}{kz}\Phi_s(\frac{z}{L}) \tag{A.1}$$

The value $\bar{s}$ represents the average value (ensemble or time average) of a variable per unit mass of air, s_* is the characteristic size parameter which has the unit of variable s and is defined by the vertical flux of this variable, the density of air and the friction velocity u_*:

$$s_* = \frac{F_s}{\rho u_*} \tag{A.2}$$

The parameter L is the length scale of Monin Obukhov which is defined as:

$$L = -\frac{\rho C_p T u_*^3}{kgH} \tag{A.3}$$

H is the latent heat ($H = \rho C_p \bar{w\theta}$), g is the gravitational constant, T is temperature, C_p is the specific heat capacity and k is von Kármán's constant which usually takes the value 0.41, Φ_s is a universal function which takes different values depending on the stability of the boundary layer. The turbulent diffusion of s is defined as the ratio of flux and the vertical gradient of s:

$$k_s = -\frac{F_s}{\rho\frac{\partial\bar{s}}{\partial z}} \tag{A.4}$$

in combination with Equation (A.1) we get:

$$ks = \frac{ku_*z}{\Psi_s} \tag{A.5}$$

If $s = \bar{u}$ the velocity in the x direction, the flux becomes $F_s = \rho u_*^2 = \tau$ and we get:

$$\frac{\partial\bar{u}}{\partial z} = \frac{u_*}{kz}\Phi_m(\frac{z}{L}) \tag{A.6}$$

$$k_m = \frac{ku_*z}{\Phi_m} \tag{A.7}$$

By integrating Equation (A.6) with the condition $\bar{u} = 0$ for $z = z_0$ (roughness length) we get:

$$\bar{u}(z) = \frac{u_*}{k}\left[f_m(\frac{z}{L}) - f_m(\frac{z_0}{L})\right] \tag{A.8}$$

where

$$f(\frac{z}{L}) = \int_0^z \frac{\Phi_m(\frac{z}{L})}{z}dz \tag{A.9}$$

In a neutral atmosphere $\Phi_m = 1$ and Equation (A.6) and Equation (A.7) can be simplified to:

$$\frac{\partial\bar{u}}{\partial z} = \frac{u_*}{kz}k_m = ku_*z,\ \bar{u}(z) = \frac{u_*}{k}ln\frac{z}{z_0} \tag{A.10}$$

So, it follows that by dividing the expression for $\bar{u}(10)$ with $\bar{u}(2)$:

$$\frac{\bar{u}(10)}{\bar{u}(2)} = ln\left(\frac{10}{2} - \frac{2}{z_0}\right) \tag{A.11}$$

And finally, we get the expression the velocity at the 2 m height:

$$\bar{u}(2) = \frac{\bar{u}(10}{ln(\frac{10}{z_0} - \frac{2}{z_0})} \tag{A.12}$$

A.2.2 Pointe-à-Pitre (Guadeloupe)

In Figure A.5 it can be observed that the winds for Guadeloupe have a predominant westerly component, with north-westerly wind occurring in December-March. Lower velocities are observed in April and then August-November.

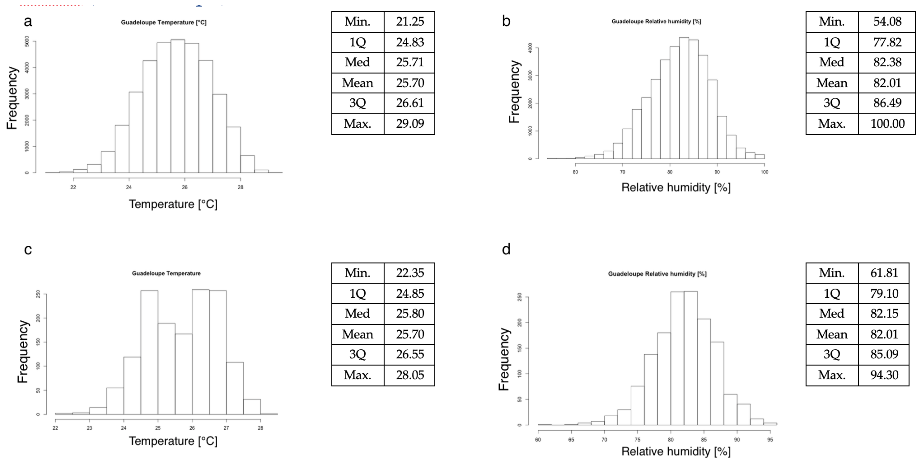

a

Min.	21.25
1Q	24.83
Med	25.71
Mean	25.70
3Q	26.61
Max.	29.09

b

Min.	54.08
1Q	77.82
Med	82.38
Mean	82.01
3Q	86.49
Max.	100.00

c

Min.	22.35
1Q	24.85
Med	25.80
Mean	25.70
3Q	26.55
Max.	28.05

d

Min.	61.81
1Q	79.10
Med	82.15
Mean	82.01
3Q	85.09
Max.	94.30

Figure A.2: ERA5 temperature and relative humidity for Pointe-à-Pitre (Guadeloupe) hourly (a,b) and daily (c,d).

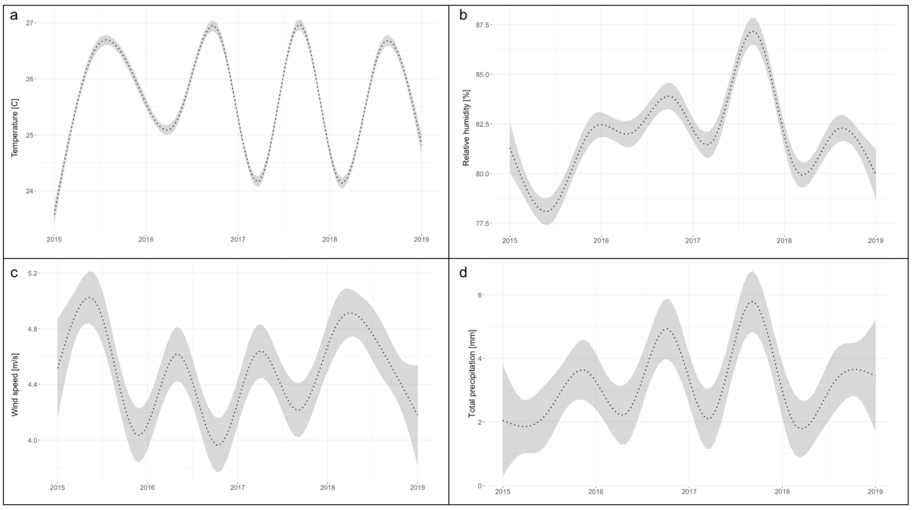

Figure A.3: GAM smooth (a) daily temperature; (b) relative humidity; (c) 10 m wind; (d) precipitation time-series for Pointe-à-Pitre (Guadeloupe).

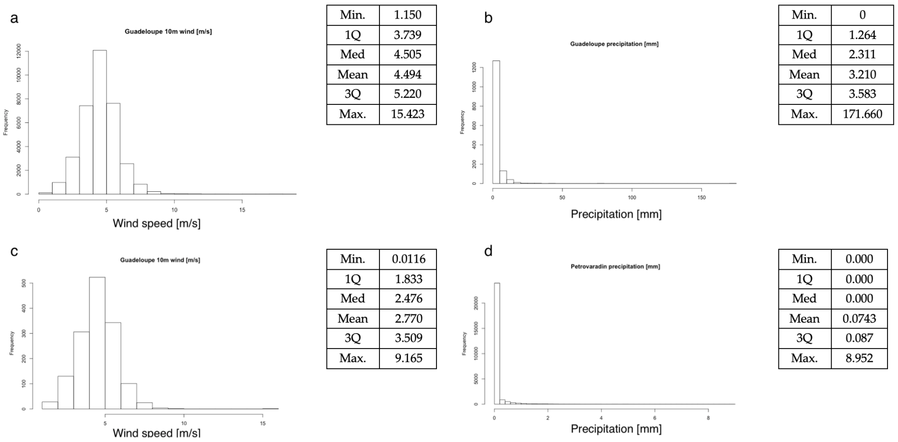

a

Min.	1.150
1Q	3.739
Med	4.505
Mean	4.494
3Q	5.220
Max.	15.423

b

Min.	0
1Q	1.264
Med	2.311
Mean	3.210
3Q	3.583
Max.	171.660

c

Min.	0.0116
1Q	1.833
Med	2.476
Mean	2.770
3Q	3.509
Max.	9.165

d

Min.	0.000
1Q	0.000
Med	0.000
Mean	0.0743
3Q	0.087
Max.	8.952

Figure A.4: ERA5 wind speed and precipitation for Pointe-à-Pitre (Guadeloupe) hourly (a,b) and daily (c,d).

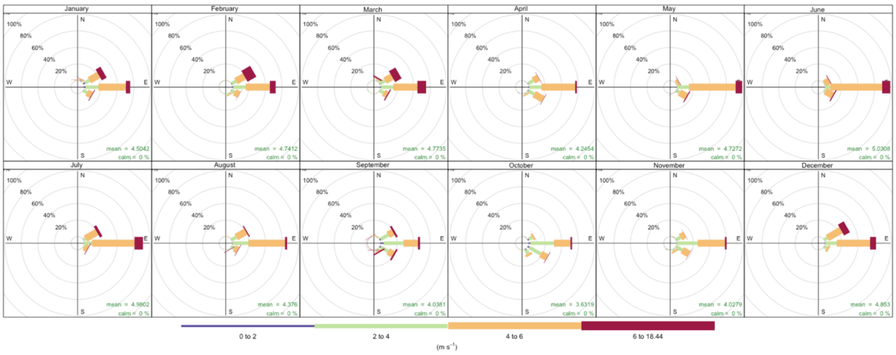

Figure A.5: Monthly frequency of counts by wind direction [%] for Guadeloupe. The wind speed is indicated by the color gradient: 0–2 m/s (blue); 2–4 m/s (green); 4–6 m/s (orange); and 6-19 m/s (red).

A.2.3 Bahariya (Egypt)

In the figure below the complete time-series, and frequency and kernel density plots for the observed meteorological variables are shown for each study site.

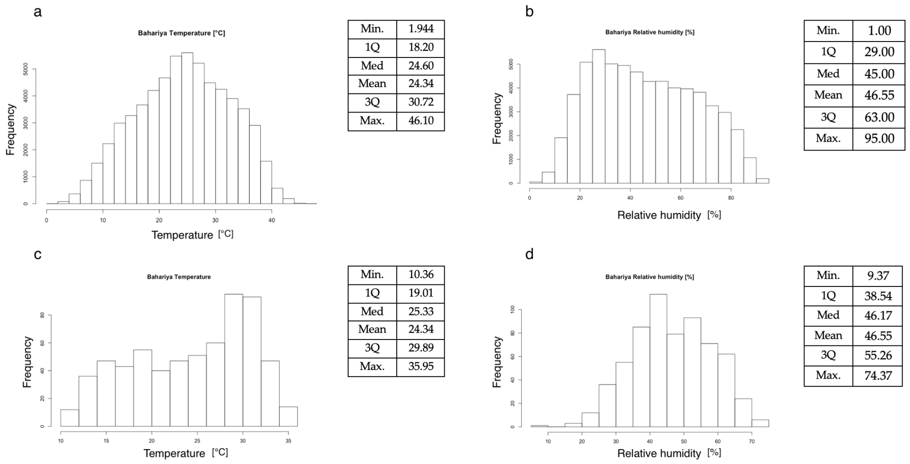

a

Min.	1.944
1Q	18.20
Med	24.60
Mean	24.34
3Q	30.72
Max.	46.10

b

Min.	1.00
1Q	29.00
Med	45.00
Mean	46.55
3Q	63.00
Max.	95.00

c

Min.	10.36
1Q	19.01
Med	25.33
Mean	24.34
3Q	29.89
Max.	35.95

d

Min.	9.37
1Q	38.54
Med	46.17
Mean	46.55
3Q	55.26
Max.	74.37

Figure A.6: Observed temperature and relative humidity for a location in Bahariya (Egypt) 15 min (a,b), daily mean (c,d).

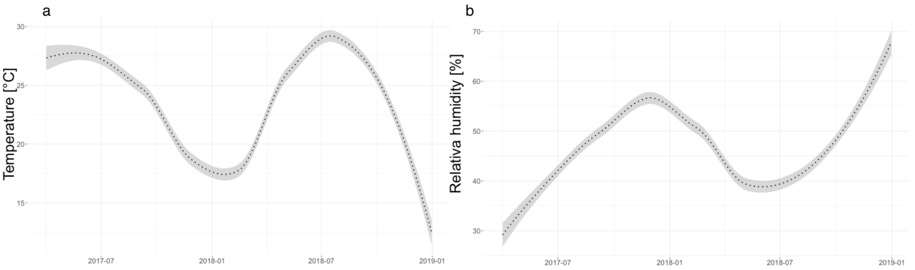

Figure A.7: GAM smooth of daily temperature and relative humidity time-series for a location in Bahariya (Egypt) for the period 2017–2018 (x axis).

In Figure A.8 we can see a clear regime shift for the wind speed in 2017 and 2018. When analysing the monthly frequency of counts for wind direction a strong westerly component in Figure A.9 for Jan-March is observed. The latitude-characteristic north-easterlies are observed in March-September. Moreover, we see that the magnitude is small for November and December for both years.

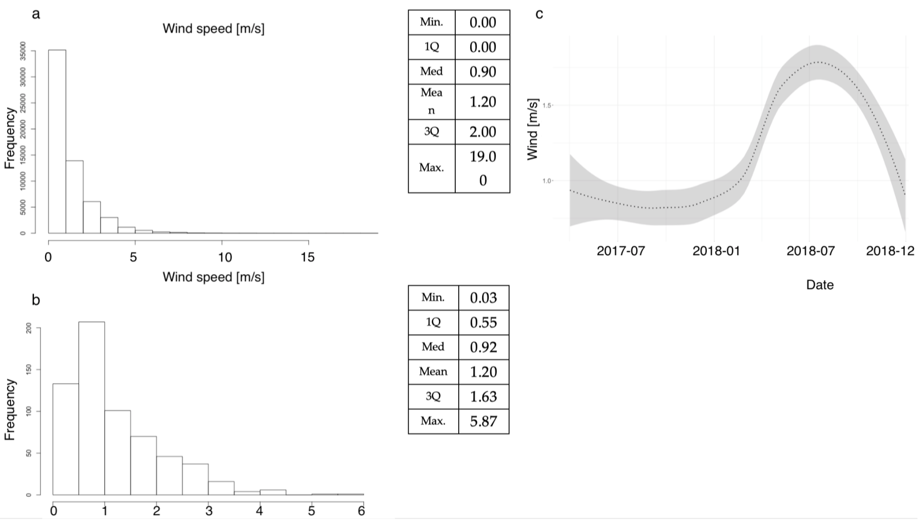

Min.	0.00
1Q	0.00
Med	0.90
Mean	1.20
3Q	2.00
Max.	19.00

Min.	0.03
1Q	0.55
Med	0.92
Mean	1.20
3Q	1.63
Max.	5.87

Figure A.8: Observed wind speed for a location in Bahariya (Egypt) 15 min (a), daily mean (b), GAM smoothed avg. daily time-series (c) for 2017–2018.

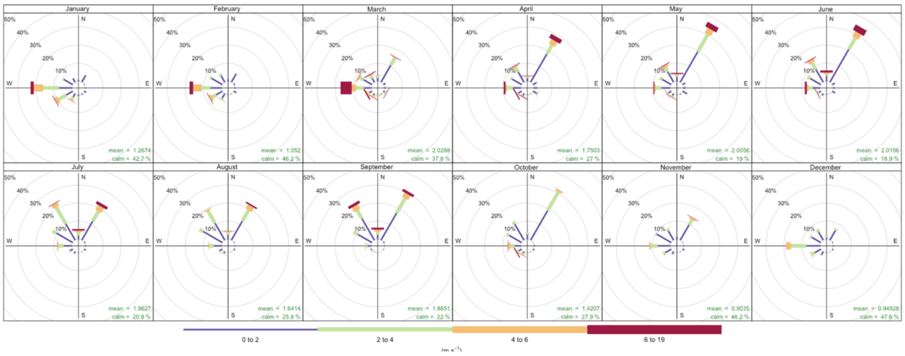

Figure A.9: Monthly frequency of counts by wind direction [%] for Bahariya. The wind speed is indicated by the color gradient: 0–2 m/s (blue); 2–4 m/s (green); 4–6 m/s (orange); and 6-19 m/s (red).

A.2.4 Petrovaradin (Serbia)

Low wind speeds are observed for the Petrovaradin study site throughout the year (Figures A.12 and A.13.).

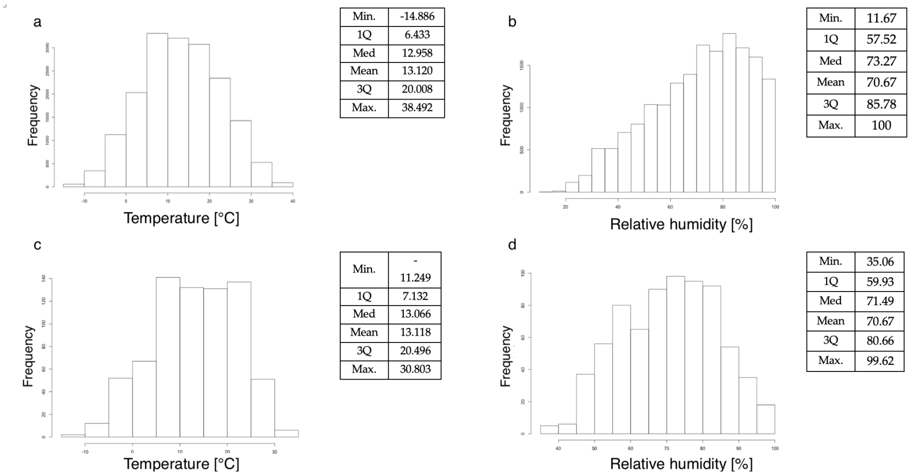

	a
Min.	-14.886
1Q	6.433
Med	12.958
Mean	13.120
3Q	20.008
Max.	38.492

	b
Min.	11.67
1Q	57.52
Med	73.27
Mean	70.67
3Q	85.78
Max.	100

	c
Min.	- 11.249
1Q	7.132
Med	13.066
Mean	13.118
3Q	20.496
Max.	30.803

	d
Min.	35.06
1Q	59.93
Med	71.49
Mean	70.67
3Q	80.66
Max.	99.62

Figure A.10: Observed temperature and relative humidity for a location in Petrovaradin (Serbia) 15 min (a,b), daily mean (c,d).

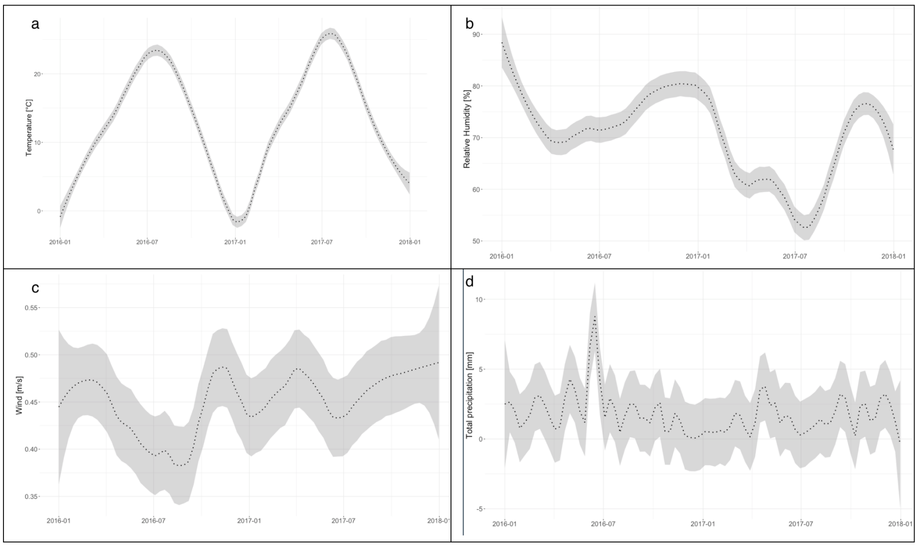

Figure A.11: GAM smooth daily temperature, relative humidity, wind and precipitation time-series for Petrovaradin (Serbia) for the period 2016–2017.

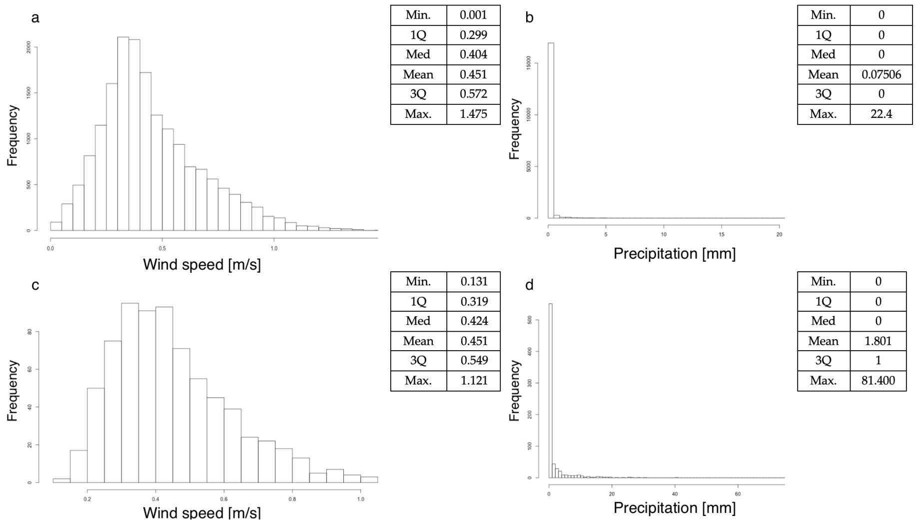

a

Min.	0.001
1Q	0.299
Med	0.404
Mean	0.451
3Q	0.572
Max.	1.475

b

Min.	0
1Q	0
Med	0
Mean	0.07506
3Q	0
Max.	22.4

c

Min.	0.131
1Q	0.319
Med	0.424
Mean	0.451
3Q	0.549
Max.	1.121

d

Min.	0
1Q	0
Med	0
Mean	1.801
3Q	1
Max.	81.400

Figure A.12: Observed wind speed and precipitation for a location in Petrovaradin (Serbia) 15 min (a,b), daily mean (c,d).

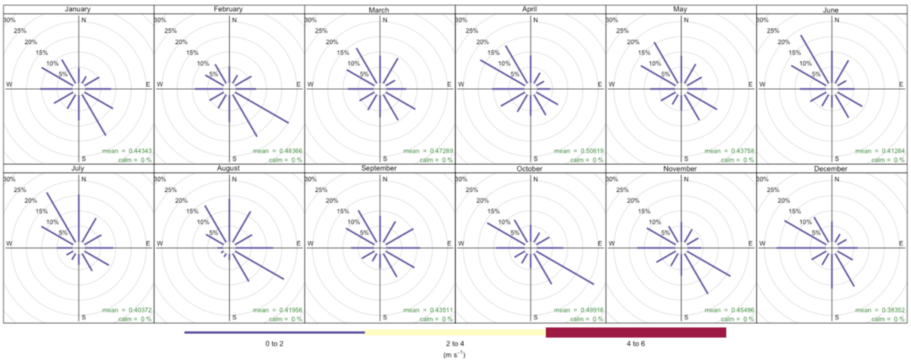

Figure A.13: Monthly frequency of counts by wind direction [%] for Petrovaradin. The wind speed is indicated by the color gradient: 0–2 m/s (blue); 2–4 m/s (green); 4–6 m/s (orange); and 6-19 m/s (red).

A.3 APPENDIX C - Entomological observations

Table A.2: Overview of observed entomological data.

Locations		Time series	Lat [°]	Lon [°]	Altitude [m]	TS type	Frequency	Species of interest
Bahariya		01/04/2017 31/12/2018	28.41	28.93	97	Regular	Daily	*Cx. pipiens*
Guadeloupe	CRB	11/2015–10/2018	16.207	-61.507	4	Regular	Week-Month	*Ae. aegypti*
	HFR	11/2015–10/2017	16.347	-61.776	6	Irregular	Week-Month	*Ae. aegypti*
	HMC	11/2015–05/2019	16.212	-61.500	5	Irregular	Week-Month	*Ae. aegypti*
	HCB (CAB)	11/2015–10/2018	16.207	-61.507	10	Irregular	Week-Month	*Ae. aegypti*
	Zoo	11/2017-04/2019	16.180	-61.752	164	Irregular	Week-Month	*Ae. aegypti*
	Aporier	11/2017-02/2019	16.259	-61.693	62	Irregular	Week-Month	*Ae. aegypti*
	RV1	11/2017-04/2019	16.201	-61.649	91	Irregular	Week-Month	*Ae. aegypti*
	RV2		16.257	-61.668	41	Irregular	Week-Month	*Ae. aegypti*
	Gosier	11/2017-04/2019	16.212	-61.500	5	Irregular	Week-Month	*Ae. aegypti*
Petrovaradin		2016–2017	45.25	19.87	82	Regular	Daily	*Cx. pipiens*

A.3.1 Pointe-à-Pitre (Guadeloupe)

The field data for Gudeloupe was collected across 8 location within the MosqDyn and SmartSenZ projects for the period 2015–2018. The locations are shown in Figure A.14 and are all located on the main island of Guadeloupe.

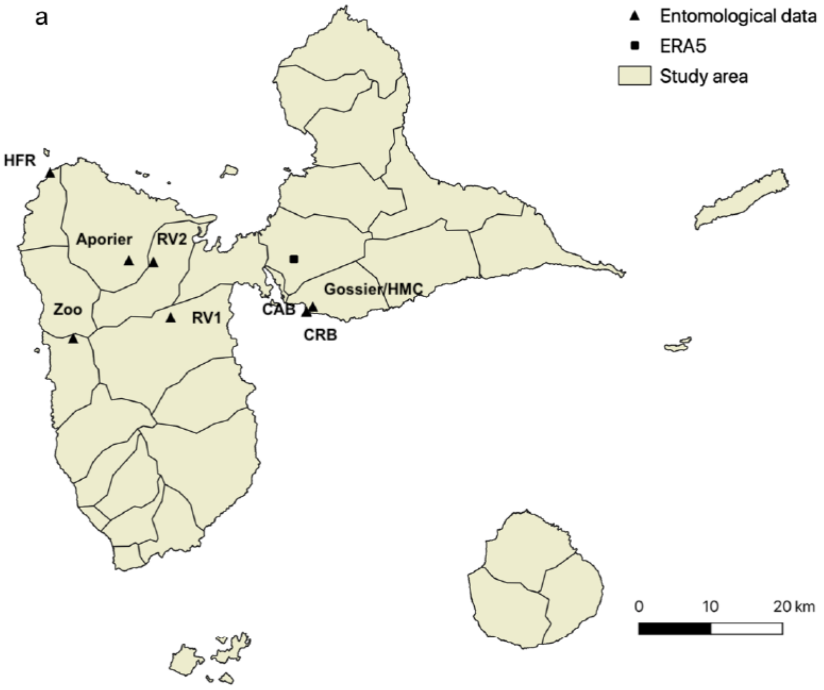

Figure A.14: Guadeloupe sampling locations

Samples were collected on a weekly and monthly basis by standardized protocols using the BG Sentinel 2 mosquito trap and the BG-GAT trap.

Description of the breeding sites for *Ae. aegypti*:

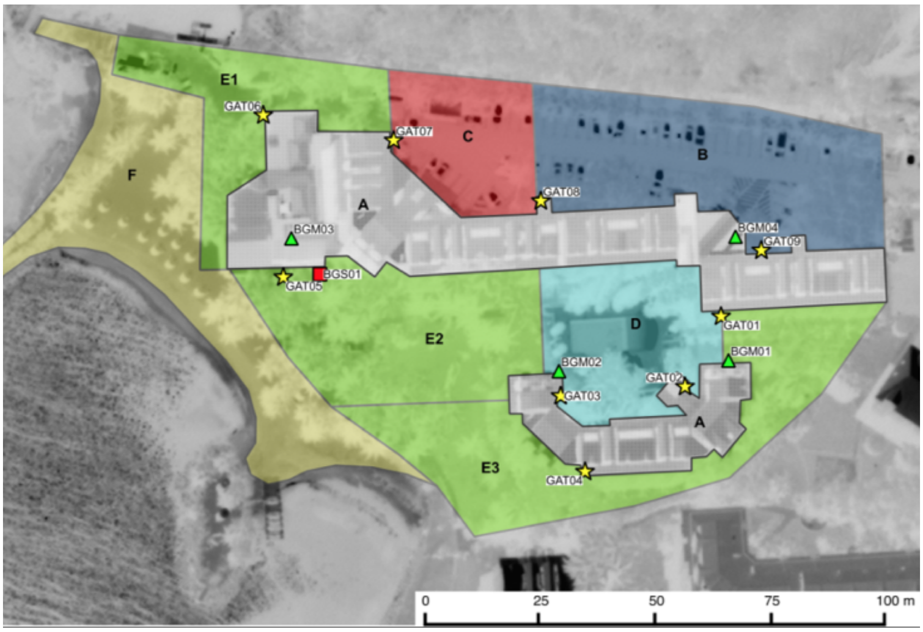

Figure A.15: The site of La Canella Beach and its surroundings. (A: Buildings, B: Parking, C: Technical Area, D: Pool & Terrace, E1-3: Park & Garden, F: Beach and Coast, Base Map Source: DigitalGlobe, WorldView 3, 2015). Identified species: *Culex quinquefasciatus* & *nigripalpus Anopheles sp*, *Aedes taeniorhynchis*, *Deinocerites magnus*.

Table A.3: Description of the breeding sites for *Ae. aegypti*:

CAB	(i) Artificial containers; (ii) Used tires
HFR	(i) Tree hollows; (ii),Water cisterns; (iii) Artificial containers
CRB	(i) Tree hollows; (ii) Concrete block hollows; (iii) Used tires; (iv) Artificial containers
HMC	(i) Tree hollows; (ii) Manhole covers; (iii) Flower pots
Aporier, Zoo, RV	NA

Culex mosquitoes were found in the flooded meadows, mangroves and metal drums.

The catches for each trap-location are shown in the sub-chapters below. The model output for the same period is discussed in chapter 4.D.

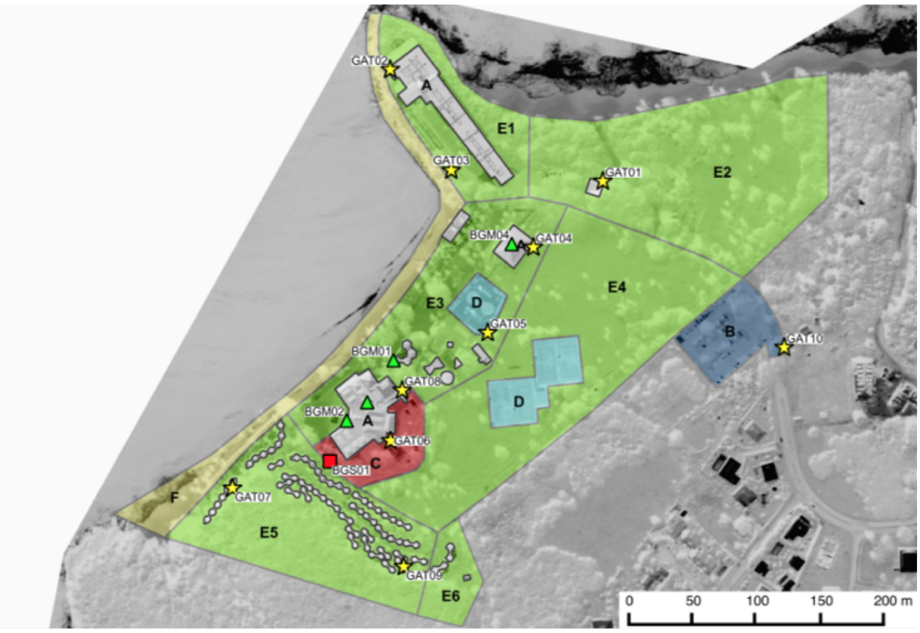

Figure A.16: The Fort Royal site and its structural areas. A: buildings; B: parking; C: technical area; D: swimming pool & terrace; E1-6: park & garden; F: beach and coast; Source base map: DigitalGlobe, WorldView 2, 2010). Identified species: *Aedes aegypti*, *Culex quinquefasciatus* & *nigripalpus*, *Aedes taeniorhynchus*, *Culex astratus.*

Figure A.17: The Creole Beach site and its structural areas. (A: buildings; B: parking; C: technical area; D: swimming pool & terrace; E1-6: park & garden; F: beach and coast; Source base map: DigitalGlobe, WorldView 2, 2015). Identified species: *Aedes aegypti*, *Culex quinquefasciatus* & *nigripalpus*.

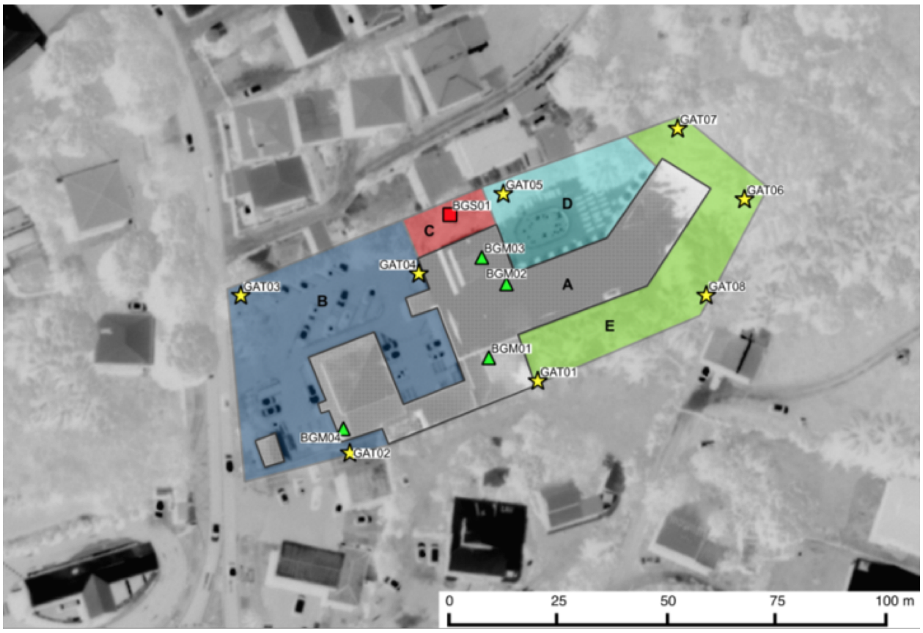

Figure A.18: The Maison Creole site and its structural areas. (A: buildings; B: parking; C: technical area; D: swimming pool & terrace; E1-6: park & garden; F: beach and coast; Source base map: DigitalGlobe, WorldView 2, 2015) Identified species: *Aedes aegypti*, *Culex quinquefasciatus* & *nigripalpus*, *Anopheles species*, *Deinocerites magnus*.

A.3.1.1 HCB(CAB)

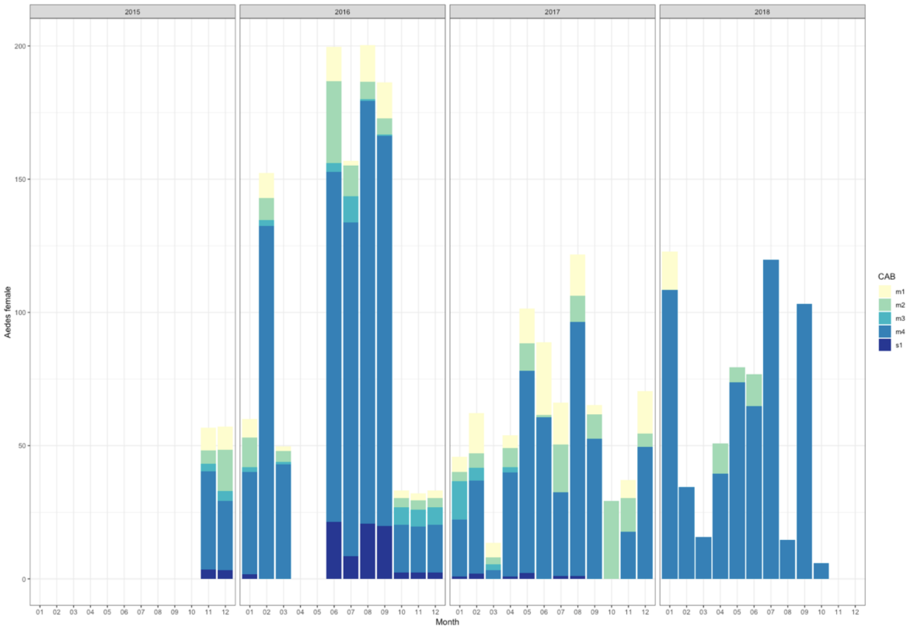

Figure A.19: Stacked bar chart of monthly *Aedes* catches from four traps (m1, m2, m3, m4, s1) site CAB.

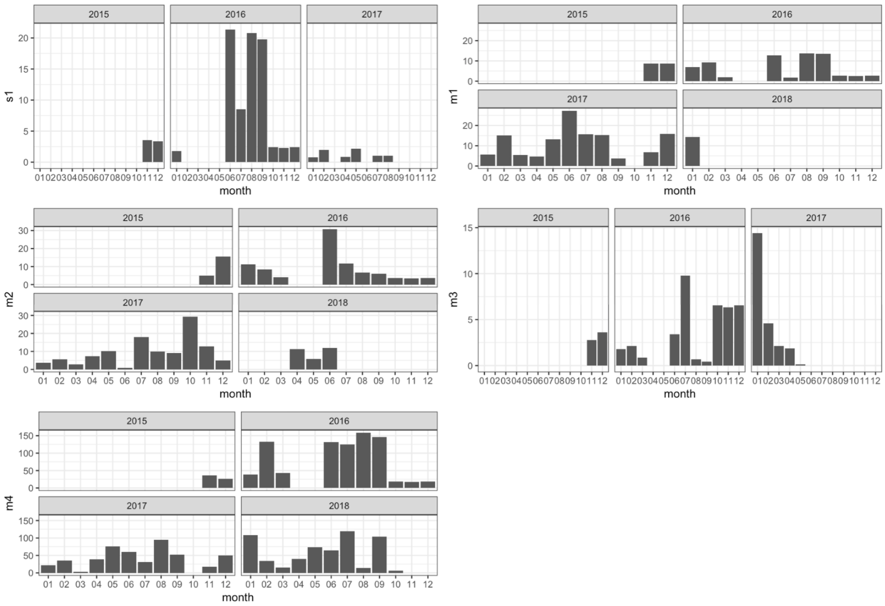

Figure A.20: Monthly *Aedes* catches from four traps (m1, m2, m3, m4, s1) site CAB – each site.

A.3.1.2 CRB

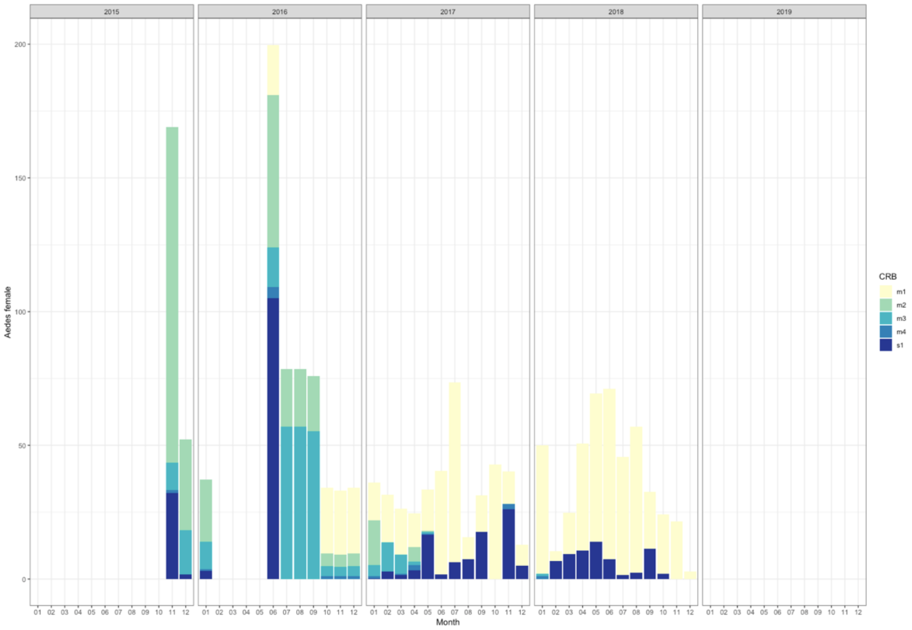

Figure A.21: Stacked bar chart of monthly *Aedes* catches from four traps (m1, m2, m3, m4, s1) site CRB.

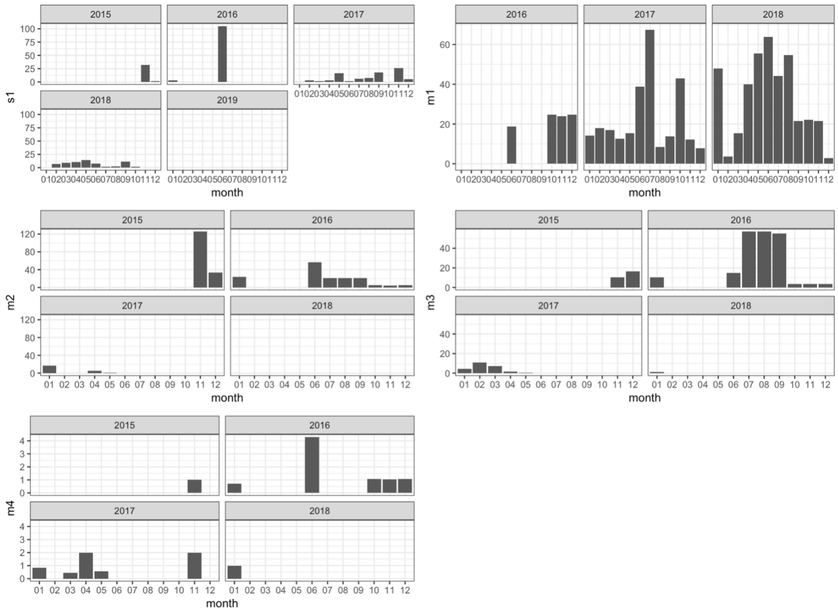

Figure A.22: Monthly *Aedes* catches from four traps (m1,m2, m3, m4, s1) site CAB – each site.

A.3.1.3 HFR

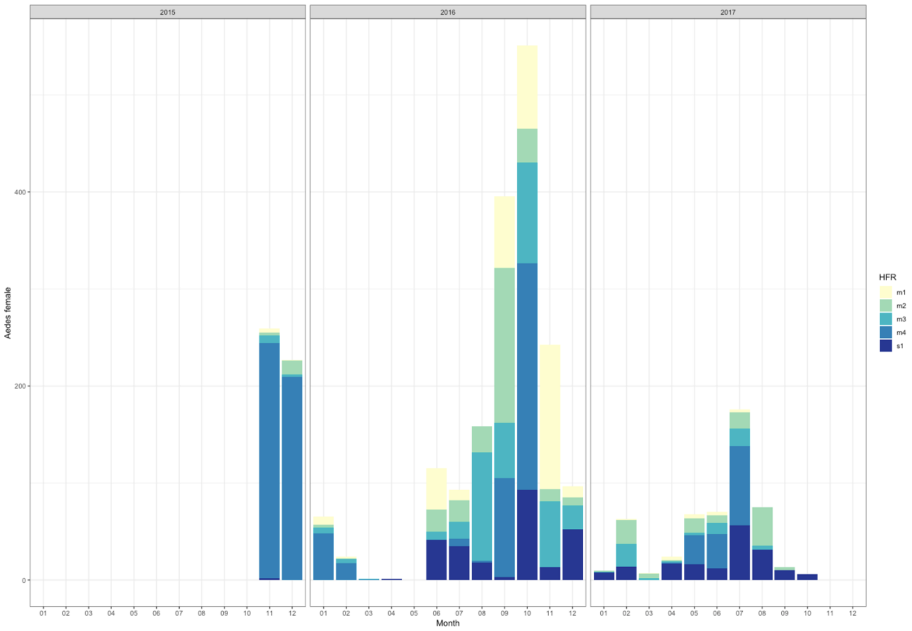

Figure A.23: Stacked bar chart of monthly *Aedes* catches from four traps (m1, m2, m3, m4, s1) site HFR.

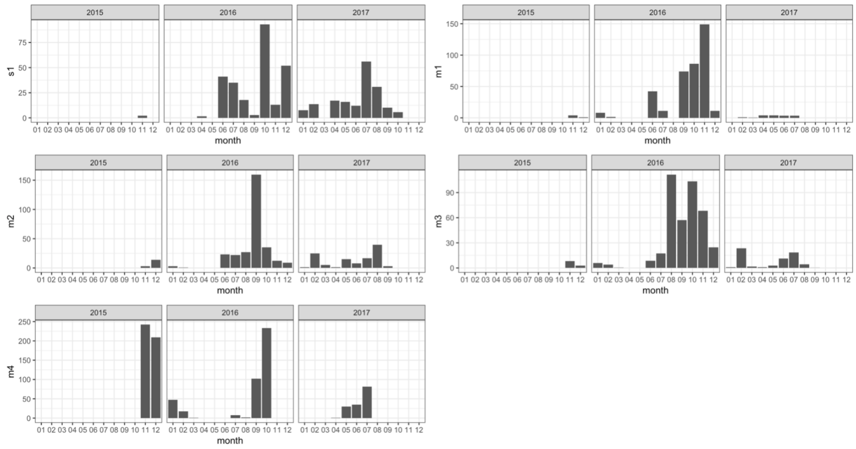

Figure A.24: Monthly *Aedes* catches from four traps (m1,m2, m3, m4, s1) site HFR – each site.

A.3.1.4 HMC

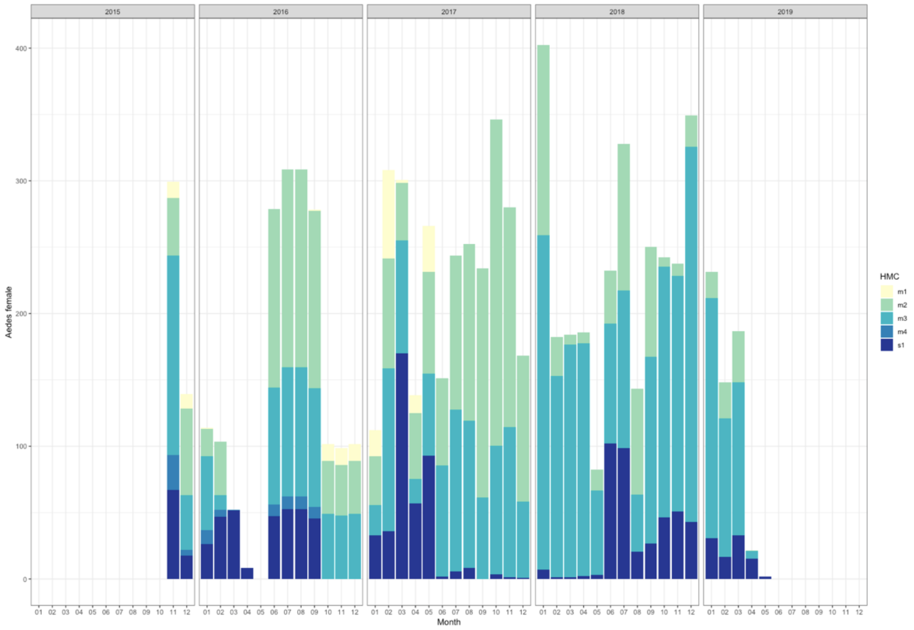

Figure A.25: Stacked bar chart of monthly *Aedes* catches from four traps (m1, m2, m3, m4, s1) site HMC.

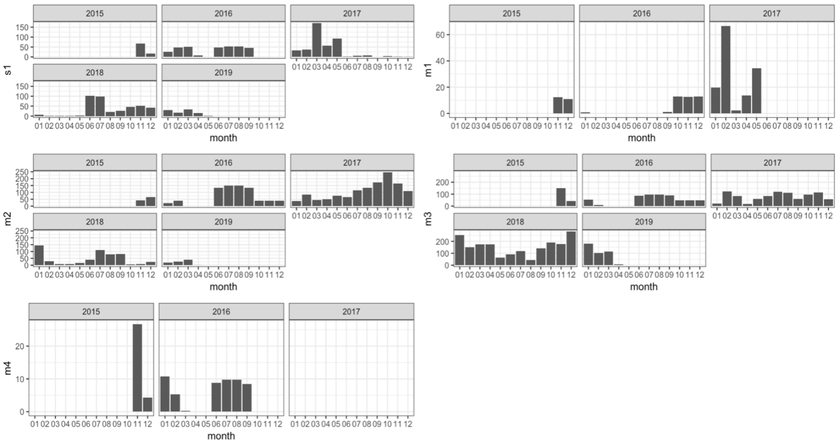

Figure A.26: Monthly *Aedes* catches from four traps (m1,m2, m3, m4, s1) site HMC – each site.

A.3.1.5 ZOO

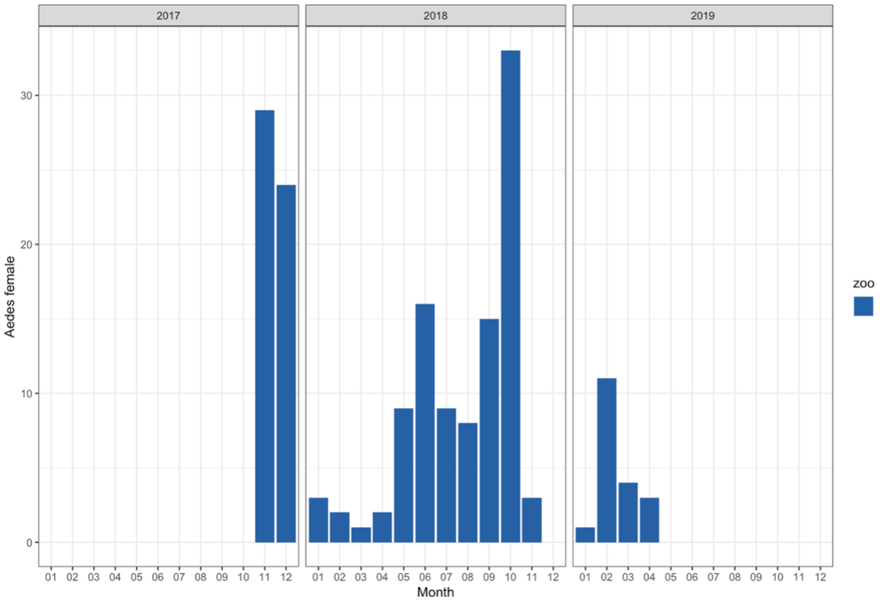

Figure A.27: Bar chart of monthly *Aedes* catches for ZOO.

A.3.1.6 Aporier

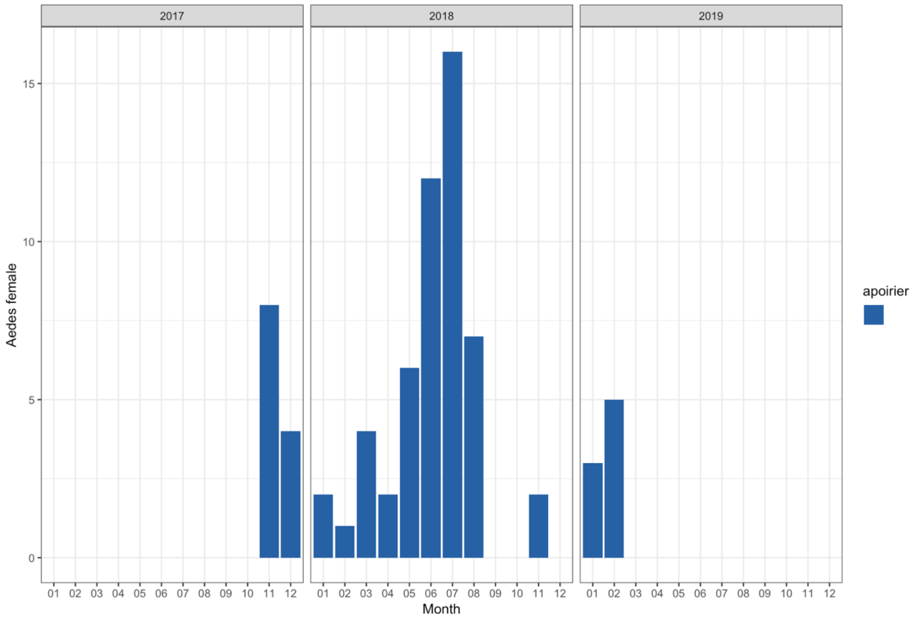

Figure A.28: Bar chart of monthly *Aedes* catches for Aporier.

A.3.1.7 RV

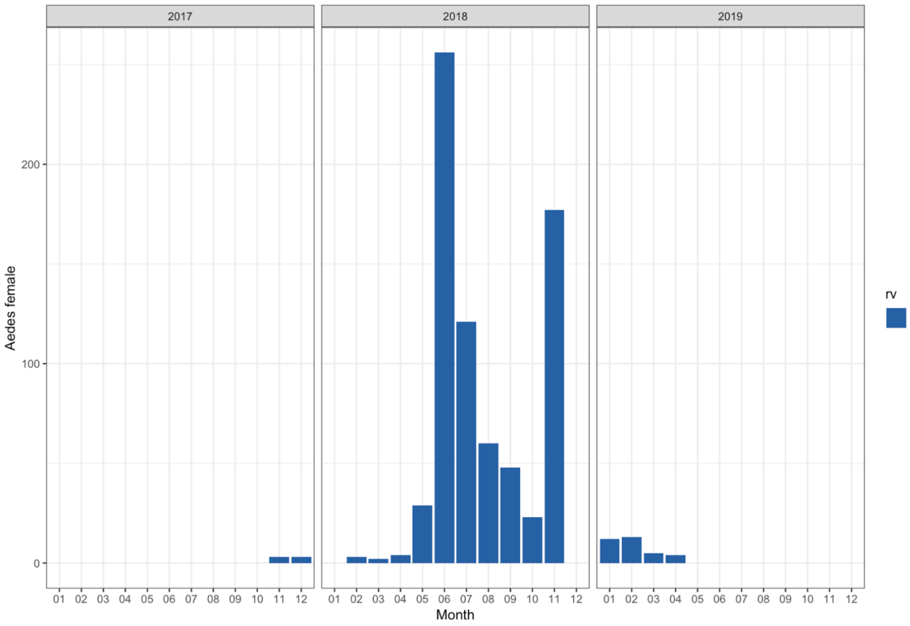

Figure A.29: Bar chart of monthly *Aedes* catches for RV.

A.3.1.8 Gosier

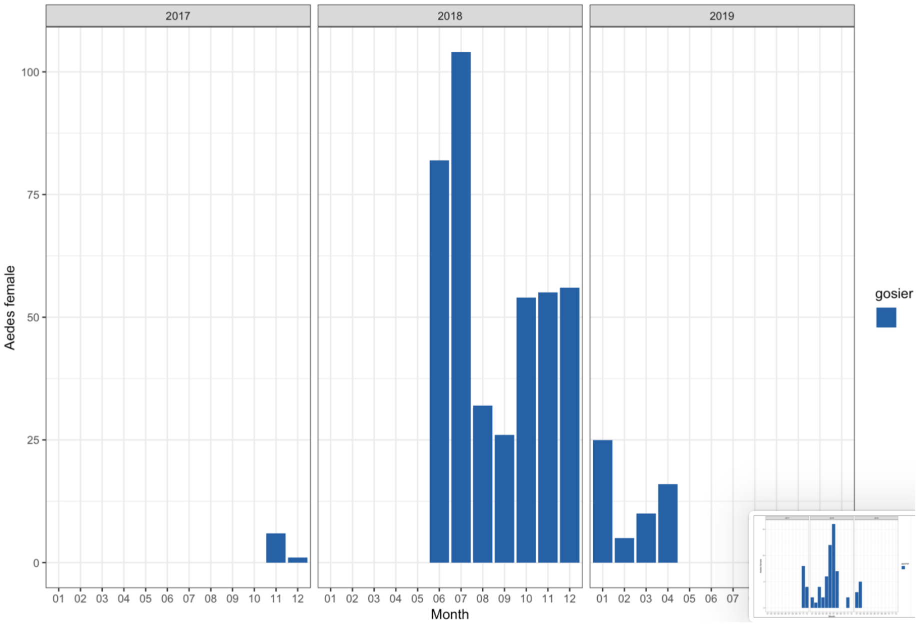

Figure A.30: Bar chart of monthly *Aedes* catches for Gosier.

A.3.2 Bahariya (Egypt)

The field data for the Bahariya oasis (Egypt) was collected within the MosqDyn project for the period 2017-2018.

Samples were collected on a daily basis by standardised protocols using the BG Sentinel 2 mosquito trap. The trap was operating without a light source (light aided traps proved not to have a significant attracting/repelling influence on *Culex* mosquitoes [215]). Several experiments were run to examine the influence of a CO_2 source attached to the trap. The CO_2 was operated with a timer and set to release for a total of 4 hours a day during intervals corresponding to maximum activity for *Cx. pipiens* (morning and evening). The CO_2 had a significant influence on the daily abundance of trapped mosquitoes, however the refiling of the bottles which had to be done in Cairo and transported to the oasis was not feasible and hence this option was abandoned. The CO_2 related counts were rescaled before comparing the simulated abundance to field data [216]. A correction for days with wind speed exceeding the wind speed limiting flight and activity of *Cx. pipiens* was implemented using a sigma function to calculate the stress factor, with 2 m/s and 5 m/s set as the threshold and saturation (limiting most blood-seeking activity) values respectively.

The doughnut chart in Figure A.31 shows the proportion of total females corresponding to the *Culex* and *Aedes* genus.

Figure A.31: (a) Descripting of the site: A – agricultura area, B – buildings, D – fountain; G – Garden; T – trees and shrubbery; C – technical area; F – Ruminant barn; R – Road and camp bounday; (b) Proportion of total female mosquitoes at DFC.

Table A.4: Count summary Bahariya 2017–2018

	Culex M	*Culex*F	*Aedes* M	*Aedes* F	Total
Count	3377	5501	641	785	10304

The *Culex* species identified in the Oasis were *Culex pipiens*, biotype *Cx. pipiens pipiens* and biotype *Cx. pipiens molestus*. The identified *Aedes* species was *Ae. caspius*. According to the IRD historical data [165] *Ae. detritus* was also found in the Oasis however it was not confirmed during our entomological survey.

The identified breeding sites were: (i) Cut-off sections of irrigation canals with stagnant water; (ii) Cesspool-canalization next to the house, with a lot of vegetation; (iii) Road-side ditches with brackish water; (iv) Natural ponds created by underground water sources forming a flooded area with brackish water; (v) Salt lakes; (vi) Irrigation canals and wells/concrete pits for irrigation. The identified Land Use types were Rural habitat, Agriculture and Nature LS types. The highest abundance of larvae corresponded to the stagnant semi-permanent water bodies i.e. small irrigation/drain pools and stagnant temporary water bodies i.e. cut-off irrigation canals and flooded road-side ditches.

Culex pipiens was the prevailing species in the oasis. At the DFC site a total of 10304 specimens were collected during the sampling period (April 2017 – December 2018) of which 3377 were *Culex pipiens* male, 5501 *Culex pipiens* female, 641 *Aedes caspius* male, and 785 *Aedes caspius* female (Table A.4).

The observed summer minimum shown in Figure A.32 could have several reasons for occurrence, but most likely due to a reduction in the total available surface of stagnant water breading sites resulting from increase evaporation in the summer months. This was reported for several breeding sites that were being monitored during the experiment. However, following this minimum, observed

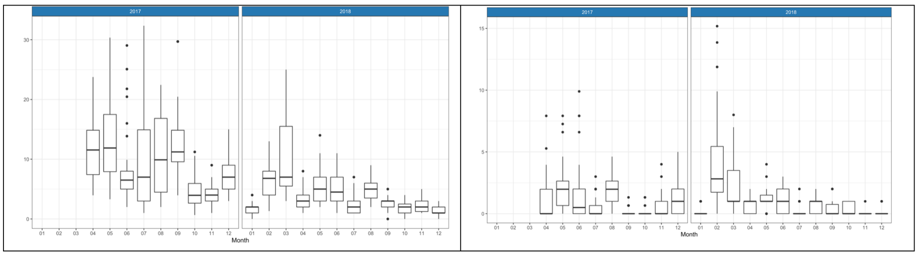

Figure A.32: Monthly abundance for (a) *Culex*; (b) *Aedes* for 2017 and 2018.

in June 2017, we see a significant increase in population. One of the possible explanations for this rise is an irrigation event that brought fresh water to the dried-out sites. A spike in relative humidity is observed for July 5 which could be a response to a major irrigation action which caused the spike in the vector count Figure A.33. However, there is no sure way to determine this and the irrigation schedule is not recorded for the Oasis. More information regarding the irrigation and water storage habits in the Oasis needs to be gathered and cross-examined with the vector data.

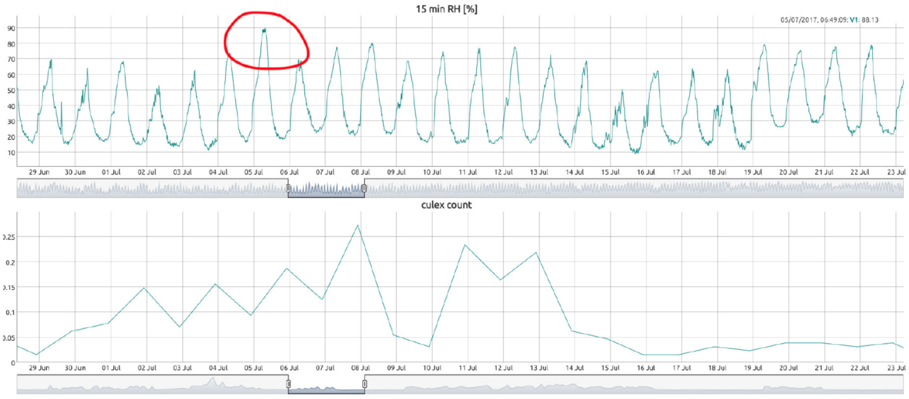

Figure A.33: Relative humidity time-series (top) and daily observed *Cx. pipiens* abundance for the period from 29 Jun – 23 July 2017 for Bahariya.

The humidity spike could also be a result of a process that was observed to occur in oases where a 60-100 m cells shifts the higher-level humidity to surface creating a temporary spike in observed RH.

The lower counts observed for 2018 when compared to 2017 can be a result of the shift in wind regime shown in Figure A.33.

A.3.3 Petrovaradin (Serbia)

The field data for Petrovaradin was collected within the VECTORNET project.

Daily collection were carried out at stationary site February – December (2016, 2017) for 670 trap nights. Weekly collection at 7 sites (rotation of the trap) for 48 trap nights (one per week).Samples were collected using the dry-ice bated EVS without a light source

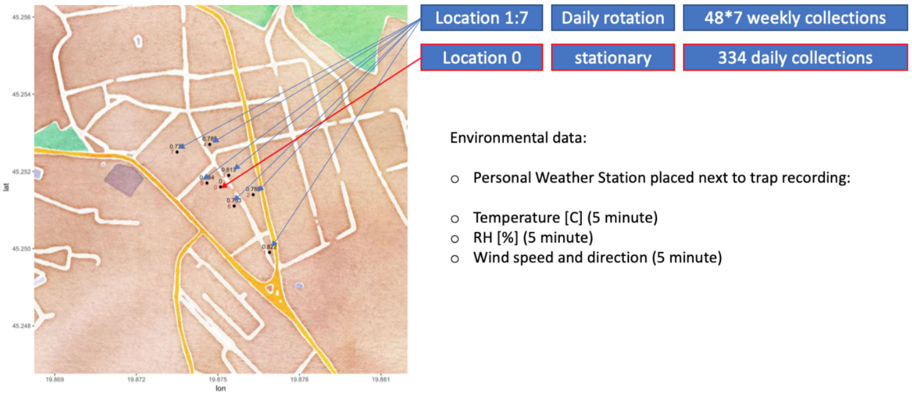

Location 1:7	Daily rotation	48*7 weekly collections
Location 0	stationary	334 daily collections

Environmental data:

- ○ Personal Weather Station placed next to trap recording:
- ○ Temperature [C] (5 minute)
- ○ RH [%] (5 minute)
- ○ Wind speed and direction (5 minute)

Figure A.34: Description of the site

The study location is a semi urban zone of Petrovaradin, Serbia with: Lots of greenery; side drainage channels; most of the houses posses backyards with many containers suitable for breeding *Culex pipiens*. The locations for the surveillance activities were identified based on the availability of 8 years weekly sampling data for *Culex pipiens* as an important vector species in Europe (WNV)

Figure A.35: Location of the site

Cullex pipiens was registered at all sampling stations, and 19,104 specimens (update for 2017) were collected; *Cx. modestus* was found extremely rare, with only one individual trapped at station 5 *Aedes albopictus*,*Cx.perexiguus*, *Cx. tritaeniorhynchus*, *Ae. aegypti*, *Ae. japonicus*, *Ae. koreicus* and *Ae. atropalpus* were absent from the samples. *An. maculipennis.l.* was present at all sampling stations, with a total of 353 specimens sampled.

A.4 APPENDIX D - Eigenvectors and eigenvalues

The characteristic equation of the ODE population dynamics model can be written as:

$$\begin{pmatrix} a_{1,1}-i\omega & 0 & 0 & 0 & 0 & 0 & a_{17} & 0 & 0 & a_{1,10} \\ a_{2,1} & a_{2,2}-i\omega & 0 & 0 & 0 & 0 & 0 & 0 & 0 & 0 \\ 0 & a_{3,2} & a_{3,3}-i\omega & 0 & 0 & 0 & 0 & 0 & 0 & 0 \\ 0 & 0 & a_{4,3} & a_{4,4}-i\omega & 0 & 0 & 0 & 0 & 0 & 0 \\ 0 & 0 & 0 & a_{5,4} & a_{5,5}-i\omega & 0 & 0 & 0 & 0 & 0 \\ 0 & 0 & 0 & 0 & a_{6,5} & a_{6,6}-i\omega & 0 & 0 & 0 & 0 \\ 0 & 0 & 0 & 0 & 0 & a_{7,6} & a_{7,7}-i\omega & 0 & 0 & 0 \\ 0 & 0 & 0 & 0 & 0 & 0 & a_{8,7} & a_{8,8}-i\omega & 0 & a_{810} \\ 0 & 0 & 0 & 0 & 0 & 0 & 0 & a_{9,8} & a_{9,9}-i\omega & 0 \\ 0 & 0 & 0 & 0 & 0 & 0 & 0 & 0 & a_{10,9} & a_{10,10}-i\omega \end{pmatrix} \begin{pmatrix} \hat{E} \\ \hat{L} \\ \hat{P} \\ \hat{A_{em}} \\ \hat{A_{b1}} \\ \hat{A_{g1}} \\ \hat{A_{o1}} \\ \hat{A_{b2}} \\ \hat{A_{g2}} \\ \hat{A_{o2}} \end{pmatrix} = -i\omega \begin{pmatrix} \hat{E} \\ \hat{L} \\ \hat{P} \\ \hat{A_{em}} \\ \hat{A_{b1}} \\ \hat{A_{g1}} \\ \hat{A_{o1}} \\ \hat{A_{b2}} \\ \hat{A_{g2}} \\ \hat{A_{o2}} \end{pmatrix}$$

with:

$$\begin{aligned}
a_{1,1} &= i\omega + \mu_E + f_E \\
a_{1,7} &= -\gamma_{Ao} \cdot \beta_1 \\
a_{1,10} &= -\gamma_{Ao} \cdot \beta_2 \\
a_{2,1} &= -f_E \\
a_{2,2} &= i\omega + m_L + f_L \\
a_{3,2} &= -f_L \\
a_{3,3} &= i\omega + m_P + f_P \\
a_{4,3} &= -f_P \sigma e^{-\mu_{em}} \\
a_{4,4} &= i\omega + m_A + \gamma_{Aem} \\
a_{5,4} &= -\gamma_{Aem} \\
a_{5,5} &= i\omega + m_A + \mu_r + \gamma_{Ab} \\
a_{6,5} &= -\gamma_{Ab} \\
a_{6,6} &= i\omega + m_A + f_{Ag} \\
a_{7,6} &= -f_{Ag} \\
a_{7,7} &= i\omega + m_A + \mu_r + \gamma_{Ao} \\
a_{8,7} &= -\gamma_{Ao} \\
a_{8,8} &= i\omega + m_A + \mu_r + \gamma_{Ab} \\
a_{8,10} &= -\gamma_{Ao} \\
a_{9,8} &= -\gamma_{Ab} \\
a_{9,9} &= i\omega + m_A + f_{Ag} \\
a_{10,9} &= -f_{Ag} \\
a_{10,10} &= i\omega + m_A + \mu_r + \gamma_{Ao}
\end{aligned}$$

The parameters functions are listed in Chapter 3, Table 3.4. Solving for T = 20 °C. We get the following eigenvalues:

$$\begin{aligned}
\lambda_1 &= 2.14444\\
\lambda_2 &= 1.973\\
\lambda_3 &= 1.41022\\
\lambda_4 &= 1.18034\\
\lambda_5 &= 0.834429 - 0.144502i\\
\lambda_6 &= 0.834429 + 0.144502i\\
\lambda_7 &= 0.130386 - 0.282081i\\
\lambda_8 &= 0.130386 + 0.282081i\\
\lambda_9 &= 0.154534\\
\lambda_{10} &= -0.124548
\end{aligned}$$

λ_5 and λ_6 and λ_7 and λ_8 are complex conjugates pairs.
Expressing the solutions in the terms of frequencies $\omega = i\lambda$:

$$\begin{aligned}
\omega_1 &= -\frac{2.14444}{i} = 2.14444i\\
\omega_2 &= -\frac{1.973}{i} = 1.973i\\
\omega_3 &= -\frac{1.41022}{i} = 1.41022i\\
\omega_4 &= -\frac{1.18034}{i} = 1.18034i\\
\omega_5 &= -\frac{0.834429 + 0.144502i}{i} = 0.834429i - 0.144502\\
\omega_6 &= -\frac{0.834429 - 0.144502i}{i} = 0.834429i + 0.144502\\
\omega_7 &= -\frac{0.130386 + 0.282081i}{i} = 0.130386i - 0.282081\\
\omega_8 &= -\frac{0.130386 - 0.282081i}{i} = 0.130386i + 0.282081\\
\omega_9 &= -\frac{0.154534}{i} = 0.154534i\\
\omega_{10} &= \frac{0.124548}{i} = -0.124548i
\end{aligned}$$

The list of eigenvectors is given below:

$$\psi_1 = \begin{pmatrix} -0.976662 + 0 \cdot i \\ 0.213921 + 0 \cdot i \\ -0.00280433 + 0 \cdot i \\ 0.000143807 + 0 \cdot i \\ -0.000147524 + 0 \cdot i \\ 0.0000679707 + 0 \cdot i \\ 0.0134056 + 0 \cdot i \\ 0.000148434 + 0 \cdot i \\ -0.00006839 + 0 \cdot i \\ -0.0134883 + 0 \cdot i \end{pmatrix} \psi_2 = \begin{pmatrix} 0.972424 + 0.i \\ -0.232052 + 0.i \\ 0.00332357 + 0.i \\ -0.000208641 + 0.i \\ 0.000252957 + 0.i \\ -0.00012797 + 0.i \\ -0.000117673 + 0.i \\ 0.0190153 + 0.i \\ -0.00961976 + 0.i \\ -0.0088457 + 0.i \end{pmatrix} \psi_3 = \begin{pmatrix} 0.946847 + 0.i \\ -0.319913 + 0.i \\ 0.00658171 + 0.i \\ -0.00156438 + 0.i \\ 0.0047057 + 0.i \\ -0.00350965 + 0.i \\ -0.000756277 + 0.i \\ 0.0258325 + 0.i \\ -0.0192666 + 0.i \\ -0.00415167 + 0.i \end{pmatrix}$$

$$\psi_4 = \begin{pmatrix} -0.866933 + 0.i \\ 0.352852 + 0.i \\ -0.00883434 + 0.i \\ -0.0152021 + 0.i \\ 0.115762 + 0.i \\ -0.107085 + 0.i \\ -0.0175776 + 0.i \\ -0.2289 + 0.i \\ 0.211741 + 0.i \\ 0.0347567 + 0.i \end{pmatrix} \psi_5 = \begin{pmatrix} -0.865373 + 0.i \\ 0.491935 - 0.0914337i \\ -0.0169051 + 0.00682171i \\ -0.0021835 + 0.0000320456i \\ -0.00834113 - 0.00596841i \\ 0.0133824 + 0.00548172i \\ 0.00152544 + 0.000830517i \\ 0.00413865 + 0.00456872i \\ -0.00716177 - 0.00492536i \\ -0.000790147 - 0.000682235i \end{pmatrix} \psi_6 = \begin{pmatrix} -0.865373 + 0.i \\ 0.491935 + 0.0914337i \\ -0.0169051 - 0.00682171i \\ -0.0021835 - 0.0000320456i \\ -0.00834113 + 0.00596841i \\ 0.0133824 - 0.00548172i \\ 0.00152544 - 0.000830517i \\ 0.00413865 - 0.00456872i \\ -0.00716177 + 0.00492536i \\ -0.000790147 + 0.000682235i \end{pmatrix}$$

$$\psi_7 = \begin{pmatrix} -0.134951 - 0.518544i \\ 0.840505 + 0.i \\ -0.00269413 + 0.0789545i \\ -0.000973651 + 0.00326187i \\ -0.00230867 + 0.00341954i \\ -0.0118301 - 0.00333284i \\ -0.000876096 - 0.000384644i \\ -0.000711938 - 0.00158551i \\ 0.00381881 - 0.00349591i \\ 0.000332154 - 0.000228307i \end{pmatrix} \psi_8 = \begin{pmatrix} -0.134951 + 0.518544i \\ 0.840505 + 0.i \\ -0.00269413 - 0.0789545i \\ -0.000973651 - 0.00326187i \\ -0.00230867 - 0.00341954i \\ -0.0118301 + 0.00333284i \\ -0.000876096 + 0.000384644i \\ -0.000711938 + 0.00158551i \\ 0.00381881 + 0.00349591i \\ 0.000332154 + 0.000228307i \end{pmatrix} \psi_9 = \begin{pmatrix} -0.120407 + 0.i \\ 0.564298 + 0.i \\ -0.443248 + 0.i \\ -0.020195 + 0.i \\ -0.0263591 + 0.i \\ -0.337634 + 0.i \\ -0.0268629 + 0.i \\ 0.0462151 + 0.i \\ 0.591968 + 0.i \\ 0.0470983 + 0.i \end{pmatrix}$$

$$\psi_{10} = \begin{pmatrix} 0.367119 + 0.i \\ -0.924714 + 0.i \\ -0.100003 + 0.i \\ -0.0036022 + 0.i \\ -0.00356542 + 0.i \\ -0.00906271 + 0.i \\ -0.000632393 + 0.i \\ -0.00158088 + 0.i \\ -0.00401833 + 0.i \\ -0.000280398 + 0.i \end{pmatrix}$$

The corresponding set of normal modes is:

$$\Omega_1(t) = \Omega_1(0) \cdot e^{-214444t} \tag{A.13a}$$

$$\Omega_2(t) = \Omega_2(0) \cdot e^{-1.973t} \tag{A.13b}$$

$$\Omega_3(t) = \Omega_3(0) \cdot e^{-1.41022t} \tag{A.13c}$$

$$\Omega_4(t) = \Omega_4(0) \cdot e^{-1.18034t} \tag{A.13d}$$

$$\Omega_5(t) = \Omega_5(0) \cdot e^{(-0.834429-0.144502i)t} \tag{A.13e}$$

$$\Omega_6(t) = \Omega_6(0) \cdot e^{(-0.834429+0.144502i)t} \tag{A.13f}$$

$$\Omega_7(t) = \Omega_7(0) \cdot e^{(-0.130386-0.282081i)t} \tag{A.13g}$$

$$\Omega_8(t) = \Omega_8(0) \cdot e^{(-0.130386+0.282081i)t} \tag{A.13h}$$

$$\Omega_9(t) = \Omega_9(0) \cdot e^{-0.154534t} \tag{A.13i}$$

$$\Omega_{10}(t) = \Omega_{10}(0) \cdot e^{0.124548t} \tag{A.13j}$$

Relating to the eigenvalues we see that eq. (A.13e) and eq. (A.13f), as well as eq. (A.13g) and eq. (A.13h) are complex conjugate pairs. The modes with amplitude set to 1 are visualized in Figure A.36.

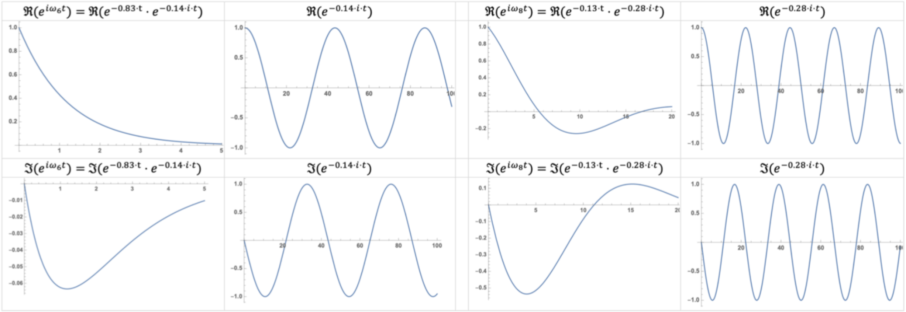

Figure A.36: The real (top) and imaginary (bottom) parts of the exponential terms corresponding to Ω_6(1^{st} and 2^{nd}column) and Ω_8(3^{rd} and 4^{th}column) are shown. With the combined decaying and oscillatory (1^{st} and 3^{rd} column) and only the oscillatory terms (2^{nd} and 4^{th}).

A.5 APPENDIX E - Normal mode initialization

We have obtained the set of modes that are present in the ODE system evaluated at a fixed temperature. We see that, depending on the temperature, the frequency of the modes can assume a wide range of values. The high-frequency modes generate noisy oscillations in the output that might not correspond to reality and could be considered undesirable. The normal mode initialization technique provides a way of eliminating the unwanted harmonics, by transforming the original set of equations into a system that allows initialization which controls the amplitudes of the modes in such a way that the high-frequency modes are not excited.

In this section we will examine the feasibility of applying normal modes initialization for a specific run of the ODE *Culex pipiens* model. With the main aim of producing a more balanced integration which would result in a smoother and less noisy curve.

We continue the analysis presented in Section 6.3.2. The steps of the initialization procedure which are outlined in the previous section can be summarised as follows: (i) Linearise the system around the state corresponding to a specific temperature; (ii) Express the dependent variables as $y = y \cdot e^{i\omega t}$; (iii) Formulate the eigenvalue problem $[M - \lambda I]\, \Psi = 0$, where $\lambda = -i\omega$; solve $detM = 0$ for ω; (iv) Diagonalize the matrix as $GDG^T = M$. Where G is a matrix of eigenvectors; (v) Transform to eigenspace; (vi) Formulate the normal mode system of equations; (vii) Solve for E and P, keeping the adult stages and the aquatic larva stage constrained (X_s); (viii) Transform back to real space.

From equations 6.45 and A.13 we can rewrite $(E(t), L(t), ...A_{o2}(t))$ in terms of the eigenvectors and normal modes as follows:

$$\hat{E}(t) = \psi_1^E \cdot \Omega_1 + \psi_2^E \cdot \Omega_2 + \psi_3^E \cdot \Omega_3 + \psi_4^E \cdot \Omega_4 + \psi_5^E \cdot \Omega_5 + \psi_6^E \cdot \Omega_6 + \psi_7^E \cdot \Omega_7 + \psi_8^E \cdot \Omega_8 + \psi_9^E \cdot \Omega_9 + \psi_{10}^E \cdot \Omega_{10} \tag{A.14}$$

which can be expanded to:

$$\begin{gathered}
\hat{E}(t) = \psi_1^E \cdot \Omega_1(0) \cdot e^{-214444t} + \\
\psi_2^E \cdot \Omega_2(0) \cdot e^{-1.973t} + \\
\psi_3^E \cdot \Omega_3(0) \cdot e^{-1.41022t} + \\
\psi_4^E \cdot \Omega_4(0) \cdot e^{-1.18034t} + \\
\psi_5^E \cdot \Omega_5(0) \cdot e^{(-0.834429-0.144502I)t} + \\
\psi_6^E \cdot \Omega_6(0) \cdot e^{(-0.834429+0.144502I)t} + \\
\psi_7^E \cdot \Omega_7(0) \cdot e^{(-0.130386-0.282081I)t} + \\
\psi_8^E \cdot \Omega_8(0) \cdot e^{(-0.130386+0.282081I)t} + \\
\psi_9^E \cdot \Omega_9(0) \cdot e^{-0.154534t} + \\
\psi_{10}^E \cdot \Omega_{10}(0) \cdot e^{0.124548t}
\end{gathered} \tag{A.15}$$

ψ_i^E (i = 1,10) are defined in Appendix A.4, and $\Omega_i(0)$ (i = 1,10) can be written in terms of $\hat{E}(0), \hat{L}(0), \hat{P}(0), \hat{Aem}(0)$... from the relation $|\Omega_1(0)\ \Omega_2(0)\ ...\ \Omega_{10}(0)|^T = E^T\, |E(0)\ L(0)\ ...\ A_{o2}(0)|^T$. The same can be performed for the other 9 variables.

Here we see that we have moved from the original coupled ODE system to a decoupled set of equations.

An arbitrary initial state would have non-zero initial amplitudes Ω_i. , From the normal mode system of equations (eq. (A.13)), we see that by setting the initial amplitudes $\Omega_i(0)$ to zero they would remain zero for all t.

The objective of the initialization is to find the set of $(\hat{E}_1\ \hat{L}_1\ ...\hat{A}_{o21})$ at t=0 that lead to the elimination of the high-frequency motions. This values are calculated by setting $\Omega_i(0) = 0$. By solving this system of equations we get the desired relationship between $(\hat{E}_1\ \hat{L}_1\ ...\hat{A}_{o21})$. However, to find the actually initialization state we need to keep a subset of the variables constrained and calculate the rest from the equality. Here it is assumed that $(\hat{E}, \hat{A}_{em}, \hat{A}_{b1}, \hat{A}_{g1}, \hat{A}_{b1}, \hat{A}_{o1}, \hat{A}_{b2}, \hat{A}_{g2}, \hat{A}_{o2})$ are constrained and we solve for $\hat{E}$ and $\hat{P}$.

After solving for the unknown variables, the results of the analysis yielded negative solutions for E and P which is not realistic. This is because the system is mathematically well defined over $\mathbb{R}^{10}$; however, the region of interest for a real vector population is defined as:

$$\Delta = \left\{ \begin{array}{lr} & E \geq 0 \\ & L \geq 0 \\ & P \geq 0 \\ & A_{em} \geq 0 \\ (E, L, P, A_{em}, & A_{b1} \geq 0 \\ A_{b1}, A_{g1}, A_{o1}, & A_{g1} \geq 0 \\ A_{b2}, A_{g2}, A_{o2}) & A_{o1} \geq 0 \\ & A_{b2} \geq 0 \\ & A_{g2} \geq 0 \\ & A_{o2} \geq 0 \end{array} \right\} \tag{A.16}$$

Non-the-less, log transforming the negative values we see that the initialization does results in a smooth integration with an integration that does not excite the high-frequency oscillatory modes.

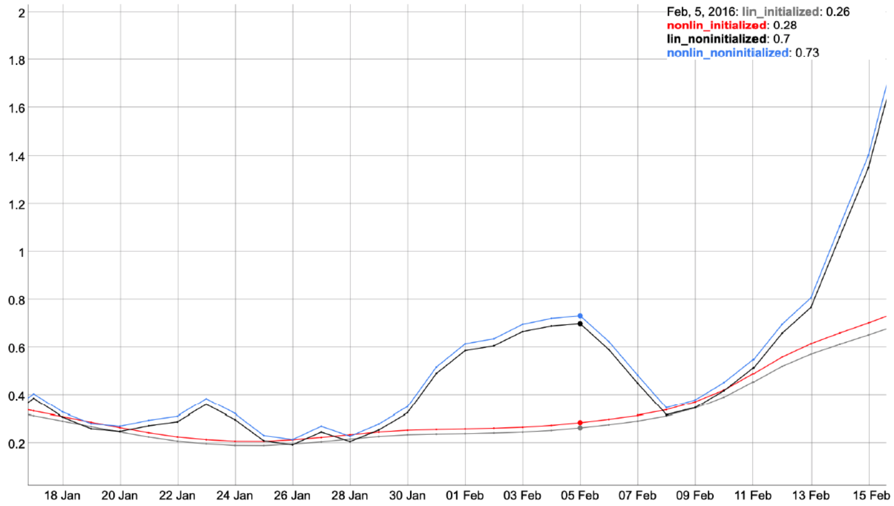

Figure A.37: log(Y+a) transformed simulations showing two initialized (red and gray) model runs and two non-initialized (black and blue) runs. For the linearised and non-linearised set of model equations.

A.6 APPENDIX F - Overview of model parameters

The parameter functions for the temperature interval [-10 °C, 40 °C] are presented in Figures A.38 and A.39. Moreover the simulated range for Bahariya (2017-2018), Petrovaradin (2016-2017) and Guadeloupe (2015 – 2018) are shown in Table A.5.

Table A.5: Simulated parameter ranges

Parameter	Bahariya	Petrovaradin	Guadeloupe
f_E	(0.1254, 0.9966)	(0.01697, 0.551357)	(1,1)
f_L	(0.003088, 0.175938)	(0.001386, 0.231622)	(0.4135, 0.9277)
f_P	(0.01235, 0.70375)	(0.0005544, 0.0926489)	(0.6823, 1.5307)
f_{Ag}	(0.0000, 0.4275)	(0.0000, 0.34406)	(0.1583, 0.2330)
m_A	(0.02329, 0.25000)	(0.02330, 0.2500)	(0.06033, 0.07760)
m_P	(0.01460, 0.03207)	(0.01460, 277.18647)	(0.12,0.12)
m_L	(0.03040, 0.04787)	(0.03040, 277.20227)	(0.03670, 0.03671)

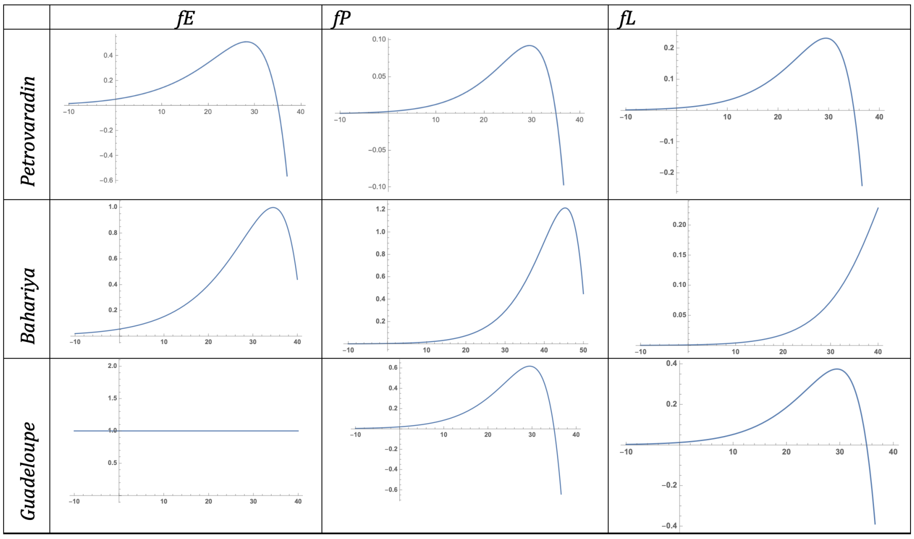

Figure A.38: Aquatic development rates: the development rate [$1/day$] (y-axis) is shown as a funciton of temperature [$°C$] (x-axis).

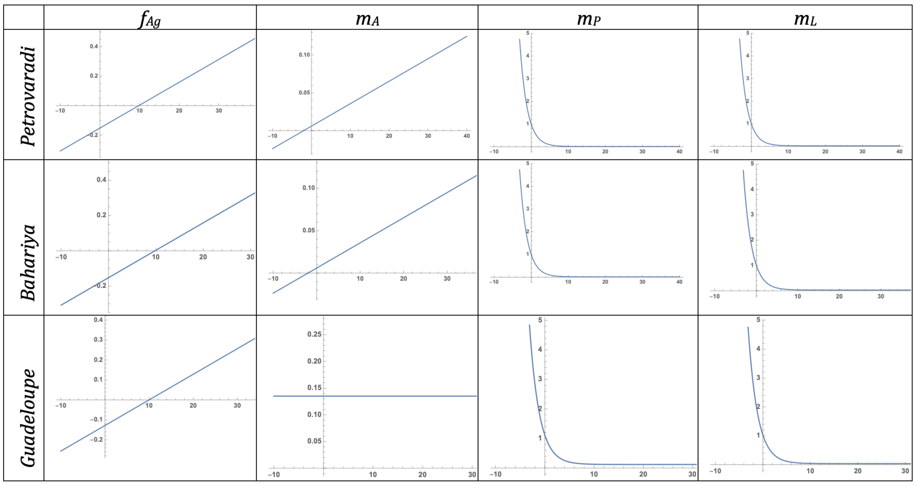

Figure A.39: Adult mortality rates and development rates [$1/day$] as a function of temperature [$°C$] (x-axis).

A.7 APPENDIX G - 2nd equilibrium

$\boldsymbol{X}_{eq}^2 = (E^*, L^*, P^*, A_{em}^*, A_{b1}^*, A_{g1}^*, A_{o1}^*, A_{b2}^*, A_{g2}^*, A_{o2}^*)$. The trivial solution is $\mathbf{X}_{eq}^1 = 0$ and the second equilibrium has the following solution for L:

$$L = -\frac{W_n\left(-\frac{c \cdot e^{\left(-\frac{ac}{b}\right)}}{b}\right)}{c} - \frac{a}{b} \tag{A.17}$$

W_n is the principle solution of the Lambert W function with b, c $\neq 0$. where a, b, c are:

$$a = \frac{(f_L + m_L) \cdot (f_E + \mu_E)}{f_E \cdot \gamma_{Ao}} \cdot e^{\mu_{em}} \cdot \frac{1}{\xi} \tag{A.18}$$

$$b = \frac{m_L \cdot (f_E + \mu_E)}{f_E \cdot \kappa_L \cdot \gamma_{Ao}} \cdot e^{\mu_{em}} \cdot \frac{1}{\xi} \tag{A.19}$$

$$c = -\frac{\mu_{em} f_L}{(m_P + f_P) \cdot \kappa_P}$$

where ξ is:

$$\xi = \Bigg(\frac{f_{Ag} f_L f_P \beta_1 \gamma_{Ab} \gamma_{Aem} \sigma}{(f_{Ag} + m_A)(f_P + m_P)(m_A + \gamma_{Aem})(m_A + \gamma_{Ab} + \mu_r)(m_A + \gamma_{Ao} + \mu_r)}$$

$$+ \frac{f_{Ag}^2 f_L f_P \beta_2 \gamma_{Ab}^2 \gamma_{Aem} \gamma_{Ao} \sigma}{(f_{Ag} + m_A)^2 (f_P + m_P)(m_A + \gamma_{Aem})(m_A + \gamma_{Ab} + \mu_r)^2}$$

$$\frac{1}{(m_A + \gamma_{Ao} + \mu_r)^2 (1 - \frac{f_{Ag} \gamma_{Ab} \gamma_{Ao}}{(f_{Ag}+m_A)(m_A+\gamma_{Ab}+\mu_r)(m_A+\gamma_{Ao}+\mu_r)}} \Bigg)$$

The other variables expressed through L are:

$$E = \frac{\gamma_{Ao} \left(\frac{Ag_2 \cdot f_{Ag} \cdot \beta_2}{m_A+\gamma_{Ao}+\mu_r} + \frac{e^{-\mu_{em} \cdot (1+\frac{f_L \cdot L}{\kappa_P \cdot (f_P+m_P)})} f_{Ag} f_L f_P L \beta_1 \gamma_{Ab} \gamma_{Aem} \sigma}{(f_{Ag}+m_A)(f_P+m_P)(m_A+\gamma_{Aem})(m_A+\gamma_{Ab}+\mu_r)(m_A+\gamma_{Ao}+\mu_r)} \right)}{f_E + m_E} \tag{A.20a}$$

$$P = \frac{f_L \cdot L}{f_P + m_P} \tag{A.20b}$$

$$A_{em} = \frac{e^{-\mu_{em}(1+\frac{f_L L}{\kappa_P (f_P+m_P)})} f_L f_P L \sigma}{(f_P + m_P)(m_A + \gamma_{Aem})} \tag{A.20c}$$

$$A_{b1} = \frac{e^{-\mu_{em}(1+\frac{f_L L}{\kappa_P (f_P+m_P)})} f_L f_P L \sigma \gamma_{Aem}}{(f_P + m_P)(m_A + \gamma_{Aem})(ma + \gamma_{Ab} + \mu_r)} \tag{A.20d}$$

$$A_{g1} = \frac{e^{-\mu_{em}(1+\frac{f_L L}{\kappa_P (f_P+m_P)})} f_L f_P L \sigma \gamma_{Ab} \gamma_{Aem}}{(f_P + m_P)(m_A + \gamma_{Aem})(ma + \gamma_{Ab} + \mu_r)(f_{Ag} + m_A)} \tag{A.20e}$$

$$A_{o1} = \frac{e^{-\mu_{em}(1+\frac{f_L L}{\kappa_P (f_P+m_P)})} f_L f_P L f_{Ag} \sigma \gamma_{Ab} \gamma_{Aem}}{(f_P + m_P)(m_A + \gamma_{Aem})(ma + \gamma_{Ab} + \mu_r)(f_{Ag} + m_A)(m_A + \gamma_{Ao} + \mu_r)} \tag{A.20f}$$

$$A_{b2} = \frac{e^{-\mu_{em}(1+\frac{f_L L}{\kappa_P (f_P+m_P)})} f_L f_P L f_{Ag} \sigma \gamma_{Ab} \gamma_{Aem} \gamma_{Ao}}{(f_P + m_P)(m_A + \gamma_{Aem})(ma + \gamma_{Ab} + \mu_r)^2 (f_{Ag} + m_A)(m_A + \gamma_{Ao} + \mu_r)} \tag{A.20g}$$

$$\cdot \left(\frac{1}{1 - \frac{f_{Ag}\gamma_{Ab}\gamma_{Ao}}{(f_{Ag}+m_A)(m_A+\gamma_{Ab}+\mu_r)(m_A+\gamma_{Ao}+\mu_r)}} \right)$$

$$A_{g2} = \frac{e^{-\mu_{em}(1+\frac{f_L L}{\kappa_P(f_P+m_P)}} f_L f_P L f_{Ag} \sigma \gamma_{Ab}^2 \gamma_{Aem} \gamma_{Ao}}{(f_P + m_P)(m_A + \gamma_{Aem})(ma + \gamma_{Ab} + \mu_r)^2 (f_{Ag} + m_A)^2 (m_A + \gamma_{Ao} + \mu_r)} \tag{A.20h}$$

$$\cdot \left(\frac{1}{1 - \frac{f_{Ag}\gamma_{Ab}\gamma_{Ao}}{(f_{Ag}+m_A)(m_A+\gamma_{Ab}+\mu_r)(m_A+\gamma_{Ao}+\mu_r)}} \right)$$

$$A_{o2} = \frac{e^{-\mu_{em}(1+\frac{f_L L}{\kappa_P(f_P+m_P)})} f_L f_P L f_{Ag}^2 \sigma \gamma_{Ab}^2 \gamma_{Aem} \gamma_{Ao}}{(f_P + m_P)(m_A + \gamma_{Aem})(ma + \gamma_{Ab} + \mu_r)^2 (f_{Ag} + m_A)^2 (m_A + \gamma_{Ao} + \mu_r)^2} \tag{A.20i}$$

$$\cdot \left(\frac{1}{1 - \frac{f_{Ag}\gamma_{Ab}\gamma_{Ao}}{(f_{Ag}+m_A)(m_A+\gamma_{Ab}+\mu_r)(m_A+\gamma_{Ao}+\mu_r)}} \right)$$

A.8 APPENDIX H

Here we examine weather the daily ERA5 2 m temperature for four different points across the island is sufficiently similar to justify to use a single model output (at Pointe-à-Pitre) for the whole island. In the graphs below we see an example interval with all four forcing temperature time-series (Figure A.40) and the corresponding model outputs (Figure A.41).

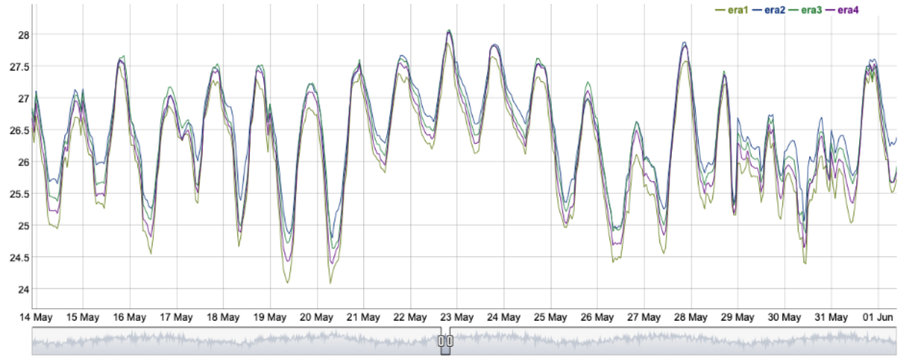

Figure A.40: ERA5 t2m forcing temperature for the ERA1−4 points points from the ERA5 native grid.

Figure A.41: Model output (emerging adults) produced by ERA5 forcing for the ERA1−4.

We see that the temperature and model series are almost identical for the examined interval. To quantify the similarity between the time series we examine a composite ARIMA model fitted to both time series and then an F test to confirm that the parameters are significantly similar. Moreover, in a second step the similarity between the two time-series is assessed by considering the ability of one time series to forecast the other using the Granger test.

A.8.1 ARIMA and F test

In the table below we see that the ARIMA parameters are very similar (table A.6) and the F-test and p-values indicating that the true ratio of variance is different than 1 can be rejected (table A.7).

Table A.6: Model coefficients

		Coefficients				
	Model	AR1	AR2	AR3	AR4	MA1
Era1	ARIMA (4,0,0)	1.2444	-0.2394	-0.0052	-0.1211	-0.9844
Era2	ARIMA (4,0,1)	1.3639	-0.4123	0.0511	-0.1119	-0.9807
Era3	ARIMA (4,0,1)	1.3314	-0.3356	0.0187	-0.1297	-0.9812
Era4	ARIMA (4,0,1)	1.2980	-0.2859	0.0026	-0.1340	-0.9817

Table A.7: F test; p values (alternative hypothesis: true ratio of variance is not equal to 1

Era1	Era2	Era3	Era4
Era1			
Era2	0.8881		
Era3	0.9242	0.9636	
Era4	0.9554	0.9324	0.9687

A.8.2 Granger causality test

The Granger causality test is a statistical hypothesis test to ascertain the degree to which one time series can be suitable for forecasting another time series. A time series X is said to Granger-cause Y if it can be shown, applying a series of t-tests and F-tests on lagged values of X and Y, that those X values provide statistically significant information about future values of Y.

Table A.8: F test, p-values

Era1	Era2	Era3	Era4
Era1			
Era2	$2.2 \cdot 10^{-16}$		
Era3	$2.2 \cdot 10^{-16}$	$2.2 \cdot 10^{-16}$	
Era4	$2.2 \cdot 10^{-16}$	$5.9 \cdot 10^{-13}$	$2.2 \cdot 10^{-16}$

About the author

Mina Petrić (1988) graduated in 2015 as Master of Science in Physics (University of Novi Sad, Serbia). During her studies she completed courses on fluid dynamics, dynamic meteorology and micrometeorology with special focus on the physics of the turbulent Planetary Boundary Layer (PBL) and surface and boundary layer parameterization schemes.

Her MSc thesis focused on modelling the current and future climatic suitability for the establishment of *Aedes albopictus* in Serbia through the use of three mechanistic models. Expected change in spatial patterns of the vector and general trends concerning future distributions were analysed with results obtained from climatic projections from four different statistical and dynamical regional climate models.

Mina joined Avia-GIS in 2016 as a PhD student under the MosqDyn project, where she works with the design and implementation of meteorological wireless sensor networks (WSN) within an IAP project of the European Space Agency (ESA).

Acknowledgements

Results of the research presented in this dissertation were realised under the MosqDyn #IWT.155010 research and development project by Avia-GIS funded by the Flanders Innovation and Entrepreneurship agency (VLAIO), the VectorNet #OC/EFSA/AHAW/2013/02 joint initiative of the European Food Safety Authority (EFSA) and the European Centre for Disease Prevention and Control (ECDC), the SmartSenZ service developed by Avia-GIS NV within the VECMAP Demo European Space Agency (ESA) IAP demonstration project #4000104503/11/NL/US and the SenZitall #4000123267/18/NL/MM/gm ESA IAP project.

University of Novi Sad
Ghent University
Key word documentation

Accession number: **ANO**	
Identification number: **INO**	
Document type: **DT**	Monograph documentation
Type of record: **TR**	Textual printed material
Contents code: **CC**	Doctoral dissertation
Author: **AU**	Mina Petrić
Mentor: **MN**	Prof. dr. Branislava Lalić Prof. dr. Milica Pavkov Hrvojević Prof. dr. Piet Termonia Dr. Bert Van Schaeybroeck
Industrial promoters: **IP**	Dr. Els Ducheyne Cedric Marsboom
Title: **TI**	*Modelling the influence of meteorological conditions on mosquito vector population dynamics (Diptera, Culicidae)*
Language of text: **LT**	English
Language of abstract: **LA**	English/Serbian/Dutch.
Country of publication: **CP**	Serbia/Belgium
Locality of publication: **LP**	Vojvodina/Flanders
Publication year: **PY**	2020
Publisher: **PU**	Author's reprint
Publication place: **PP**	Faculty of Sciences, University of Novi Sad, Trg Dositeja Obradovića 4, Novi Sad; Faculty of Sciences, Ghent University, Krijgslaan 281 9000 Gent

Physical description: **PD**	9 chapters / 203 pages / 110 figures / 45 tables / 216 references / 8 appendices
Scientific field **SF**	Physics
Scientific discipline **SD**	Meteorology and environmental modelling
Subject, Key words **SKW**	Vector population dynamics modelling, *Aedes aegypti, Culex pipiens*
UC	
Holding data: **HD**	Library of Department of Physics, Faculty of Sciences in Novi Sad Library of Department of Astronomy and Physics, Faculty of Sciences in Ghent
Note: **N**	Results of the research presented in this dissertation were realised under the MosqDyn *#IWT.155010* research and development project by Avia-GIS funded by the Flanders Innovation and Entrepreneurship agency (VLAIO), the VectorNet *#OC/EFSA/AHAW/2013/02* joint initiative of the European Food Safety Authority (EFSA) and the European Centre for Disease Prevention and Control (ECDC), the SmartSenZ service developed by Avia-GIS NV within the VECMAP Demo European Space Agency (ESA) IAP demonstration project *#4000104503/11/NL/US* and the SenZitall *#4000123267/18/NL/MM/gm* ESA IAP project.
Abstract: **AB**	Meteorological conditions have a significant influence on the time of occurrence, abundance and activity of the mosquito vector. In the current context of climate change, it is of great importance to assess the impact of shifts in climatic conditions on the suitability for the establishment and annual activity of the vector species. Moreover, changes in the variability of meteorological elements and their extremes can generate unexpected changes in the mosquito vector population which in turn have an important effect on human health. One of the ways to put these causes and effects into perspective is to simulate the activity of the vector within a process-based framework which allows for the analysis of the contribution of individual factors on the different life stages of the vector. Such analysis is presented by use of sophisticated dynamical models simulating the characteristics of the biological population, forced by observed meteorological data, capturing the local

micro-environment of the vector habitat, and validated by the observed entomology.

Numerical models are being developed to model vector population dynamics and the expected circulation of the virus within a closed system. Two modelling approaches are standardly applied to modelling vector population dynamics: Mechanistic and Stochastic. The advantage of mechanistic over statistical models is that they can provide a deterministic framework allowing for the isolated evaluation of each input parameter and their effect on the modelled system. Mechanistic dynamical models are used to describe the biophysical processes or part of the process as a response to changes in the meteorological conditions.

The work carried out in this thesis can be summarized as follows: (i) Analysis of the association between the most important abiotic drivers influencing the population dynamics, annual activity and time of occurrence of *Culex pipiens* and *Aedes aegypti*; (ii) Identifying the most important climatic factors and model settings as a function of climatic characteristics of the study region; (iii) Modelling the vector population dynamics and stability analysis of the dynamical system (iv) Analysis of different verification techniques and implications in terms of model application; (v) Feasibility analysis of improving the model with a Land-Surface Parametrization scheme and short-range forecasting of pest population dynamics.

Accepted on Scientific Board on: **AS**	12/05/2020
Defended: **DE**	
Thesis Defence Board: **DB**	
President:	Prof. dr. Vladimir Djurdjevic, University of Belgrade, Serbia
Member:	Prof. dr. Igor Balaž, University of Novi Sad, Serbia
Member:	Prof. dr. Rafiq Hamdi, Ghent University, Belgium
Member:	Dr. Guy Hendrickx, Avia-GIS NV, Belgium

Univerzitet u Novom Sadu
Univerzitet u Gentu
Ključna dokumentacijska informacija

Redni broj: **RBR**	
Identifikacioni broj: **IBR**	
Tip dokumentacije: **TD**	Monografska dokumentacija
Tip zapisa: **TZ**	Tekstualni štampani materijal
Vrsta rada (dipl., mag., dokt.): **VR**	Doktorska disertacija
Ime i prezime autora: **AU**	Mina Petrić
Mentor (titula, ime, prezime, zvanje): **MN**	Prof. dr. Branislava Lalić Prof. dr. Milica Pavkov Hrvojević Prof. dr. Piet Termonia Dr. Bert Van Schaeybroeck
Naslov rada: **NR**	*Modeliranje uticaja meteoroloških uslova na dinamiku populacije komarca vektora (Diptera: Culicidae)*
Jezik publikacije: **JP**	Engleski
Jezik izvoda: **JI**	Engleski/Srpski/Holandski
Zemlja publikovanja: **ZP**	Srbija/Belgija
Uže geografsko područje: **UGP**	Vojvodina/Flandrija
Godina: **GO**	2020
Izdavač: **IZ**	Autorski reprint
Mesto i adresa: **MA**	Prirodno-matematički fakultet, Trg Dositeja Obradovića 4, Novi Sad; Prirodno-matematički fakultet, Krijgslaan 281 9000 Gent

Fizički opis rada: **FO**	9 poglavlja / 203 stranica / 110 slika i grafikona / 45 tabela / 216 referenci / 8 priloga
Naučna oblast: **NO**	Fizika
Naučna disciplina: **ND**	Meteorologija i modeliranje životne sredine
Predmetna odrednica, ključne reči: **PO**	Modeliranje dinamike populacije vektora, *Aedes aegypti, Culex pipiens*
UDK	
Čuva se: **ČU**	Biblioteka departmana za fiziku, PMF-a u Novom Sadu Biblllioteka departmana za astronomiju i fiziku, PMF-a u Gentu
Važna napomena: **VN**	Rezultati istraživanja koji su prikazani u disertaciji su ostvareni u okviru MosqDyn *#IWT.155010* projekta: Flandrijske Agencije za Inovaciju i Preduzetništvo (VLAIO), VectorNet projekta *#OC/EFSA/AHAW/2013/02* ostvarenog u okviru EFSA i ECDC inicijative, SmartSenZ Avia-GIS projekta ostvarenog unutar VECMAP IAP projekta *#4000104503/11/NL/US* Evropske Svemirske Agencije (ESA) i SenZitall *#4000123267/18/NL/MM/gm* IAP ESA projekta.
Izvod: **IZ**	Meteorološki uslovi bitno utiču na vreme pojave, brojnost vektora i njihovu aktivnost. U uslovima evidentnih promene klime, od ogromne je važnosti sagledati uticaj očekivanih promena klime na pogodnost uslova na pojavu izabranih vektora. Takodje, značajne promene kolebanja meteoroloških elemenata u odnosu na višegodišnji prosek i sve češće pojave nepovoljnih vremenskih prilika dovode do neočekivanog ponašanja populacije komarca što značajno utiče na kvalitet života i zdravlje ljudi. Jedini način da se sagledaju uzroci i posledice navedenih pojava zasniva se na simulaciji aktivnosti i brojnosti vektora uz mogućnost testiranja uticaja svakog pojedinačnog faktora. Ovu mogućnost pružaju samo visoko sofistikovani dinamički modeli koju su prošli proces kalibracije i validacije zasnovan na izmerenim vrednostima meteoroloških elemenata i karakteristika biološke populacije. Sofistikovani modeli za simulaciju dinamike populacije vektora i očekivane cirkulacije vektorskih transmisivnih bolesti se koriste sa ciljem modeliranja potencijalnog rizika od zaraze i epidemije. Modeli za

simulaciju dinamike vektora mogu da se podele na dve glavne grupe: Mehanističke i Statističke. Prednost mehanističkih modela nad statističkim je što mogu da se koriste za evaluaciju uticaja izolovanog faktora na dinamički sistem i odgovarajuće promene brojnosti unutar svake faze u razvoju vektora. Mehanistički dinamički sistemi se koriste kako bi se opisao mehanizam biofizičkog procesa ili dela procesa u zavisnosti od forsirajuće veličine.

Predmet istraživanja u ovom radu jeste identifikovanje najznačajnijih bioloških i fizičkih procesa kao i odgovarajućih faktora koji utiču na brojnost i aktivnost vektora roda *Aedes* i *Culex*. Ciljevi istraživanja mogu da se sumiraju na sledeći način: (i) analiza najznačajnijih meteoroloških parametara koji utiču na vreme pojave, brojnost i aktivnost vektora *Aedes* i *Culex* roda; (ii) definisanje najznačajnijih klimatskih faktora i stepena osetljivosti procesa na njih; (iii) modeliranje dinamike populacije vektora i analiza stabilnosti dinamičkog sistema; (iv) verifikacija i analiza metoda verifikacije i validacije dinamičkog modela; (v) kratkoročna prognoza dinamike populacije komarca i formulacija hidrološkog modula upotrebom SURFEX površinske šeme sa ECOCLIMAP fiziogeografskim podacima.

Datum prihvatanja teme od strane NN veća: **DP**	12/05/2020
Datum odbrane: **DO**	
Članovi komisije: **KO**	
Predsednik	Prof. dr. Vladimir Đurđević, Vanredni profesor, Fizički fakultet u Beogradu, Srbija
Član	Prof. dr. Igor Balaž, Docent, Poljoprivredni fakultet u Novom Sadu, Srbija
Član	Prof. dr. Rafiq Hamdi, Vanredni profesor, Prirodno-matematički fakultet u Gentu, Belgija
Član	Dr. Guy Hendrickx, CEO, Avia-GIS NV, Belgija

Universiteit Gent
Universiteit Novi Sad
Trefwoord documentatie

Toegangsnummer: **TNO**	
Identificatie Nummer **INO**	
Type document: **DT**	Monografie documentatie
Type record: **TR**	Tekstueel bedrukt materiaal
Inhoud code: **IC**	Proefschrift
Auteur: **AU**	Mina Petrić
Mentor: **MN**	Prof. dr. Branislava Lalić Prof. dr. Milica Pavkov Hrvojević Prof. dr. Piet Termonia Dr. Bert Van Schaeybroeck
Industriële promotors: **IP**	Dr. Els Ducheyne Cedric Marsboom
Titel: **TI**	*Modellering van de invloed van meteorologische omstandigheden op de populatiedynamiek van muggenvector (Diptera, Culicidae)*
Taal van de tekst: **TT**	Engels
Taal van abstract: **TA**	Engels/Servisch/Nederlands
Land van publicatie: **LP**	Servië/België
Plaats van publicatie: **PP**	Vojvodina/Vlaanderen
Publicatiejaar: **PJ**	2020
Uitgeverij: **UG**	Herdruk van de auteur
Publicatie plaats: **PP**	Faculteit wetenschappen, Universiteit Novi Sad, Trg Dositeja Obradovića 4, Novi Sad; Faculteit wetenschappen, Universiteit Gent, Krijgslaan 281 9000 Gent
Fysieke beschrijving: **FB**	9 hoofdstukken / 203 pagina's / 110 figuren / 45 tabellen / 216 referenties / 8 bijlagen
Wetenschappelijk veld: **WV**	Fysica

Wetenschappelijke discipline: **WD**	Meteorologie en milieumodellering
Onderwerp, trefwoorden: **OTW**	Vector populatiedynamiek modellering, *Aedes aegypti, Culex pipiens*
UC	
Gegevens vasthouden: **GV**	Bibliotheek van de afdeling Fysica, faculteit Wetenschappen in Novi Sad; Bibliotheek van Afdeling Fysica en Sterrenkunde, Faculteit Wetenschappen in Gent
Notitie: **N**	Resultaten van het onderzoek gepresenteerd in dit proefschrift werden gerealiseerd onder het MosqDyn *#IWT.155010* onderzoeks- en ontwikkelingsproject van Avia-GIS gefinancierd door de Vlaamse Agentschap Innoveren & Ondernemen (VLAIO), binnen het gezamenlijk initiatief VectorNet *#OC/EFSA/AHAW/2013/02* van de Europese Autoriteit voor Voedselveiligheid (EFSA) en het Europees Centrum voor ziektepreventie en -bestrijding (ECDC), met behulp van de SmartSenZ service ontwikkeld door Avia-GIS NV, binnen het IAP demonstratie project voor VECMAP *#4000104503/11/NL/US* van de Europese Ruimtevaartorganisatie (ESA) en het SenZitall *#4000123267/18/NL/MM/gm* IAP project van de Europese Ruimtevaartorganisatie.
Abstract: **AB**	Meteorologische omstandigheden hebben een significante invloed op het tijdstip van voorkomen, het aantal en de activiteit van de muskiet vector. In de huidige context van klimaatverandering is het van groot belang om de verwachte impact van verschuivingen in klimatologische omstandigheden in te schatten op de geschiktheid voor de vestiging en de jaarlijkse activiteit van de vectorsoort. Bovendien kunnen veranderingen in de variabiliteit van meteorologische elementen en hun extremen, onverwachte veranderingen in de populatie van muggenvectoren veroorzaken die op hun beurt een belangrijk effect hebben op de menselijke gezondheid. Eén van de manieren om deze oorzaken en gevolgen in perspectief te plaatsen, is door de activiteit van de vector te simuleren binnen een procesgebaseerd kader dat de bijdragen van individuele factoren op de verschillende levensfasen van de vector analyseert. Een dergelijke analyse wordt uitgevoerd door gebruik te maken van geavanceerde dynamische modellen voor het simuleren van de eigenschappen van de biologische populatie, gedreven door waargenomen meteorologische gegevens, het incorporeren van de

lokale micro-omgeving van de vectorhabitat en gevalideerd door de waargenomen entomologie.

Numerische modellen worden ontwikkeld om vectorpopulatiedynamica en de verwachte circulatie van het virus binnen een gesloten systeem te modelleren. Twee modelleringsbenaderingen worden standaard toegepast op dynamische vectorpopulatie modellen: mechanistisch en stochastisch. Het voordeel van mechanistisch ten opzichte van statistische modellen is dat ze een deterministisch raamwerk kunnen bieden voor de geïsoleerde evaluatie van elke invoerparameter en hun effect op het gemodelleerde systeem. Mechanistische dynamische modellen worden gebruikt om de biofysische processen of een deel van het proces te beschrijven als een reactie op een verandering in een meteorologische toestand.

Het werk in dit proefschrift kan als volgt worden samengevat: (i) De analyse van het verband tussen de belangrijkste abiotische factoren die de populatiedynamiek, de jaarlijkse activiteit en het tijdstip van aanwezigheid van *Culex pipiens* en *Aedes aegypti* beïnvloeden; (ii) De identificatie van de belangrijkste klimatologische factoren en modelinstellingen als functie van de klimatologische kenmerken van de onderzoeksregio; (iii) De dynamische modellering van de vectorpopulatie en stabiliteitsanalyse van het dynamische systeem. (iv) De analyse van verschillende verificatietechnieken en de implicaties voor de toepassing van het model; (v) De haalbaarheidsanalyse van het verbeteren van het model met een parametrisatie voor het landgebruik en voorspelling op korte afstand van de dynamiek van de plaagpopulatie.

Geaccepteerd in de Wetenschappelijke Raad op: **WR**	12/05/2020
Verdedigde **VE**	
Thesis Defend Board: **DB**	
Voorzitter van de jury:	Prof. dr. Vladimir Djurdjevic, Universiteit van Belgrado, Servië
Lid van de jury:	Prof. dr. Igor Balaž, Universiteit Novi Sad, Servië
Lid van de jury:	Prof. dr. Rafiq Hamdi, Universiteit Gent, België
Lid van de jury:	Dr. Guy Hendrickx, Avia-GIS NV, België